ISOSPIN EQUILIBRATION IN FERMI-ENERGY HEAVY-ION NUCLEAR COLLISIONS

A Dissertation

by

LARRY WAYNE MAY JR.

Submitted to the Office of Graduate and Professional Studies of
Texas A&M University
in partial fulfillment of the requirements for the degree of

DOCTOR OF PHILOSOPHY

Chair of Committee,	Sherry J. Yennello
Committee Members,	Joseph B. Natowitz
	Charles M. Folden III
	Che-Ming Ko
	Aldo Bonasera
Head of Department,	François Gabbaï

August 2015

Major Subject: Chemistry

ABSTRACT

The nuclear Equation of State and the density dependence of the asymmetry energy have been explored via heavy-ion collisions of 35 MeV/nucleon ^{70}Zn,^{64}Ni+^{64}Zn and ^{64}Zn+^{70}Zn,^{64}Ni. The experimental data were collected on the NIMROD-ISiS (Neutron-Ion Multidetector for Reaction Oriented Dynamics with Indiana Silicon Sphere) 4π charged particle detector array coupled with the TAMU Neutron Ball at the Texas A&M University Cyclotron Institute which provides excellent isotopic resolution, event characterization and coverage of charged particles along with event-by-event measurement of neutron multiplicities.

The nature of isospin equilibration was examined via the use of the iBUU04 transport model and the Constrained Molecular Dynamics (CoMD) model coupled with the GEMINI statistical decay model. Both models provided insight into the nature of the heavy-ion collisions studied but both models must also be better understood in order to replicate the effects seen in the experimental data. An improved method of experimental impact parameter determination was demonstrated with the CoMD results.

Experimental measurements of the isoscaling parameter α, isobaric yield ratio for the A=3 isobar and reconstructed quasi-projectile isospin asymmetry were conducted with respect to the centrality of the collision. A new signature of isospin equilibration was proposed and observed in the experimental data: convergence of the quasi-projectile and quasi-target isospin asymmetries to each other as the interaction time increases. Finally, a direct comparison was made to previous works and found that the reaction systems studied experienced an isospin equilibration of approximately 75%.

DEDICATION

"If I have seen further it is by standing on the shoulders of giants."

- Sir Isaac Newton

ACKNOWLEDGEMENTS

I would like to thank my family and friends for their love and support during my graduate school career. The Cyclotron Institute faculty and staff were invaluable in their support of the experiment. The SJY research group was instrumental in helping to guide, refine and hone the knowledge and skills that allowed me to pursue this project. And finally I would like to thank Professor Sherry J. Yennello for her patience and guidance during this process, without her mentorship I firmly believe that I would not have been able to complete this degree. Thanks Sherry, for everything.

TABLE OF CONTENTS

LIST OF FIGURES

FIGURE Page

LIST OF TABLES

1. INTRODUCTION

A major goal in the field of nuclear science is to better understand the nuclear Equation-of-State (nEoS), the relationship between thermodynamic variables that describes the nature of nuclear matter. Specifically, the form of the nEoS for asymmetric nuclear matter (N≠Z) is not very well-known. Investigating this aspect of the nEoS and improving the measurements of experimental constraints will help to improve our knowledge of the nEoS as a whole. One method for examining asymmetric nuclear matter with respect to the nEoS is through the use of heavy-ion collisions (HICs) and the ability of these collisions to probe nuclear matter at asymmetries, densities and temperatures that differ from that of ground-state nuclei. The nEoS is an emergent property of nuclear matter that results from the individual nucleon-nucleon interactions within nuclei and has a wide impact on a variety of different nuclear as well as astrophysical processes.

1.1 Nuclear Equation of State

Ground-state nuclei are composed of nuclear matter at temperature T=0 MeV and a nuclear matter density of ρ_0=0.16 nucleons/fm^3 (known as saturation density). The Weizsäcker, or semi-empirical, mass formula [1, 2] was proposed in 1935 and reasonably describes ground-state nuclei through the use of a liquid-drop model. The form of the semi-empirical mass formula is seen in Equation 1.1 where BE is the binding energy in MeV and is calculated using the charge (Z), mass (A) and number of neutrons (N) in the nucleus through a variety of terms [1, 3].

$$BE(MeV) = a_v A - a_s A^{2/3} - a_C \frac{Z^2}{A^{1/3}} - a_{asy} \frac{(N-Z)^2}{A} \pm \delta \tag{1.1}$$

The first term is the volume term (a_v) which accounts for the positive value of the binding energy. The next three terms all decrease the binding energy: the surface term (a_s), the Coulomb term (a_C) and the asymmetry term (a_{asy}). The final term of the equation (δ) is the pairing term and refers to the change in binding energy due to the pairing of like nucleons such that the binding energy is increased for even-even nuclei (even numbers of protons and neutrons) and decreased for odd-odd nuclei (odd numbers of protons and neutrons) relative to the non-pairing odd-even and even-odd nuclei (odd proton-even neutron and even proton-odd neutron numbers, respectively). The semi-empirical mass formula can be fit to experimental binding energies in order to determine the values of the coefficients in each term [1, 3]. A plot of select experimentally-determined binding energies as a function of mass (blue points) is seen in Figure 1.1. The green curve represents a fit of the semi-empirical mass formula to the experimental binding energies though the pairing terms was not used in this particular fit. The quality of the resulting fit demonstrates that the liquid drop model is a good approximation for ground-state nuclei (cold nuclear material at saturation density).

While the nature of ground-state nuclear matter is relatively well understood and studied, the properties of nuclei away from their ground-state, namely hot nuclear matter or matter at either sub- or supra-saturation density, is more difficult to analyze [5]. The nEoS forms a description of infinite nuclear matter at varying temperature, density and isospin asymmetry from the ground-state. Isospin asymmetry is defined by $m_s = \frac{N-Z}{A}$ where m_s is the isospin asymmetry parameter of the source and Z, A and N refer to the charge, mass and neutron number of the source, respectively[1].

[1]It is important to note that the isospin asymmetry parameter m_s has had many designations in the literature. While our group has used m_s in recent publications [6–8], this same value has been designated by I [9] and δ [10–12] in previous works by other researchers. The m_s term will

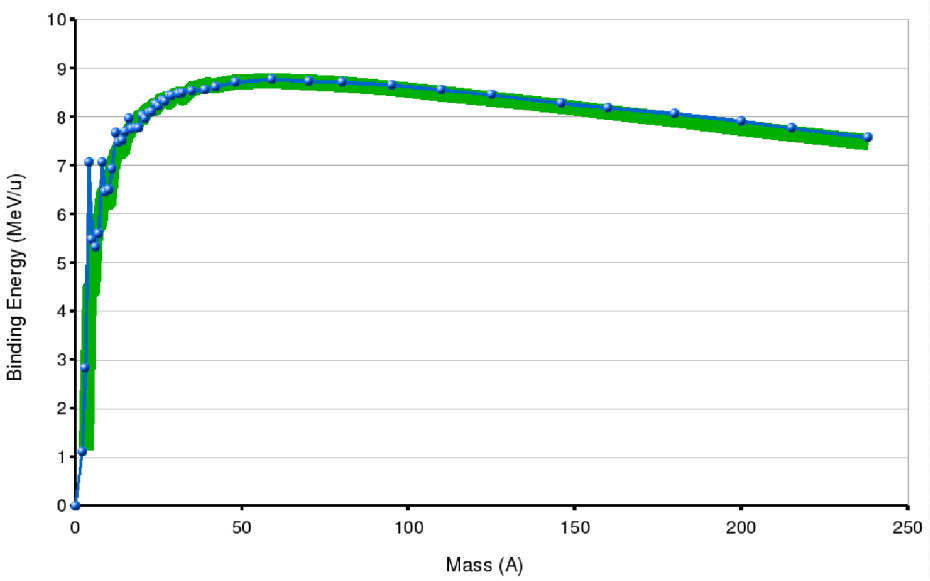

Figure 1.1: Binding energy per nucleon versus mass for the most stable isotopes of each mass. The blue circles are experimentally determined binding energies from Ref. [4]. The green line is the binding energy per nucleon calculated from the Weizsäcker mass formula without the pairing term (Eq. 1.1).

When trying to isolate the effect of the neutron-to-proton asymmetry, the nEoS can be expressed in a parabolic form as seen in Eq. 1.2. The binding energy, $E(\rho, I)$, is a function of the nucleon density ρ and isospin concentration, I, of infinite nuclear matter[13].

$$E(\rho, I) = E(\rho, 0) + E_{asy}(\rho)I^2 \tag{1.2}$$

$$I = \frac{\rho_n - \rho_p}{\rho_{total}} \approx \frac{N_s - Z_s}{A_s} = m_s \tag{1.3}$$

The isospin concentration, I, is defined as the fractional difference of the neutron (ρ_n) and proton (ρ_p) densities relative to the total nucleon density (ρ_{total}). The first term of Eq. 1.2 has no dependence on I and so represents the binding energy as a function of density for symmetric (N=Z) nuclear matter. The second term

be used throughout the remainder of this work for the sake of consistency.

specifically refers to the asymmetry energy which is dependent on the density and is scaled by I^2 in its contribution to the nEoS. Qualitatively the asymmetry energy is the amount of energy required to change all protons in symmetric nuclear matter into neutrons. Therefore, the asymmetry energy can also be defined as the difference between the binding energy of pure neutron matter, $E(\rho, 1)$, and symmetric nuclear matter, $E(\rho, 0)$.

Modern theoretical models show good agreement for the asymmetry energy of the nEoS near saturation density (ρ_0=0.16 fm^{-3}) but can diverge wildly at sub- and supra-saturation densities [13–20]. An improved understanding of the nEoS, and the form of the asymmetry energy, provides information on fundamental nucleon-nucleon interactions, general properties of nuclear matter as well as various astrophysical processes and phenomena [17, 19, 21–36]. Specifically, predications about the density profile, mass to radius ratio, cooling process and proton fraction of neutron stars have all been made based on the selection of different forms of the density dependence of the asymmetry energy [17, 23, 25, 26, 37–40]. Therefore, placing tighter experimental constraints on the density dependence of the asymmetry energy will help enhance the accuracy of predictions of astrophysical phenomena in addition to the behavior of nuclear matter at both high and low densities and temperatures.

Heavy-ion collisions provide the ability to probe the nEoS of asymmetric nuclear matter away from ground-state density and temperature. Numerous recent experimental results have been used to place constraints on the density dependence of the asymmetry energy ($\mathrm{E}_{asy}(\rho)$) [5, 22, 30, 39, 41–58]. These experimental constraints were based on a variety of observables: free neutron-proton ratios [5, 59, 60], isobaric yield ratios [10, 61–63], isoscaling [11, 12, 56, 62, 64–72], isospin diffusion [12, 21, 73–77], collective flow [45, 46, 53, 78–81] and neck dynamics/emission [42, 82–87]. Taken collectively, these constraints suggest an "asy-stiff" density dependence of the asym-

metry energy [5, 54, 57]. For the work presented in this thesis, isospin equilibration (Sec. 1.2) effects will be analyzed using isobaric yield ratios, isoscaling and the quasi-projectile reconstruction technique.

1.2 Isospin Equilibration

Isospin transport in heavy-ion nuclear collisions is described as the exchange of nucleons between projectile and target during the momentum damping phase of a nuclear collision and can be affected by the isospin asymmetry content of the projectile and target nuclei. The exchange of nucleons can be broadly broken into two categories: nucleon drift and nucleon diffusion. Drift (Eq. 1.4) is defined as the motion of a nucleon due to a density gradient while diffusion (Eq. 1.5) is the motion of a nucleon due to an isospin-asymmetry gradient [88].

$$D_q^\rho = ct \left(\frac{\delta \mu_q}{\delta \rho} \right)_{I,T} \tag{1.4}$$

$$D_q^I = -ct \left(\frac{\delta \mu_q}{\delta I} \right)_{\rho,T} \tag{1.5}$$

In Eqs. 1.4 and 1.5 the D_q^ρ and D_q^I represent the drift and diffusion coefficients, respectively, where q is the particle species and can be either neutrons (n) or protons (p). The ct term is a scaling coefficient while μ is the chemical potential of neutrons or protons, ρ is the total nucleon density, I is the isospin asymmetry defined in Eq. 1.3 and T is the nuclear temperature. Therefore, the drift (Eq. 1.4) of a particular nucleon is driven by the partial derivative of the chemical potential of that species with respect to the total nucleon density for a fixed isospin asymmetry and temperature. Similarly, the diffusion (Eq. 1.5) of a particular nucleon is driven by the partial derivative of the chemical potential of that species with respect to the isospin asymmetry for a fixed nucleon density and temperature. This shows that

nucleon drift and diffusion are the driving mechanisms for nucleon exchange along density and isospin asymmetry gradients, respectively, in a nuclear collision.

Nucleon drift is primarily observed in the formation of the neck region in heavy-ion collisions at mid-peripheral impact parameters. This is due to the relatively low density region that forms between projectile and target gaining nucleons from the relatively high density projectile and target regions. Many predictions [15, 67, 82, 86, 88–92] have shown that the neck region that forms is neutron-rich in composition due to the asy-stiffness of the asymmetry energy [19, 88, 89] and has been verified by numerous experimental results [5, 75, 84, 85, 93, 93–96]. This is due to the fact that for stiffer forms of the asymmetry energy the difference between local neutron and proton chemical potentials is very density gradient-dependent around saturation density and so the flow of nucleons into the neck region is predominately neutron-rich [89].

In contrast to nucleon drift, nucleon diffusion, or isospin diffusion, can drive nucleons through the neck region into the projectile or target. While drift is the dominant component of nucleon transport in heavy-ion collisions, in the limit of an infinitely long interaction time within a system once the neck region forms the strength of drift as a driving force diminishes since the projectile, target and neck region have similar total nucleon densities. However, any isospin asymmetry between these three sources (either from initial asymmetry between target and projectile or due to the neutron-richness of the neck region during and after formation) will cause isospin diffusion to take place. This diffusion component will tend to smooth out the isospin asymmetries in the system through the exchange of protons and neutrons in order to balance the asymmetry across the system as a whole. If a projectile and target were brought into contact with an infinite amount of contact time, one would expect that on average the final equilibrated product would be homogenous

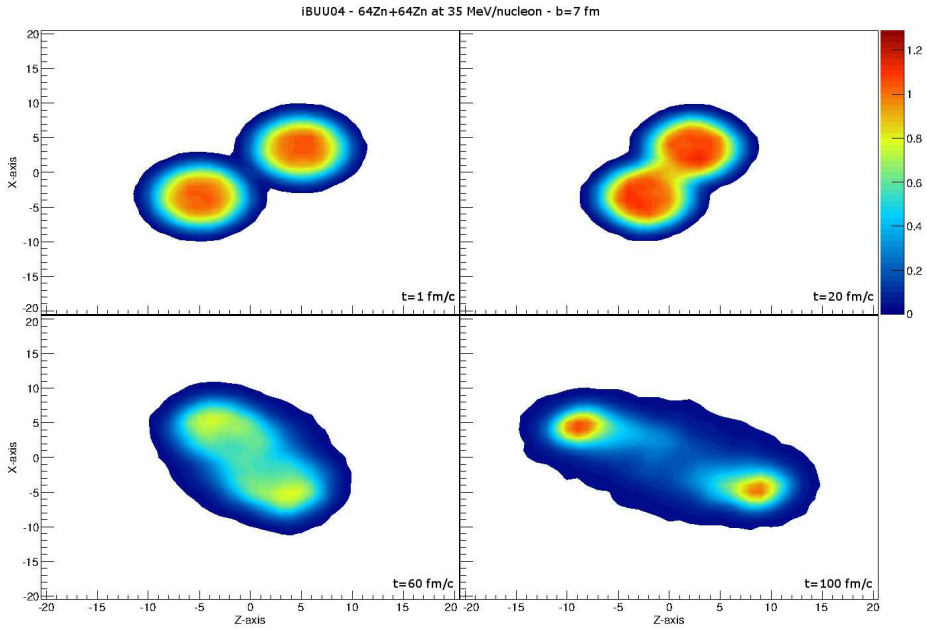

Figure 1.2: An iBUU04 simulation of ^{64}Zn+^{64}Zn at 35 MeV/nucleon at impact parameter b=7 fm showing the total nucleon density of the system over reaction time. As time advances we can see the projectile and target contact each other, form a dense neck region and finally separate into a quasi-projectile and quasi-target.

in isospin content throughout the reaction system. Since the contact time is not infinite, measuring the amount of equilibration that has occurred can help lead to an understanding of the strength of the drift and diffusion components of nucleon transport.

Early isospin equilibration work used isotopic ratios to demonstrate the beam energy dependence of equilibration in the Fermi energy regime [97–100]. However, in order to exactly measure the amount of equilibration that has occurred in a nuclear reaction, ideally the composition of the quasi-projectile (QP), quasi-target (QT) and any remaining neck-like structure immediately after separation would be measured. Understanding the amount of nucleon equilibration that has taken place can also be achieved by measuring the isospin asymmetry of the hot source after the reaction and

comparing it to the initial state. For instance, comparing the QP isospin asymmetry to the initial projectile and target asymmetries. One method of obtaining such a comparison is derived from the use of the Isospin Transport Ratio (ITR, Eq. 1.6). This equation was originally formulated by Rami *et. al.* [101] and the ITR has been used in a multitude of studies in order to measure equilibration in nuclear systems [5, 9, 10, 12, 14, 15, 21, 42, 76, 88, 101–103].

$$R_i = \frac{2x_i - x_{NR} - x_{NP}}{x_{NR} + x_{NP}} \tag{1.6}$$

The isospin transport ratio calculates an R_i value by calculating the relative position of an observable for a specific source (x_i) between that same observable calculated for a neutron-rich (x_{NR}) and neutron-poor (x_{NP}) source. By definition the neutron-rich source (NR) will give a value of $R_{NR} = 1$ and the neutron-poor source (NP) will give and $R_{NP} = -1$ so that any source that is mixed between these will yield an R_i value between -1 and 1. Ideally the isospin asymmetry (m_s) of the QP could be compared to the m_s of the projectile and target in order to calculate the amount of equilibration that occurs [10]. However, due to the fragmentation of the QP from its excitation energy as well as evolution of the system due to pre-equilibrium emission, this comparison will not yield a complete description of the equilibration of the system. Instead, studies began using observables that were linearly-dependent [10, 76] on the isospin composition of a source as a surrogate for the actual m_s. Several observables have been suggested that fit this criteria including free n/p ratios [5, 60], isobaric yield ratios [61, 63, 76], charged pion ratios [60] and the isoscaling parameter α [10, 12, 56, 67].

The first demonstration of the ITR as a probe of nucleon equilibration was performed by Rami *et. al.* by using the proton yield and triton/helium-3 (t/^{3}He) ratios

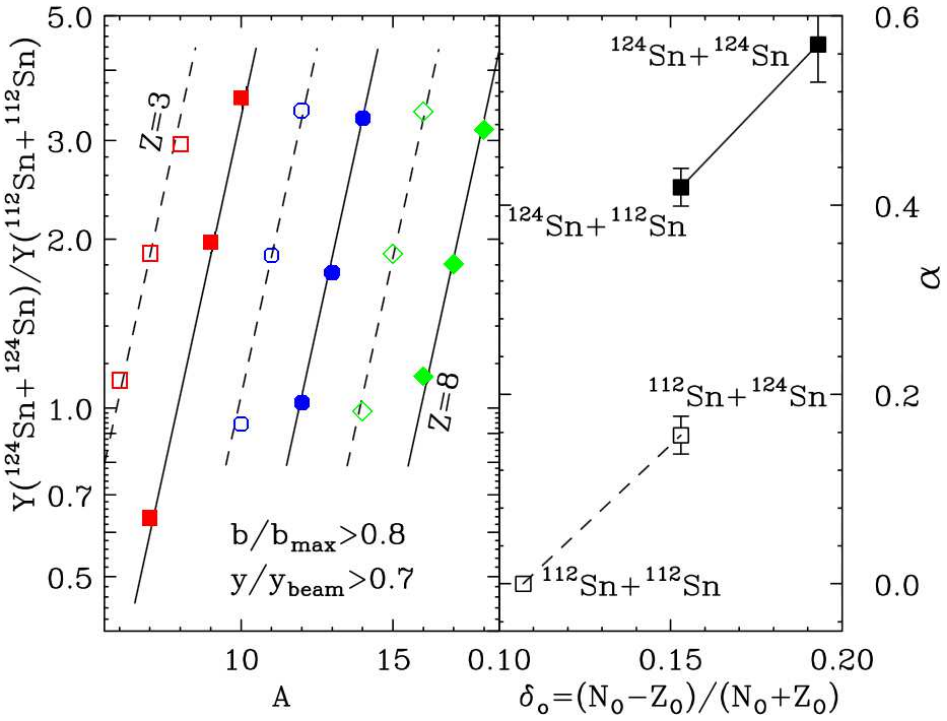

Figure 1.3: The left panel shows an example isoscaling plot taken by scaling the isotopic yields of a ^{124}Sn+^{124}Sn reaction over the yields of a ^{112}Sn+^{112}Sn reaction both at 50 MeV/nucleon. The fit to the points requires a fixed α (slope) and β (spacing between lines). The extracted α parameter is then plotted on the right side of the plot for four different pairwise combinations of systems as a function of the total system asymmetry of the neutron-rich system in each pair. Figure adapted from Tsang *et al.* [12].

as the isospin dependent observables [101]. This work shows a tendency toward system equilibration as the impact parameter of the reaction becomes more central. More central reactions provide more overlap between projectile and target and therefore more momentum damping and longer contact times. These longer interaction times between projectile and target allow for more time for equilibration to take place [104–106]. It is therefore expected that signatures of equilibration should be more prevalent in strongly momentum-damped (more central) collisions [107].

The seminal work in isospin equilibration comes from the 2004 study by Tsang

et. al. in using the isoscaling parameter α as a surrogate for the m_s in the ITR (using particles from the reactions of 50 MeV/nucleon ^{124,112}Sn+^{124,112}Sn) and comparing the measured experimental equilibration to that determined by a Boltzmann-Uehling-Uhlenbeck (BUU) transport model calculation [12]. Their experimental data were measured using a combination of the Large Area Silicon Strip Array (LASSA) and the Miniball array at the National Superconducting Cyclotron Laboratory at Michigan State University. The experimenters selected peripheral collisions by gating on the charged particle multiplicity and minimized neck fragment emission by selecting fragments within a certain rapidity range ($y/y_{beam} \geq 0.7$) of the incident particle beam. These selections were applied in order to select fragments from clean peripheral collision sources.

The resulting fragments were then isoscaled and the results are shown in the left panel of Figure 1.3. Isoscaling is a method by which the individual isotopic particle yields from one source are scaled by the individual isotopic particle yields from another source as in Eq. 1.7. By convention, the yields from the more neutron-rich source (Y_2(N,Z)) are used as the numerator and the yields from the more neutron-poor source (Y_1(N,Z)) are used as the denominator. The three most abundant isotopes for each Z=3-8 were used in the analysis and the yield ratio of each isotope between the most neutron rich (^{124}Sn+^{124}Sn) and most neutron poor (^{112}Sn+^{112}Sn) is shown. Scaling the particle yields by this method, the data can be fit using Eq. 1.8 where α and β are the isoscaling parameters for neutrons and protons, respectively. The fit lines in Figure 1.3 correspond to fixed global values of α (slope) and β (line spacing) over the whole range of isotopes. The α parameter extracted from the fit is then plotted on the right hand side of Figure 1.3 as a function of the composite system isospin asymmetry for all four reaction systems. The researchers determined from the right hand panel that the cross reactions had achieved approximately 50%

equilibration due to the α values of the two cross reactions positioned at approximately 50% of the distance between the symmetric system values and the mid point between the symmetric systems.

$$R_{21}(N,Z) = \frac{Y_2(N,Z)}{Y_1(N,Z)} \tag{1.7}$$

$$R_{21}(N,Z) = C\exp(\alpha N + \beta Z) \tag{1.8}$$

In addition to the experimental measurement of the isoscaling α parameter, the Tsang *et al.* work also performed a model calculation using a BUU transport code. Using both an asy-stiff and asy-soft parametrization of the asymmetry energy they traced the isospin asymmetry of the QP over the course of the reaction time. Figure 1.4 shows the results of this calculation. The top panel shows the evolution of the QP isospin asymmetry via the ITR for the ^{124}Sn+^{112}Sn and ^{112}Sn+^{124}Sn reactions (top and bottom curves, respectively) over the course of the interaction for the asy-stiff case. Super-imposed on the top panel is the reaction plane density profile at various time steps, showing the evolution of the reaction with time. As the projectile and target first interact, isospin mixing occurs which begins to add target-like character to the projectile. Once separation of the QP and QT occurs (at approx. 100 fm/c) we can see the isospin asymmetry levels off as no more interaction between QP and QT occurs. For the asy-stiff case, only partial isospin equilibration takes place, represented by the ITR R_i value leveling off at approximately 0.5 and -0.5. In contrast, in the asy-soft case (bottom panel of Fig. 1.4) full isospin equilibration appears to occur as the curves for the two asymmetric cross systems converge at approximately R_i=0. From this and the experimental values obtained from the isoscaling data, Tsang *et al.* concluded that an asy-stiff interpretation of the asymmetry energy best represents the experimental data [12].

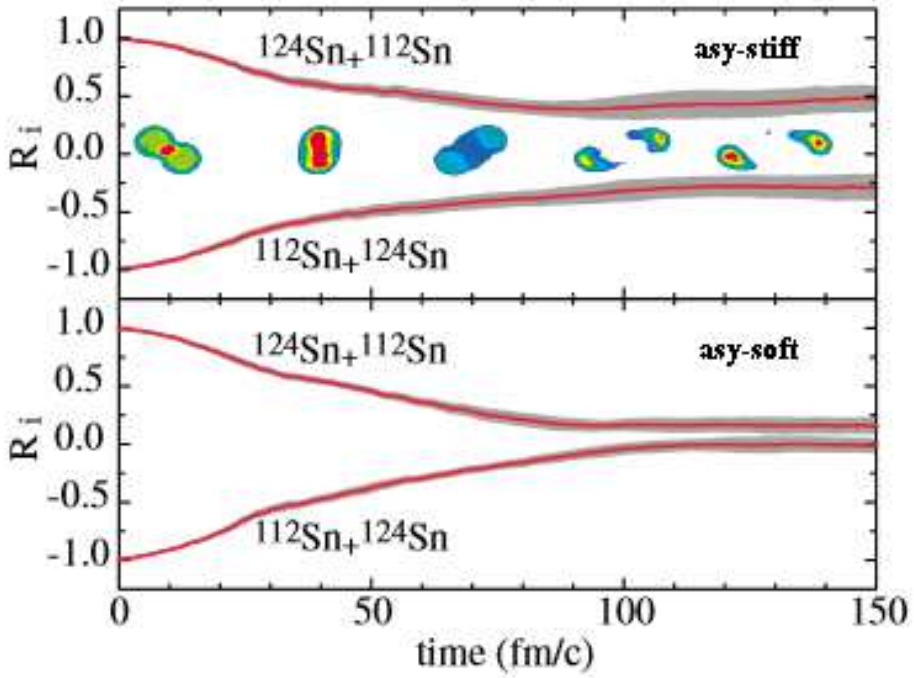

Figure 1.4: The top panel shows the evolution of the QP isospin asymmetry for the ^{124}Sn+^{112}Sn and ^{112}Sn+^{124}Sn reactions over the course of the interaction for the asy-stiff case via the ITR method. Super-imposed on the top panel is the density profile in the reaction plane at various time steps, showing the evolution of the reaction with time. The bottom panel shows the isospin asymmetry evolution versus time for the asy-soft case. Figure adapted from Tsang *et al.* [12].

Since the Tsang *et al.* work, many studies have continued to probe isospin equilibration in Fermi energy range reactions. Various experiments [5, 10, 21, 68, 75, 76, 94, 96, 102, 108–110] as well as theoretical predictions [73, 74, 88, 91, 111] have continued working on placing constraints on the asymmetry energy via isospin transport and equilibration. A review study by Tsang *et al.* found that while numerous experimental measurements exist and an asy-stiff asymmetry energy is generally agreed upon, the exact form of the asymmetry energy is still relatively unconstrained [57].

One study, by Keksis *et al.*, used an improved novel technique of reconstructing the hot post-interaction quasi-projectile from its breakup into various charged particle fragments [108, 112] that was first developed by Rowland [113]. Using the FAUST charged particle array to measure reactions of 32 MeV/nucleon ^{40,48}Ca+^{112,124}Sn, Keksis *et al.* found that by making appropriate cuts on the detected charged particles to remove contamination from pre-equilibrium emission and neck region emission, the remaining particles could be used to backtrack and reconstruct what was believed to be the hot QP immediately following the separation of the QP-QT pair. Using this reconstruction, it was found that the amount of equilibration that took place in the reaction was approximately 53%, consistent with the Tsang *et al.* work [12, 108]. This marked the first attempt at experimentally determining the asymmetry of the source directly (rather than relying on a surrogate for the isospin asymmetry) and applying it to an equilibration study. Furthermore, while not used for isospin equilibration, the work of Wuenschel *et al.* on the NIMROD-ISiS array determined that the quality of isoscaling fits could be greatly improved by selecting not only on reconstructed QPs but also by including free neutron information into the reconstruction method and selecting on the "complete" QP isospin asymmetry [70].

1.3 Outline

In this dissertation, new experimental results from the reactions of 35 MeV/nucleon ^{70}Zn,^{64}Ni+^{64}Zn and ^{64}Zn+^{70}Zn,^{64}Ni will be presented. Chapter 2 will discuss the experimental details, method of particle identification, energy calibration procedure and the construction and logic of the final physics tapes. The experimental results and discussion of isospin equilibration studies will be covered in Chapter 3. Comparison to theoretical models will also be discussed. Finally, Chapter 4 will summarize the work and provide conclusions and outlooks.

2. EXPERIMENTAL

Isospin Transport was investigated via quasi-projectile reconstruction (Chapter 3) of ^{70}Zn,^{64}Ni+^{64}Zn and ^{64}Zn+^{70}Zn,^{64}Ni reactions at 35 MeV/nucleon taken on the NIMROD-ISiS (Neutron-Ion Multidetector for Reaction Oriented Dynamics with Indiana Silicon Sphere) 4π charged particle detector array coupled with the TAMU Neutron Ball at the Texas A&M University Cyclotron Institute [114]. These projectile and target asymmetric cross-reactions between the ^{70}Zn,^{64}Zn and ^{64}Zn,^{64}Ni pairs were measured as a complement to the set of 35 MeV/nucleon ^{70}Zn+^{70}Zn, ^{64}Zn+^{64}Zn and ^{64}Ni+^{64}Ni projectile and target symmetric reactions obtained by Z. Kohley on the same detector array [78]. From this set of 7 reactions two sets of reaction pairs were chosen such that each set of reactions has two symmetric and two asymmetric reactions: the ^{70,64}Zn set and the ^{64}Zn,^{64}Ni set, labeled the Zn and A=64 sets, respectively. This configuration was chosen due to the nature of isospin transport studies, where the symmetric reactions undergo zero net transport between projectile and target, while the asymmetric systems have isospin driven transport between projectile and target.

The description of the experiment is provided in Section 2.1. The configuration of the detector array, including electronics, is provided in Section 2.2. Sections 2.3 and 2.4 deal with the methods of particle identification and energy calibration of identified particles, respectively. Finally, Section 2.5 will describe the structure and production of the final "physics tapes" which contain the determined Z and A identification and energy calibration of all particles detected in the array.

2.1 Description of Experiment

The Texas A&M University Cyclotron Institute K500 Superconducting Cyclotron was used to accelerate beams of ^{70}Zn, ^{64}Zn and ^{64}Ni to 35 MeV/nucleon as a part of two separate data collection campaigns. The first campaign occurred in July 2009 for the doctoral thesis of Z. Kohley and involved the reaction of ^{70}Zn, ^{64}Zn and ^{64}Ni at 35 MeV/nucleon on stationary targets of ^{70}Zn, ^{64}Zn and ^{64}Ni, respectively. The complete experimental procedures and setup can be found in Reference [78]. The second campaign was conducted in April-November of 2010 and consisted of 35 MeV/u beams on stationary targets for the four following reactions: ^{70}Zn on ^{64}Zn, ^{64}Zn on ^{70}Zn, ^{64}Zn on ^{64}Ni, and ^{64}Ni on ^{64}Zn. A summary of all 7 reaction systems used in the two campaigns is presented in Table 2.1. The experimental setup and details matched those used by Kohley as closely as possible so that the two data sets would be compatible in efficiency and analysis. The ^{64}Zn and ^{64}Ni targets were purchased from MicroMatter [115] while the ^{70}Zn target was fabricated by Argonne National Laboratory Target Lab [116]. The ^{70}Zn target materials and all beam materials were purchased from Trace Sciences [115]. A summary of target characteristics can be seen in Table 2.2. The beam intensity fluctuated between 150-350 electrical pA over the course of data collection. This resulted in an average detector/electronics dead time of $\sim$50% and an average event rate of 100-240 raw events per second.

Calibration beams were taken as a part of both campaigns and are summarized in Table 2.3. The calibration beams were selected to give a large variety of known energy points in the largest portion of detectors possible in order to assist with the energy calibrations discussed in Section 2.4.

Table 2.1: Summary of all 7 reaction systems used through both campaigns.

Reaction	^{70}Zn+^{70}Zn	^{70}Zn+^{64}Zn	^{64}Zn+^{70}Zn	^{64}Zn+^{64}Zn	^{64}Zn+^{64}Ni	^{64}Ni+^{64}Zn	^{64}Ni+^{64}Ni
Projectile Energy (MeV/nucleon)	35	35	35	35	35	35	35
Proj. Charge State	22+	22+	21+	21+	21+	21+	21+
Composite System (N-Z)/A	0.1429	0.1045	0.1045	0.0625	0.0938	0.0938	0.1250

Table 2.2: Target thickness and target purity for each target used in the campaign.

Target	^{70}Zn	^{64}Zn	^{64}Ni
Target Thickness	0.985 mg/cm^2	1.0 mg/cm^2	1.14 mg/cm^2
Target Purity	95%	99.85%	97.92%

Table 2.3: The calibration beam and target combinations along with the energy of the calibration beam.

Calibration Beam	$^{1}H_2$	^{20}Ne	^{4}He	^{1}H-^{2}D
Beam Energy (MeV/nucleon)	55	35	25, 55	30
Targets	^{197}Au	^{197}Au	^{197}Au	^{197}Au

2.2 Experimental Setup

The NIMROD-ISiS array [109, 114, 117] consists of total 4π coverage of Si-CsI detector telescopes. The forward angles (lab $\theta = 0 - 90^\circ$) of the array consist of the NIMROD array while the backward angles (lab $\theta = 90 - 180^\circ$) are comprised of the forward hemisphere of the former ISiS array [118] as seen in Figure 2.1. Both portions make up the 4π charged particle coverage of the array and are housed inside the TAMU Neutron Ball which is used for neutron multiplicity measurements. The coverage and excellent isotopic resolution of the array, due to complete ΔE-E Si-CsI coverage, make the NIMROD-ISiS array an ideal setup for isospin equilibration studies. With isotopic resolution of reaction fragments from Z=1 up to Z=18, many isospin-sensitive observables can be examined in addition to reconstruction of the hot primary source immediately following the reaction, the quasi-projectile.

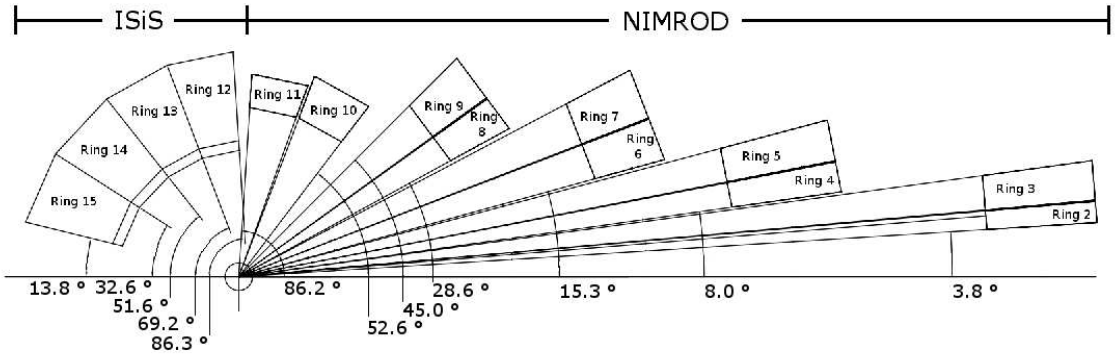

Figure 2.1: Side view of the charged particle detectors of the NIMROD-ISiS array. Each ring is labeled with the corresponding lab angle. The projectile beam is traveling from the left to the right in this figure.

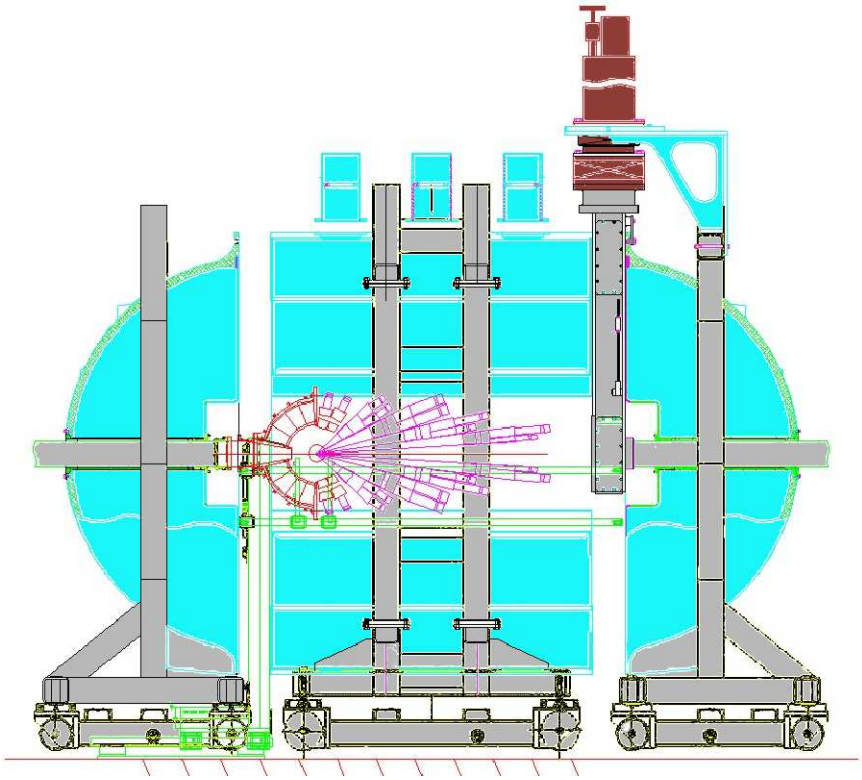

Figure 2.2: Schematic of the NIMROD-ISiS array showing the charged particle array housed inside the neutron ball. The projectile beam is traveling from the left to the right in this figure.

2.2.1 NIMROD-ISiS

The full coverage of the NIMROD-ISiS array is from 3.6° to 167° in lab and consists of 14 concentric rings, numbered 2-15 from forward to backward angles, as seen in Figure 2.1. The charged particle array is housed inside the TAMU Neutron Ball [119] and is shown schematically in Figure 2.2. The rings of the original NIMROD array (rings 2-9) are modeled on the same geometry as the INDRA array from GANIL [120]. The backward angles of NIMROD-ISiS, Rings 12-15, are covered by the original forward section of the Indiana Silicon Sphere (ISiS) [118]. Rings 10 and 11 [114] were modeled after the ISiS layout and designed specifically to couple the original NIMROD array to the existing ISiS section. The sealed array is brought under a vacuum of 8.0 x 10^{-6} to 1.8 x 10^{-5} torr during experimentation through the use of three separate turbo molecular pumps.

Each ring of the NIMROD-ISiS array consists of either 12 (Rings 2-9) or 18 (Rings 10-15) telescope modules. The modules in Rings 10-15 consist of a 300 μm thick silicon (Si) wafer in front of a light-tight thallium-doped cesium-iodide (CsI(Tl)) crystal that is optically coupled to a photodiode (PD). In rings 2-9, ten of the twelve modules consist of a single 150 μm, 300 μm or 500 μm Si detector placed in front of a CsI(Tl) crystal that is optically coupled to a photo-multiplier tube (PMT). The 2 remaining modules in each of rings 2-9 are labeled "super telescopes" and consist of two Si detectors (a 150 μm in front of a 500 μm) in front a CsI(Tl) crystal and PMT. The super telescope allows for the addition of a second ΔE-E (Si1 vs Si2) detector pair in a single module, beyond the primary ΔE-E detector arrangement (discussed below) provided by the Si-CsI pair which expands the possible energy range of detection for particle identification. Each module is also designed to be able to utilize gas-filled ionization chambers for detection of heavy fragments, however no

ionization chambers were used in this experiment.

An important feature of the Si wafer in Rings 2-9 is that the front and back planes of the Si are decoupled which allows for the ability to set the full scale range of the detector energy for both the front and back planes of each Si separately in the electronics. This capability allowed the gains to be set such that the Si Front vs. CsI comparison maximized the isotopic resolution of particles while the Si Back vs. CsI comparison maximized the Z identification of particles up to and including elastically scattered beam particles (in the most forward rings of NIMROD) which is discussed further in Section 2.3.2.

Every Si back plane is a single solid plane, while the front plane of each Si is segmented into 2, 3 or 4 segments, which provide separate energy signals for each segment. The segmentation top to bottom allowed for the separation of two adjacent rings in identification. For example, Si detectors in Rings 2-3 are segmented "top" and "bottom" where the "top" corresponds to Ring 2 and the "bottom" corresponds to Ring 3. While a single physical Si detector per module spans two geometric rings, the segmentation allows for collecting signals corresponding to each ring separately. Si wafers segmented into 3 or 4 segments not only have this vertical segmentation but a lateral segmentation as well splitting the "bottom" only (in the 3 segment case) or splitting both "top" and "bottom" (in the 4 segment case). This allows better granularity in certain rings (specifically Rings 7 and 9) by doubling the number of signals in the ring as seen in Table 2.4.

Energy resolution of the silicon detectors is exceptionally important in providing clean particle identification. To this end the silicon detectors were reversed biased to increase the semiconductor band gap in the silicon wafer. In order to further clean up registered signals, an effort was made to reduce the amount of free electrons produced in the beam line that struck the Si wafers. One method of reducing electron

Table 2.4: The θ range, $\Delta\phi$, number and thickness of single telescopes, number of super-telescopes, PMT or PD attached to CsI, and CsI length for each ring of the NIMROD-ISiS array.

Ring	θ Range	$\Delta\phi$ of CsI	# of Single Telescopes and thickness	# of Super-Telescopes	PMT or PD attached to CsI	CsI(Tl) Length (cm)
2	3.6^o-5.0^o	30^o	10 (300 μm)	2	PMT	10.0
3	5.0^o-7.6^o	30^o	10 (300 μm)	4	PMT	10.0
4	8.0^o-10.8^o	30^o	10 (300 μm)	4	PMT	10.0
5	10.8^o-14.7^o	30^o	10 (300 μm)	4	PMT	10.0
6	15.3^o-20.9^o	30^o	5 (300 μm) 5 (150 μm)	4	PMT	6.5
7	20.9^o-27.6^o	15^o	10 (300 μm) 10 (150 μm)	4	PMT	6.5
8	28.6^o-35.8^o	30^o	6 (300 μm) 4 (150 μm)	4	PMT	6.0
9	35.8^o-45.0^o	15^o	12 (300 μm) 8 (150 μm)	4	PMT	6.0
10	52.7^o-69.2^o	20^o	18 (300 μm)	0	PMT	4.0
11	70.1^o-86.3^o	20^o	18 (300 μm)	0	PMT	3.0
12	93.5^o-110.8^o	20^o	18 (500 μm)	0	PD	2.8
13	110.8^o-128.4^o	20^o	18 (500 μm)	0	PD	2.8
14	128.4^o-147.4^o	20^o	18 (500 μm)	0	PD	2.8
15	147.4^o-167.0^o	20^o	18 (500 μm)	0	PD	2.8

background was the placement of a 365 μg/cm^2 thick sheet of aluminized mylar in front of each module in Rings 2-9. This was achieved by attaching the mylar to the otherwise empty ionization chamber frame. The final method of reducing scattered electron background was by positively biasing the aluminum target ladder to 15 kV in order to capture δ electrons produced upstream of the NIMROD chamber or electrons from the reaction with the target.

2.2.2 TAMU Neutron Ball

The entirety of the NIMROD-ISiS charged particle array is housed inside of the TAMU Neutron Ball [119]. The Neutron Ball is a neutron calorimeter and is used to measure neutron multiplicities from intermediate energy heavy-ion collisions [117, 119]. The original Neutron Ball consisted of two hemispheres and nine thin wedge-shaped in-plane sections. The Neutron Ball was then modified by removal of the nine wedges and inclusion of four long wedge-shaped extensions whose combined geometry consist of a cylindrical region between the hemispheres as seen in Figure 2.3. The three sections of the Neutron Ball (the two hemispheres and the central cylindrical region) are placed on rails such that each section can be moved independently of the others allowing access to the NIMROD-ISiS charged particle array housed inside.

The Neutron Ball detects neutrons via scintillation of a 0.3% wt. gadolinium (Gd) doped pseudocumene (1,2,4-trimethylbenzene) liquid solution. The attached PMTs record a signal generated by photons which can come from the interaction of the neutrons with the gadolinium in the organic scintillator but also originates from the prompt gamma flash induced by Fermi energy heavy-ion collisions. This prompt production of gamma rays produces a very distinct and well-defined signal that allows it to be differentiated from that of signals originating from neutrons. Following the prompt gamma flash, the Neutron Ball will receive signals from the

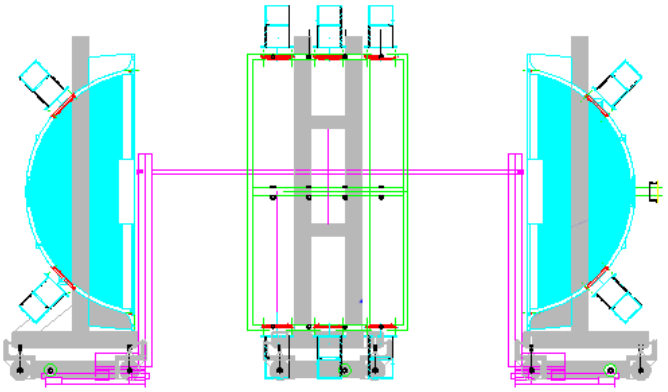

Figure 2.3: Side-view depiction of the TAMU Neutron Ball (without charged particle array). The three sections, consisting of two hemispheres and the center cylinder, are shown separated demonstrating the ability to move each section of the neutron ball independently.

capture reaction of neutrons on the Gd. Neutrons from the nuclear collision are thermalized through neutron-proton collisions. These thermalized neutrons can then be captured by the Gd in the pseudocumene due to the high neutron capture cross-section of Gd [119]. On average, this process produces three gamma rays with a total energy of approximately 8 MeV. Photomultiplier tubes mounted with fish-eye lenses to the Neutron Ball sections then detect the light from the neutron capture reaction. Due to the drift time of thermalized neutrons in the scintillator solution, an electronic gate of 50-100 μs is required to count the delayed neutron capture flashes, each of which corresponds to a single neutron. It is important to note that the Neutron Ball measures multiplicities but is not capable of measuring neutron energies.

2.2.3 Electronics

The NIMROD-ISiS array incorporates a wide variety of electronic modules for the conversion of analog signals from the various detectors to digital signals that are then recorded by the data acquisition software (DAQ). The master trigger for

the electronics was generated as an OR from the CsI signals and Si back signals in rings 2-7. The electronics layout will be described according to silicon detectors, CsI(Tl)-PMT, CsI(Tl)-PD, Neutron Ball PMTs and finally the trigger logic.

The silicon detectors from rings 2-9 use custom motherboards that attach directly to the outside of the detector chamber. These motherboards supply bias voltage to the silicon detectors, hold Zepto Systems pre-amplifiers for the Si signal outputs and also supply the +/- 12V power for the pre-amps [121]. Silicon detectors in rings 10-15 used pre-fabricated motherboards from Zepto Systems as well as Zepto System pre-amps. The Si bias voltage was supplied using Tennelec High-Voltage power supplies and the pre-amp +/- 12V was supplied by a Dual-Channel Voltage Supply (DC).

The Si signal leaves the NIMROD-ISiS chamber through vacuum-tight feedthroughs and is then amplified by the on-board pre-amps. From there the analog signal is sent to a shaping amplifier. For rings 2-9 a CAMAC Pico Systems Shaping Amplifier [124] was used for the Si fronts and a CAMAC Pico Systems Shaper Discriminator for the Si backs. The Shaper Discriminators used on the Si back signals allow for receiving OR and SUM signals that are subsequently used for trigger logic as seen in Figure 2.4. CAMAC Phillips peak-sensing ADCs were used for the conversion to digital signals to be read by the DAQ.

Rings 10-11 also used CAMAC Pico Systems Shaping Amplifiers but signals are then fed into VME peak-sensing ADCs. The ISiS portion of the array (rings 12-15) used a modified version of the original ISiS shaping amplifiers that were used with the hemisphere of ISiS upon its transfer to TAMU. These signals were then also processed using VME peak-sensing ADCs. The similarity in electronics processing between rings 10-11 and rings 12-15 is due to the ring 10-11 modules being designed as replicas of the ISiS module design. The modifications made to the ISiS shaping amplifiers were to remove a built-in pre-amplifier from the module since the signals

Table 2.5: Short description, abbreviations and examples of the electronic modules used in the experimental campaign. Additional information about the electronics modules can be found in Refs.[122, 123]

Module Name	Abv.	Function	Example Modules
Leading Edge Discriminator	LED	Determines if a signal is above a threshold.	LeCroy 623B, Pico Sys. Shaper Disc.
Constant Fraction Discriminator	CFD	Determines if the signal is above a threshold based on a constant fraction of peak amplitude, which provides a consistent triggering time.	LeCroy 3420, Tennelec 454
Peak Sensing Analog to Digital Converter	ADC	Converts analog peak height to digital signal.	Phillips 7164
Peak Integrating Analog to Digital Converter	QDC	Converts peak integral to digital signal.	LeCroy 1885F, Phillips 7166
Fast Amplifier	FA	Amplifies the signal without changing its shape.	LeCroy 612A
Shaping Amplifier	-	Amplifies, integrates, and differentiates the signal producing a uni- or bipolar signal.	Pico Systems Shaper and Shaper Discriminator

TABLE 2.5. Continued from previous

Module Name	Abv.	Function	Example Modules
Charge-Sensitive Pre-Amplifier	Pre-Amp	Integrates the charge from the detector and provides initial amplification.	Zepto Systems Pre-Amplifier
Logic Fan in Fan out	FI/FO	Creates a single logic signal if any input fired.	LeCroy 429A, PS 757,756
Linear Fan in Fan out	FI/FO	Creates a linear sum of the input signals. with both OR and SUM signals available.	LeCroy 428F
Overlap	-	Produces a logic signal when the selected signal(s) overlap with a gate.	LeCroy 356AL
Bit Register	-	Marks a bit assigned to each fired CsI-PMT when event is triggered.	LeCroy 4448, 2341A
Gate Generator	-	Creates an adjustable width logic signal.	LeCroy 222, PS 794, GG 8000,8010
Scaler	-	Counts signals received.	LeCroy 4434

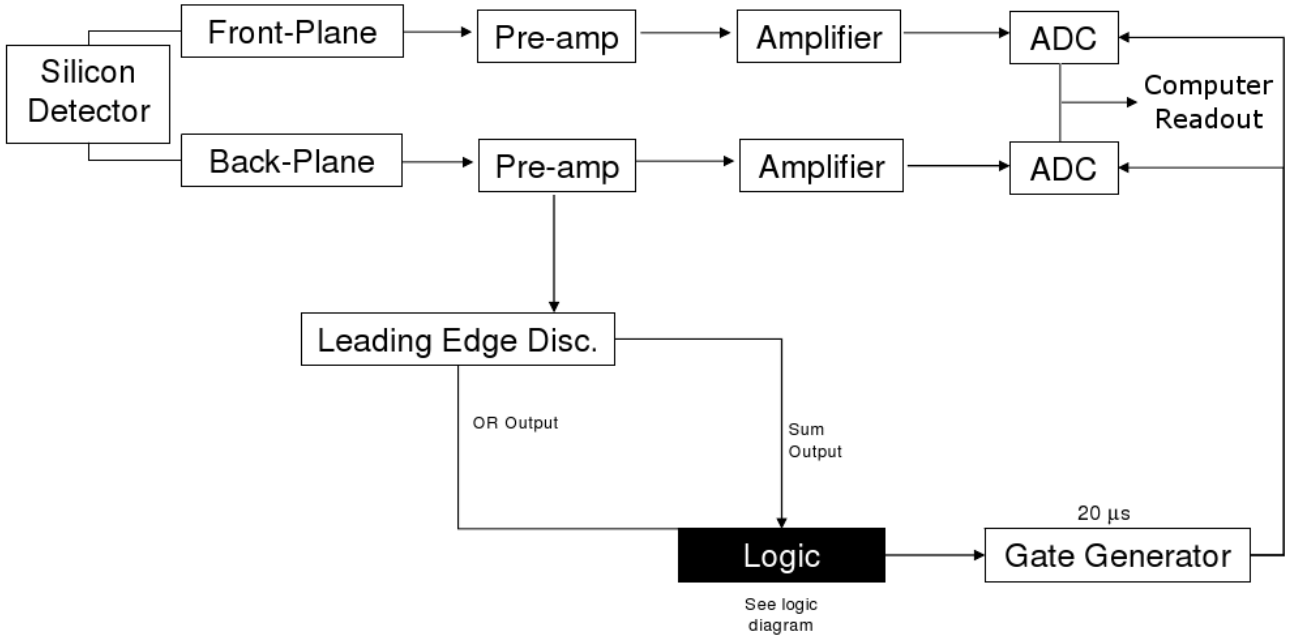

Figure 2.4: Electronics diagram for the front-plane and back-plane silicon signals which were collected in Rings 2-15 and Rings 2-7, respectively.

were being pre-amplified upon their exit from the reaction chamber. Upon receipt of a trigger corresponding to a "good" event a 20 μs gate is produced in which all of the digital ADC signals are read into the DAQ.

The structure of the electronics is separate for the NIMROD and ISiS portions of the array. This is due in large part to the CsI crystals being read out by photomultiplier tubes (PMT) in NIMROD (rings 2-11) and by photodiodes (PD) in ISiS (rings 12-15). Due to the nature of the CsI(Tl) excitation, the signal generated in the PMTs can be split into a fast and a slow component, which allows for a pulse-shape discrimination analysis for light fragment identification (discussed in Section 2.3.1). Custom designed resistor-chain power boards were created to distribute the correct voltage to each dynode of the PMT and the supply voltage was generated by a LeCroy 1440 High Voltage power supply. The PMT output signal is split after it exits the chamber. The first copy of the signal is used in the trigger logic for the array. This signal is put through a fast amplifier and then sent through a constant fraction discriminator. The discriminator produces both a SUM and an OR signal that are then fed into the trigger logic setup for determining "good" events. If a "good" event is triggered by the master then a 400 ns gate is created and sent to a dynamic range QDC for recording the fast and slow portions of the other PMT signal copy.

The PMT signal copy used for energy collection is sent to a custom built splitter/attenuator for processing. This custom unit produces two additional copies of the original PMT signal that are individually attenuated. The CsI-PMT signal is delayed 300 ns such that the QDC gate starts at the peak of the CsI-PMT signal as seen in Figure 2.6. Additionally, a 1 μs gate is produced 1 μs later that records the slow tail of the signal. The relative positions of the fast (400 ns) and slow (1 μs) gates can have a dramatic effect on the resolution of particle identification in

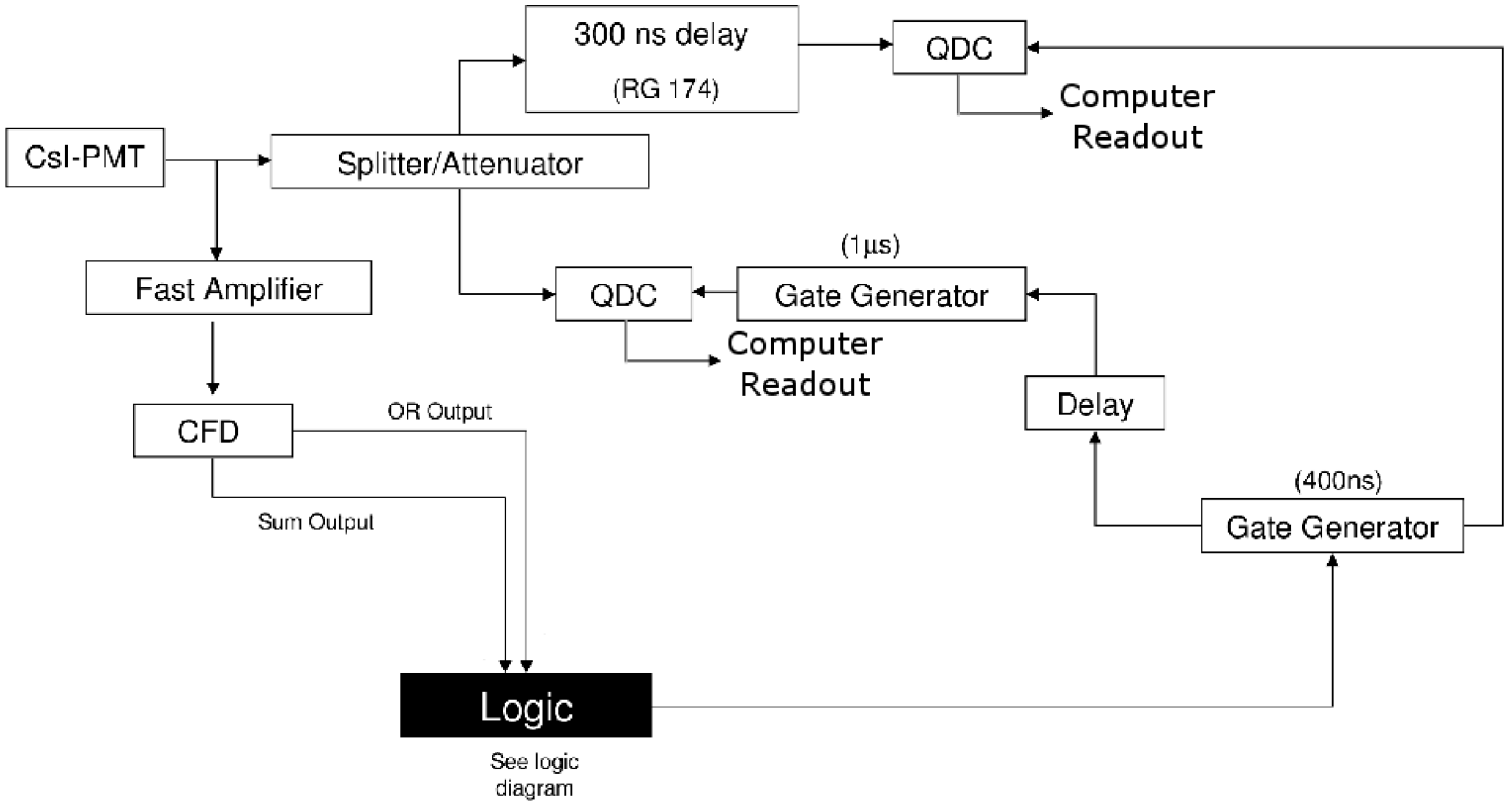

Figure 2.5: Electronics diagram for the CsI-PMT signals of rings 2-11.

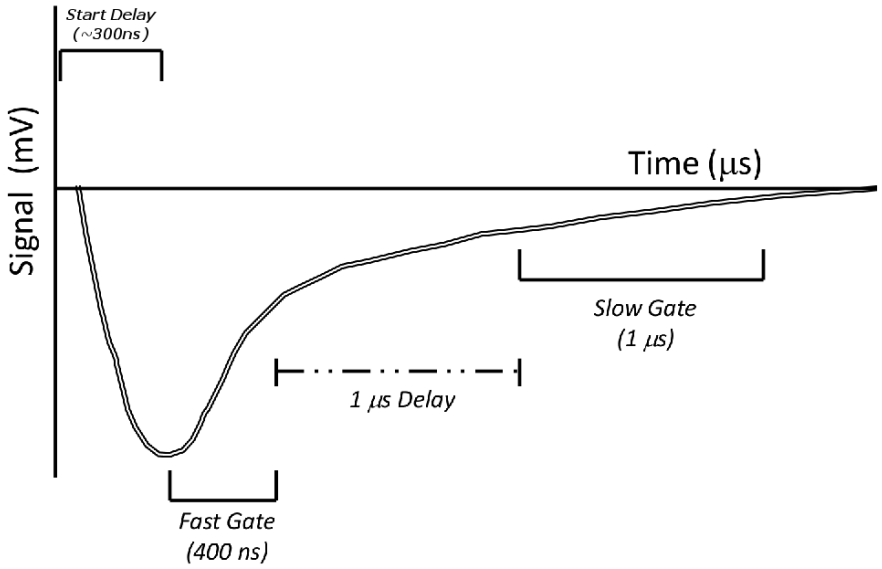

Figure 2.6: Illustration of the signal resulting from the CsI-PMT detector. Both the fast and slow signal gates are shown along with the 1 μs delay and the start delay (300 ns).

pulse-shape discrimination. The positions of the two gates were chosen to maximize the isotopic resolution of particles in the range Z=1-3 for the analysis of Z. Kohley [78] and the same positioning was kept in this experiment due to the similarity of the experimental beams.

The ISiS portion of the detector array uses CsI(Tl) crystals coupled to photodiodes (PD). The nature of photodiodes required a different arrangement of electronics for processing the CsI signal. Since these detectors covered the backward direction of the reaction (lab $\theta = 90 - 180°$) the signals were not used in the trigger logic. Pulse-shaped discrimination was not needed in this case because the detectors were in the backward direction and it was not expected that particles larger than Z=2 would be seen and so gains were set so that all fragments could be identified by ΔE-E in the Si-CsI. Since only a single copy of the PD signal was needed, the setup for the

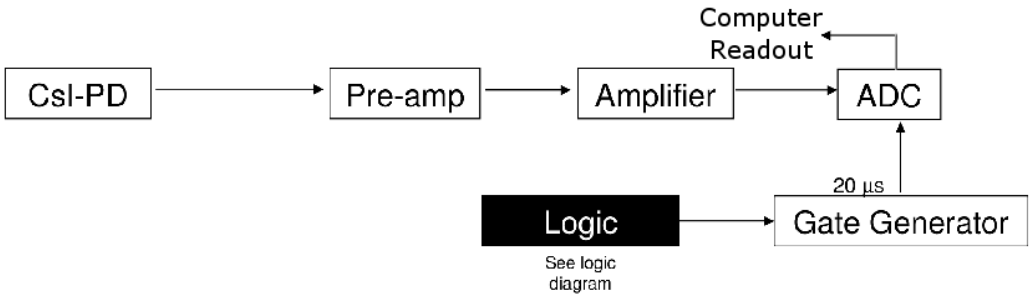

Figure 2.7: Electronics diagram for the CsI-PD signals of rings 12-15.

CsI-PD is identical to that of the ring 12-15 silicons with changes to the amplification and shaping times of the CsI-PD signals as seen in Figure 2.7.

The Neutron Ball electronics setup was configured to record a background neutron multiplicity as well as the event neutron multiplicity in an effort to correct for neutrons from background sources. Signals from the Neutron Ball PMTs were sent to a fast amplifier and then a constant fraction discriminator (CFD). The efficiency of the neutron ball was "tuned" by adjusting the CFD thresholds until the measured neutron emission from a ^{252}Cf source matched the simulated efficiency from a GEANT-3/GCALOR simulation of the NIMROD-ISiS array [117]. The neutron detection efficiency from that simulation was found to be ~70% per neutron. An above-threshold CFD signal generates a logic signal from the CFD that is then sent to a logic Fan-In/Fan-Out (FIFO). All PMTs from a single Neutron Ball section are fed into the same FIFO channel so that the FIFO OR signal corresponds to a single neutron present in that section of the Neutron Ball.

Two 100 μs gates are used to record the event multiplicity and background multiplicity for each event. The first 100 μs gate is opened by the master trigger after a 5 ns delay in order to start the gate after the prompt gamma flash has already

passed through the Neutron Ball. The output of a scaler that takes the FIFO OR signals from each Neutron Ball segment is read out as the event multiplicity within this first gate. Immediately following this gate, a second 100 μs gate is opened in which the same scaler quantity is recorded as a "background" count of the neutrons. This second gate is considered background because any neutrons recorded now will have been captured at least 100 μs after the reaction which is much longer than the typical timescale for particle emission in reactions at these energies. The diagram for this can be seen in Figure 2.8.

The recording of each portion of data requires a master trigger signal to open the gates in which digital signals are taken by the DAQ. The overall trigger logic is shown in Figure 2.9. The triggering criteria for this experiment was either a signal from the CsI-PMT in rings 2-11 or a Si back signal from rings 2-7. The SUM and OR outputs required for the trigger logic were generated by CFD modules for the CsI-PMTs and by leading-edge discriminators in the Si back signals. The OR signals for the Si back and CsI-PMT signals were combined using a logic FIFO while the SUMs were combined using a linear FIFO. Events were broadly characterized in three separate categories: minimum bias events, high multiplicity events and pulser events. A minimum bias trigger means that an event has triggered that has at least one identified signal in the triggering modules. This is the most inclusive of the live event triggers and accepts all events regardless of their multiplicity. The minimum bias trigger uses the combined OR signals of the CsI-PMTs and Si backs processed through a logic FIFO since the trigger does not need to know how many signals fire, just that at least one was recorded. For the high multiplicity trigger, the SUM signals are fed into a linear FIFO so that the output of the FIFO is proportional to the number of signals that fired in triggering modules. This SUM is then fed through a CFD and the CFD threshold is set such that a minimum number of signals must

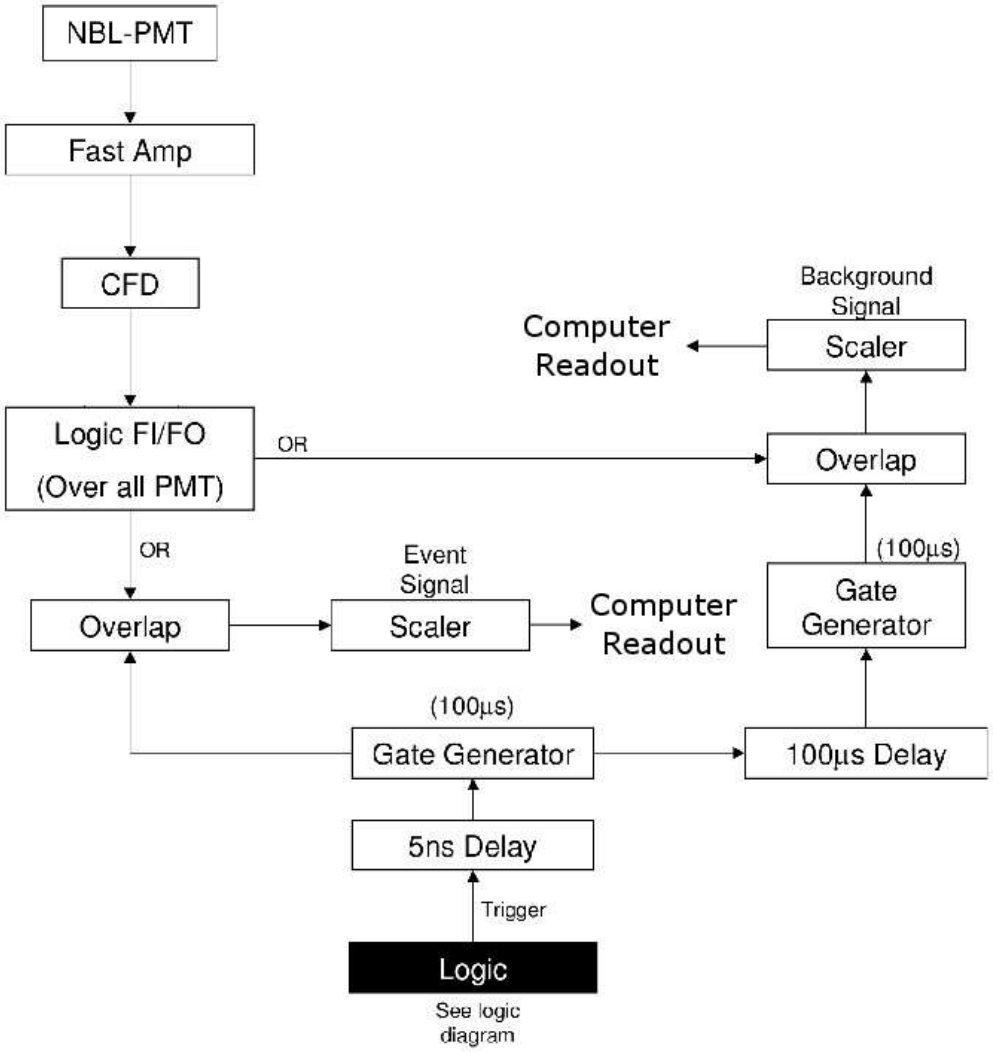

Figure 2.8: Electronics diagram for the PMT signals of the Neutron Ball.

have fired in order for the event to be read. In this experiment as in the previous experiment by Z. Kohley [78] a CFD threshold of 3 detectors must have fired for a high multiplicity trigger signal to be created. The third event type used a pulser to randomly trigger an "event". The primary purpose of the pulser events were to examine noise in the detectors and, primarily, in the Neutron Ball by collecting data that is decoupled form any actual beam events.

All three types of event trigger send signals to a Prescaler module once an event is triggered in order to "downscale" specific event types. For example, the minimum bias and pulser events both had a scaledown factor of 10 so that 1/10th of the actual events triggered in these manners were recorded into the data stream. This was done to reduce the number of events with little physics interest in the data stream and to help increase the live time of the electronics. The high multiplicity event trigger contains all of the events of interest and so the scaledown was set to 1 such that all high multiplicity events that triggered were recorded. The Prescaler module then sends a signal to a bit register that tracks how many of each kind of trigger occurs and another signal to a logic FIFO which sends a signal to the trigger module which initiates the DAQ trigger, provided the DAQ is not busy processing an event already.

A veto signal can be sent that blocks the trigger module signal if the DAQ is currently busy. This also blocks the CsI CFD from firing which is important in this setup because the CsI CFD only remains dead for 250 ns after firing and so could fire multiple times during the ~5 μs decay of the CsI signal based of detection of the residual tail of the CsI signal. The dead time of the DAQ is ~3 ms and so the beam current was adjusted to keep the number of events vetoed by the computer at just under 50%.

The signal from the trigger module starts the collection gates on the Si, CsI and Neutron Ball electronics as seen previously in their respective electronics diagrams.

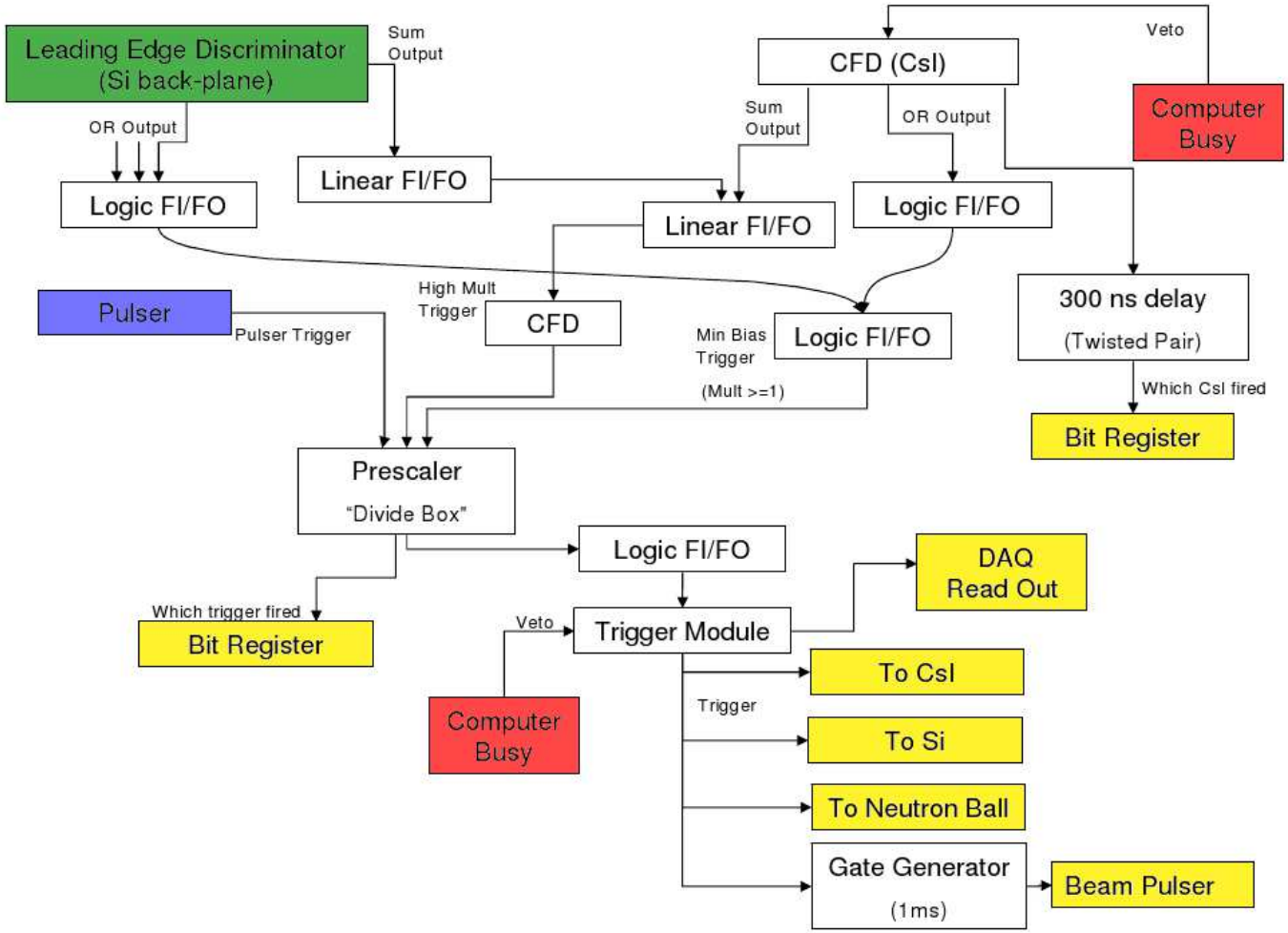

Figure 2.9: Electronics diagram for the trigger logic.

This signal also prompts the computer to read out all of the QDC, ADC and scaler modules which now potentially have data inside their collection gates. Finally, the trigger signal also gets sent to the beam pulser which is used to shut off the beam from the cyclotron temporarily while the event is recorded in order to minimize the background rate on the Neutron Ball caused by multiple beam bursts inside the relatively long Neutron Ball gates. However, it is important to note that while this shuts the beam off, there is still approximately 25 μs of beam packets in the beamline between when the beam pulser stops the beam and the NIMROD-ISiS array.

2.3 Charged Particle Identification

Particle identification (PID) in the NIMROD-ISiS array can be achieved by three separate types of plots: Si vs Si (Si-Si), Si vs CsI (Si-CsI) and CsI Fast vs CsI Slow (CSI F-S). Due to different gains and setup, the arrangement of these detector combinations allows for isotopic identification from the range of Z=1-20 and elemental identification up to Z=32 which in the heaviest system is Z=Z_{beam}+2. All PID methods follow the general form of utilizing a linearization method to linearize the 2D spectra and projecting them onto a 1D plot. The projected 1D is then fit with a series of gaussian functions corresponding to each individual isotope and/or element as resolution allows. This gaussian method allows for a quantitative measure of the resolution and contamination of one peak into another.

2.3.1 CsI Fast vs Slow

Pulse-shape discrimination in CsI is possible because CsI crystals exhibit a two-component decay to their signals because of the interactions of charged particles with the crystal structure [123]. The fast component of the signal comes from radiative excited states which are favored by high ionization densities, while the slow component comes from metastable excited states in the CsI crystal which are preferentially

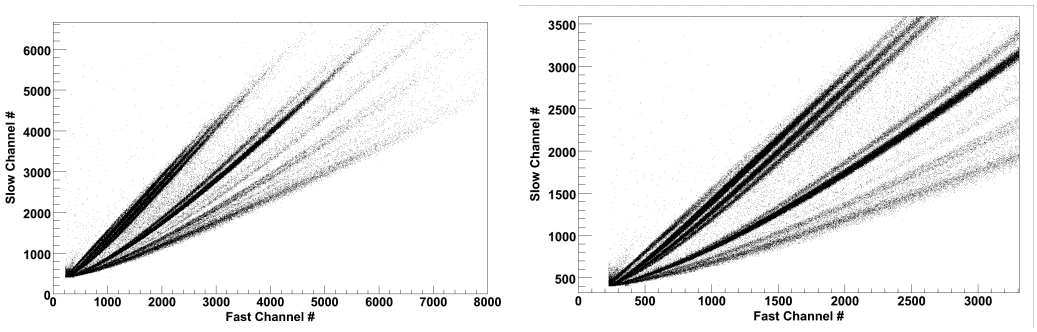

Figure 2.10: Full scale (left) and zoomed-in (right) CsI Fast versus Slow plot.

produced by low ionization densities. The magnitude of the ionization density is dependent on the dE/dx profile of the ionizing radiation that reacts with the CsI crystal [122]. In general, a heavier ion will generate a high ionization density in a CsI crystal which creates a preference for radiative states over metastable states. Conversely, a light ion will have a much lower ionization density and therefore will preferentially produce metastable states to radiative states. It is therefore possible to use the comparison of radiative (fast component) to metastable (slow component) states to identify heavy ions from light ions.

The thallium doping of the CsI crystal provides a decay path for the excited electrons to decay back into the valence band. This is achieved by populating the normally forbidden energy gap in the CsI structure with additional energy levels corresponding to thallium. This also causes a shift in the wavelength of the light emitted from the electron due to de-exciting from the forbidden region to the valence band, rather than from the conduction band to the valence band. This shift also happens to push the wavelength into a region where the PMT response is much greater which improves the efficiency of the charged particle signal detection [122].

Pulse-shape discrimination allows for isotopic resolution for the range Z=1-3 by

comparison of CsI Slow vs CsI Fast signals as seen in Figure 2.10. Protons (^{1}H), deuterons (^{2}H), tritons (^{3}H), helions (^{3}He), alphas (^{4}He), ^{6}He and ^{8}He fragments can all be identified via this pulse-shape discrimination method. In some cases, the primary isotopes of Z=3 (^{6}Li, ^{7}Li, and ^{8}Li) can also be identified though beyond Z=3 there is not enough difference in the ionizing energy deposited to be able to distinguish different elements from each other. It is worth noting that the ^{8}He line is actually a superposition of ^{8}He particles and 2α double-hits. The identification and separation of these can be found in Section 2.3.6.

2.3.2 Si vs CsI

The primary method of identifying larger charged particles (Z>3) in the NIMROD-ISiS array is by plotting the energy lost by a particle passing through a thin Si (ΔE) versus the total energy deposited by a particle stopping in a block of CsI crystal (E). The resulting ΔE/E plot can provide isotopic resolution up to from Z=3 to Z=20. Every module in the array is outfitted with Si-CsI coverage in order to maximize the detection of isotopically resolved heavy fragments in the lab frame. As mentioned previously (Section 2.2.1), the Si detectors in rings 2-7 have the front and back planes of the Si gained separately. This allows the gains on the front to be set to maximize the isotopic resolution from Z=3-20 while the gains on the back plane are set to cover the elemental range up to and slightly exceeding the Z of the beam. This combination allows for maximizing the detection of particles over the widest range of isotopes and elements possible. An example of this comparison from the CsI energy plotted as a function of the Si front and Si back signals side-by-side can be seen in Figure 2.11. In this example we can clearly see isotopic resolution of Z=17 using the Si front signal and elemental resolution of Z=30 from the Si back signal.

Using the loss of energy, dE/dx, of a charged particle through a material we can

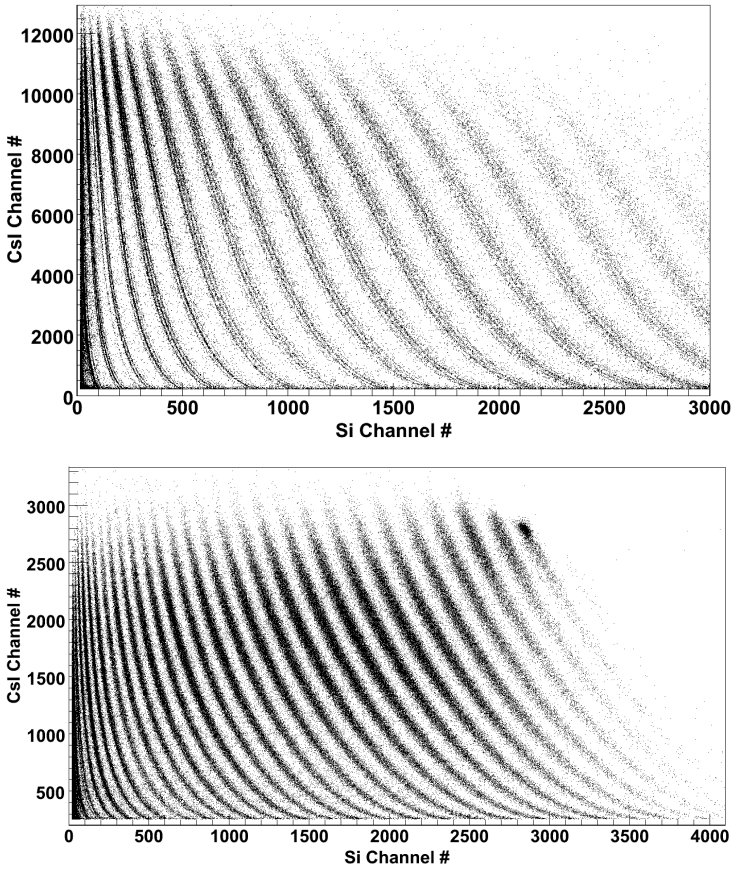

Figure 2.11: Silicon front-plane signal versus CsI signal (top) and silicon back-plane signal versus CsI signal (bottom).

see that different elements and isotopes should separate themselves into bands based on their energy loss according to the Bethe-Bloch formula [123].

$$-\frac{dE}{dx} \propto \frac{Z^2}{v^2} \propto \frac{Z^2 \cdot A}{KE} \tag{2.1}$$

Equation 2.1 shows a simplified form of the Bethe-Bloch formula that demonstrates this behavior, where Z is the particle charge, A is the particle mass and KE is the kinetic energy of the particle.

2.3.3 Si vs Si

As previously discussed in Section 2.2.1 there are two super-telescope modules per ring from rings 2-9. These super-telescopes not only provide Si-CsI but also Si-Si detector pairs for PID. Each Si-Si combination consists of a 150 μm Si detector in front of a 500 μm Si detector. By plotting the energy loss in the first (thin) Si as a function of the energy lost in the second (thicker) Si, another ΔE/E plot is created that, in general, has much better resolution than that of a Si-CsI pair. This better resolution is attributed to the use of two Si detectors as both the ΔE and E detectors since Si typically has a better energy resolution than that of a CsI crystal.

2.3.4 Linearization

As mentioned in Section 2.3, a linearization method is used to take the 2D energy spectra and project them onto a 1D axis in order to identify the isotopic/elemental lines. Points along the elemental lines are hand picked using a custom Graphical User Interface (GUI) that follow along the curvature of the data. For each line of hand picked points, a spline fit is used to connect and smooth out the hand-drawn curve. Along this spline fit (blue lines), 100 evenly spaced points (blue circles) are calculated along the curvature of the smoothed spline (Figure 2.12a).

a)

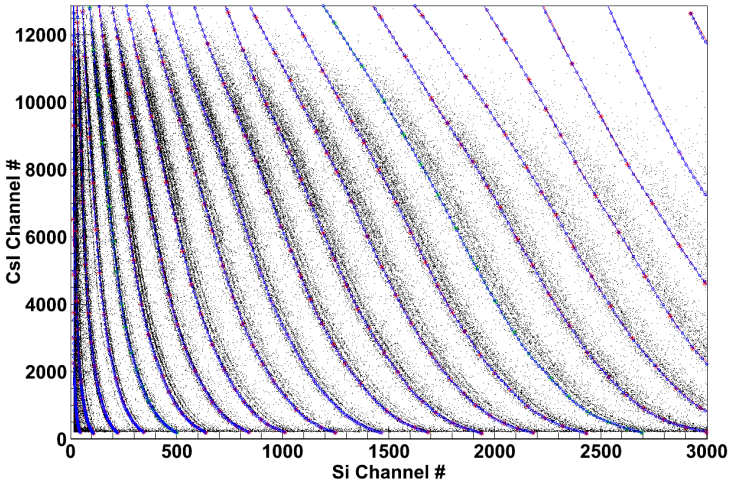

b)

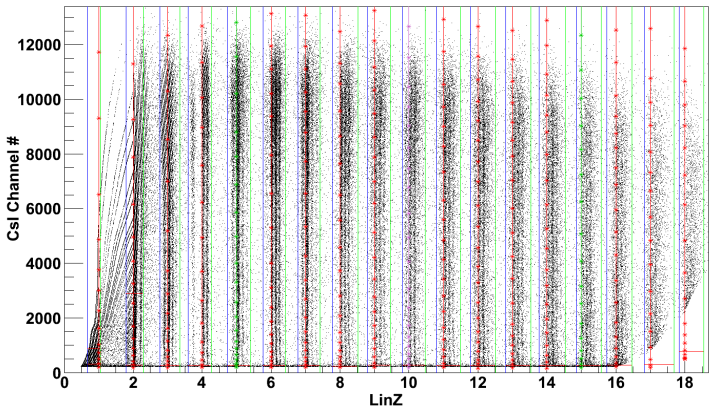

c)

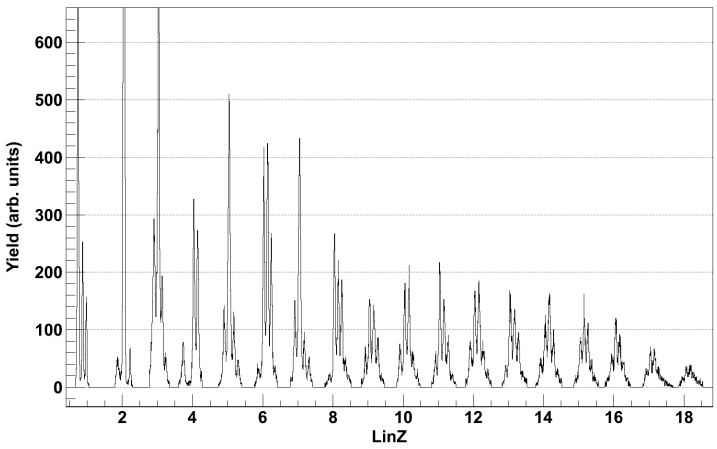

Figure 2.12: The linearization process is presented showing a 2-D Si-CsI plot (Panel a), the linearized 2-D plot (Panel b), and the 1-D projection (Panel c) of the linearization.

The curved lines are then linearized by calculating the relative distance of each data point to the two nearest spline curves. The spline fits are approximated by line segments connecting each successive pair of the 100 calculated points along the spline. This method calculates the distance from the point to the curve with a high degree of accuracy while greatly reducing computational time during this step. This method calculates a linearized Z value (LinZ) for each data point, such that the LinZ represents the position of the data point between two curves. For example, if a data point exists 30% of the way between the boron (Z=5) line and the carbon (Z=6) line, the linearization method will calculate a LinZ=5.3. There are three possible cases to calculate: Equation 2.2 handles the case where the data point is left of all the lines, Equation 2.3 handles the case where the data point is between two lines (most common) and Equation 2.4 handles the case where the data point is right of all the lines. In all three cases, the terminology is the same, $d1$ and $d2$ refer to the distance from the point to lines 1 and 2, respectively, while $L1$ and $L2$ refer to the Z value of lines 1 and 2, respectively. Line 1 is always the left-hand line while line 2 is the right-hand line in any adjacent pair of lines being used in the calculation.

$$LinZ = \frac{d2}{|d2 - d1|} L1 - \frac{d1}{|d2 - d1|} L2 \tag{2.2}$$

$$LinZ = \frac{d1}{|d1 + d2|} L2 + \frac{d2}{|d1 + d2|} L1 \tag{2.3}$$

$$LinZ = \frac{d1}{|d1 - d2|} L2 - \frac{d2}{|d1 - d2|} L1 \tag{2.4}$$

As previously stated, the spline lines are approximated by connecting line segments using the 100 evenly-spaced line points that were calculated. This creates 99 line segments that approximate the curvature of the spline curve. The distance between a data point and a curve of interest is actually calculated as the distance from

the data point to all 99 line segments of the curve. The minimum distance of this cohort corresponds to the closest line segment of the curve and, therefore, approximates the shortest distance to the line. This process is repeated for the other spline line and the resulting distances are used in Equations 2.2-2.4 to calculate LinZ. Once a LinZ value has been determined for every data point from a 2D spectra, the points are plotted on another 2D plot where the y-axis is still the E signal value from the 2D spectra, but the x-axis is now the LinZ value. This produces a 2D linearized version of the original spectra where the data has been straightened according to the hand-picked elemental lines (Figure 2.12b). This 2D plot is then projected on to the x-axis such that the resulting 1D projection demonstrates gaussian peaks corresponding to isotopic and elemental resolution from the original ΔE/E spectra (Figure 2.12c).

In processing the 2D linearized plot in Figure 2.12b, limits were imposed on the data. Left and right hand limits (seen as vertical blue and green lines, respectively) were applied to separate the various elements and clean up any noise that may exist between elements. More notably, however, are the horizontal red lines near the bottom of the plot. These thresholds were set to remove the noise caused by edge-effects in the LinZ calculation resulting from data pile-up around the punch-through energies in the silicon. The 1D projection only includes data within these three limits for each isotope/element. Once the projection is complete, clear separation of elements and isotopes can be seen in the peak structure in Figure 2.12c where the identity of each element/isotope can be determined by the Gaussian Fitting method described below (Section 2.3.5).

2.3.5 Gaussians

Gaussian functions were fit to each identified peak in the 1D LinZ spectra in order to clearly determine the identity of each peak as well as to provide an indication of

the amount of contamination that may occur between isotopes in their identification. An example of a Si-CsI 1D projection with high isotopic resolution can be seen in Figure 2.13. Here we can see that each isotope is fit using an individual gaussian function of the form

$$G(x) = C \cdot \exp\left(-\frac{1}{2} \cdot \left(\frac{x-\mu}{\sigma}\right)^2\right) \tag{2.5}$$

where C is the height, μ is the centroid and σ is the width of the Gaussian peak. The parameters of the Gaussian functions were determined by minimizing the error in the sum of each isotopic Gaussian within a single element. One distinct advantage to fitting a Gaussian function to each isotope rather than using limits to set isotopic identification or drawing "banana gates" around isotopes on the 2D spectra is that the overlap of the isotopic Gaussians allows for a characterization of the contamination between identified particles. A percent contamination value is determined for each particle by

$$\%Contamination = \frac{\left(\sum_{i=1}^{N_{Gauss}} G_i(LinZ)\right) - G_{Max}(LinZ)}{G_{Max}(LinZ)} \tag{2.6}$$

where N_{Gauss} is the number of Gaussian functions for a specific element, $G_i(LinZ)$ are the individual Gaussian values at point LinZ and $G_{Max}(LinZ)$ is the maximum Gaussian value at point LinZ. The identity of the particle found at point LinZ is set as the Z and A of the Gaussian G_{Max} and given a contamination value based on Equation 2.6. The particle is also assigned a fractional sigma value calculated via

$$SigmaFrac = \frac{|LinZ - \mu|}{\sigma} \tag{2.7}$$

where μ and σ are the Gaussian parameters for $G_{Max}(LinZ)$. This fractional sigma value is a representation of how many sigmas away from the mean the particle is and can be used as another contamination parameter. For instance, if a 95% confidence on the identification of a particle is required, a 2σ (~95.45%) limit condition could be set using a SigmaFrac=2 or less requirement. The SigmaFrac and %Contamination parameters combine to give an estimate of the purity of the PID as well as a method of selecting on more tightly constrained confidence in the PID. Once the SigmaFrac is determined, the particle has been assigned a Z, A, %Contamination and a SigmaFrac and is now considered "identified". It should be noted that Eqs. 2.6 and 2.7 calculate %Contamination and SigmaFrac values, respectively, for a single LinZ value. Each particle is assigned a %Contamination and SigmaFrac value based on the LinZ value calculated for that specific particle and the particles are then individually filtered based on these properties. In order to maximize statistics for the yield scaling methods used in the analysis (Section 3.5) %Contamination=0.2 and SigmaFrac=2.5 were selected for the experimental constraints in this work. It should be noted that while the %Contamination=0.2 implies that up to 20% of the particles identified with that %Contamination value could be contamination from an adjacent isotope, this selection is still more restrictive in isotopic identification requirement than in the case of a hard limit on LinZ separating the isotopes.

Once every isotope is identified with Gaussian peaks, the Z and A value of the peaks must be confirmed. This was done for light elements by comparison of the integral of the Gaussian peaks to the natural abundances of the isotopes in nature. Even for very neutron-rich systems, these correspond very well up to about neon (Z=10). For the heavier elements, the Gaussian total integrals were compared to experimental yield abundances measured using similar reactions on the MARS spectrometer [125] as well as comparison to previous NIMROD-ISiS experiments [78, 109, 126]. In

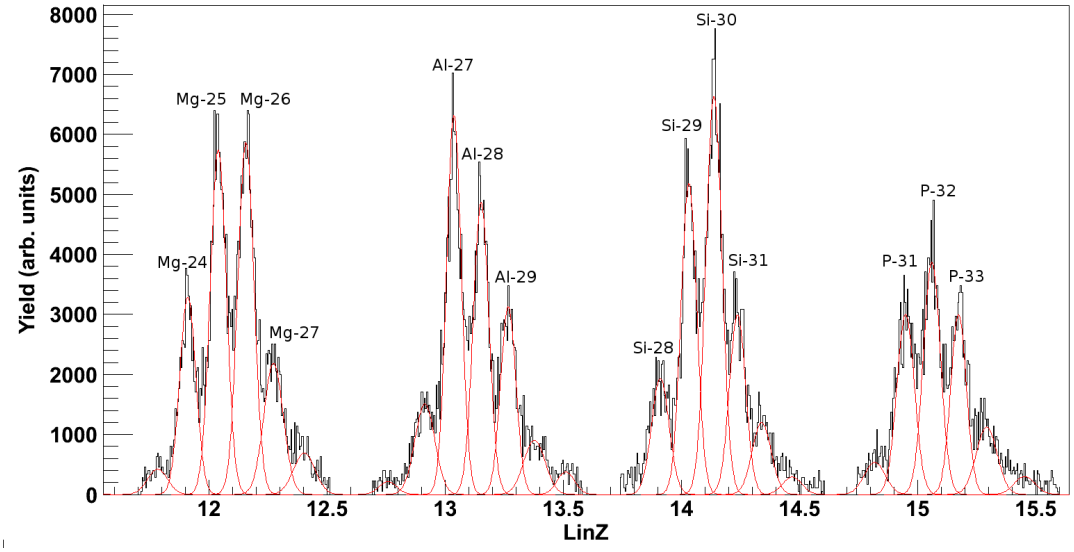

Figure 2.13: 1-D projection of Si-CsI plot showing the Gaussian fits to the Z=12-15 isotopes.

situations where isotopic resolution was not possible, a single Gaussian function was fit to the entire element and each particle was given the un-physical but easily recognized identification of A=0. As part of the PID logic in Section 2.3.6 these particles will be assigned a "GuessA" that corresponds to the most probable A value for the given Z for use in estimations of event characteristics in which isotopic resolution is not a requirement.

This linearization-Gaussian fitting procedure was used to identify all charged particles in the array, regardless of the detector geometry they came from. In some cases, a particle could therefore be identified in multiple detector geometry configurations (for example, a heavy fragment identified in both the Si Front Vs CsI as well as the Si Back vs CsI or a light fragment identified in a Si Front vs CsI and a CsI Fast vs Slow). In the case that a particle is identified in multiple ways, the logic discussed in Section 2.3.6 will outline how the correct Z and A identification are determined.

Table 2.6: Particle identification labels and descriptions.

Label	Description
CsIZ	Z identification obtained from CsI Fast vs. Slow
CsIA	A identification obtained from CsI Fast vs. Slow
SiFrontZ	Z identification obtained from front-plane silicon vs. CsI
SiFrontA	A identification obtained from front-plane silicon vs. CsI
SiBackZ	Z identification obtained from back-plane silicon vs. CsI
SiBackA	A identification obtained from back-plane silicon vs. CsI
SiCsIZ	Z identification obtained from either front- or back-plane vs. CsI
SiCsIA	A identification obtained from either front- or back-plane vs. CsI
SiSiZ	Z identification obtained from super-telescope (Si1 vs. Si2)
SiSiA	A identification obtained from super-telescope (Si1 vs. Si2)

2.3.6 PID Logic

The final step of the PID process is the determination and verification of the particle Z and A based on a hierarchy of confidence in order to account for the situations where a particle is "identified" in multiple ways. All particles require a SigmaFrac value of 3.0 or less in order to be considered "good" particles. This cuts out the extreme outliers in the Gaussian distributions and removes ~0.2% of the total number of particles.

Each particle is labeled according to Table 2.6 based on each method that was used to assign an identification to the particle. This same nomenclature will be used in the flowcharts throughout this section in analyzing the logic for determining good PID. These identifications are then used in creating the physics tapes to label which identification method was used in determining the final PID of the particle.

The procedure for checking the PID assignment of each particle is shown in the flow chart in Figure 2.14. Once a particle is either accepted as good or rejected as bad, it exits the flow chart and a new particle is analyzed. The first step is

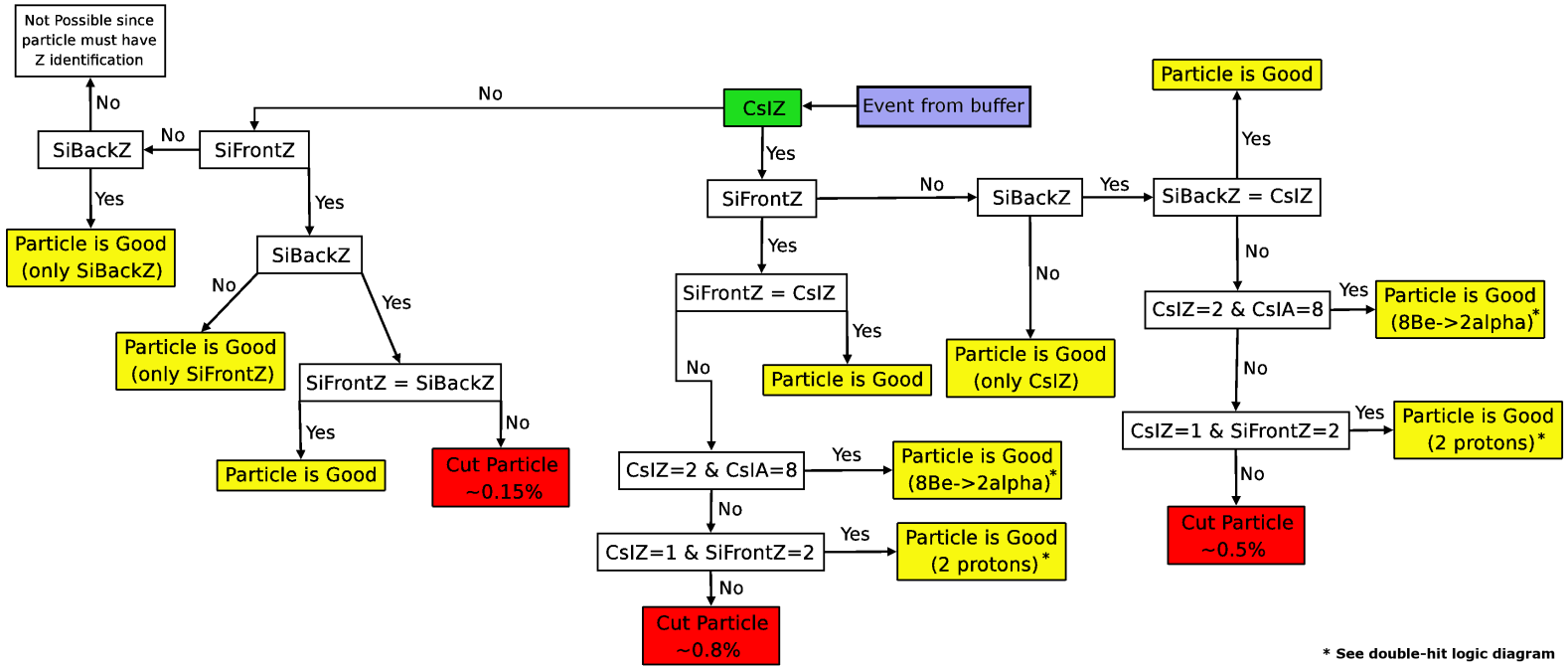

Figure 2.14: Flow chart depicting the process for checking and comparing the particle identifications in different detector types.

to determine whether the particle received a Z identification in the CsI (green box). This would only occur for a particle with Z$\leq$3 coming from a CsI Fast vs Slow (CsIZ). If the particle is identified with a CsIZ then the particle is checked to see if it was identified in the Si Front vs CsI (SiFrontZ) and, if it was, the identification assigned from CsIZ and SiFrontZ are compared to each other. If CsIZ=SiFrontZ the particle is accepted as good. If CsIZ$\neq$SiFrontZ, then the particle is checked to see if it could be a double-hit event - either double-alpha or double-proton. If the particle has CsIZ=2 and CsIA=8 or if it has CsIZ=1 and SiFrontZ=2, these particles are considered possible double-hits and are set aside for further analysis discussed below. If neither of these conditions are true, the particle is rejected as bad (~0.8% of total particles). If the particle did not receive an identification for the SiFrontZ but is identified in the CsI, then it is checked for identification in the Si Back vs CsI (SiBackZ). If the particle has a CsIZ but no SiFrontZ or SiBackZ, then the particle is accepted as having only a CsI identification. If the particle has a valid identification then the same procedure as the SiFront case is followed, accepting particles with matching identifications, setting aside possible α and proton double hits for further analysis and rejecting particles with mismatched identifications (~0.5% of total particles).

If the particle did not have a CsI identification at all (true for all particles Z>3), then the SiFrontZ and SiBackZ were analysed and compared. If the particle received a valid identification in only one of either the SiFront or SiBack, the particle was accepted with that assigned identification. However, if the particle received both a SiFront identification as well as a SiBack identification, the two were compared and if the identifications were mismatched the particle was removed (~0.15% of total particles) while particles with matching identifications in the SiFront and SiBack were accepted.

As previously mentioned, particles resulting from possible double hits were given

special consideration. Double hits could result from either 2α breakup of ^{8}Be or 2p hits from highly-correlated protons. When a double-hit event passes through a detector, the total amount of energy deposited by both particles is recorded which gives a signal higher than that of either of the individual particles. For an α double-hit, it had been previously shown [117] that the signal in a CsI Fast vs Slow will show up as a Z=2, A=8 particle. Since ^{8}He is very short lived, a comparison can be made with the signal seen in the Si Front vs CsI. Even if the particle is not strictly marked as "identified" in the Si Front vs CsI, the LinZ value is used to categorize the particle as a double hit or not. If the potential 2α signal has a SiFront LinZ of around Z=3 or higher, the particle is marked as a 2α double-hit by assigning it a Z=4 and GuessA=8 identification since the two particles are either highly correlated alphas or more likely came from the breakup of the unstable ^{8}Be. Otherwise, if the SiFront LinZ has a value closer to Z=2, the particle is identified as a Z=2, A=8 particle corresponding to ^{8}He. Similarly a 2p signal will show up in the CsI Fast vs Slow in the Z=1 isotopes, but outside of the Z=1, A=1 band. If the particle is determined to be a 2p double-hit, the particle is marked as a Z=2, GuessA=2 double-hit, otherwise it is rejected as unidentified.

Once every particle from an event is identified via the logic found in Figure 2.14, each event particle is then compared to all of the other particles in the event in order to determine whether they both came from the same detector module. The geometry of some modules in the NIMROD-ISiS array are such that two interesting cases can occur: one Si detector in front of two or three CsI crystals, as well as two Si detectors in front of a single CsI crystal. Both of these cases must be examined and checked. The first case, where a single Si detector (SiID number) is present in front of two or more CsI crystals is resolved via the process in Figure 2.15. The particle of interest (PoI) is compared to all other particles in the event (P_i). Each

comparison consists of first checking to see if both particles were identified by SiCsI and if either of them were not identified in the SiCsI then the comparison is marked "good" and a new comparison is started. If both particles were identified by SiCsI, then the Si detector numbers of both particles are compared to make sure that they were not both detected in the same Si. If the particles were detected in different Si detectors, the comparison is marked as "good" and a new comparison is started. If the particles were both detected in the same Si detector, then the final check is to see if the PoI was independently identified in the CsI and if so, then the particle is marked as "good". Otherwise, the SiCsI identification cannot be trusted because two particles were both identified in the same Si which would cause the identification values to appear in the wrong place. In this case, the PoI is removed (<0.2% of total particles). The process is the same for both Si Front and Si Back detectors.

The second case occurs when a module has two Si detectors placed in front of a single CsI crystal which only occurs in super-telescopes as described above (Section 2.2.1). Similar to the previous case, each PoI is compared to all the other P_i. However, as seen in Figure 2.16 the first step is to test whether both particles were identified in super-telescopes. If not, the comparison is marked good and the next particle is tested. If both particles are detected in a super-telescope, then the CsI ID value of the PoI is checked to see if there is 1 or 2 CsI crystals behind the Si and if there are 2 CsI crystals behind the Si then the particle is accepted because it was not a double-hit. If only one CsI crystal is behind the Si detectors, then the SiSiZ identification is checked for both particles since if either particle has a SiSiZ identification then the particle was not a double-hit and the pair is accepted. Finally, the two particles are tested to see if they were detected in adjacent Si detectors. If so, the pair constitute a double-hit in the CsI crystal behind the Si detector in the super-telescope and are removed. This eliminated <0.1% of all particles.

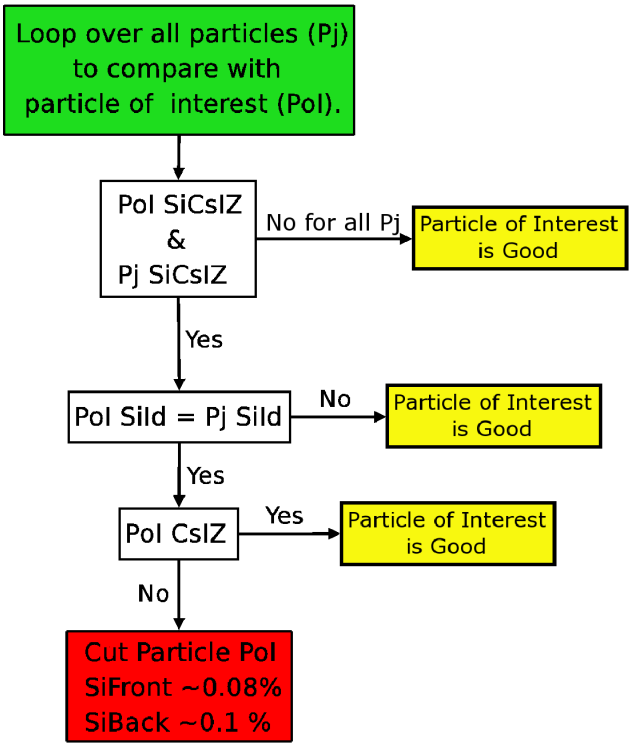

Figure 2.15: Flow chart depicting the process in which particles were compared in order to make sure that two particles were not identified in a detector module in which one silicon detector was placed in front of two CsI detectors.

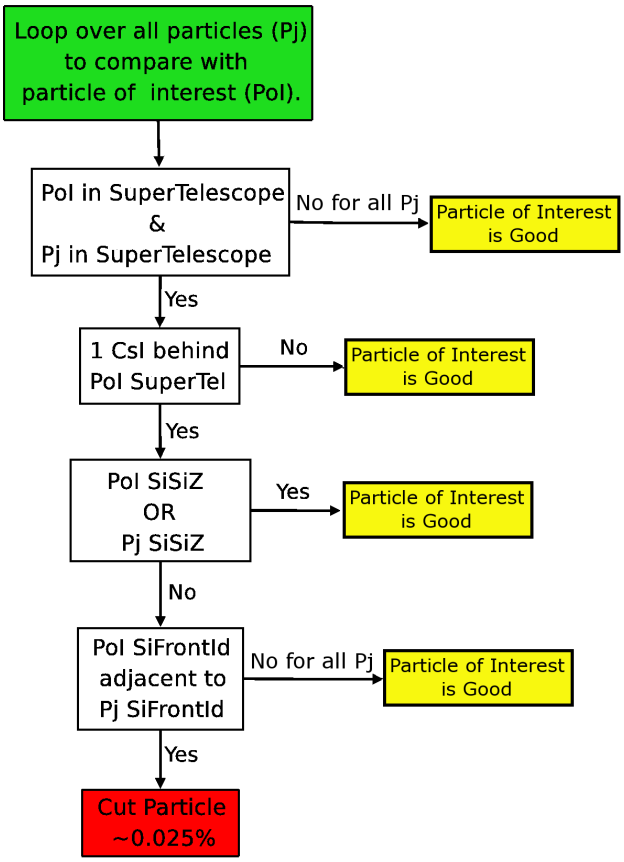

Figure 2.16: Flow chart depicting the process in which particles were compared in order to make sure that two particles were not identified in a supertelescope in which two silicon detectors were placed in front of 1 CsI.

Table 2.7: The calibration particles and scatter energies produced in rings 2-11 of the NIMROD-ISiS array from the different calibration reaction systems.

Reaction	55 MeV/u $^{1}H_2$+^{197}Au	55 MeV/u α+^{197}Au	35 MeV/u ^{20}Ne+^{197}Au	25 MeV/u α+^{197}Au	30 MeV/u ^{1}H-^{2}D+^{197}Au	
Calibration Particles	55 MeV proton	220MeV alpha	700 MeV ^{20}Ne	100 MeV alpha	30MeV proton	60MeV deuteron
Ring 2	55.0 MeV	220.0 MeV	697.8 MeV	99.9 MeV	30.0 MeV	60.0 MeV
Ring 3	55.0 MeV	219.9 MeV	697.3 MeV	99.9 MeV	30.0 MeV	60.0 MeV
Ring 4	55.0 MeV	219.8 MeV	696.3 MeV	99.9 MeV	30.0 MeV	60.0 MeV
Ring 5	55.0 MeV	219.7 MeV	694.7 MeV	99.8 MeV	30.0 MeV	60.0 MeV
Ring 6	55.0 MeV	219.5 MeV	691.1 MeV	99.7 MeV	30.0 MeV	59.9 MeV
Ring 7	54.9 MeV	219.1 MeV	685.5 MeV	99.5 MeV	30.0 MeV	59.9 MeV
Ring 8	54.9 MeV	218.5 MeV	676.3 MeV	99.3 MeV	29.9 MeV	59.8 MeV
Ring 9	54.8 MeV	217.8 MeV	664.6 MeV	98.9 MeV	29.9 MeV	59.7 MeV
Ring 10	54.7 MeV	215.3 MeV	627.6 MeV	97.8 MeV	29.8 MeV	59.3 MeV
Ring 11	54.5 MeV	212.8 MeV	592.2 MeV	96.7 MeV	29.7 MeV	59.0 MeV

Once each particle has been fully identified and checked for accuracy by the previous logic schemes, the now-verified Z, A, GuessA, %Contamination and SigmaFrac are applied to the particle for writing to the Physics Tapes (described in detail in Section 2.5). The final Z and A are found by comparing every Z and A identification for the particle and accepting the identification with the smallest %Contamination and are marked with the associated identification label (see Table 2.7). For any particle without a clear isotopic value from any identification method, the particle was given the un-physical A=0 value and assigned a GuessA consistent with the most probable A for that Z value.

2.4 Energy Calibration

After all the particles have been identified, their kinetic energies are determined. To help in this process a series of calibration beams were collected (Table 2.3) such that the fixed energy beam projectiles were elastically scattered off a ^{197}Au target into the NIMROD-ISiS array. From the scattering angle (given by the detector that the particle was identified in) the energy of the scattered calibration beam projectile can be determined. This gives a series of known calibration points in the detector array that can be used to energy calibrate the channel numbers recorded from the ADCs. Table 2.7 shows the list of calibration beams and the energies of their scattered particles in each of the rings from 2-11. Data is not shown for rings 12-15 because the cross-section to elastically scatter in the backward direction is too low to obtain reasonable calibration points. Calibration points from the various calibration beams were used in conjunction with data collected from a ^{228}Th source as well as the punch-through points of the Si detectors in order to calibrate the NIMROD-ISiS array.

The primary method of calibrating the Si detectors is by using the energy of

the punch-through points and was cross-checked with either a ^{228}Th source or the 35 MeV/nucleon ^{20}Ne. The punch-through point on a Si is defined as the point on a 2D ΔE/E plot (where a Si detector is the ΔE) that corresponds to the energy where a given isotope just passes through the detector to give the minimal signal in the E detector. On a Si-CsI plot, this punch-through energy is the lowest value Si signal for a given isotope that has a corresponding valid CsI signal demonstrating that the particle had just enough energy to pass through the Si and enter the CsI. In a Si-Si ΔE/E plot, two punch-through points can be see, one corresponding to punch-through of each of the two Si detectors. Once the channel number value of each punch-through point has been determined, the energy required for the isotope to punch-through the Si is calculated using standard energy loss tables [127]. The gains on the Si detectors for rings 10-15 were low enough that a ^{228}Th α source was used to calibrate the detectors. The energy resolution on these detectors was able to resolve 6 distinct peaks in the α-chain decay spectra that could positively be identified with known energies.

To calculate the calibration between channel number and energy a linear fit was assumed between particle energy and Si signal such that

$$Energy = SiChannel\# \cdot m + b \tag{2.8}$$

where m and b take the usual form of the slope and intercept of the linear fit, respectively. An example of this can be seen for a Si-CsI in Figure 2.17 where a linear fit of the form in Equation 2.8 has been applied to the punch-through points (seen in blue). The two green squares correspond to a 100 MeV α and a 500 MeV ^{20}Ne coming from the calibration beams. This double-check demonstrates excellent agreement between the calibration beam calibration points and those derived from

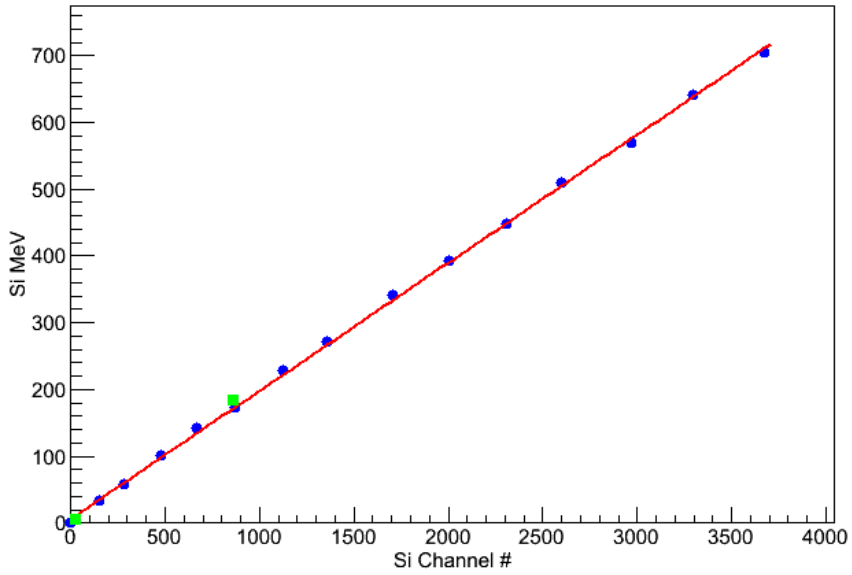

Figure 2.17: Example of a silicon calibration. The silicon energy from the punch-through points is plotted as a function of the silicon signal channel number (blue circles). The fitted energy calibration, Equation 2.8, is shown as the black line. The calibration points from the 100 MeV α and 500 MeV ^{20}Ne beams are shown as the green squares.

the Si punch-through energies. The back plane of the Si detectors are calibrated off the front calibrations. Since any particle passing through the Si detector would deposit energy that is collected as electrons on one plane and holes on the other plane, both the front and back plane of the Si should register the same energy for any given particle. However, since the fronts and backs are gained separately, the calibration values for the back will differ from the front. In Figure 2.18 we can see the Si front calibrated energy as a function of the Si back channel number. The linear fit provides the energy calibration parameters for the Si back and the high-linearity of the plot provides confirmation that the back can be calibrated off the front.

Calibration points from the light-ion calibration beams were used to calibrate the CsI-PMT signals. These values were then compared to energy spectra previously

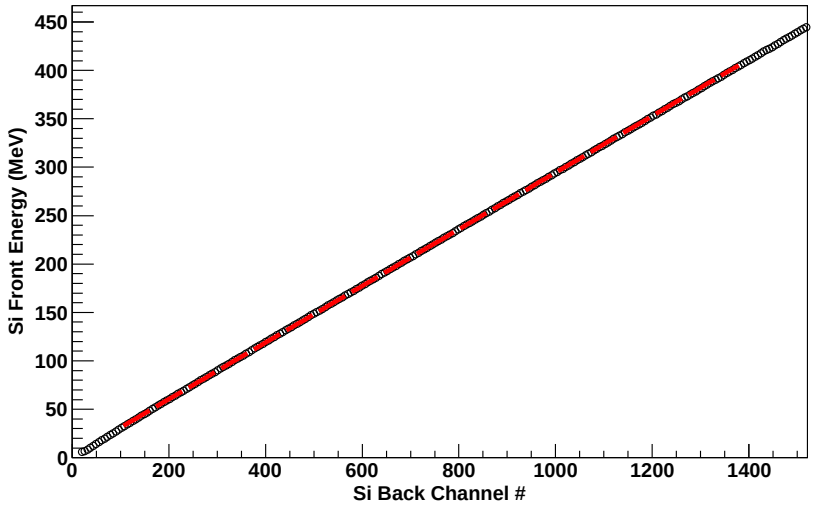

Figure 2.18: The energy determined from the front-plane silicon calibration is shown as a function of the silicon back-plane channel number (open circles). The calibration was determined by fitting Equation 2.8 (red dashed line) to the data.

taken for similar systems, namely the ^{70}Zn+^{70}Zn reaction at 35 MeV/A taken on the NIMROD-ISiS array [78]. Because of possible saturation of the CsI Fast signal at high energies, the CsI Slow signal was used to complete the energy calibration for all detectors. Unfortunately the energy calibration for CsI does not follow a linear relationship like the Si detectors but instead exhibits a dependence on the Z and A of the fragment. Equation 2.9 demonstrates a relationship derived from the Birks formula [122, 123, 128] that compares the light output (CsI signal) from a PMT to the particle energy. Equation 2.9 is defined as

$$E = \sqrt{h^2 + 2\rho h\left(1 + \ln(1 + \frac{h}{\rho})\right)} \tag{2.9}$$

where

$$\rho = \eta Z^2 A \tag{2.10}$$

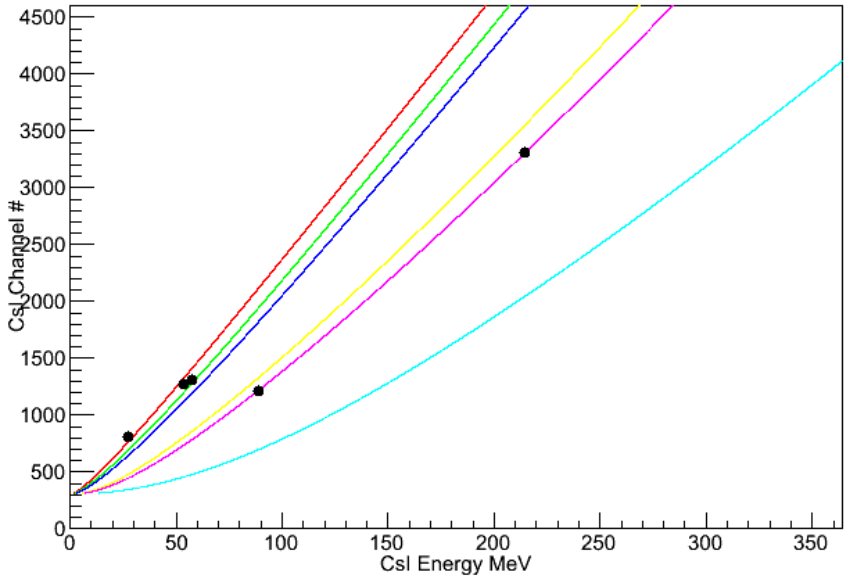

Figure 2.19: Example of CsI calibration showing the CsI slow signal channel versus the energy. The calibration points (black circles) were used to constrain the parameters of Equation 2.9. The energy calibration for protons (red line), deuterons (green line), tritons (blue line), ^{3}He (yellow line), α (pink line), and ^{7}Li (light blue line) are shown.

and

$$h = \frac{Chan\# - Pedestal}{Scale} \tag{2.11}$$

such that Chan# is the CsI-PMT slow signal, Pedestal is the pedestal of the detector, Z is the charge of the particle, A is the mass of the particle and η and Scale are fitting parameters. The calibration points calculated in Table 2.7 are used to fit Equation 2.9 as seen in Figure 2.19. The fit is applied by minimizing the error between the function and the calibration beam data points and the fit shown is in good agreement with the calibration points.

Once all of the detectors have been energy calibrated, the total energy of each particle must be calculated from the energy deposited in each detector the particle

passed through. For all particles Z≥4 the total energy was taken as the sum of the energy deposited in the Si detector and the residual energy deposited in the CsI, where the CsI residual energy was calculated via the energy loss tables [127] and the energy deposited in the Si detector. This was done because the residual energy left for heavy fragments in the CsI is not as clean of a signal as the energy lost as the particle passes through the Si. For rings 2-11, all Z=1 and Z=2 particles had their total energy determined by using the residual energy from the CsI detectors as calculated by the CsI calibration and the energy deposited in the Si calculated via energy loss tables, then summing the two. The Si detector calibration could not be used for Z=1 and Z=2 particles because the gains on the Si detectors caused these signals to be highly compressed at the low end of the spectrum. Because of this same gaining issue, the Z=3 particles had their energies determined using the method for Z=1 and Z=2 in ring 2, while using the method for Z≥4 in rings 3-11. In ISiS (rings 12-15) the silicon gains were set such that the silicon energy calibration and energy loss table were used for all particles (Z=1 and Z=2). Figure 2.20 shows an example of the resulting energy spectra for the 35 MeV/A ^{70}Zn+^{64}Zn system for all of the NIMROD-ISiS array (rings 2-15). The energy spectra for all particles in each ring can be found in Appendix A.

2.5 Physics Tapes

Once all of the particle identity and energy information has been determined, the experimental data must be written to disk. The legacy-name of "physics tapes" refers to this process by which the "raw tapes" undergo PID and energy calibration and are written to disk. The initial raw tapes refers to the raw data collected during the experiment that consists of simple event structures recording digitized channel numbers from the ADCs and QDCs and is stored as the T041910Event C++

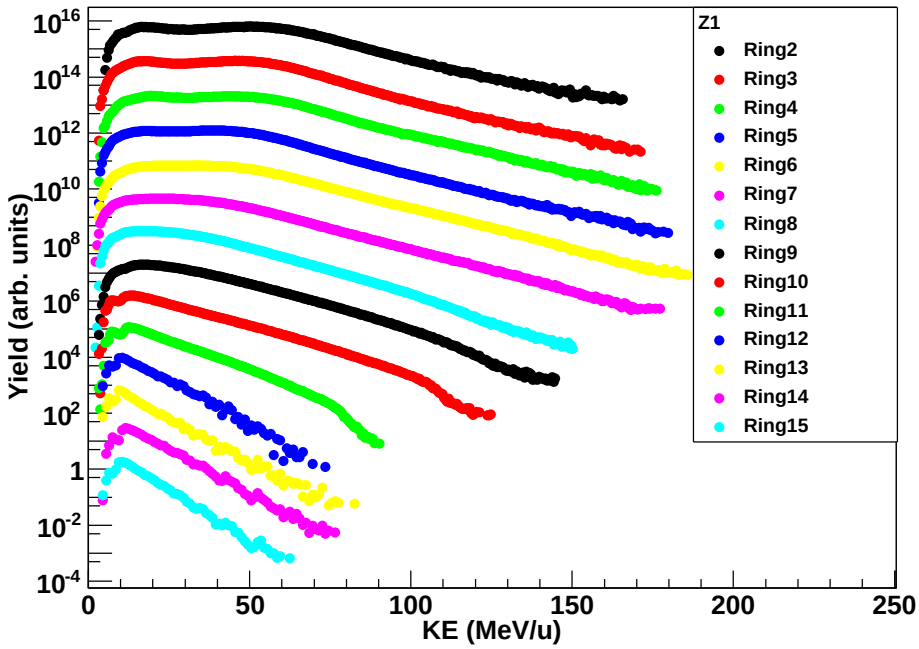

Figure 2.20: Energy spectra of the Z=1 fragments for each ring of the NIMROD-ISiS array for the 35 MeV/nucleon ^{64}Ni+^{64}Ni system.

object. The raw tapes then undergo the linearization process outlined in Section 2.3.4 and are converted into PID tapes. The PID tapes are based on the PIDEvent and PIDParticle structures. The PID tapes are constructed in an event-by-event format where the PIDEvent object records information such as the event multiplicity and event trigger type. Each event contains a PIDParticle object for every particle associated with that event. The PIDParticle object holds such information as the Z, A, LinZ value, %Contamination, SigmaFrac and raw signals from the detectors the particle encountered.

The final step is the production of the physics tapes which follow the PhysEvent and PhysParticle structure. The physics tapes are considered "final" and represent the experimental data in a form where each particle is fully identified with their correct total energies. These tapes are then used in the subsequent analysis of the experiment to examine the physics that has taken place, hence the name. The process of converting the PID tapes to physics tapes includes both the PID logic and energy calibration steps (Sections 2.3.6 and 2.4 respectively). It is important to note that no information is removed from the raw tapes to PID tapes step, but that the physics tapes only contain particles that have a valid PID and total energy. The PhysEvent structure contains such data as the charged particle multiplicity, the neutron multiplicity, the background neutron multiplicity and the event trigger.

The PhysParticle object holds all of the information about the individual particles that will be used in the analysis. The particle angles (both theta and phi) are determined by the detector number that was hit. The PhysParticle object contains the theta and phi value corresponding to the center of the detector hit as well as a theta and phi that is calculated by a Monte-Carlo calculation over the surface of the detector to simulate a "real" theta and phi for the particle. The final PID mass and charge value, %Contamination and SigmaFrac are also recorded as well as what

identification method was used to determine those values. It is important to note that if a particle was charge identified but did not have a good mass identification, then the mass was set A=0 and a GuessA based on the most probable A for that Z is set. It is also important to note that keeping these values in the physics tape allows for the possibility of constraining the PID requirements based on stricter cuts in both the %Contamination and SigmaFrac if it is decided this is needed later in the analysis. The constraints set on this work were set at %Contamination<20% and SigmaFrac<2.5 during the analysis, unless otherwise specified.

In addition to the identification source and the calibrated energy of the particle, an energy flag is set for each particle designating the assigned energy as "good", "acceptable" or "bad". This was done by comparing the energy spectra for every detector in a given ring and assigning every well behaved detector as "good". The detector was labeled as "acceptable" if it had a high energy threshold or if there were small deviations in the spectra as compared to the bulk of the "good" spectra in the ring. Finally, if the spectra exhibited wildly divergent or unexpected behavior, the energy flag for that detector was set to "bad". The PhysParticle structure also contains momentum and velocity vector information in both the lab and center-of-mass reference frames that was calculated from the energy and angle of the particles. This complete structure holds all of the necessary event and particle information for use in a physics analysis.

Finally, it is important to note that this structure and technique is very similar to that used by Z. Kohley in his thesis experiment [78]. This similarity is by design. In order to maximize the amount of data for isospin transport studies, the decision was made early on to utilize the symmetric system data collected in that previous experiment and that the data collected for this experiment would comprise exclusively of two of the possible three pairs of reaction cross-systems from the Kohley

Table 2.8: Physics tape run numbers corresponding to each of the experimental reaction systems are presented.

Reaction System	Date of Data Collection	Physics Tape Run Numbers
35 MeV/u ^{64}Zn+^{64}Zn	Summer 2008	1013 - 1091
35 MeV/u ^{70}Zn+^{70}Zn	Summer 2008	1094 - 1201
35 MeV/u ^{64}Ni+^{64}Ni	Summer 2008	1234 - 1297
35 MeV/u ^{70}Zn+^{64}Zn	Spring 2010	20-84, 307-374
35 MeV/u ^{64}Zn+^{70}Zn	Summer 2010	95-143
35 MeV/u ^{64}Zn+^{64}Ni	Summer 2010	144-199
35 MeV/u ^{64}Ni+^{64}Zn	Fall 2010	204-283

experiment. In Table 2.8 is listed each of the reaction systems collected, their dates of collection and what run numbers in the analysis correspond to each system. Due to issues with the ECR ion sources during runs 95-120, the overall statistics for the ^{64}Zn+^{70}Zn reaction system are roughly a factor of five reduced as compared to the other systems. This low statistics issue will be shown to impact some of the analysis in Section 3.5.

3. ISOSPIN EQUILIBRATION

The isospin transport between projectile and target has been investigated for reactions of 35 MeV/nucleon ^{70}Zn,^{64}Zn+^{70}Zn,^{64}Zn and ^{64}Zn,^{64}Ni+^{64}Zn,^{64}Ni. A preliminary analysis for testing the sensitivity of the quasi-projectile (QP) asymmetry to the density dependence of the asymmetry energy using the iBUU04 transport model is discussed in Section 3.1. The reconstruction and selection of quasi-projectiles from charged particles and neutrons measured in this experiment are described in Section 3.2. A selection of methods for estimating the experimental impact parameter via Constrained Molecular Dynamics (CoMD) simulations are described in Section 3.4. Finally, experimental results of isoscaling, isobaric yield ratios and reconstructed QP asymmetry are analyzed using the isospin transport ratio (ITR) to determine the degree of isospin transport in Section 3.5. The experimental results from Section 3.5 will also be compared to CoMD simulations.

3.1 iBUU04 Simulations

The isospin-dependent Boltzmann-Uehling-Uhlenbeck (iBUU04) transport model is a mean-field test particle model for nuclear reactions induced by neutron-rich nuclei [74, 129–131]. The model utilizes a single nucleon potential that is derived within the Hartree-Fock approach and uses a modified Gogny effective interaction that is a momentum-dependent interaction (MDI) [129]. This MDI interaction, implemented in the code as the input parameter x, can be adjusted in order to vary the predictions of the density dependence of the asymmetry energy $E_{asym}(\rho)$. Figure 3.1 demonstrates the density dependence of the asymmetry energy in iBUU04 for values of x from +1 to -2. Every theoretical model has different forms of the asymmetry energy, but most use the general terms “asy-stiff” and “asy-soft” when discussing the

form of the density dependence of the asymmetry energy. In general, the "asy-soft" asymmetry potential is more repulsive for neutrons below saturation density than in the "asy-stiff" case. For the iBUU04 model, the x=1 parameter is considered "asy-soft" while the x=-2 parameter is considered "asy-stiff". This trend is reversed above the saturation density where the x=-2 parameterization continually increases while the x=1 parameterization bends over and even decreases. The reason for this is that the asymmetry energy is essentially a measure of the energy "cost" for having more neutrons than protons in nuclear material at a given density. For the "asy-stiff" case, the cost of adding more neutrons is lower at sub-saturation densities, but steadily grows and continues growing as the density increases to supra-saturation densities. In contrast, while the "asy-soft" case starts with a higher energy "cost" associated with neutron excess (at sub-saturation density), this declines in strength at densities higher than saturation density and can even in some cases (as in the x=1 parameterization in iBUU04) turn over so far as to eventually reach zero at which point excess neutrons can be added at essentially no extra energy cost which is an un-physical result and clearly the formalism breaks down in the most extreme of "asy-soft" cases.

The iBUU04 transport code was used to simulate reactions of 35 MeV/nucleon ^{70}Zn+^{70}Zn, ^{70}Zn+^{64}Zn, ^{64}Zn+^{64}Zn, ^{64}Zn+^{64}Ni and ^{64}Ni+^{64}Ni. In total, each system was calculated for 200 primary events utilizing 193 test particles per nucleon for each discrete impact parameter of b=4,5,6,7,8,9,10 and 11 fm as well as for each parameterization of the asymmetry energy using the MDI x=1,0,-1 and -2. The data for the ^{64}Zn+^{70}Zn and ^{64}Ni+^{64}Zn systems were determined by simply inverting the ^{70}Zn+^{64}Zn and ^{64}Zn+^{64}Ni systems, respectively, about the center of mass. A similar procedure was performed in order to double the statistics on the three symmetric reaction systems: ^{70}Zn+^{70}Zn, ^{64}Zn+^{64}Zn and ^{64}Ni+^{64}Ni.

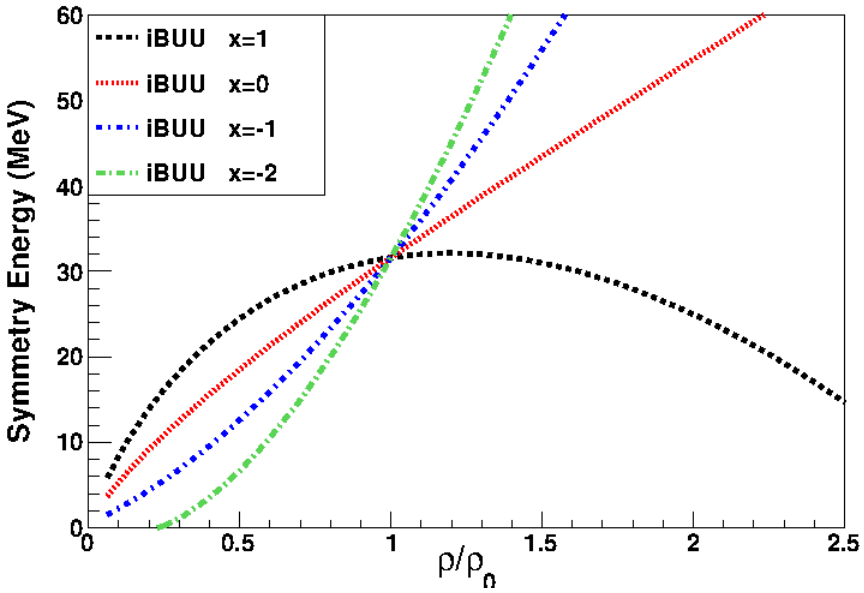

Figure 3.1: The x=1, x=0, x=-1 and x=-2 forms of the density dependence of the asymmetry energy in iBUU04. The x=1 parameterization is considered "asy-soft" while the x=-2 parameterization is "asy-stiff".

All iBUU simulations were run for 100 fm/c in order allow the QP and QT (quasi-target) to separate as much as possible without losing a significant fraction of the test particles to the edges of the bounding box used in the calculation (40 fm x 40 fm x 40 fm). While all test particles remained inside the simulation box, it was found that approximately 13% of the test particles had left the reaction region (defined by the density contours in Figure 3.2) due to a mixture of pre-equilibrium emission and test-particle bleed. For each system, impact parameter and asymmetry energy combination, the following was performed in order to determine the identity, composition, size and velocity of the QP and QT.

A schematic diagram showing the regions defining the QP, QT and neck between them is shown in Figure 3.2. Naively, the QP and QT could be defined by which

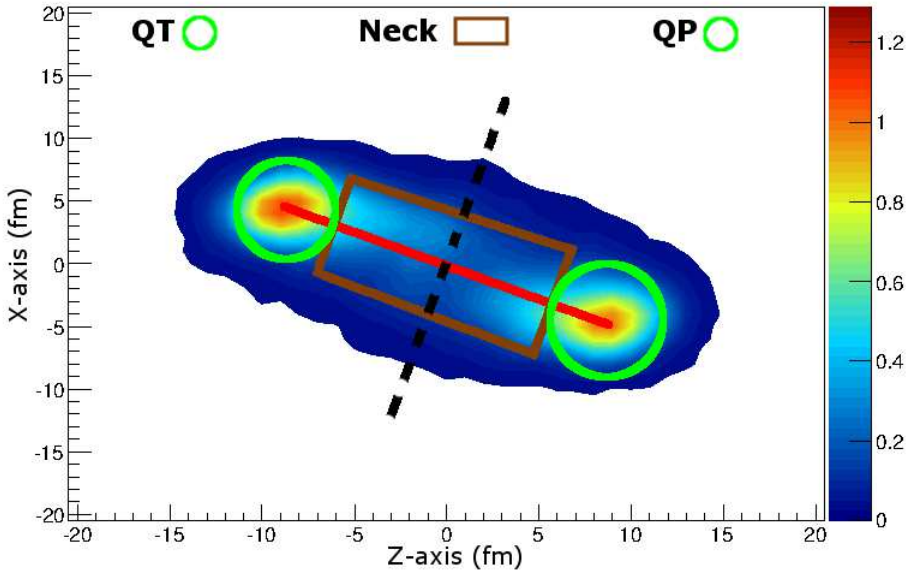

Figure 3.2: Reaction plane density plot for ^{64}Zn+^{64}Zn at b=7 fm and t=100 fm/c from iBUU calculations demonstrating the determination of the QT, neck and QP regions. The solid red line connects the high density centers of the QP (+Z axis) and QT (-Z axis) while the dashed black line represents the perpendicular bisector to the red line. The green circles represent the projected radius of the spherical density cut defining the QP and QT and the brown box gives the reaction plane projection of the cylinder that defines the neck region of the reaction.

side of the perpendicular bisector (black dotted line) each nucleon is on. However, this ignores the fact that there is a significant amount of material in a "neck" region that clearly does not belong to either a QP or QT source. In order to provide a more realistic definition of the QP and QT in the iBUU data, first the highest density centers forward (QP) and backward (QT) of the center of mass are determined. A red line connects these two points in Figure 3.2. All test particles forward (positive position value on the Z-axis) of the dotted black line were run through a calculation determining the local density around the test particle. For each event, an array of 150 unit vectors was determined (as seen in Figure 3.3) that defined the surface of a sphere centered on the high density center of the QP. The same procedure is then repeated for the QT. Each vector was expanded into the space surrounding the high density center until the density along the vector length dropped below $\rho = \frac{\rho_0}{10}$ at which point the length of the vector was recorded. The lengths of all 150 vectors were then averaged together to get the average distance from the center at which the density dropped below $\rho = \frac{\rho_0}{10}$. This average distance was then used as the radius for a spherical cut where all test particles inside this radius were associated with the QP (or QT) and all other test particles were excluded. The projection of this cut into the reaction plane is represented by the green circles for the QP (+Z axis) and QT (-Z axis) in Figure 3.2.

The brown box represents the reaction plane projection of the neck region connecting the QP and QT. This region is defined by defining two planes perpendicular to the line connecting the high density centers of the QP and QT but tangent to the spherical cut defining the QP and QT. Between these parallel planes, all test particles within a certain distance (the QP radius) of the line connecting the QP and QT were taken as part of the neck region. This process is performed event-by-event for all primary events in the simulations. Once all test particles are defined as be-

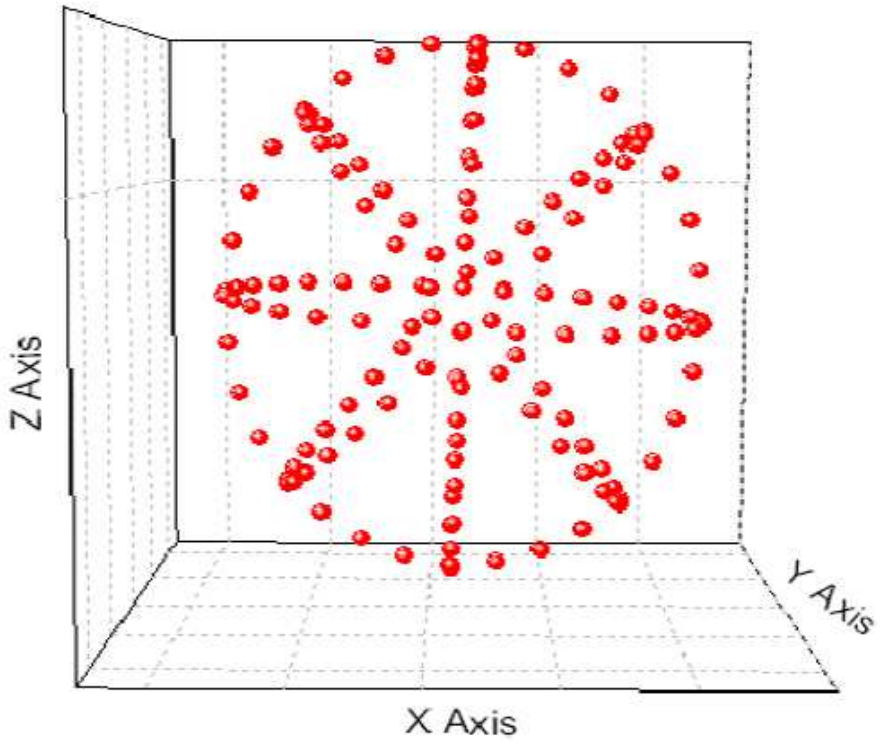

Figure 3.3: Array of vectors defining a spherical shell. A similar array, centered at the high density center of the QP (and QT) was used to search along the length of the vector to determine when the local density had fallen below $\rho = \frac{\rho_0}{10}$.

ing part of the QP, QT, neck or outside all three regions for a particular event, all observables from the iBUU data (such as QP velocity, composition, etc.) are then determined by taking averages over the event-by-event values.

Once the QP, QT and neck regions were defined, some basic characteristics of the QP were analyzed. The primary characteristic of the QP of interest in isospin equilibration studies is the isospin composition of the QP source. The QP neutron-to-proton ratio (N/Z) for a mid-peripheral reaction (b=8 fm) is shown in Figure 3.4. The iBUU results in this figure are presented in a similar manner as that of the experimental results of Tsang *et al.* seen in Figure 1.3. Here the isospin observable

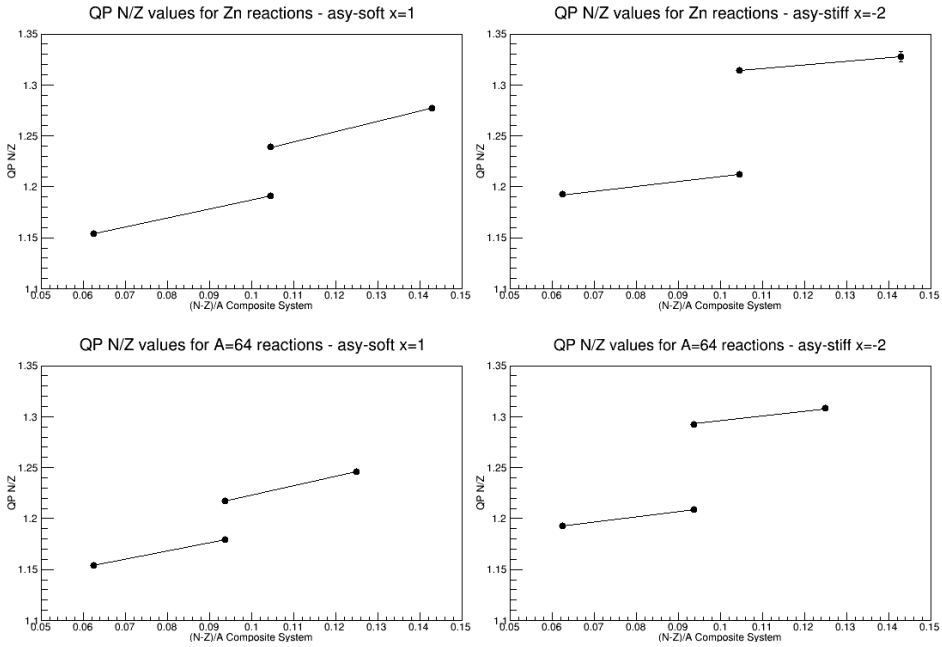

Figure 3.4: Analysis of the iBUU04 "asy-soft" and "asy-stiff" forms of the asymmetry energy comparing to Figure 1.3 for the Zn (^{70,64}Zn+^{70,64}Zn) and A=64 (^{64}Zn,Ni+^{64}Zn,Ni) reaction systems at b=8 fm. The top left panel shows the QP N/Z for the Zn reaction sets and "asy-soft" parameterization of the asymmetry energy while the top right shows the same data for the "asy-stiff" parameterization of the asymmetry energy. The bottom row of panels show the "asy-soft" (left) and "asy-stiff" (right) iBUU04 data for the A=64 set of reactions.

measured is the N/Z of the defined QP from the iBUU simulations and this value is plotted versus the composite system isospin asymmetry for each reaction. The top left panel shows the Zn set of reactions (^{70,64}Zn+^{70,64}Zn) while the bottom left shows the A=64 set of reactions (^{64}Zn,Ni+^{64}Zn,Ni) both for the "asy-soft" form of the asymmetry energy used in iBUU. Meanwhile, the right side of Figure 3.4 shows the Zn (top) and A=64 (bottom) reaction sets for the "asy-stiff" form of the asymmetry energy.

In examining this figure, there are three main features to note. First, the separation between the two cross systems is nearly the same for the Zn set of reactions and the A=64 set of reactions. The iBUU does not seem to predict much difference in the amount of equilibration observed at a fixed impact parameter just due to a Coulomb gradient existing in the A=64 set of reactions. Secondly, the separation between the cross systems does differ dramatically from the "asy-soft" form of the asymmetry to the "asy-stiff" form of the asymmetry. In the "asy-soft" case, the QP N/Z values for the two cross systems are approximately halfway towards the predicted equilibration point: the midpoint between the symmetric systems. However, in the "asy-stiff" case, the cross systems have only covered approximately a quarter of the distance to the predicted equilibration. It should be reiterated here that this is true at the fixed impact parameter b=8 fm shown in the figure. The increased equilibration in the "asy-soft" case is consistent with previous model predictions and will be discussed in more depth below. The last important feature of this plot is that while the "asy-stiff" case is less equilibrated than the "asy-soft" case, the "asy-stiff" QP N/Z values see a very noticeable increase in neutron content relative to the "asy-soft" case. This behavior was unexpected and interesting and so the iBUU data was further studied as a function of the impact parameter to see what effect the centrality of the collision would have on the QP N/Z.

First, the QP radius was examined as a function of the impact parameter (Figures 3.5 & 3.6) to be certain that the definition of the QP from this model was stable with increasing centrality. In Figure 3.5, the calculated radius of the QP is shown as a function of impact parameter for all 7 reaction systems given a fixed form of the asymmetry energy (x=-2). We can see here that while slight systematic differences based on initial projectile mass can be seen, in general the radius of the determined QP is consistent between all 7 reaction systems. The same holds true when a single reaction system (^{70}Zn+^{70}Zn) is taken and compared to all four forms of the asymmetry energy used in the simulations as in Figure 3.6. There is no systematic difference seen in the size of the QP with the form of asymmetry energy used in the calculation. In all cases, it is clearly seen that the calculated radius of the QP decreases as the impact parameter decreases. This occurs because a larger overlap of projectile and target material induces more interaction between the projectile and target and therefore more nucleon and momentum transfer between the two. This gives rise to a more massive neck region, and thus there is less material left in the QP and QT.

The correlation between QP velocity and impact parameter is shown in Figure 3.6 for all 7 reaction systems and all four forms of the asymmetry energy. The calculated QP velocities are in such good agreement that no significant differences between reaction system or form of the asymmetry energy can be seen. Over the range of impact parameters from the most peripheral (b=11 fm) to mid-central (b=4 fm), the velocity of the QP experiences a damping of approximately 20%. At b=4 fm there is significant overlap of projectile and target during the reaction, but the separation in the reaction plane is still large enough that a clearly defined QP and QT are formed. At more central impact parameters (b$\leq$3 fm) the centrality of the collision is such that the system multifragments prior to clear formation of a QP

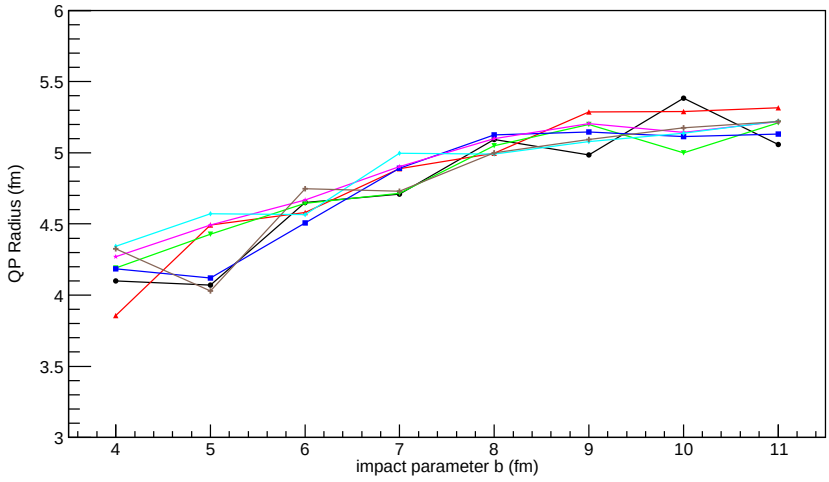

Figure 3.5: QP radius as a function of impact parameter for x=-2 and all 7 reaction systems: ^{70}Zn+^{70}Zn (black circles), ^{70}Zn+^{64}Zn (red triangles), ^{64}Zn+^{70}Zn (green inverted triangles), ^{64}Zn+^{64}Zn (blue squares), ^{64}Zn+^{64}Ni (pink stars), ^{64}Ni+^{64}Zn (light blue diamonds) and ^{64}Ni+^{64}Ni (brown crosses).

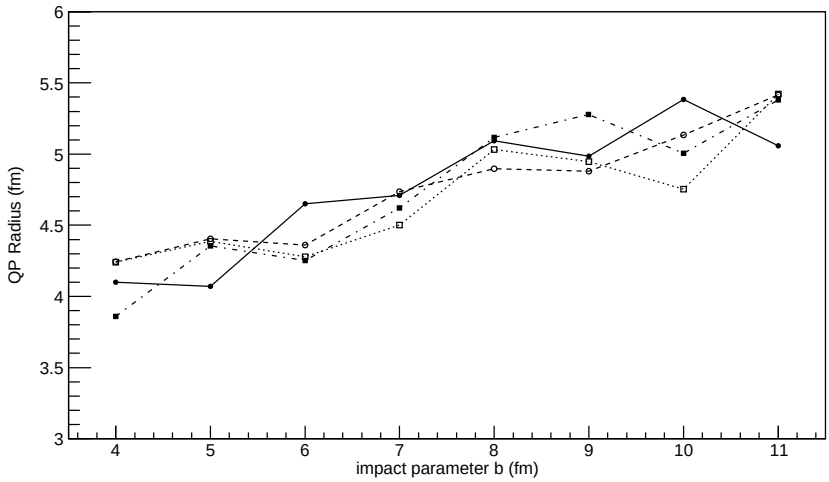

Figure 3.6: QP radius as a function of impact parameter for all four parameterizations of the asymmetry energy for the ^{70}Zn+^{70}Zn reaction system. The four parameterizations are x=1 (solid circles), x=0 (open circles), x=-1 (solid squares) and x=-2 (open squares).

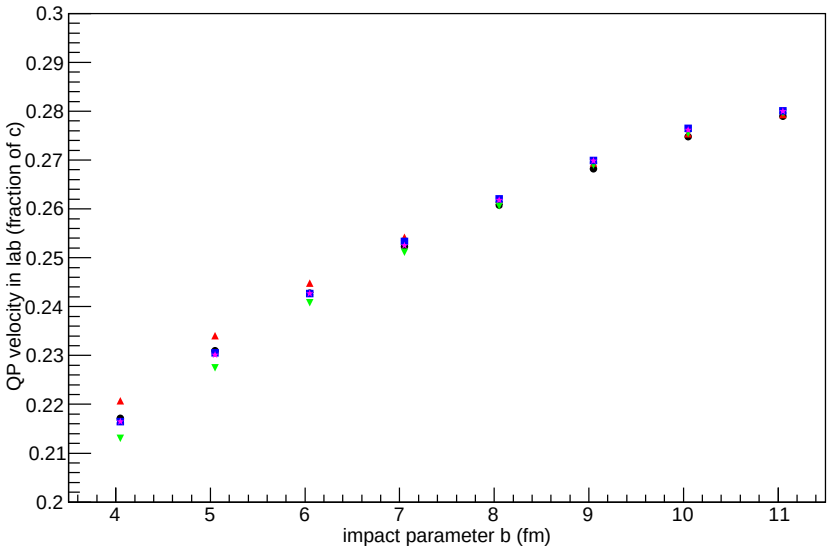

Figure 3.7: QP velocity in the lab frame as a function of impact parameter for all 4 parameterizations of the asymmetry energy and all 7 reaction systems.

or QT and so below b=4 fm the reaction is too central to be able to determine a well-defined QP, so this range in impact parameters was not studied. Because of the strong correlation of the QP velocity with impact parameter, the QP velocity was considered for the impact parameter surrogate analysis on the experimental data that is described in Section 3.4.

The degree of isospin equilibration is a result of the amount of mixing of nucleons between target and projectile, which in turn is dependent on the contact time and the slope of the potential driving the equilibration. While the former is challenging to probe experimentally and the latter impossible, both can be examined within the context of a model to provide insight on the mechanics of the equilibration process. This can be achieved in the iBUU04 model since iBUU provides a method of tracking whether each test particle originated from the projectile or the target. Figure 3.8

shows the fraction of test particles in each source (QP and QT) that originated from the projectile as a function of impact parameter for the ^{70}Zn+^{70}Zn reaction system. The fraction of the QP that originated in the projectile is seen in the top two curves where the solid circles are the x=1 parameterization of the asymmetry energy and the open circles are the x=-2 parameterization of the asymmetry energy. The bottom two curves are the corresponding results for QT nucleons that originated in the projectile. No significant difference was seen between systems or between parameterizations of the asymmetry energy. The significant exchange of matter between projectile and target demonstrates that whether or not isospin equilibration occurs in the system, there is a large amount of nucleon transport carried out during the interaction.

Since all test particles originated in either the projectile or target, the fraction of test particles that originate in the target can be found by simply taking the complement (one minus the projectile fraction). It is important to note, however, that the QP and QT are not the only possible regions in which test particles will end up and so the values for the fraction of projectile in the QP and QT do not necessarily have to sum to 1. At the most peripheral impact parameter, b=11 fm, the fraction of the QP that originates in the projectile is nearly unity as expected in a grazing reaction. Similarly, the target fraction (complement to the projectile fraction) of the QT is also near unity. As the impact parameter becomes more central, the fraction of the QP that originates from the projectile steadily decreases. This is consistent with the idea that more central collisions allow for a deeper interaction between projectile and target which increases contact time and allows for a greater degree of mixing between projectile and target. Given an infinite amount of contact time, a projectile and target would on average eventually reach a state where the composition of the QP and QT would have equal fractions of nucleons originating from projectile and target (in the absence of populating other sources, such as pre-equilibrium emission

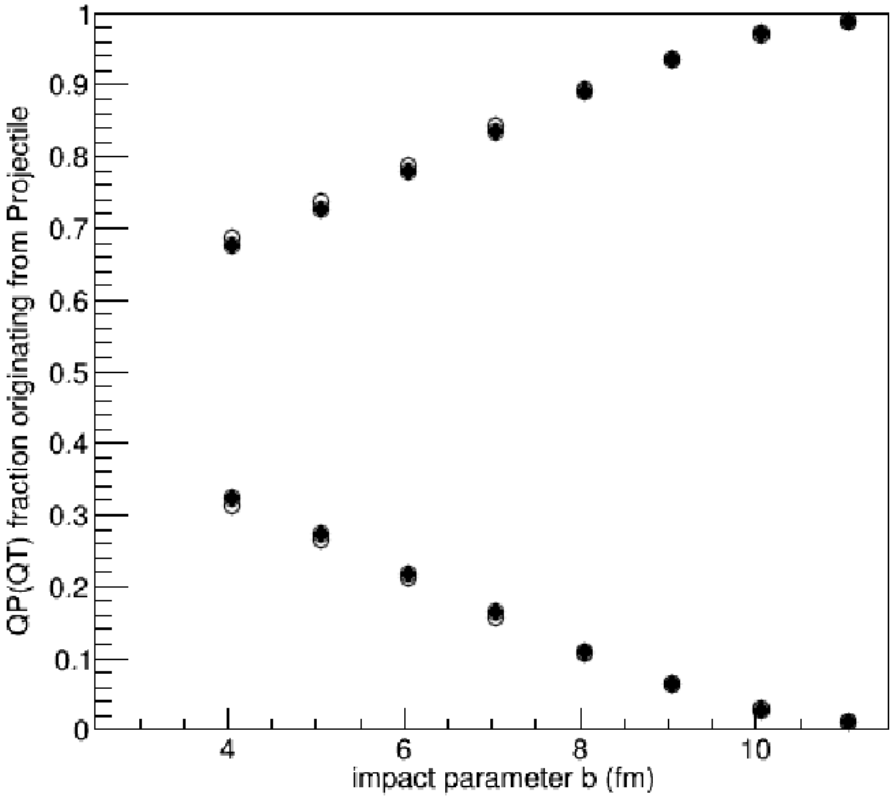

Figure 3.8: Fraction of test particles in the QP (top curve) and QT (bottom curve) that originated from the projectile as a function of impact parameter. Reaction is ^{70}Zn+^{70}Zn with filled circles the x=1 parameterization of the asymmetry energy while the open circles are the x=-2 parameterization of the asymmetry energy.

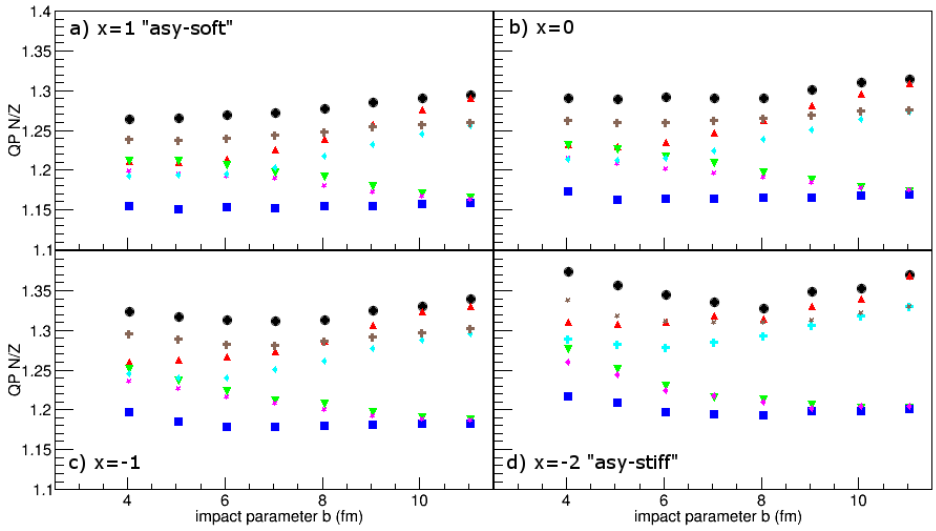

Figure 3.9: QP N/Z as a function of impact parameter for all 7 reaction systems. Each panel demonstrates the results for a separate parameterization of the asymmetry energy: a) x=1 "asy-soft" b) x=0 c) x=-1 and d) x=-2 "asy-stiff". The seven systems are represented as black circles (^{70}Zn+^{70}Zn), red triangles (^{70}Zn+^{64}Zn), green inverted triangles (^{64}Zn+^{70}Zn), blue squares (^{64}Zn+^{64}Zn), pink stars (^{64}Zn+^{64}Ni), light blue diamonds (^{64}Ni+^{64}Zn) and brown crosses (^{64}Ni+^{64}Ni).

and neck formation). While bulk nucleon transport is influenced strongly by nucleon drift and isospin diffusion, individual nucleon movement is governed by the particle-particle interactions inside the system. This is important to note since a system can be in equilibrium while still exchanging nucleons between projectile and target.

In order to examine the isospin equilibration that takes place, the QP neutron to proton ratio (N/Z) was chosen as the isospin dependent observable. Figure 3.9 shows the QP N/Z from iBUU as a function of the impact parameter. The seven systems are represented as black circles (^{70}Zn+^{70}Zn), red triangles (^{70}Zn+^{64}Zn), green inverted triangles (^{64}Zn+^{70}Zn), blue squares (^{64}Zn+^{64}Zn), pink stars (^{64}Zn+^{64}Ni), light blue diamonds (^{64}Ni+^{64}Zn) and brown crosses (^{64}Ni+^{64}Ni). Each of the four panels represents a different parameterization of the asymmetry energy: a) x=1 "asy-soft" b)

x=0 c) x=-1 and d) x=-2 “asy-stiff”.

In panel a) of Figure 3.9 it can be seen that for the b=11 fm case the 7 reaction systems clearly separate into 3 distinct groups: the black circles and red triangles (^{70}Zn+^{70}Zn and ^{70}Zn+^{64}Zn), the brown crosses and light blue diamonds (^{64}Ni+^{64}Ni and ^{64}Ni+^{64}Zn) and finally the blue squares, green inverted triangles and pink stars (^{64}Zn+^{64}Zn, ^{64}Zn+^{70}Zn and ^{64}Zn+^{64}Ni, respectively). It is interesting to note that these three groupings correspond to the three different projectile nuclei used. Following the three symmetric systems (black circles - ^{70}Zn+^{70}Zn, blue squares - ^{64}Zn+^{64}Zn and brown crosses - ^{64}Ni+^{64}Ni) with impact parameter we see that the symmetric systems change very little in N/Z content with increased contact time between projectile and target (more central collisions). This is due to the symmetric systems already being in isospin equilibrium at the start of the reaction between the projectile and target. The N/Z content of the two most neutron-rich symmetric systems (black circles - ^{70}Zn+^{70}Zn and brown crosses - ^{64}Ni+^{64}Ni) does decrease slightly with more central impact parameter which is consistent with predictions and experimental results of the formation of a neutron-rich neck region [5, 88, 89, 93, 94].

Examining the two pairs of asymmetric reactions, both the Zn cross reactions (red triangles - ^{70}Zn+^{64}Zn and green inverted triangles - ^{64}Zn+^{70}Zn) and A=64 cross reactions (pink stars - ^{64}Zn+^{64}Ni and light blue diamonds - ^{64}Ni+^{64}Zn) have QP N/Z values that start almost identical to that of the QP N/Z from reactions with the same projectile. However, in the case of the cross reactions, as the impact parameter becomes more central and allows for increased contact time between projectile and target, the QP N/Z of each pair of cross reactions evolve toward each other. At b=6 fm we see that the ^{70}Zn+^{64}Zn and ^{64}Zn+^{70}Zn (red triangles and green inverted triangles) of the Zn cross systems converge and stay together through b=4 fm. The same is true of the ^{64}Zn+^{64}Ni and ^{64}Ni+^{64}Zn (pink stars and light blue diamonds)

of the A=64 cross systems. This indicates that for the "asy-soft" parameterization (x=1) of the asymmetry energy, a large amount of isospin equilibration takes place.

Comparing the "asy-soft" parameterization of the asymmetry energy (panel a) of Figure 3.9) to that of the other three forms of the asymmetry energy (panels b), c) and d) of Figure 3.9) we see two distinct differences. The first major difference between the asymmetry energy forms is that the degree to which isospin equilibration occurs weakens as the asymmetry energy approaches the "asy-stiff" case. In panel d) it can be clearly seen that at the b=4 fm case neither the Zn cross system pair (red triangles - ^{70}Zn+^{64}Zn and green inverted triangles - ^{64}Zn+^{70}Zn) nor the A=64 cross system pair (pink stars - ^{64}Zn+^{64}Ni and light blue diamonds - ^{64}Ni+^{64}Zn) converge, whereas in the "asy-soft" case each pair of cross reactions converged as far out in centrality as b=6 fm. This is because as for the "asy-stiff" form of the asymmetry energy, the energy cost to increase the neutron excess in low density regions is very low. This allows for the formation of a very neutron rich neck region. However, once the neck region forms, the energy cost to drive neutron excess back out of the neck region and into the QP and QT is much higher for the "asy-stiff" case. Since the low density asymmetry energy is much closer to the saturation asymmetry energy in the "asy-soft" case, this energy penalty is reduced and allows for more nucleon transfer from the neck region and back into the QP and QT, facilitating greater equilibration in the "asy-soft" case as opposed to the "asy-stiff" case. This can also be seen in the increasing neutron richness of the neck region with "stiffer" asymmetry energy as indicated in Figure 3.10.

The N/Z of the neck region is shown as a function of the impact parameter in Figure 3.10 for all 7 reaction systems (using the same symbols as Figure 3.9) and each of the 4 forms of the asymmetry energy (panels a) through d) for x=1 through x=-2, respectively). The N/Z of the neck region is more neutron rich than the QP

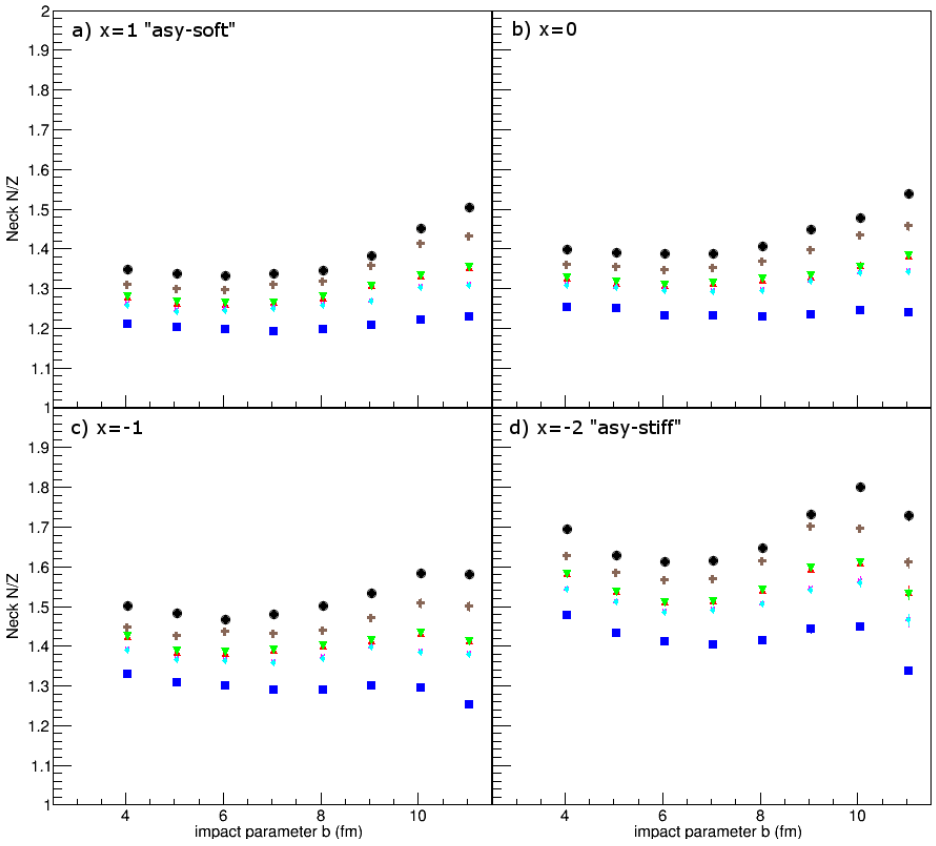

Figure 3.10: Neck region N/Z as a function of impact parameter for all 7 reaction systems. Each panel demonstrates the results for a separate parameterization of the asymmetry energy: a) x=1 "asy-soft" b) x=0 c) x=-1 and d) x=-2 "asy-stiff". The seven systems are represented as black circles (^{70}Zn+^{70}Zn), red triangles (^{70}Zn+^{64}Zn), green inverted triangles (^{64}Zn+^{70}Zn), blue squares (^{64}Zn+^{64}Zn), pink stars (^{64}Zn+^{64}Ni), light blue diamonds (^{64}Ni+^{64}Zn) and brown crosses (^{64}Ni+^{64}Ni).

for every reaction system and in the case of each form of the asymmetry energy. This is in agreement with both predictions and experimental observations [88, 93]. For the "asy-soft" case, panel a), at large impact parameter the N/Z of the neck region is very neutron rich for the neutron-rich systems and as the collision becomes more central, the N/Z value slowly decreases and levels off. This is because at very peripheral collisions, the brief contact time between projectile and target causes very little transport of nucleons and what nucleons are transferred are dominated by neutron-rich matter because of the low-density nature of the neck region. As impact parameter decreases, the increased overlap between projectile and target as well as increased contact time causes the low-density neck region to slowly approach a more saturation-like density which dampens the neutron-rich transport of matter into the neck. For the "asy-soft" case the asymmetry energy is relatively flat over a range of density just below saturation density. However, as we move toward the more "asy-stiff" case an interesting shape occurs where the N/Z of the neck region first dips in the b=6-8 fm range and then rises to be relatively neutron rich again at b=4 fm. The relative spacing and ordering between the systems is consistent in the neck region regardless of the form of the asymmetry energy.

The second major difference seen in the QP N/Z (as well as in the neck N/Z) as the form of the asymmetry energy goes from the "asy-soft" case to the "asy-stiff" case is that the overall N/Z values for any given system and impact parameter increase as the form of the asymmetry "stiffens". This behavior can be explained by looking at the low density "gas" region beyond the QP/QT/Neck regions of the reaction. By averaging the N/Z of the volume of the reaction not associated with QP, QT or neck, the gas N/Z is measured. Figure 3.11 is the complement of Figures 3.9 & 3.10 for the gas region measurement where the seven reaction systems use the same symbols for the reaction systems as before and the four panels correspond to

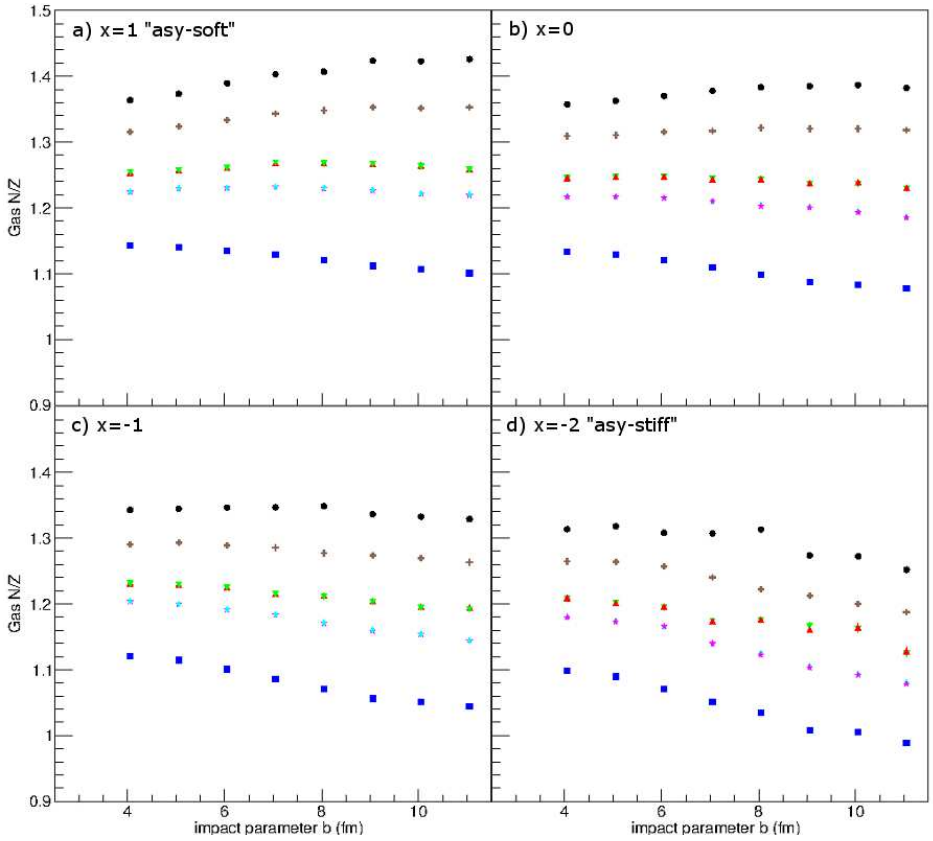

Figure 3.11: Gas region N/Z as a function of impact parameter for all 7 reaction systems. Each panel demonstrates the results for a separate parameterization of the asymmetry energy: a) x=1 "asy-soft" b) x=0 c) x=-1 and d) x=-2 "asy-stiff". The seven systems are represented as black circles (^{70}Zn+^{70}Zn), red triangles (^{70}Zn+^{64}Zn), green inverted triangles (^{64}Zn+^{70}Zn), blue squares (^{64}Zn+^{64}Zn), pink stars (^{64}Zn+^{64}Ni), light blue diamonds (^{64}Ni+^{64}Zn) and brown crosses (^{64}Ni+^{64}Ni).

the four different forms of the asymmetry energy. Here we see the unexpected cause of the rise in N/Z of both the QP and the neck region with increasing stiffness in the asymmetry energy, namely that the gas region N/Z is much lower in value than either the QP or neck region for the "asy-stiff" case. It is also interesting to note that the N/Z of the b=4 fm gas region does not change very much with the different asymmetry energy forms, whereas the b=11 fm gas region N/Z lowers dramatically for all seven systems as the form of the asymmetry energy goes from "asy-soft" to "asy-stiff".

This impact parameter dependence of the "gas" region asymmetry can also be seen in that the slopes of the lines trend with the system asymmetry in the "asy-soft" case: the more neutron-rich systems have a "gas" that gets more neutron rich as the reaction becomes more peripheral while the more neutron-poor systems see a decrease in "gas" asymmetry with increasing impact parameter. However, in the "asy-stiff" case, the "gas" region of all 7 reaction systems gets progressively more neutron-deficient as the reaction becomes more peripheral. This effect can be explained in that the neck region of the reaction has a lower density at high impact parameter and therefore there is less of a driving force to push excess neutrons out of the neck region and into the "gas" for the "asy-stiff" since the densities of those regions are more similar. In the "asy-soft" case, however, the high asymmetry energy value just below saturation density drives more neutron-rich matter out of the neck and into the "gas" region causing the "gas" in the "asy-soft" case to be more neutron-rich than in the "asy-stiff" case. One way in which this could be investigated further would be to run the iBUU04 simulation to output individual test particle information at multiple time steps. This would allow for the investigation of the dynamics of the neck and "gas" region asymmetries over time to see how these develop. As the neck region reached higher densities, it should cause increasingly neutron-rich matter to

be emitted into the "gas" region for the "asy-soft" asymmetry energy form, whereas the "asy-stiff" will exhibit this behavior to a lesser degree.

In order to better see the degree of equilibration that takes place in the QP from the iBUU simulations, Figure 3.12 shows the QP N/Z for a sample symmetric system (black circles - ^{70}Zn+^{70}Zn) and both pairs of cross systems, the Zn pair of systems (red triangles - ^{70}Zn+^{64}Zn and green inverted triangles - ^{64}Zn+^{70}Zn) and the A=64 pair of systems (pink stars - ^{64}Zn+^{64}Ni and light blue diamonds - ^{64}Ni+^{64}Zn), relative to the projectile, target and composite system N/Z values for the two most extreme forms of the asymmetry energy ("asy-soft" (x=1) on the left and "asy-stiff" (x=-2) on the right). The top row of the figure shows the QP (solid) and QT (open) N/Z values for the ^{70}Zn+^{70}Zn reaction. We can see that the N/Z as a function of impact parameter is relatively flat in both the "asy-soft" as well as "asy-stiff" cases. However, the QP(QT) N/Z values in the "asy-soft" case are lower in N/Z value than the composite system N/Z while in the "asy-stiff" case the QP(QT) N/Z values are slightly higher in value relative to the composite system. The middle row shows the same information for the Zn pair of cross systems (^{70}Zn+^{64}Zn and ^{64}Zn+^{70}Zn). As in Figure 3.9 we see that the reaction pair reach convergence in the "asy-soft" case while in the "asy-stiff" case the two systems do not quite converge although they are approaching one another. The same holds true in the bottom row of the plot for the A=64 pair of cross systems (^{64}Zn+^{64}Ni and ^{64}Ni+^{64}Zn). However, there are two interesting things to note. First, there does not seem to be any significant effect on the equilibration that takes place between projectile and target due to the Coulomb gradient in the A=64 cross reactions relative to the Coulomb symmetric Zn cross reactions as predicted by the iBUU04 model. Secondly, while the convergence of the cross reactions occurs near the composite system N/Z in the "asy-soft" case as previously assumed [12], the near-convergence seen in the "asy-stiff" case occurs at

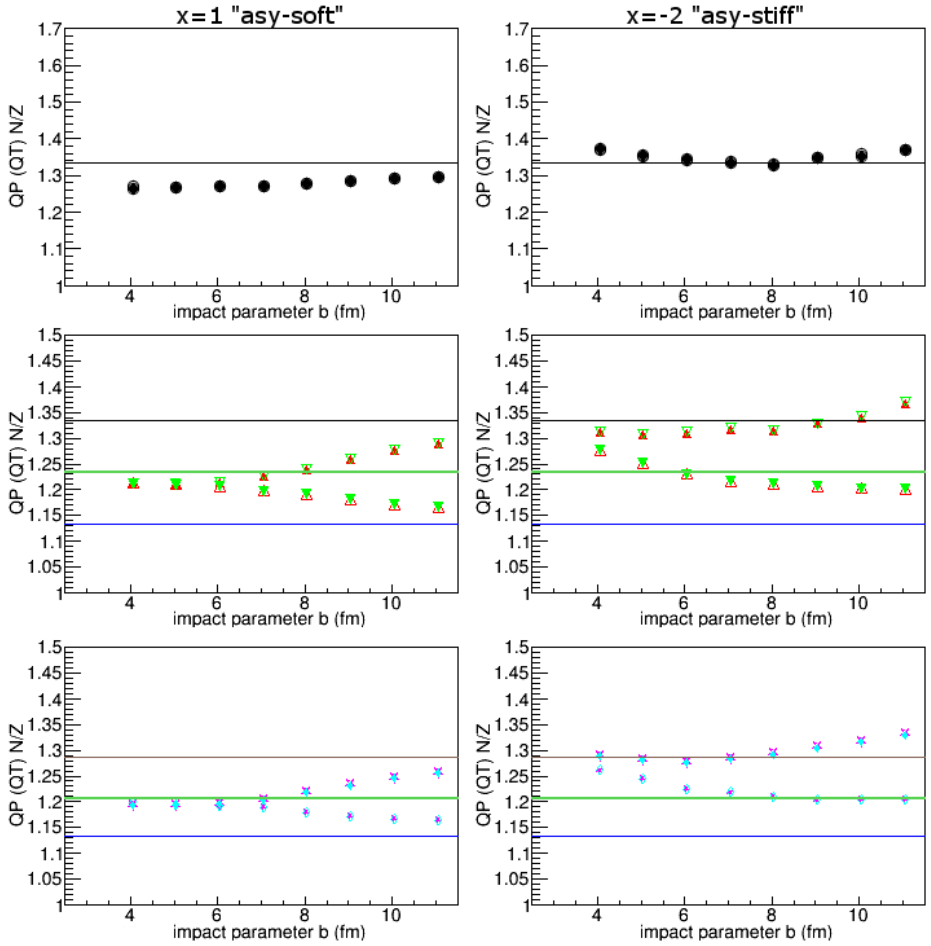

Figure 3.12: Composite figure of QP (solid symbol) and QT (open symbol) N/Z values as a function of impact parameter. The left and right side correspond to the "asy-soft" and "asy-stiff" parameterizations of the asymmetry energy, respectively. Top row: ^{70}Zn+^{70}Zn (black circles) QP and QT N/Z values compared to the projectile/target/composite system N/Z value (black line). Middle row: ^{70}Zn+^{64}Zn (red triangles) and ^{64}Zn+^{70}Zn (green inverted triangles) QP and QT N/Z values compared to the ^{70}Zn (black line), ^{64}Zn (dark blue line) and composite system (light green thick line) N/Z values. Bottom row: ^{64}Zn+^{64}Ni (pink stars) and ^{64}Ni+^{64}Zn (light blue diamonds) QP and QT N/Z values compared to the ^{64}Ni (brown line), ^{64}Zn (blue line) and composite system (green thick line) N/Z values.

an N/Z value much higher than the composite system. Since this effect was traced to the composition of the gas phase, it can be seen that loss or transport of nucleons to regions other than the QP and QT can have an effect on the isospin asymmetry value measured. Most notable is the large neutron enrichment of the neck region relative to the QP and QT. For this reason, I propose that rather than approaching a specific asymmetry value (such as the composite system isospin asymmetry) convergence of the QP and QT isospin asymmetries (or between two cross reaction QPs) is a better indication of isospin equilibration in heavy-ion collisions.

3.2 Quasi-projectile Reconstruction

A similar quasi-projectile reconstruction to that of the iBUU simulations is also performed on the experimental and Constrained Molecular Dynamics (CoMD) data, though the process for completing the reconstruction is very different in nature. Since the particles identified in the NIMROD-ISiS detector array cannot be traced back directly to a specific source, a series of calculations and source cuts are performed in order to select a well-defined QP source in the experimental data set event by event. This method was first used by D. J. Rowland as part of his thesis taken on the FAUST array at Texas A&M University. This method takes the detected fragments from the experiment and applies various cuts on the data to select fragments believed to originate in the hot QP right after separation in the reaction [113]. These fragments, now considered the QP, and their combined characteristics can be used to select sources with similar attributes. This method was refined by A. Keksis as part of his thesis on the same detector array (FAUST) for use in isospin equilibration studies [112]. Quasi-projectile reconstruction has since been used in various studies by the Yennello Research Group at the Cyclotron Institute at Texas A&M University over a wide range of subjects: isospin equilibration [108, 112, 113], improved particle

Table 3.1: Particle velocity cut based on the work by Steckmeyer *et al.* [137].

Particle Type	Velocity Cut
Z=1	$0.35 \cdot V_{z,PLF} < V_{z,i} < 1.65 \cdot V_{z,PLF}$
Z=2	$0.40 \cdot V_{z,PLF} < V_{z,i} < 1.60 \cdot V_{z,PLF}$
Z≥3	$0.55 \cdot V_{z,PLF} < V_{z,i} < 1.45 \cdot V_{z,PLF}$

source definition [65, 70, 126, 132], fragment yield ratio studies [7, 50, 133, 134] and temperature studies [8, 32, 135, 136]. The reconstruction method used in this work will follow that of McIntosh *et al.* [8] with slight variations and is described below.

The QP reconstruction starts by taking every particle in a given event and determining the heaviest fragment. This fragment is denoted as the Projectile-Like Fragment or PLF. The lab frame velocity in the beam direction of every fragment ($V_{z,i}$) in the event is then compared to the beam direction velocity of the PLF ($V_{z,PLF}$) and a cut is applied using the methodology of Steckmeyer *et al.* [137] with numerical values of the cuts in Table 3.1. Particles of Z=1 must have parallel velocities within ±65% of the parallel velocity of the PLF. Similarly, Z=2 particles are required to have V_z within ±60% $V_{z,PLF}$ and all particles Z≥3 must have V_z within ±45% $V_{z,PLF}$. Particles outside these velocity windows were considered to originate from non-QP sources and were removed from the QP reconstruction routine.

After the removal of particles via the velocity cut, the reconstructed QP was characterized. The fragments in the event are taken in the center of mass (CoM) frame of the colliding system and the momentum vectors of all fragments (determined from mass identification, lab kinetic energy, and lab theta and phi from the detector the particle struck) are summed together. The location of this summed center of momentum from the detected fragments, who are now all associated with the QP source, is taken as the center of the so-called "QP Frame". In effect, this determines

the center of mass frame for fragments that only come from a QP. Using this new QP Frame center, new momentum vectors are calculated for each fragment in the QP Frame. This also generates new QP Frame angles for each fragment.

At this point an isotopic identification requirement is applied. In order to calculate the QP momentum center, fragments that were Z identified but not A identified can still be used by assuming the A value of the fragment based on the most probable A for the given Z from fragment yield distributions as discussed in Section 2.3.5. The isotopic identification condition that is applied to the QP requires that every fragment in the reconstructed QP has a well defined Z and A value from the particle identification and energy calibration. Only QPs that are fully isotopically identified are considered in this analysis. While this condition has a dramatic effect on the experimental statistics (this condition removes approximately 99.5% of reconstructed QPs), forcing this condition means that the summed Z and summed A value of the reconstructed QP can be exactly determined in the experimental data within measurement uncertainties.

From the charged particles and neutrons that are classed as belonging to the QP, quantities describing characteristics of the QP can be calculated, such as the asymmetry of the QP source (m_s) or the excitation energy of the QP source (E^*). Since the TAMU Neutron Ball measures event neutron multiplicities but not neutron energies, several values are calculated for the QP source with and without consideration of the free neutron multiplicity. The measured neutron multiplicity for the QP in a specific event is calculated by correcting the raw neutron multiplicity by the background neutron multiplicity for that event and then correcting the result by the efficiency of the Neutron Ball in detecting neutrons associated with the QP as determined by Marini *et al.* as seen in Equation 3.1 [132]. The number of free neutrons associated with the QP (N_{QP}) depends on the background corrected detected

neutron multiplicity (N_{det}), the number of neutrons in the projectile and target (N_P and N_T, respectively), the efficiencies for detecting free neutrons from the QP and QT (ε_{QP}=0.75 and ε_{QT}=0.75, respectively), the efficiency for detecting free neutrons from a ^{252}Cf source (ε_{Cf}=0.7) and the calculated efficiency of detecting free neutrons from a ^{252}Cf source from a GEANT-3 simulation of the TAMU Neutron Ball ($\varepsilon_{Cf_{GEANT}}$=0.6) [117, 132].

$$N_{QP} = \frac{N_{det}}{\left(\varepsilon_{QP} + \frac{N_T}{N_P}\varepsilon_{QT}\right)\frac{\varepsilon_{Cf}}{\varepsilon_{Cf_{GEANT}}}} \tag{3.1}$$

The corrected value of the free neutrons associated with the QP are then used to calculate a sum A, an isospin asymmetry (m_s) and an excitation energy (E^*), each with and without free neutrons. The excitation energy (E^*) is calculated via Eq. 3.3 where $K_{t,CP}(i)$ is the kinetic energy for charged particle i in the transverse direction, M_{CP} is the charged-particle multiplicity, M_N is the free neutron multiplicity, $\langle K_N \rangle$ is the average kinetic energy of the free neutrons and Q is the Q-value for the composition of the QP. Since neutron kinetic energies are not measured in the experiment, the $\langle K_N \rangle$ is estimated by Coulomb correcting the kinetic energy spectra for protons for QPs of similar charged particle composition. The excitation energy is calculated using the kinetic energies in the transverse direction in order to remove the contribution of dynamical effects from the beam direction. The excitation energy for charged particles only (E^*_{CP}) is seen in Eq. 3.2 and is the same as Eq. 3.3 with the neutron term removed. Unless otherwise noted, all values used in this study assume the QP corrected free neutron multiplicities are used.

$$E^*_{CP} = \sum_{i}^{M_{CP}} \frac{3}{2} K_{t,CP}(i) - Q \tag{3.2}$$

$$E^* = \sum_{i}^{M_{CP}} \frac{3}{2} K_{t,CP}\,(i) + M_N \langle K_N \rangle - Q \tag{3.3}$$

Once the QP is reconstructed and the sum Z and sum A values are calculated, a set of sum Z and sum A cuts are applied in order to remove QPs that differ significantly from the initial projectile of the system. These cuts can also be used to select on very narrow ranges (including individual isotopes) of QP compositions. In this study a very wide range in Sum Z ($15 \leq$ Sum Z ≤ 35) and Sum A ($48 \leq$ Sum A ≤ 76) were used in order to maximize the range of isospin asymmetries of the QPs studied.

Finally, a sphericity shape cut was applied to the reconstructed QPs. A shape parameter (S_{event}) is calculated via Eq. 3.4 where $p_{z,i}$ is the momentum in the beam direction of particle i, $p_{t,i}$ is the momentum in the transverse direction for particle i and summations are taken over all detected charged particles in the event (the charged particle multiplicity, M_{CP}). This quantity will equal 1 for spherically shaped events in momentum space. Due to the nature of this equation, an S value of 10 is the same magnitude of deformation as an S value of 0.1, where S=10 is an elongation in the beam direction and S=0.1 is a deformation in the transverse direction. For this reason a symmetric deformation constraint of -0.3 $< log_{10}(S_{event}) <$ 0.3 is applied to select a class of QPs that are on average spherical in nature. The reason for this cut is that it is believed that shape equilibration is a much slower process than isospin or thermal equilibration and so a shape equilibrated QP should on average already be thermally and isospin equilibrated within itself (though this does not affect the amount of equilibration between the QP and QT, which occurs on a much faster time scale) [135].

$$S_{event} = \frac{2 \cdot \sum_{i}^{M_{CP}} p_{z,i}^2}{\sum_{i}^{M_{CP}} p_{t,i}^2} \tag{3.4}$$

Once each of the source cuts are applied, the final cohort of reconstructed QPs are labeled "good" and subsequently used in the analysis. As previously mentioned, all QPs used in this study were reconstructed using the above method and all QP values assume fully isotopically identified QPs with corrected free neutron multiplicities unless otherwise specifically noted.

3.3 Constrained Molecular Dynamics Model

In the analysis of the Constrained Molecular Dynamics (CoMD) simulation, QPs are reconstructed and treated in the same manner as the experimental data. This is done because the CoMD model is a molecular dynamics model that utilizes gaussian wave packets to simulate the wavefunctions of individual nuclei that then are propagated through the use of a momentum-independent Skyrme interaction [138, 139]. This allows the event-by-event particle output from CoMD to be treated like experimental data. The asymmetry term of the Skyrme interaction used by the CoMD model can be varied in order to affect different forms of the density dependence of the asymmetry energy as seen in Figure 3.13. The three forms of the asymmetry energy expressed in Figure 3.13 are labeled by CoMD as "asy-soft", "asy-stiff" and "asy-super-stiff" though it is important to note that the "asy-soft" asymmetry energy form in the CoMD is relatively "stiff" compared to the forms utilized by the iBUU04 model shown in Figure 3.1.

An important aspect of the CoMD model is the method by which the model enforces the Pauli Exclusion Principle. Since the Pauli Exclusion Principle forbids

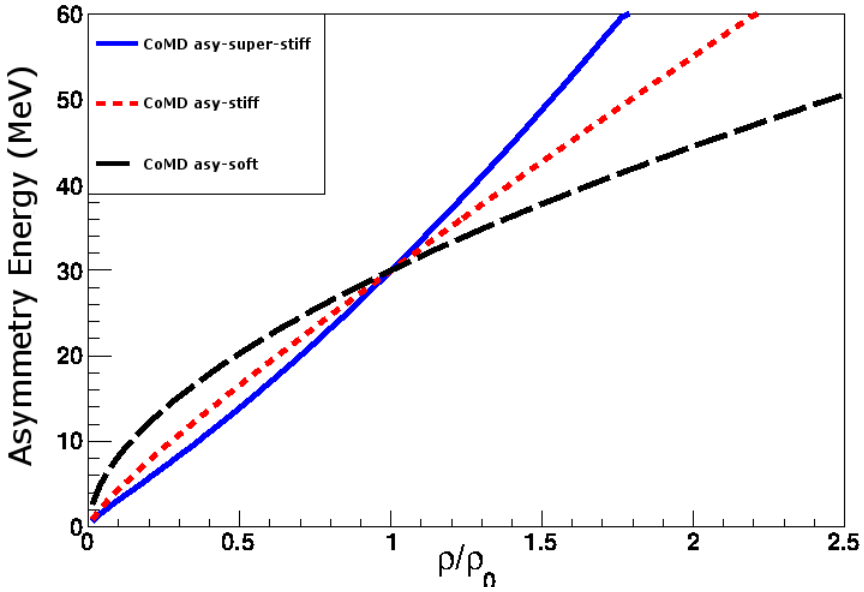

Figure 3.13: The "asy-soft", "asy-stiff" and "asy-super-stiff" forms of the density dependence of the asymmetry energy in CoMD. All three parameterizations expressed here are relatively "stiff" as compared to the iBUU04 simulation shown in Figure 3.1.

two identical fermions (and both protons and neutrons are fermions) from occupying the same quantum state simultaneously [3], some method must be employed that prevents two particle wavefunctions from completely overlapping each other in the model. In some models (such as the quantum molecular dynamics(QMD) model) a Pauli potential is used which prevents two nucleons of the same isospin and spin state from occupying the same phase space, however, this adds a repulsive potential that does not exist in nature. In CoMD, the Pauli Principle is enforced by calculating the occupation density of each nucleon at each calculation time step. If the occupation density exceeds 1, this represents a violation of the Pauli Principle. The CoMD model corrects this violation by randomly changing the momentum of all the neighboring particles until the occupation density is below 1 with special consideration taken to ensure that the total momentum and total kinetic energy of the system is conserved. M. Papa *et al.* [138] compared results from the CoMD model to that of QMD in order to show the importance of the treatment of the Pauli Principle. One major advantage of the CoMD model's treatment of the Pauli Principle is that this allows for a marked improvement in computational time over models that use more complex methods of invoking the Pauli Principle such as the antisymmetrized molecular dynamics (AMD) model, as shown by Kohley [78].

The CoMD model was used to calculate approximately $5 \cdot 10^6$ primary events for all three forms of the asymmetry energy shown in Figure 3.13 over a triangular impact parameter distribution from b=0-10 fm for the five systems: ^{70}Zn+^{70}Zn, ^{70}Zn+^{64}Zn, ^{64}Zn+^{64}Zn, ^{64}Zn+^{64}Ni and ^{64}Ni+^{64}Ni. Only one system in each of the pairs of cross reactions (the ^{70}Zn+^{64}Zn system from the Zn cross systems and the ^{64}Zn+^{64}Ni from the A=64 cross systems) was calculated using the model. The other two cross systems (^{64}Zn+^{70}Zn and ^{64}Ni+^{64}Zn, respectively) were created by inverting the ^{70}Zn+^{64}Zn and ^{64}Zn+^{64}Ni systems in the center of mass of the colliding system, similar to the

treatment of the iBUU04 data. The simulation was allowed to proceed dynamically to 600 fm/c at which point the output was cooled statistically using the GEMINI code (discussed below). Use of the GEMINI de-excitation code allowed the hot CoMD data from each event to be de-excited up to eight times, effectively increasing the number of raw events per system per asymmetry energy parameterization to approximately $4 \cdot 10^7$ over the range of impact parameters. This gave approximately 5-10% the statistics from CoMD relative to the experimental data depending on the reaction system.

The GEMINI de-excitation code that was used on the CoMD results is a statistical decay code that uses the excitation energy, angular momentum, charge and mass of a hot nuclear fragment and calculates a decay path to cool the fragment via a Monte Carlo method over a series of sequential binary decays [140]. The Hauser-Feshbach formalism is used to calculate the decay widths of light charged particles from neutrons and protons up to ^{8}Li fragments. The Bohr-Wheeler formalism is used to calculate the fission decay channel. This combined fission and light charged particle emission gives the GEMINI model the available paths to decay hot fragments down to a ground state. There are a couple of assumptions in combining the GEMINI decay model with the CoMD model: the GEMINI de-excitation code assumes the hot fragments it is cooling are spherical and at normal nuclear density. This is not strictly valid, since the hot fragments coming out of CoMD at 600 fm/c are deformed and at sub-saturation density, but it does provide a way for the hot fragments to release their excitation energy in a reasonable computation time.

Once the CoMD data is de-excited by the GEMINI code, the resulting cooled events are processed through an experimental software filter known as the NIM Filter (short for NIMROD-ISiS Experimental Software Filter). The NIM Filter is a software replica of the geometry and energy thresholds of the NIMROD-ISiS detector

array. Each particle from the CoMD-GEMINI data is processed through the NIM Filter to see if the particle would hit a detector in the NIMROD-ISiS array and whether that particle would have enough energy to be detected based on the energy thresholds. If simulated particles do not pass the criteria in the NIM Filter they are marked in the event as "bad" and for filtered CoMD-GEMINI data, only "good" particles are used in the analysis. Particles that hit detectors in the array and are accepted have new filter angles added to their data structure, the theta and phi of the particle are randomized by a Monte Carlo calculation over the surface of the detector hit, just like in the experimental data (Section 2.5).

After all particles have been examined by the filter, the events are reconstructed using the procedure described in Section 3.2. From this point in the analysis on, the simulated CoMD-GEMINI data is treated the same as the experimental data and all analysis code operates on each data type equally. The simulated data still retains some information about the simulation, for instance the actual impact parameter of the event and actual angles of the particles, but in general the only information used from the simulated data are variables that correspond to information found in the experimental data. One notable exception is the actual impact parameter which is only used in the impact parameter determination analysis discussed below (Section 3.4). Unless otherwise noted, all simulated data from the CoMD-GEMINI calculation shown in this work comes from filtered, QP reconstructed events that pass the same source cuts as the experimental data. Primarily the "asy-soft" CoMD will be shown in the discussion in Section 3.5 since the differences between "asy-soft", "asy-stiff" and "asy-super-stiff" are very small. However, example plots of all three forms of the asymmetry energy and the experimental data can be seen in full in Appendix D.

3.4 Impact Parameter Determination

As seen in the iBUU04 analysis discussed in Section 3.1, the impact parameter determination is important for understanding isospin equilibration in nuclear reactions. Since impact parameter is not directly measurable in the experimental data, an experimental observable that can act as a surrogate for the impact parameter must be determined. One measurable quantity that may be correlated with the impact parameter is the excitation energy per nucleon (E*/A) of the reconstructed QP [22, 56, 65, 70, 125, 134, 141]. Many other possible surrogates can be used as long as the surrogate has a high degree of correlation to the impact parameter of the reaction. Using the CoMD model, six different impact parameter surrogates were tested and used: excitation energy per nucleon (E*/A) of 1 MeV/A width, excitation energy per nucleon for charged particles only (E^*_{CP}/A) of 1 MeV/A width, excitation energy per nucleon with equally mass weighted bins (E*/A %wt. bin), excitation energy per nucleon for charged particles only with equally mass weighted bins (E^*_{CP}/A %wt. bin), reconstructed QP deflection angle by equally mass weighted bins (θ_{QP}) and reconstructed QP velocity in the beam direction by equally mass weighted bins ($V_{z,QP}$). The reason for the bins of equal mass weighting will be discussed below.

A comparison of the four primary observables (E*/A, E^*_{CP}/A, θ_{QP} and $V_{z,QP}$) used in the impact parameter surrogate analysis are shown as a function of the impact parameter (b) in Figure 3.14 for the ^{70}Zn+^{64}Zn reaction system using the "asy-soft" CoMD calculation. The top left panel shows E*/A vs b, the top right panel shows E^*_{CP}/A vs b, the bottom left panel shows θ_{QP} vs b and the bottom right panel shows $V_{z,QP}$ vs b. In all four cases it can be seen that the impact parameter surrogate demonstrates a roughly linear dependence on the impact parameter albeit with very broad distributions. While the approximately linear behavior of these observables

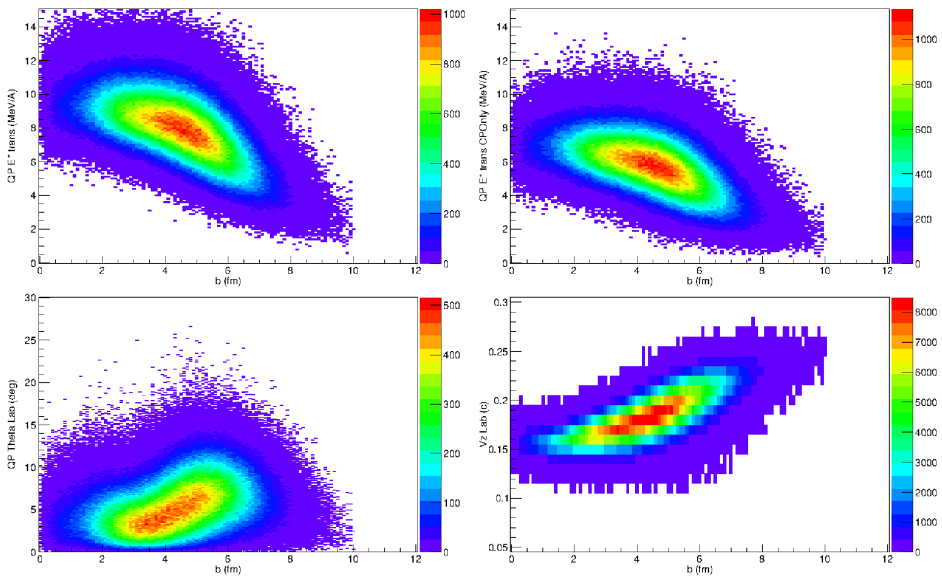

Figure 3.14: The various impact parameter surrogates as a function of actual impact parameter (b) from the "asy-soft" CoMD data of the ^{70}Zn+^{64}Zn system. Each of the four panels represents a different impact parameter surrogate: top left is excitation energy E*/A, top right is charged particle excitation energy E^*_{CP}/A, bottom left is QP deflection angle θ_{QP} and bottom right is $V_{z,QP}$. Similar plots for the other six reaction systems can be found in Appendix B.

with impact parameter demonstrate that each impact parameter surrogate could be used as an indicator of the true impact parameter, the width of the distributions causes uncertainty in the determination of a specific impact parameter value and therefore only general knowledge about the relative violence of the collision can be defined by these impact parameter surrogates.

In analyzing the quality of the four primary observables of impact parameter surrogates, the E^*/A distribution for each reaction system was normalized to the total counts in each system and is shown in the top left panel of Figure 3.15. While slight differences between systems (different color curves) are visible, the E^*/A distribution for all 7 reaction systems are very similar in shape and value. In the top right panel of Figure 3.15 we see that this is not necessarily true of the CoMD data. The top right panel shows the same distribution for the "asy-soft" CoMD calculation. In the case of the CoMD data, the 4 cross systems (black - ^{70}Zn+^{64}Zn, red - ^{64}Zn+^{70}Zn, green - ^{64}Zn+^{64}Ni and blue - ^{64}Ni+^{64}Zn) curves all lie on top of each other, however, the symmetric reaction systems (pink - ^{70}Zn+^{70}Zn, light blue - ^{64}Zn+^{64}Zn and brown - ^{64}Ni+^{64}Ni) exhibit a very different behavior. The two most neutron rich symmetric systems (^{70}Zn+^{70}Zn and ^{64}Ni+^{64}Ni) show a slightly higher E^*/A while the more neutron poor symmetric system (^{64}Zn+^{64}Zn) has a lower E^*/A than the cross systems. This implies that the CoMD experiences an isospin dependence on the E^*/A in reconstructed QPs that is not seen in the experimental data. In order to see if this is somehow affected by the addition of the free neutrons, the bottom row of Figure 3.15 shows the same data as the top row but for the E^*_{CP}/A calculated from QPs of charged particles only, with no free neutrons added. In general the removal of the free neutron measurement shifts the excitation energy spectra to lower values (since the excitation energy contribution of the free neutrons is missing) but otherwise, the distributions behave similarly to that of the E^*/A distributions: the experimental

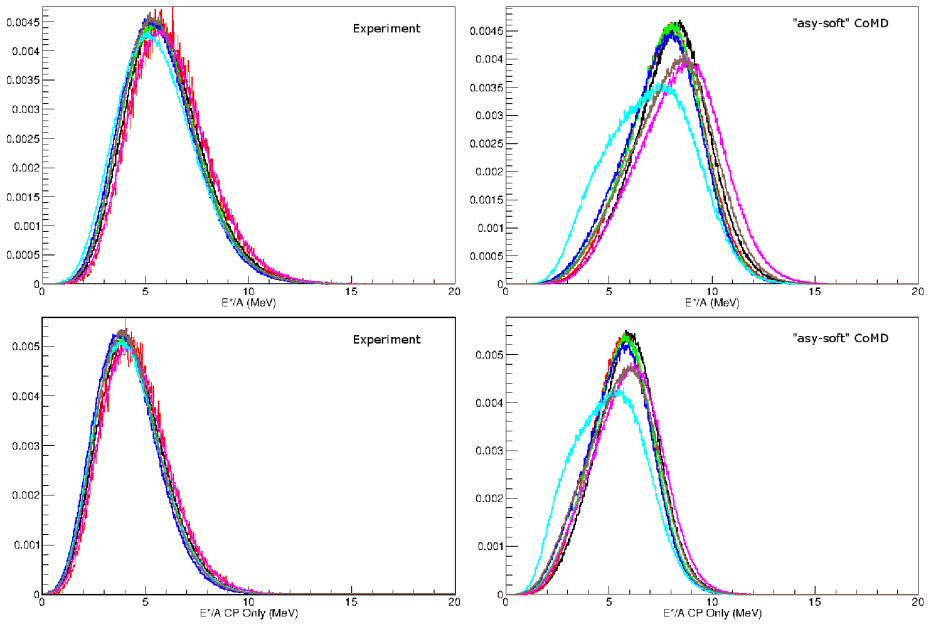

Figure 3.15: The E^*/A distribution for all 7 reaction systems: black - ^{70}Zn+^{64}Zn, red - ^{64}Zn+^{70}Zn, green - ^{64}Zn+^{64}Ni, blue - ^{64}Ni+^{64}Zn, pink - ^{70}Zn+^{70}Zn, light blue - ^{64}Zn+^{64}Zn and brown - ^{64}Ni+^{64}Ni. The plots on the left show the results for the experimental data while the plots on the right show the results from the "asy-soft" CoMD data. The top row is the E^*/A with neutrons in the reconstructed QP while the bottom row is the E^*_{CP}/A with no free neutrons added.

data shows all 7 reaction systems to have roughly the same distribution while the CoMD exhibits a slight isospin asymmetry dependence. The "asy-stiff" and "asy-super-stiff" CoMD measurements also have the same behavior as the "asy-soft" case (see Figures B.3, B.4, B.7 and B.8 in Appendix B).

The other notable difference between the experimental data and the CoMD is that the excitation energies calculated from reconstructed QPs in the CoMD have a much higher E^*/A (and E^*_{CP}/A) on average than that of the experimental data. This presents a problem when using fixed width (of 1 MeV) excitation energy bins as an impact parameter surrogate: for instance, an excitation energy range of 2.5-

3.5 MeV/A in the experimental data could be sampling a very different event type relative to the same excitation energy range in the CoMD data. To correct this, an alternative method for determining an impact parameter surrogate was proposed: instead of using fixed width bins in excitation energy, the excitation energy distribution was split into 10 bins of variable width that represented equal portions (10%) of the total integral of the distribution. This led to the creation of the E^*/A %wt. bin and E^*_{CP}/A %wt. bin impact parameter surrogates. A similar method of binning the θ_{QP} and $V_{z,QP}$ distributions (found in Appendix B) was also performed using 10 bins in each case such that each bin comprised approximately 10% of the total statistics from each distribution. The nature of this method of binning allows each reaction system to have slightly different binning parameters and widths so that regardless of the shape or value of the distribution all four of the weighted impact parameter surrogate observables (E^*/A %wt. bin, E^*_{CP}/A %wt. bin, θ_{QP} and $V_{z,QP}$) contain approximately 10% of the total statistics from that distribution for each system.

Once the impact parameter surrogate binning was determined, the quality of the impact parameter selection was analyzed. This was done by plotting the actual impact parameter distribution for each bin from CoMD for the given impact parameter surrogate used. The results of this analysis are summarized in Figure 3.16 for the ^{70}Zn+^{64}Zn system. Similar plots for each of the other reaction systems can be found in Appendix B. In Figure 3.16, panel a) shows the impact parameter distributions for each bin in the fixed width E^*/A case. The effect the fixed width bin size has on creating bins of variable statistics can clearly be seen in the varying height of the impact parameter surrogate bins. It is worth noting that the means of the impact parameter surrogate bins follow a steady progression as expected from the relative linearity of the E^*/A distribution with impact parameter (top left panel of Figure 3.14). The width of the impact parameter distributions for each E^*/A bin can be

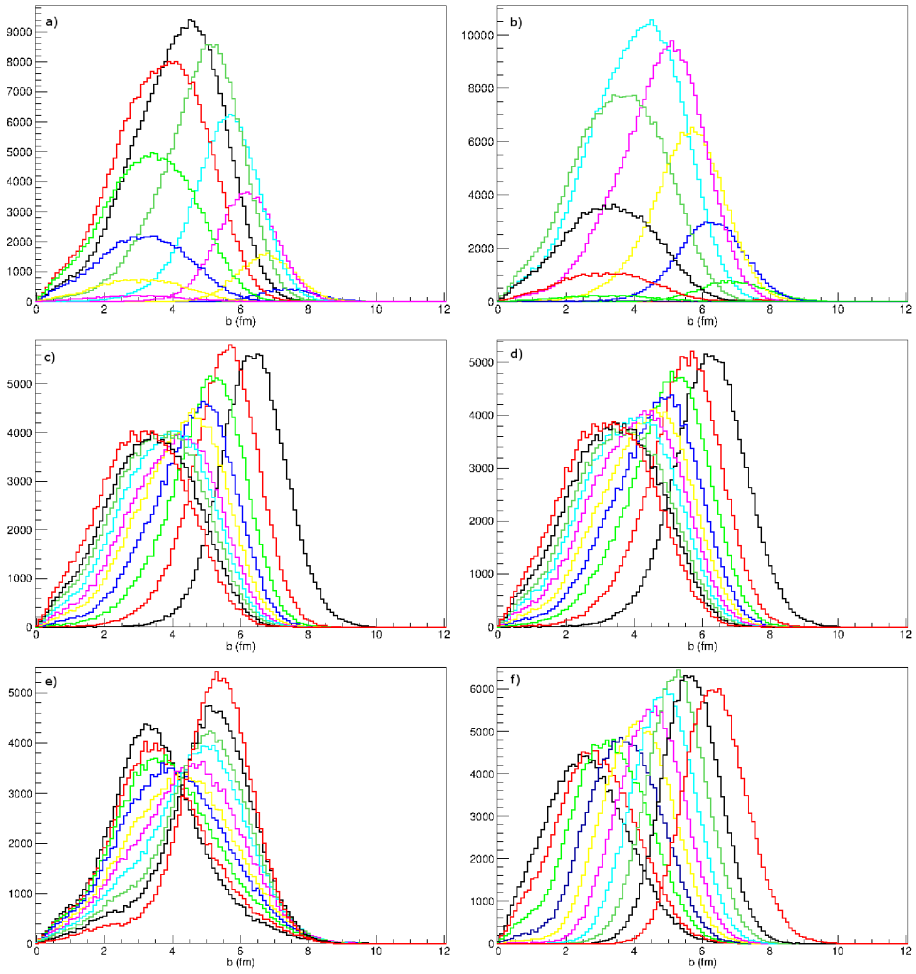

Figure 3.16: Actual impact parameter distribution as a function of impact parameter surrogate bins for the six different surrogates proposed. Data represents "asy-soft" CoMD simulation for the ^{70}Zn+^{64}Zn reaction system. The six impact parameter surrogates shown are: a) E*/A, b) E^*_{CP}/A, c) E*/A %wt. bin, d) E^*_{CP}/A %wt. bin, e) θ_{QP} and f) $V_{z,QP}$.

seen to be very wide and exhibit a high degree of overlap between adjacent bins. Similar results are observed in panel b) for the E^*_{CP}/A as no significant change is seen by removing the free neutrons from the impact parameter surrogate.

Panels c) and d) of Figure 3.16 demonstrate the results of the weighted E^*/A %wt. bin and E^*_{CP}/A %wt. bin impact parameter surrogates. By utilizing a mass weighted binning scheme, it is immediately visible that the means of the impact parameter surrogate bins are well ordered with respect to the actual impact parameter. In addition, the widths in actual impact parameter of the surrogate binning are on average more similar, although the bins corresponding to more central (lower value) impact parameters are wider than those for the more peripheral (higher value) impact parameters. This is due in part to the fact that at more central impact parameters, it is more difficult to form and identify well-defined QPs (as discussed in Section 3.1). Another reason for the increased width and "bunching" at more central impact parameters is that due to the triangular nature of the raw impact parameter distribution, there are far fewer instances of central collisions than of peripheral collisions.

The θ_{QP} impact parameter surrogate shown in panel e) of Figure 3.16 is also well-ordered with respect to the actual impact parameter but exhibits a very strange behavior in that the distributions of the θ_{QP} bins corresponding to low and high impact parameter values are narrower than those of the middle impact parameter values. This comes directly from the θ_{QP} distribution as a function of impact parameter seen in the lower left panel of Figure 3.14. The width of the two dimensional distribution can be seen to broaden in the middle impact parameter value range (b=4-6 fm) which corresponds to the region in which the actual impact parameter distributions broaden. It can also be seen that because of this broadening effect in the middle regions, there is significantly more overlap between impact parameter

surrogate bins for the θ_{QP} than in either the E*/A %wt. bin or E^*_{CP}/A %wt. bin case.

Finally, the $V_{z,QP}$ impact parameter surrogate is shown in panel f) of Figure 3.16. The means of the impact parameter distributions for each bin are well ordered as in the case of the E*/A %wt. bin and E*/A %wt. bin surrogates. While the widths of the distributions in each bin broaden slightly at lower impact parameter values (due to decreased statistics and poor QP definition) the distributions seen in the $V_{z,QP}$ case are slightly narrower on average than either the E*/A %wt. bin or E^*_{CP}/A %wt. bin surrogates. Due to the well-ordered behavior and slightly better resolution in determining the actual impact parameter over the other surrogates examined, the $V_{z,QP}$ impact parameter surrogate was chosen for the rest of the analysis presented, therefore all isospin equilibration observables discussed in Section 3.5 will utilize the $V_{z,QP}$ as the surrogate for impact parameter unless otherwise specified. It should also be noted, that while the actual impact parameter is kept for the CoMD data, in order to treat the simulations as closely like the experimental data as possible, the impact parameter surrogate method will be used for the selection of events in both the CoMD data and the experimental data.

3.5 Isospin Equilibration

Once the $V_{z,QP}$ parameter was selected as the impact parameter surrogate for use in the analysis, the degree of isospin equilibration present in the Zn (^{70,64}Zn+^{70,64}Zn) and A=64 (^{64}Zn,Ni+^{64}Zn,Ni) reaction sets was analyzed. The first step in the analysis was to use the analysis method developed by Tsang *et al.* found in Reference [12] and discussed below in Section 3.5.1. The analysis was then expanded to examine isospin equilibration as a function of the impact parameter surrogate $V_{z,QP}$ through the following isospin dependent observables: isoscaling parameter α (Section 3.5.2),

isobaric yield ratios (Section 3.5.3) and the reconstructed QP isospin asymmetry (Section 3.5.4).

3.5.1 Comparison to Previous Work

As stated previously in Section 1.2, the work by Tsang *et al.* [12] on isospin diffusion and equilibration provides a benchmark for isospin equilibration analyses using Fermi-energy heavy-ion collisions. To compare the experimental data in this thesis with that of Tsang *et al.*, the Zn and Ni reactions from this work were treated in a similar way. While the Tsang *et al.* work used multiplicity and rapidity cuts to define fragments from peripheral sources, the data from this work used fragments from the reconstructed QPs which were assumed to be from well-defined mid-peripheral to peripheral sources. Furthermore, due to slightly lowered detection efficiency for the ^{8}Li isotope due to the dual nature of Li isotope detection (CsI Fast-Slow in Rings 2-3 and Si-CsI in Rings 4-11 as discussed in Sections 2.3.1 and 2.3.2), only fragments from Z=4-8 were considered for the isoscaling analysis used in this comparison. Figure 3.17 demonstrates the results of this analysis.

The top left and bottom left panels of Figure 3.17 show isoscaling examples of the three most abundant isotopes of Z=4-8 from one of the Zn (^{70}Zn+^{64}Zn versus ^{64}Zn+^{64}Zn) and A=64 (^{64}Ni+^{64}Zn and ^{64}Zn+^{64}Zn) cross systems, respectively. The top left panel shows the isoscaling of the ^{70}Zn+^{70}Zn system relative to ^{64}Zn+^{64}Zn while the bottom left panel shows the isoscaling of the ^{64}Ni+^{64}Ni system relative to the ^{64}Zn+^{64}Zn. In both cases, the red fit lines correspond to the global fit of Eq. 1.8 to the data requiring fixed slope, α, and fixed spacing between the lines, β. It is important to note that since ^{64}Zn+^{64}Zn is the most neutron-poor reaction in both sets of reaction systems, it is always the denominator used in the yield scaling relationship (Eq. 1.7) and so by definition the yield scaling of ^{64}Zn+^{64}Zn to itself will

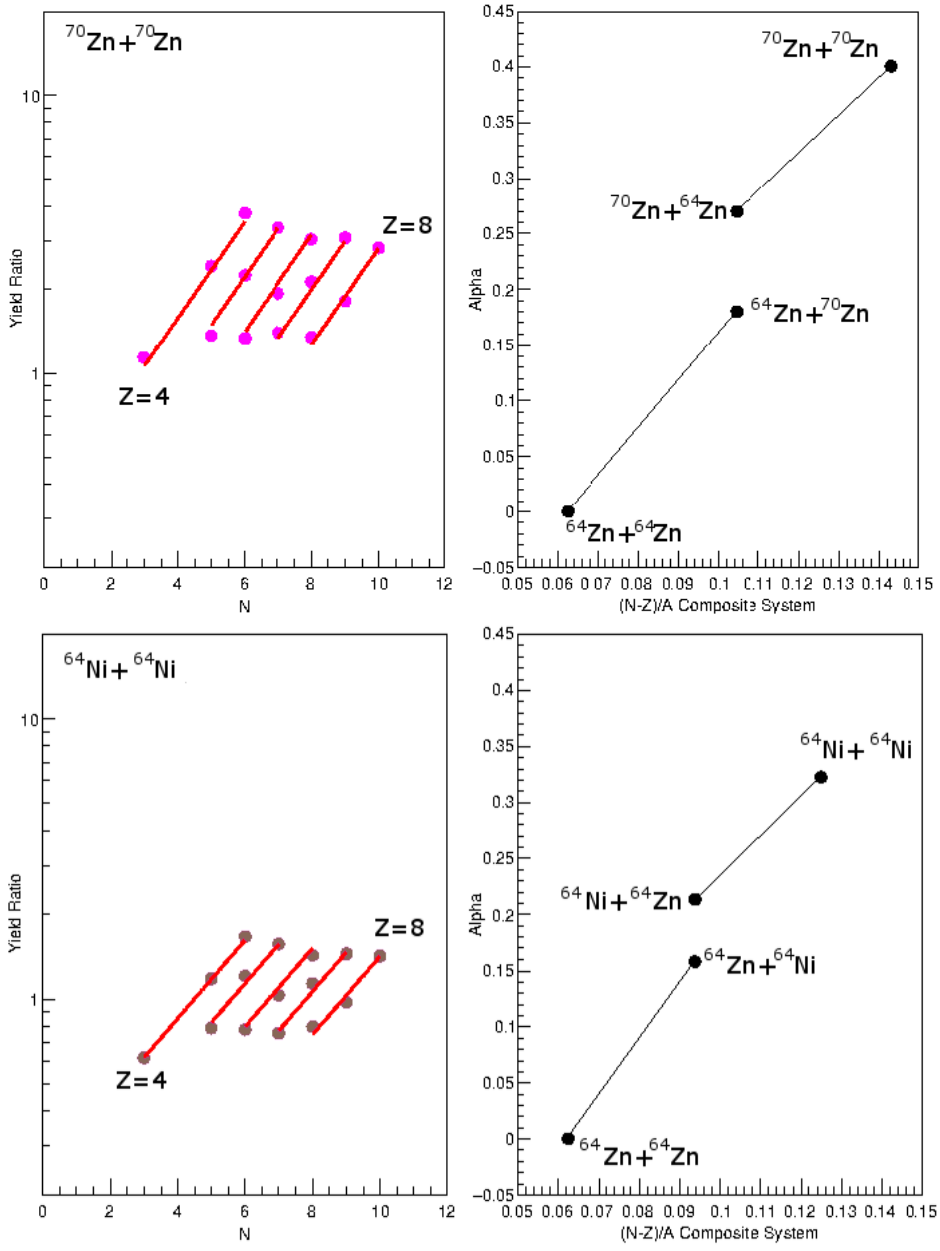

Figure 3.17: Analysis from this work reproducing Figure 1.3 for the Zn (^{70,64}Zn+^{70,64}Zn) and A=64 (^{64}Zn,Ni+^{64}Zn,Ni) reaction systems from this work. The top left panel shows the isoscaling for the three most abundant isotopes of Z=4-8 for the ^{70}Zn+^{70}Zn system while the bottom left panel shows the isoscaling for the three most abundant isotopes of Z=4-8 for the ^{64}Ni+^{64}Ni system. The top right panel shows the α values for the Zn set of systems as a function of the composite system isospin asymmetry while the bottom right panel shows the α values for the A=64 set of systems as a function of the composite system isospin asymmetry.

always result in the α parameter defined as 0. The α parameters determined from these fits are shown in the right hand panels of Figure 3.17. The top panel shows the α parameter versus composite system asymmetry for the four systems of the Zn reaction set and the bottom right panel shows the α parameter versus composite system asymmetry for the four systems of the A=64 reaction set.

The α parameter values from the isoscaling show good agreement with both Tsang's experimental work and theoretical predictions [12, 67, 88]. The values for the A=64 reaction set are consistently lower than in the Zn reaction set as expected since the composite system isospin asymmetry in the A=64 reactions are slightly lower than in the Zn reactions (see Table 2.1). The cross system points in both cases are closer to each other than in the work of Tsang *et al.* which implies a stronger degree of isospin equilibration in these systems. This is to be expected since the lower beam energy (35 MeV/nucleon in this work versus 50 MeV/nucleon in the Tsang *et al.* work) causes longer contact time between the projectile and target due to the slower projectile, which increases the time period for the isospin equilibration process to occur. It is interesting to note however that the α values for the cross reactions in both cases do not appear to be centered around the mid point between the α values of the symmetric systems. This could imply that loss of nucleons to sources other than the QP (like the neck region) could be affecting the final asymmetry at equilibrium, which is consistent with the conclusion drawn in the iBUU analysis discussed in Section 3.1.

A further comparison was performed using two other isospin observables: the triton to helium-3 (^{3}H/^{3}He) A=3 isobaric yield ratio and the reconstructed QP m_s which will be discussed in greater depth in Sections 3.5.3 & 3.5.4. Figure 3.18 shows the results of taking the ratio of tritons to helium-3 for each system as a function of the composite system isospin asymmetry (left) as well as the calculated asymmetry

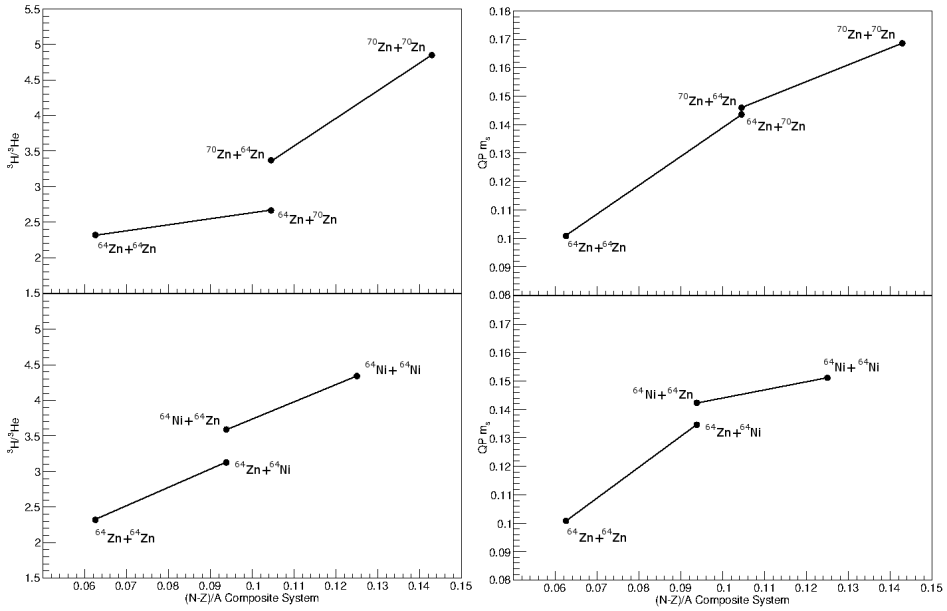

Figure 3.18: Analysis from this work reproducing the right side of Figure 1.3 for the Zn (^{70,64}Zn+^{70,64}Zn, top) and A=64 (^{64}Zn,Ni+^{64}Zn,Ni, bottom) reaction systems using the A=3 isobaric yield ratio (left) and QP m_s (right) observables. The top left panel shows the ^{3}H/^{3}He ratios for the Zn set of reaction systems while the bottom left panel shows the ^{3}H/^{3}He ratios for the A=64 set of reactions as a function of the composite system isospin asymmetry. The right side panels show the reconstructed QP m_s for the same reaction sets as a function of the composite system isospin asymmetry.

of the reconstructed QP as a function of the composite system asymmetry (right). The top row of panels are for the Zn set of reaction systems while the bottom row shows the results from the A=64 set of reactions. It is clear that in the case of these two observables, the values obtained for the cross systems in each reaction pair are not centered around the midpoint between the two symmetric systems. For the Zn reactions, the ^{3}H/^{3}He of the two cross reactions (^{70}Zn+^{64}Zn and ^{64}Zn+^{70}Zn) are centered lower than the midpoint between the symmetric Zn pairs of reactions (^{70}Zn+^{70}Zn and ^{64}Zn+^{64}Zn) while in the A=64 reactions (bottom left panel) the cross reactions (^{64}Ni+^{64}Zn and ^{64}Zn+^{64}Ni) are closer in value to the midpoint between the symmetric reactions (^{64}Ni+^{64}Ni and ^{64}Zn+^{64}Zn). In the case of the QP m_s observable on the right side of Figure 3.18 both sets of reactions (the Zn set as well as the A=64 set) have cross system values that are elevated compared to the midpoint between the symmetric reactions.

As previously discussed (both in Section 3.1 and Figure 3.17), various mechanisms could cause the asymmetry value at equilibrium to differ from the midpoint between the values measured for the symmetric systems. In order to correct incorporate such effects, a new equation (Eq. 3.5) was defined that calculates a measure of equilibration in a set of reaction systems based on how closely the cross systems resemble each other relative to the bounding systems, rather than seeking approach to a specific value. In Eq. 3.5 the variable x represents the isospin observable of choice while the subscripts NR and NP correspond to the neutron-rich and neutron-poor bounding systems, respectively. The subscripts xS1 and xS2 denote the first and second cross systems in the four reaction set. The difference between the isospin observable of the two cross reactions (x_{xS1}-x_{xS2}) is scaled by the difference between the isospin observables of the two bounding reactions (x_{NR}-x_{NP}) such that if the two cross reactions have the same isospin observable values as the bounding systems, the

equilibration is 0% and if the cross systems are identical to each other the equilibration is 100%. This formulation is consistent with the idea that equilibration of an isospin observable does not necessarily occur at a specific value, but at the point where the QP and QT converge to each other in value. It is important to note that the construction of this formula does not require that the set of four reactions be two symmetric reactions and two asymmetric reactions. Rather, any four reactions such that all four pairwise combinations of two projectiles and two targets are measured can be used in this formula.

$$\text{Percent Equilibration} = \frac{(x_{NR} - x_{NP}) - (x_{xS1} - x_{xS2})}{(x_{NR} - x_{NP}) \cdot 100\%} \tag{3.5}$$

Using this formulation, the equilibration values were calculated for various isospin observables and are summarized in Table 3.2. The calculated equilibration values of both the Zn set of reactions and well as the A=64 set of reactions are reported for each of the following observables: the isoscaling parameter α using the same isotope range as Tsang *et al.* [12], the isoscaling parameter α using the expanded isotope range available in this experiment, the ^{3}H/^{3}He isobaric yield ratio and the reconstructed QP m_s. This calculation was also applied to the raw isoscaling α values found in Reference [12] by Tsang *et al.* and the resulting 54% equilibration calculated here is consistent with the reported equilibration in that work. The higher percent equilibration (on average approximately 75-80%) in this study is also consistent with the earlier observation of the effect of the lower beam energy on the equilibration process as well as to previous studies that have reported the same trend of increasing equilibration with decreasing incident beam energy [99, 100]. The errors calculated for these equilibration values represent estimated maximum errors due to the contamination of nearby isotopes in the particle identification stage of the data. The

Table 3.2: Summary of equilibration percentages calculated in the experimental data for several isospin observables.

Equilibration observable	35 MeV/nucleon ^{70,64}Zn+^{70,64}Zn	35 MeV/nucleon ^{64}Zn,Ni+^{64}Zn,Ni	50 MeV/nucleon ^{124,112}Sn+^{124,112}Sn [12]
Isoscaling α (Z=4-8)	77±5%	83±5%	54%
Isoscaling α (Z=4-14)	76±7%	85±7%	-
^{3}H/^{3}He ratio	72±4%	77±4%	-
QP m_s	96±5%	85±5%	-

contamination values were used to calculate uncertainties in the total yield of each isotope and were propagated through the analysis assuming the worst combinations of total yield contamination and are discussed in more detail in Appendix C. Given the impact parameter dependence of the isospin asymmetry of the QP found in the iBUU and the variations in equilibration seen amongst the different isospin observables here, a further investigation of these three isospin observables (isoscaling α in Section 3.5.2, ^{3}H/^{3}He ratio in Section 3.5.3 and QP m_s in Section 3.5.4) was conducted with the intent of examining the evolution of these variables with respect to the centrality of the collision.

3.5.2 Isoscaling

The isotopes used in the isoscaling analysis described above were deliberately chosen to allow comparison with previously published work. It has also been shown by Wuenschel *et al.*, however, that the data collected on the NIMROD-ISiS array is capable of covering a much larger range of isotopes due to the high isotopic resolution of the detector telescopes [70]. By expanding the range of isotopes used in the analysis to include the most abundant isotopes for each element from Z=4-14, it is clear that

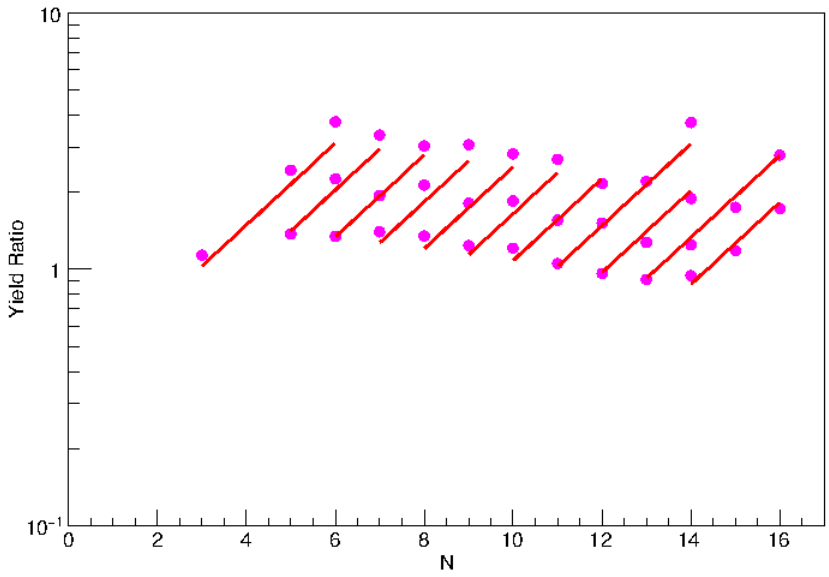

Figure 3.19: An example isoscaling plot using an expanded range in fragments. The plot shows the isoscaling of abundant isotopes from Z=4-14 for the ^{70}Zn+^{70}Zn system relative to the ^{64}Zn+^{64}Zn system. The red fit lines correspond to the resulting global fit according to Eq. 1.8.

the yield scaling feature is consistent across a wide range in detected fragments. Figure 3.19 shows the isoscaling of the ^{70}Zn+^{70}Zn system relative to the ^{64}Zn+^{64}Zn system over the expanded range of isotopes available in the NIMROD-ISiS array. The red line corresponds to the global fit of the data via Eq. 1.8 (as discussed in Section 1.2) where the equation requires parallel slopes and fixed spacing between the lines. The global fit shows good agreement with the data and so the α parameter can be extracted for use in the isospin transport ratio (ITR).

By combining the equilibration study above (Section 3.5.1, the expanded isotope range for the isoscaling plot in Figure 3.19 and the conclusion that the impact parameter has a strong affect on isospin dependent observables (Section 3.1), the isoscaling analysis was extended to look at the changes in the isoscaling parameter

α as a function of the impact parameter surrogate $V_{z,QP}$. An example of the global fits for the isoscaling of ^{70}Zn+^{70}Zn relative to ^{64}Zn+^{64}Zn can be seen for each bin in $V_{z,QP}$ in Figures D.10-D.19 in Appendix D. The change in this α parameter as a function of the $V_{z,QP}$ bins can be processed through the isospin transport ratio (ITR) described in Section 1.2 in order to measure the equilibration present.

The ITR values derived for all seven reaction systems from the isoscaling α parameter can be seen in Figure 3.20. Plotted here are the R_i values from the ITR (Eq. 1.6) as a function of the impact parameter surrogate $V_{z,QP}$ bins where lower bin values correspond to slower QPs and therefore more damped (more central) collisions. The top and bottom panels refer to the Zn and A=64 sets of reaction systems, respectively. We can see here that rather than starting near the symmetric system corresponding to the initial projectile at $V_{z,QP}$ bin=9, all four cross systems give α values that are relatively central to the range between the two symmetric systems. In addition, while the ^{64}Zn+^{64}Ni and ^{64}Ni+^{64}Zn reactions of the A=64 systems (bottom panel: green triangles and blue inverted triangles, respectively) roughly parallel each other and converge slightly, the ^{70}Zn+^{64}Zn and ^{64}Zn+^{70}Zn reactions (top panel: black circles and red squares, respectively) seem to diverge as the reactions become more central.

The A=64 result of increased convergence with respect to collision centrality is expected but the results of the Zn systems in the top panel are unexpected. However, as previously mentioned (Section 2.5) the statistics for the ^{64}Zn+^{70}Zn system are very reduced compared to the other experimental systems. Unfortunately, this can have a considerable effect on the distribution of individual isotope yields and could be contributing to the relatively odd behavior of the red data points. It is also noteworthy that the isoscaling observable has been shown to be very sensitive to secondary decay products in nuclear collisions [9, 64, 142, 143]. The result of

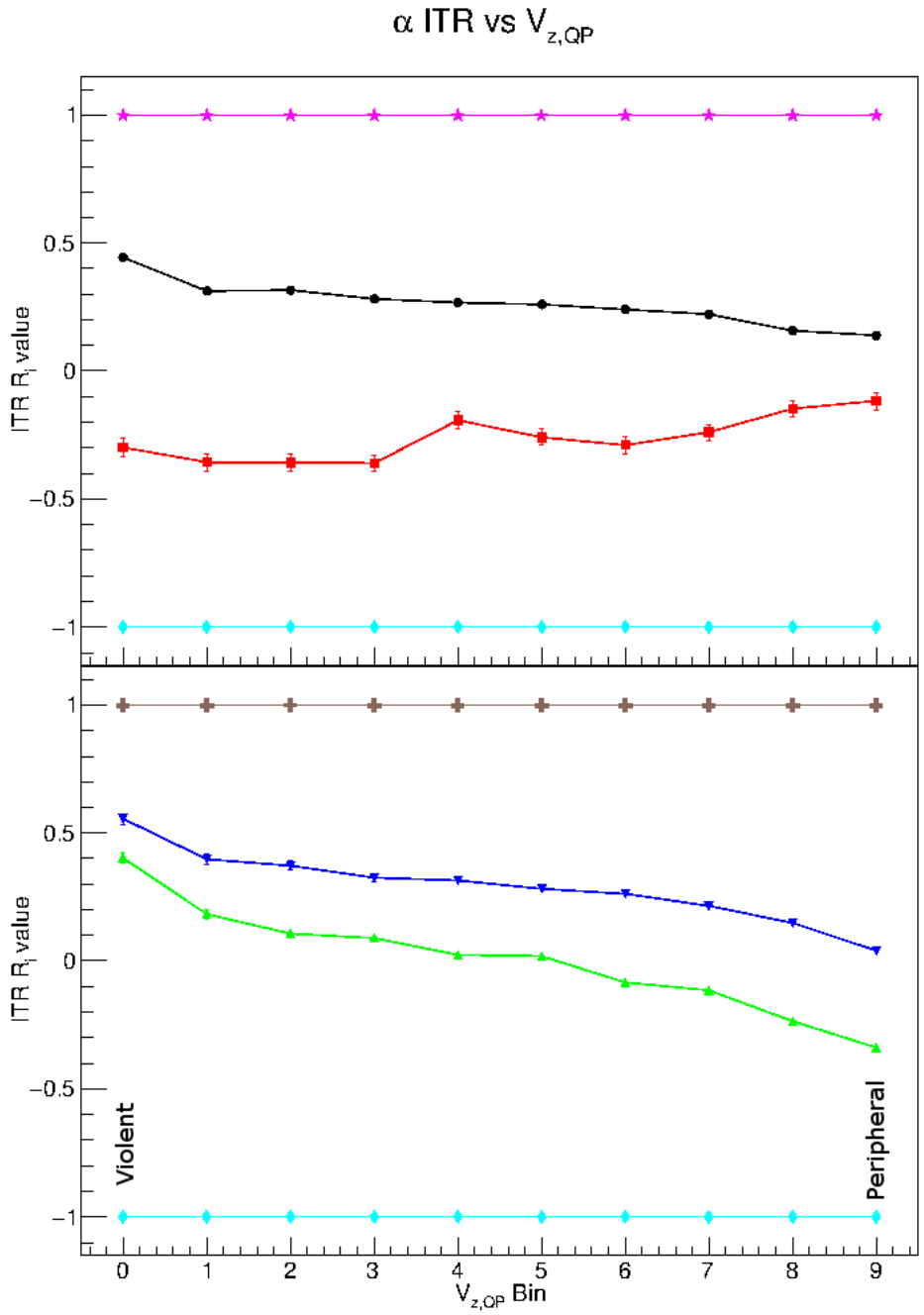

Figure 3.20: Isospin transport ratio (ITR) R_i value (Eq. 1.6) for the isoscaling α parameter as a function of $V_{z,QP}$ bin number from experimental data. Lower $V_{z,QP}$ bin number on average means a more central collision. The top panel shows the results for the Zn set of reactions while the bottom panel shows the results from the A=64 set of reactions: ^{70}Zn+^{70}Zn - pink stars, ^{70}Zn+^{64}Zn - black circles, ^{64}Zn+^{70}Zn - red squares, ^{64}Zn+^{64}Zn - light blue diamonds, ^{64}Zn+^{64}Ni - green triangles, ^{64}Ni+^{64}Zn - blue inverted triangles and ^{64}Ni+^{64}Ni - brown crosses.

influences from secondary decays could be influencing the relatively mixed state at large $V_{z,QP}$ bins (more peripheral collisions). Another cause for the relative mixing that exists at high $V_{z,QP}$ bin value is that the expected impact parameter value for bin 9 is approximately b=7 fm where touching spheres is estimated at approximately b=10 fm. Finally, the slight convergence seen in the A=64 systems occurs at an R_i value that is much higher than the R_i=0 predicted by previous works. This result is consistent with the data seen in the iBUU04 analysis in Section 3.1.

3.5.3 Isobaric Yield Ratios

Rather than relying on yield scaling a large range of isotopes from two different systems at once as in isoscaling, the isobaric yield ratio method uses a single yield ratio from a single source as the isospin-dependent observable. Specifically, the isobaric yield ratio takes the ratio of the yields of two isotopes that are isobars of each other and divides the yield of the more neutron-rich isotope ($Y_{A,NR}$) by the yield of the more neutron-poor isotope ($Y_{A,NP}$) as shown in Equation 3.6.

$$\text{Isobaric Yield Ratio} = \frac{Y_{A,NR}}{Y_{A,NP}} \tag{3.6}$$

In order to verify that the reconstructed QP was in chemical equilibrium, the free neutron-to-proton ratio (n/p) was compared to the A=3 isobar ratio (^{3}H/^{3}He or t/^{3}He) over the full range of reconstructed QP masses (QP SumA). The average neutron-to-proton asymmetry (N/Z) was compared event-by-event from these two ratios as a function of the QP SumA and can be seen in the top panel of Figure 3.21 for the ^{70}Zn+^{64}Zn reaction system. If the free n/p ratio were consistent with the t/^{3}He ratio this would be consistent with chemical equilibration. It can be seen in the top panel of Figure 3.21 that this is not exactly the case in this data set. However, this does not mean the QP source is not in chemical equilibrium. In fact, the mirroring

of the trends of the n/p ratio and t/^{3}He ratio with the QP mass would suggest that the source is in chemical equilibrium and that the differences between the N/Z of the two ratios has another explanation. One possible reason for the enhancement of the n/p ratio with respect to the t/^{3}He ratio can be seen in the bottom panel of Figure 3.21. In this panel is shown the average fraction of the QP mass that comes from each of several different particle types as a function of the size of the QP. The larger fragments in the event (Z>3, open red squares) comprise the majority of the mass of the reconstructed QP over all QP masses within the reconstruction mass cut. In fact, as the mass of the QP increases, a larger and larger fraction of the QP mass comes from these larger fragments. Another large source of the QP mass fraction comes from the emission of α particles (light blue diamonds) which on average make up approximately 20% of the QP. The third largest source comes from the emission of free neutrons (solid black circles) while the other light charged particles (p,d,t,^{3}He and Z=3) all have roughly the same contribution in terms of mass fraction of the QP. This large contribution from the α particles and Z>3 fragments could explain the increased n/p ratio due to the relatively symmetric nature of the α and Z>3 particles as compared to the t/^3He ratio. This drives the remaining neutron-excess into the gas phase as previously predicted by Baran *et al.* [88]. It is worth reiterating that in order to calculate the amount of equilibration that has taken place, the absolute value of the n/p ratio is not as important as the fact that the n/p ratio of each system tracks with the source asymmetry. To this end it is worth noting that using the free n/p ratio as an observable for the equilibration, the calculated percent equilibration via Eq. 3.5 was found to be 68±7% for the ^{70,64}Zn+^{70,64}Zn reactions and 71±7% for the ^{64}Zn,Ni+^{64}Zn,Ni reactions, which are a little lower than the calculated values for the ^{3}H/^{3}He ratio but within error bars of that result.

Since the isobaric yield ratio has been shown to be linearly dependent on the

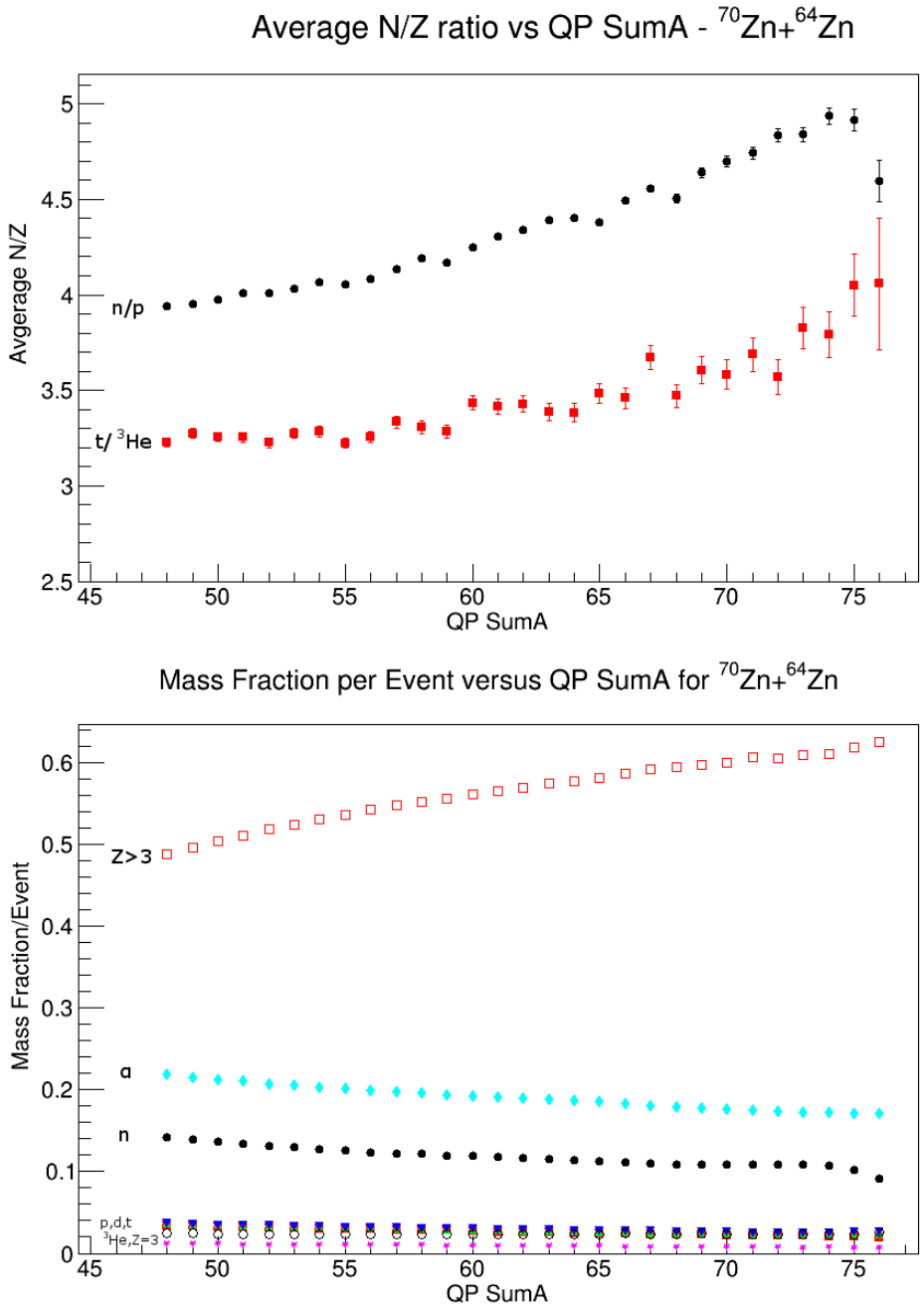

Figure 3.21: Top panel: Average neutron-to-proton asymmetry (N/Z) from the free neutron-to-proton ratio (black circles) as well as the A=3 isobar (red squares) as a function of QP SumA for the ^{70}Zn+^{64}Zn reaction system. Bottom panel: Average mass fraction in each event for various particle types as a function of QP SumA for the ^{70}Zn+^{64}Zn reaction system: neutrons (solid black circles), protons (solid red squares), deuterons (green triangles), tritons (blue inverted triangles), ^{3}He (pink stars), α (light blue diamonds), all Z=3 (open black circles) and all Z>3 (open red squares).

isospin asymmetry of the source and the QP source appears to be chemically equilibrated in this experiment, the A=3 isobar (^{3}H/^{3}He) is used to examine the isospin equilibration that occurs with increased contact time between projectile and target. Figure 3.22 shows the A=3 isobaric yield ratio as a function of the $V_{z,QP}$ bin. The top panel shows the ratio value for the Zn reaction systems. The data exhibits a rise in isobaric yield ratio for the A=3 isobar with increasing centrality (decreasing $V_{z,QP}$). This rise implies that more neutron rich particles are emitted as the centrality of the reaction increases which is consistent with the idea that more central collisions are "hotter" and therefore have more energy with which to emit neutron rich matter [8]. The experimental ratios do not appears to converge, although the low statistics of the ^{64}Zn+^{70}Zn system could be masking the true behavior (red squares). The bottom panel of Figure 3.22 demonstrates the experimental data for the A=64 reaction system set. The A=3 ratios for the A=64 data appears to converge with increasing centrality of the reaction which could imply a degree of equilibration in the reaction set.

The trends observed in the raw isobaric yield ratios in Figure 3.22 can be seen more clearly by examining the isospin transport ratio (Figure 3.23). The complete separation of the two cross systems from each other in the Zn reaction set (top panels) is clear. While the ^{70}Zn+^{64}Zn (black circles) maintains a value slightly below zero and is relatively flat over the whole range of $V_{z,QP}$, the ^{64}Zn+^{70}Zn (red squares) are relatively flat at around R_i=-0.7 for the experimental data. While the A=3 isobar should be less prone to contamination from secondary decays due to the relatively high energy cost of either ^{3}H or ^{3}He emission, the lack of change in the isobaric yield ratio for the two Zn cross systems compared to the Zn symmetric systems is somewhat unexpected especially since no clear indication of an equilibrating process can be seen. In contrast to the Zn reaction set, the experimental A=3 isobaric yield

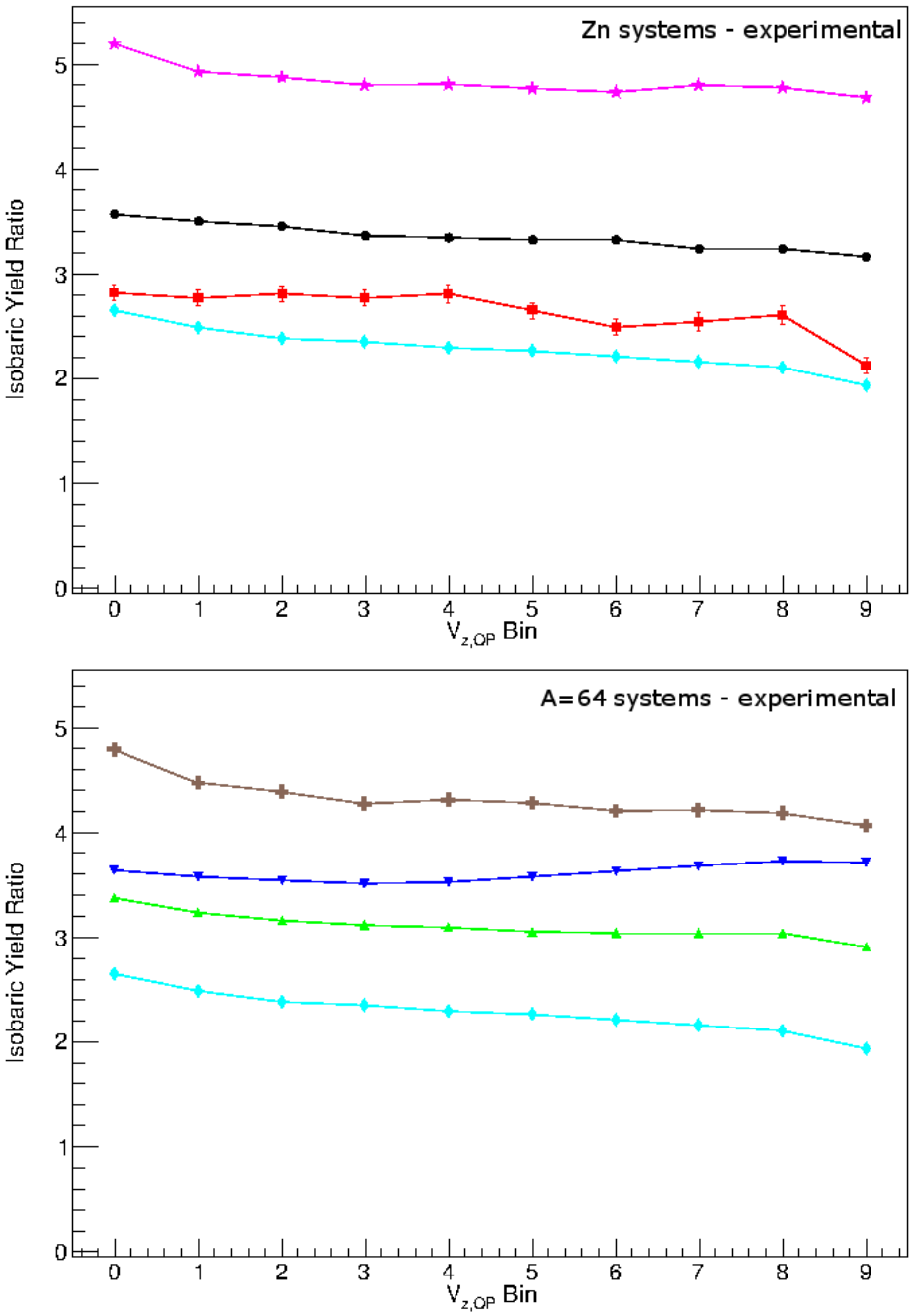

Figure 3.22: Isobaric yield ratio for A=3 isobar as a function of $V_{z,QP}$ bin. Top panel: experimental data for the Zn set of reaction systems: ^{70}Zn+^{70}Zn (pink stars), ^{70}Zn+^{64}Zn (black circles), ^{64}Zn+^{70}Zn (red squares) and ^{64}Zn+^{64}Zn (light blue diamonds). Bottom panel: experimental data for the A=64 set of reaction systems: ^{64}Ni+^{64}Ni (brown crosses), ^{64}Ni+^{64}Zn (blue triangles), ^{64}Zn+^{64}Ni (green inverted triangles) and ^{64}Zn+^{64}Zn (light blue diamonds).

ratios for the A=64 set of reactions (bottom left panel of Figure 3.23) does show a trend toward convergence for more central collisions.

3.5.4 Quasi-projectile Isospin Asymmetry

The final analysis performed was on the reconstructed quasi-projectile asymmetry. While the isoscaling α parameter and the isobaric yield ratio were used as probes of the source asymmetry, the ability of the NIMROD-ISiS array to collect such a wide range of fragments in identity, angle and energy as well as the neutron multiplicity allows for the ability to measure the source asymmetry directly. By reconstructing a well defined "hot" quasi-projectile from rigorous source cuts (Section 3.2) it is assumed that this reconstructed QP is the state immediately following the interaction of the projectile and target. Rather than guessing at the asymmetry of this source, the $\frac{N-Z}{A}$ of the QP can be measured by simply counting the nucleons that make up the QP. The R_i value from the reconstructed QP asymmetry (m_s) is shown as a function of the $V_{z,QP}$ bin in Figure 3.24. The top panel shows the Zn reaction set for the experimental data while the bottom panel shows the A=64 reaction set.

The ITR results for the QP m_s differ from that seen previously in the isoscaling and isobaric yield ratio analyses. First, the experimental data for the Zn set of reactions shows that while the QPs from the ^{70}Zn+^{64}Zn (black circles) and ^{64}Zn+^{70}Zn (red squares) reactions begin separated by very little in isospin asymmetry ($V_{z,QP}$ bin=9), as the centrality of the reaction increases, the two systems quickly converge to each other (at around $V_{z,QP}$ bin=4). This convergence implies isospin equilibration occurs in this set of reaction systems fairly strongly since the corresponding impact parameter value from Figure 3.16 to the $V_{z,QP}$ bin 4 is approximately b=4 fm. The curves also show a distinct neutron enhancement relative to the midpoint between the two symmetric systems.

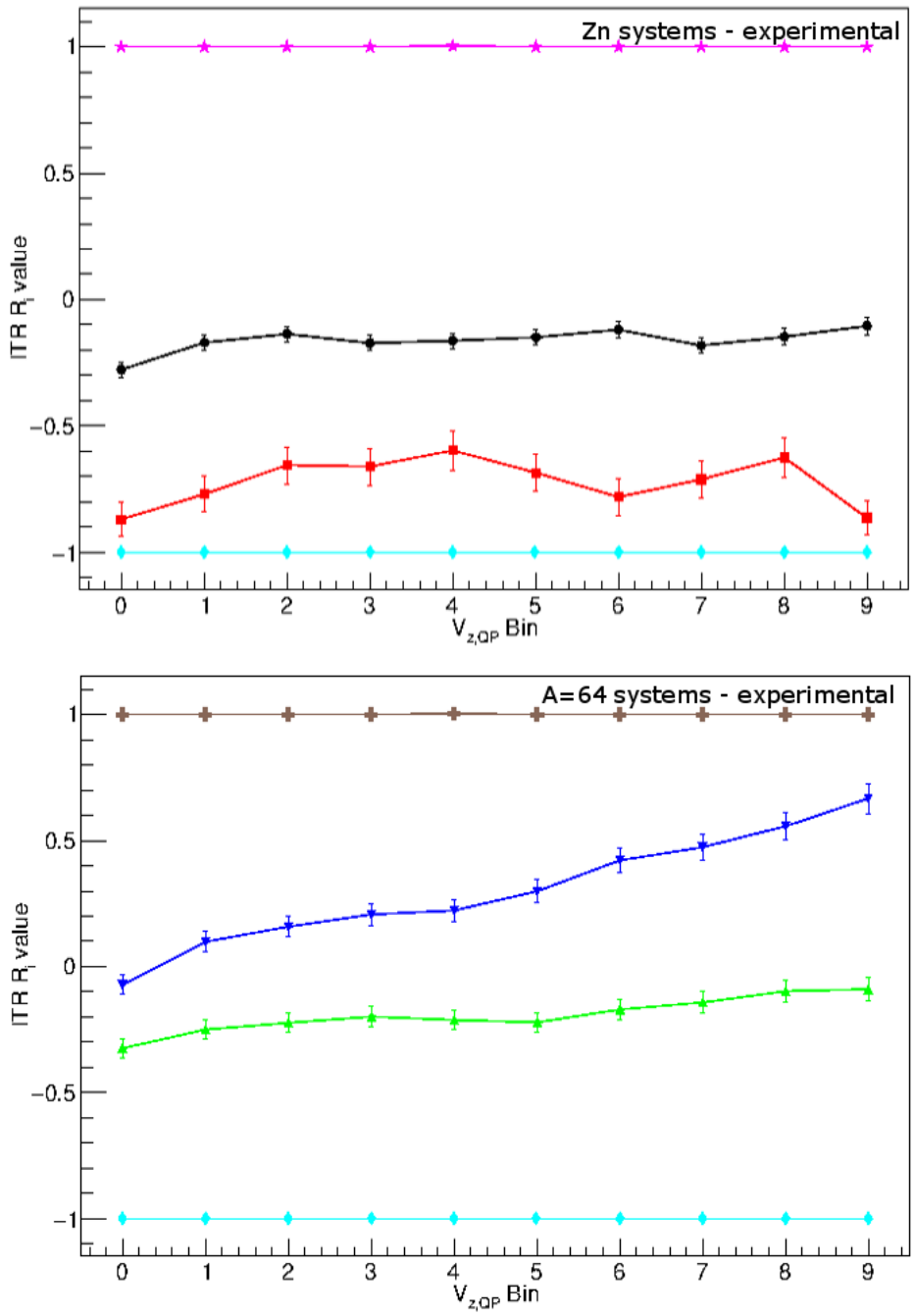

Figure 3.23: Isospin Transport Ratio R_i for the A=3 isobar as a function of $V_{z,QP}$ bin. Top panel: experimental data for the Zn set of reaction systems: ^{70}Zn+^{70}Zn (pink stars), ^{70}Zn+^{64}Zn (black circles), ^{64}Zn+^{70}Zn (red squares) and ^{64}Zn+^{64}Zn (light blue diamonds). Bottom panel: experimental data for the A=64 set of reaction systems: ^{64}Ni+^{64}Ni (brown crosses), ^{64}Ni+^{64}Zn (blue triangles), ^{64}Zn+^{64}Ni (green inverted triangles) and ^{64}Zn+^{64}Zn (light blue diamonds).

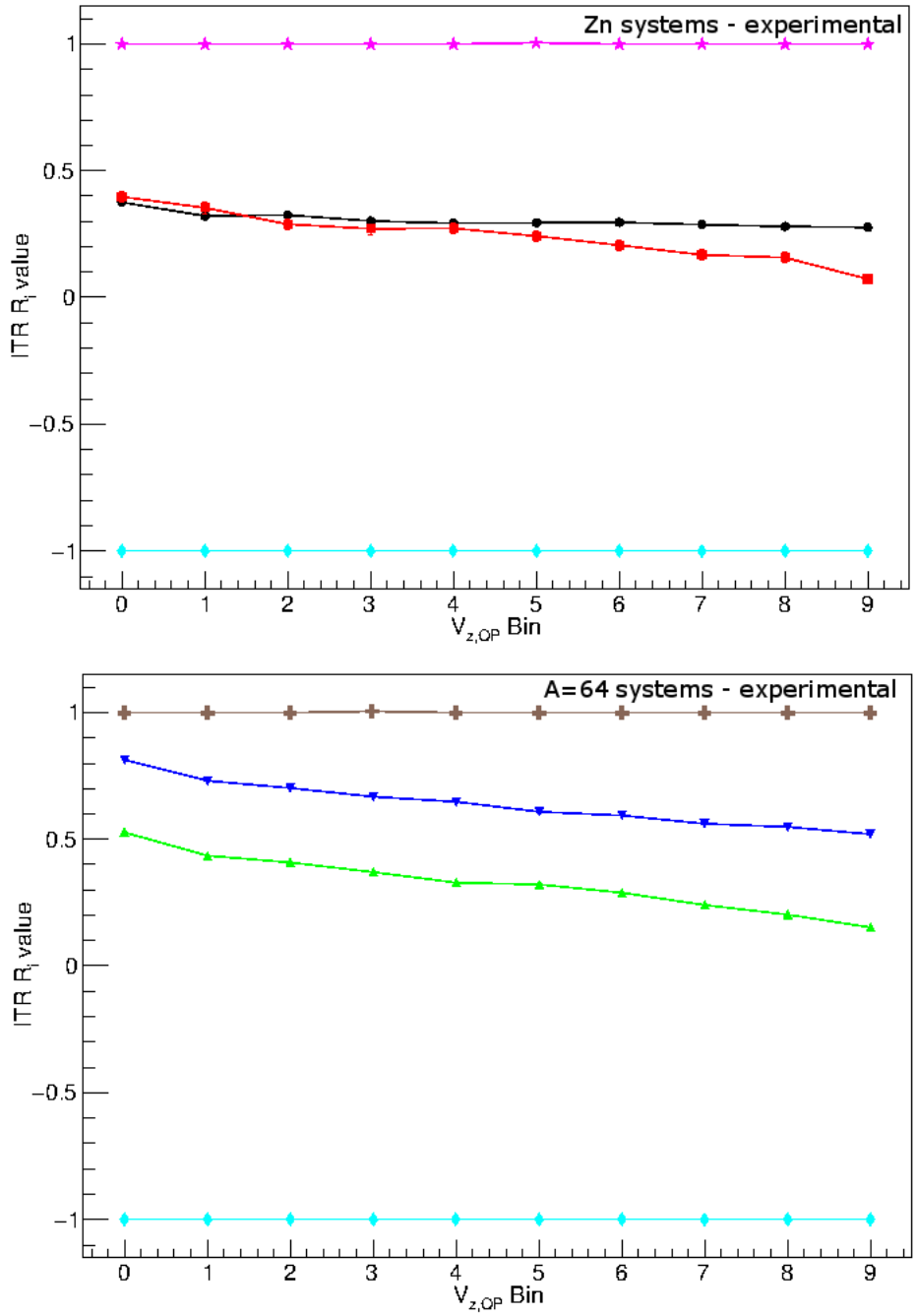

Figure 3.24: Isospin Transport Ratio R_i for the quasi-projectile m_s as a function of $V_{z,QP}$ bin. Top panel: experimental data for the Zn set of reaction systems: ^{70}Zn+^{70}Zn (pink stars), ^{70}Zn+^{64}Zn (black circles), ^{64}Zn+^{70}Zn (red squares) and ^{64}Zn+^{64}Zn (light blue diamonds). Bottom panel: experimental data for the A=64 set of reaction systems: ^{64}Ni+^{64}Ni (brown crosses), ^{64}Ni+^{64}Zn (blue triangles), ^{64}Zn+^{64}Ni (green inverted triangles) and ^{64}Zn+^{64}Zn (light blue diamonds).

However, the A=64 set of reactions systems yield some surprising results. In the isoscaling and isobaric yield ratio analysis, this set of reaction systems showed a clearer indication of an equilibration process taking place, but in the QP m_s case, the two curves for the cross-reactions (^{64}Ni+^{64}Zn - blue inverted triangles and ^{64}Zn+^{64}Ni - green triangles) seem to run parallel to each other and so no convergence is seen. The lack of isospin equilibration seen in this observable could be due to the Coulomb gradient present in the A=64 reaction set cross systems. A Coulomb gradient between projectile and target could cause protons to be transferred more strongly from the ^{64}Zn to the ^{64}Ni which could inhibit the isospin equilibration because of the added driving force that is pushing nucleons into and through the neck region that forms. As stated previously, the reason why the other two observables (isoscaling α parameter and isobaric yield ratio) gave an indication of equilibration could be because of the effects of secondary decay on the isotope yields. The A=64 QP m_s data also shows a strong neutron rich enhancement in the QP asymmetry from the cross reactions relative to the center of the two symmetric reactions. This enhancement could be caused by loss of nucleons to the "gas" region outside the QP-neck-QT reaction region as described in the iBUU04 analysis (Section 3.1).

3.6 CoMD Comparison to Experimental Data

The CoMD data was treated in an analogous manner to the experimental data (see Section 3.3). While the CoMD has access to the exact impact parameter the reaction was calculated at, the reconstructed QP impact parameter surrogate was used in order to minimize systematic differences in the treatment of the CoMD and the experiment. It should be noted that only the "asy-soft" CoMD data will be shown in this section due to the relative insensitivity of the CoMD asymmetry energy on the observables discussed, though for completeness the "asy-stiff" and "asy-super-stiff"

can both be found in Appendix D.

An attempt was made to use the CoMD analysis to produce isoscaling plots as in the experimental case. However, the particle yields obtained from the CoMD+GEMINI did not scale as predicted by the isoscaling analysis. Examples of the poor yield scaling from the CoMD can be found in Figures D.8 & D.9 in Appendix D. This can also be partially understood from Figure 3.25 in which the distribution of assigned A values for all isotopically identified fragments from all seven systems combined is shown. The experimental data (black curve) can be seen to have much higher production of heavier mass fragments than in the case of the CoMD ("asy-soft" - red dashed line, "asy-stiff" - green dotted line and "asy-super-stiff" - blue dot-dashed line). In fact, the CoMD can also be seen to overproduce many fragments A$\leq$10 as compared to the experimental data. This is most likely the cause of the poor yield scaling in attempting to isoscale the CoMD data. The raw number of counts for each is shown with no normalization, further accentuating the overproduction of the light fragments from CoMD.

The CoMD data was also used to reproduce the isobaric yield ratio calculated in Section 3.5.3. The results from the "asy-soft" CoMD can be seen in Figure 3.26. The left side of the figure gives the raw ^{3}H/^{3}He values while the right side shows the processed ITR calculation using the ^{3}H/^{3}He ratios. The top two panels correspond to the Zn set of reactions and the bottom row of panels correspond to the A=64 reaction set. It is important to note that the y-axis scales are different here than in the case of the experimental data. In general, the CoMD ratios are much higher than the corresponding experimental ratios, implying an overproduction of ^{3}H relative to ^{3}He in the CoMD data.

The "asy-soft" CoMD data for the Zn reaction set shows a similar trend to the experimental Zn data but is on average slightly higher in value. The same trend of

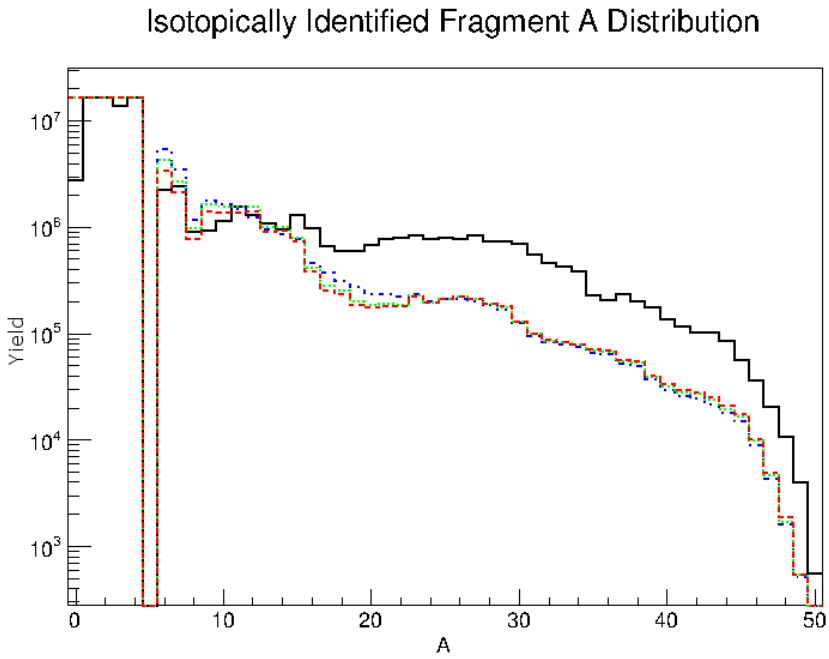

Figure 3.25: Distribution of the assigned A value for all isotopically identified fragments from all seven reaction systems combined. The solid black curve is the experimental data while the red dashed line, green dotted line and blue dot-dashed line correspond to the "asy-soft", "asy-stiff" and "asy-super-stiff" CoMD data, respectively.

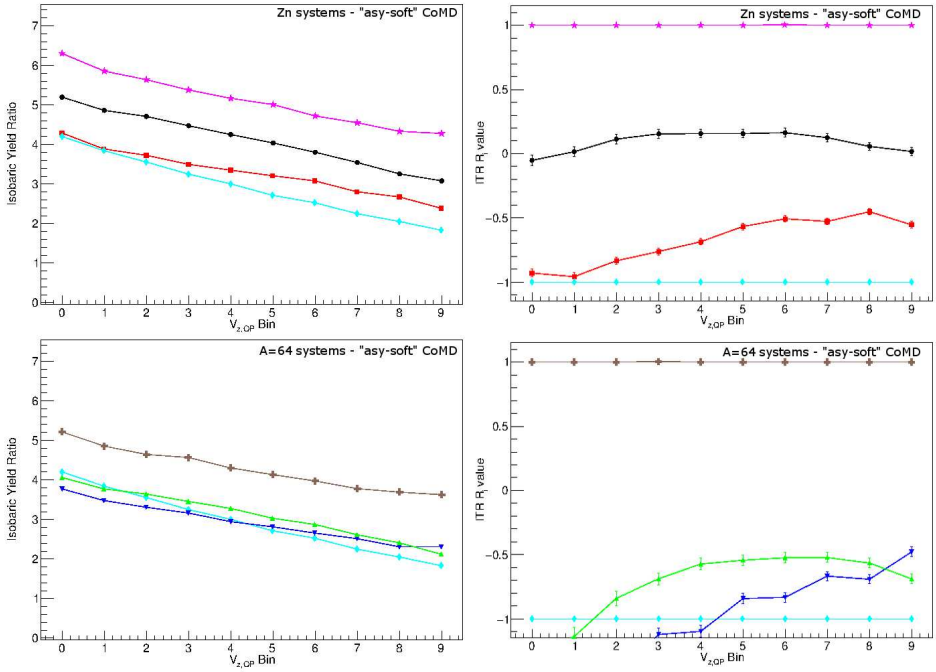

Figure 3.26: Isobaric yield ratio for A=3 isobar (^{3}H/^{3}He) and isospin transport ratio value as a function of $V_{z,QP}$ bin. Top panels: CoMD "asy-soft" data for the Zn set of reaction systems: ^{70}Zn+^{70}Zn (pink stars), ^{70}Zn+^{64}Zn (black circles), ^{64}Zn+^{70}Zn (red squares) and ^{64}Zn+^{64}Zn (light blue diamonds). Bottom panels: CoMD "asy-soft" data for the A=64 set of reaction systems: ^{64}Ni+^{64}Ni (brown crosses), ^{64}Ni+^{64}Zn (blue triangles), ^{64}Zn+^{64}Ni (green inverted triangles) and ^{64}Zn+^{64}Zn (light blue diamonds). The left side gives the raw ^{3}H/^{3}He values while the right side shows the processed ITR calculation using the ^{3}H/^{3}He ratios.

increasing production of the neutron rich isotope with increasing centrality of the reaction is also observed. The slope of the A=64 reactions for the CoMD over the full $V_{z,QP}$ range is not as pronounced as the slope in the corresponding Zn reactions, however. This could imply that the Coulomb gradient in the A=64 reactions is inhibiting the exchange of nucleons in the reaction and is suppressing the emission of the more neutron-rich fragments as a result. While the experimental data for the A=64 data converged with increasing centrality (Figure 3.22), the ^{64}Ni+^{64}Zn (blue triangles) system in the CoMD is highly damped relative to its experimental equivalent and diverges from the ^{64}Ni+^{64}Zn (green inverted triangles) system. This is a curious result especially coupled with the fact that both cross system curves in the A=64 CoMD are low in value compared to the symmetric systems but this could be related to the overall damping of the isobaric yield value in the A=64 CoMD relative to the Zn reaction set.

The trends seen in the raw ^{3}H/^{3}He ratios can also be seen in the corresponding ITR values on the right side of Figure 3.26. The "asy-soft" CoMD data for the Zn reaction set is similar in behavior to that of the experimental data, though the CoMD has a more pronounced separation between the two cross systems. The slight convergence observed in the experimental A=64 set of reactions is not reproduced in the CoMD data due to the "asy-soft" CoMD data suffering from strange behavior related to the lowered isobaric yield ratio values seen in the bottom left panel of Figure 3.26. Under normal circumstances, an isospin dependent observable for a cross reaction should not leave the bounds set by the symmetric reaction since the observable should track with source asymmetry which is bounded by the asymmetry of the initial symmetric reaction systems. However, the raw isobaric yield ratio values were so low for the two cross reactions in the A=64 set (lower left panel of Figure 3.26) that once processed through the ITR, the R_i values left the bounds of

the symmetric reactions. The reason for this overall lowering of the isobaric ratio value is unknown but as mentioned before could be related to how the CoMD model processes the Coulomb gradient between projectile and target found in the A=64 reaction set.

Finally, the CoMD data was applied to the QP m_s study to examine the evolution of the QP source isospin asymmetry according to the model. The "asy-soft" CoMD data seen in Figure 3.27 differ from the experimental data in two very significant ways. First, the ITR R_i value calculated in the CoMD data is very neutron poor in reference to the symmetric systems, especially when compared to the experimental data. The other major difference is that the curves for both cross systems (in both reaction sets) lie in relative agreement with each other. While a small separation at $V_{z,QP}$ bin=9 (comparable to the experimental Zn set of systems) exists, this separation is almost immediately closed and the values for the two curves invert in relation to the symmetric systems. Then as the reactions become more and more centralized the curves start trending towards each other again in the Zn reaction set, while they cross and diverge again in the A=64 reaction sets. This behavior of the CoMD data may be explained in part due to the observation in Figure 3.28.

The normalized reconstructed QP m_s distribution for the ^{70}Zn+^{70}Zn reaction is seen in Figure 3.28. The black curve denotes the experimental data while the three forms of the asymmetry energy for the CoMD are shown as the red dashed line, green dotted line and blue dot-dashed line for the "asy-soft", "asy-stiff" and "asy-super-stiff" data, respectively. Here it is clearly seen that the QP m_s distribution for all three forms of the CoMD asymmetry energy lie almost perfectly atop each other. While the forms of the asymmetry energy in the CoMD are very close in form to each other, this lack of change in the reconstructed QP m_s distribution would imply that the QP m_s value in the model is fairly insensitive to changes in the density

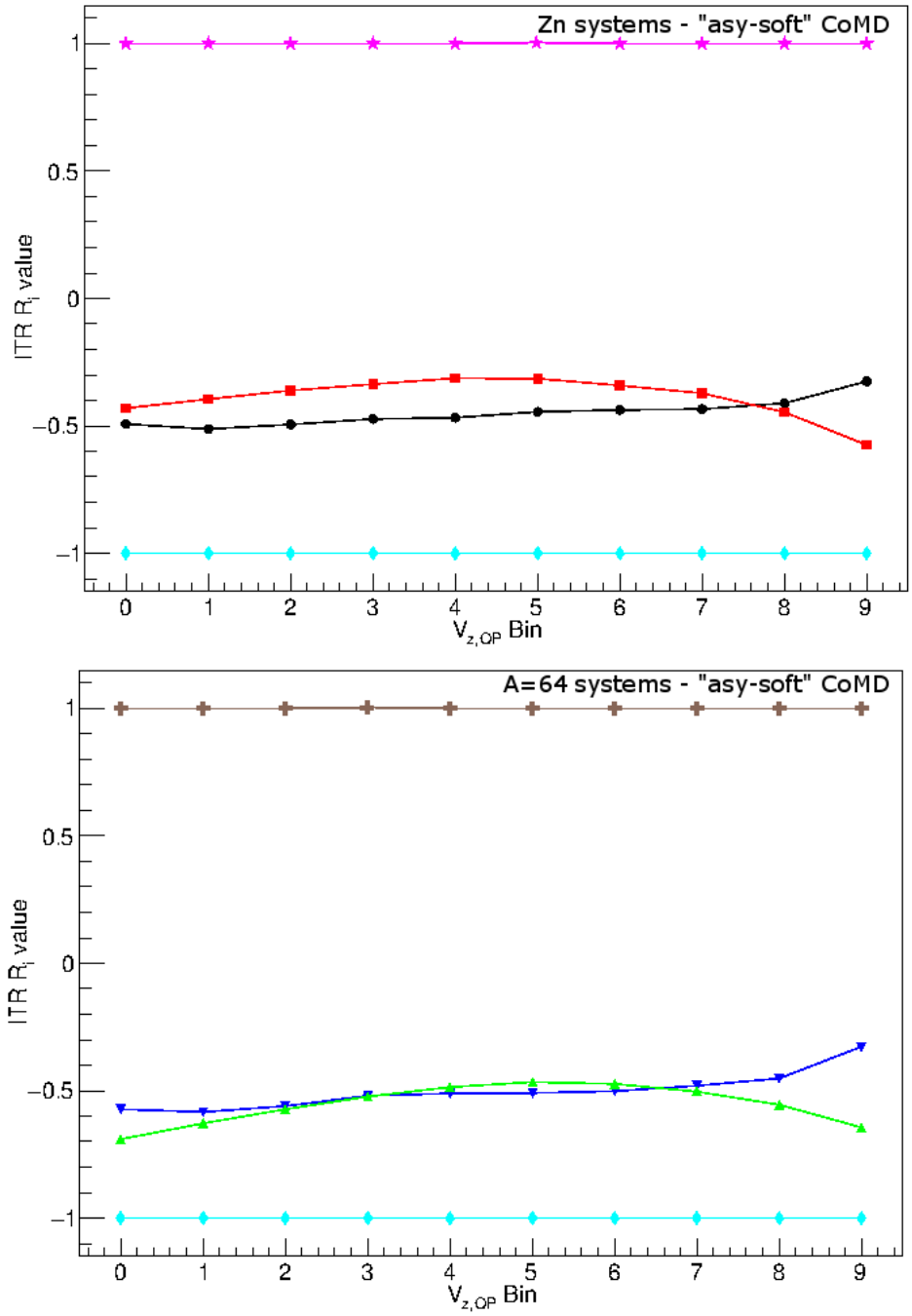

Figure 3.27: Isospin Transport Ratio R_i for the quasi-projectile m_s as a function of $V_{z,QP}$ bin. Top panel: "asy-soft" CoMD data for the Zn set of reaction systems: ^{70}Zn+^{70}Zn (pink stars), ^{70}Zn+^{64}Zn (black circles), ^{64}Zn+^{70}Zn (red squares) and ^{64}Zn+^{64}Zn (light blue diamonds). Bottom panel: "asy-soft" CoMD data for the A=64 set of reaction systems: ^{64}Ni+^{64}Ni (brown crosses), ^{64}Ni+^{64}Zn (blue inverted triangles), ^{64}Zn+^{64}Ni (green triangles) and ^{64}Zn+^{64}Zn (light blue diamonds).

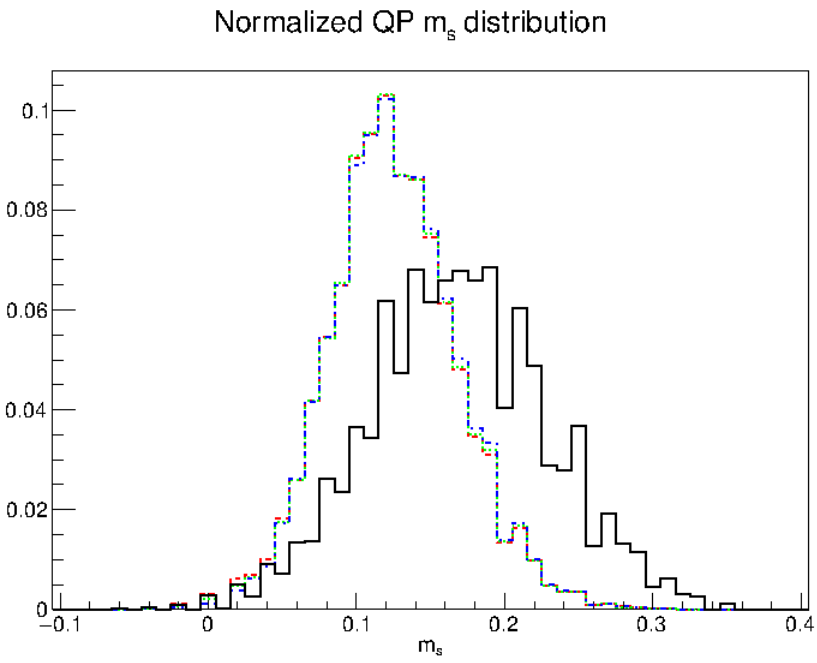

Figure 3.28: Quasi-projectile m_s distribution for the ^{70}Zn+^{70}Zn reaction system. The solid black curve is the experimental data while the red dashed line, green dotted line and blue dot-dashed line correspond to the "asy-soft", "asy-stiff" and "asy-super-stiff" CoMD data, respectively.

dependence of the asymmetry energy. This surprising result is worthy of further exploration.

It is also noted that the peak and shape of this distribution for the models is very different from that observed for the experimental data. The distribution for the experimental data peaks at a more neutron-rich value of m_s while also exhibiting a wider distribution. The higher peak value in the experiment could explain the elevated values found in Figure 3.24 for the experiment relative to the CoMD in Figure 3.27. The apparent insensitivity of the QP m_s observable to the density dependence of the asymmetry could also explain the strange behavior of the shapes of the CoMD curves in Figure 3.27 as well as the very small differences in these observables with varying CoMD asymmetry energy parameterizations (as seen in the additional figures in Appendix D).

4. CONCLUSIONS

Determining and understanding the form of the nuclear Equation of State is a major goal of the nuclear physics community. In particular, the density dependence of the asymmetry energy is not very well constrained and many experiments and theories have been conducted and formed over the last 30 years in order to better understand it [13–16, 19, 20, 22, 30, 39, 44–46, 48, 51–58]. One method of examining the density dependence of the asymmetry energy is through the process of isospin equilibration that takes place during a heavy-ion collision since the differential exchange of protons and neutrons is directly affected by the asymmetry energy. In this dissertation, the isospin equilibration of 35 MeV/nucleon ^{70}Zn,^{64}Zn+^{70}Zn,^{64}Zn and ^{64}Zn,^{64}Ni+^{64}Zn,^{64}Ni reactions was examined using probes of the isoscaling parameter α, isobaric yield ratio measurements of the A=3 isobar and the reconstructed quasi-projectile isospin asymmetry. These results were also compared to simulations performed using the iBUU04 transport model as well as the Constrained Molecular Dynamics (CoMD) model. One particular interest was to investigate whether a Coulomb gradient between projectile and target would have an affect on the amount of isospin equilibration in a reaction.

The degree of isospin equilibration as predicted by the iBUU04 model was examined. The model results showed that the quasi-projectile isospin asymmetry is highly dependent on the form of the density dependence of the asymmetry energy as previously predicted. As the density dependence of the asymmetry energy "stiffens" less isospin equilibration will occur due to the difficulty of driving neutron excess out of the neck region of the nuclear reaction compared to the ease of driving neutron excess into the low density neck region. The iBUU results also showed that contrary

to previous assumptions, the content of the neck region of the reaction as well as the surrounding particle "gas" region can have a dramatic effect on the final state asymmetry values measured in a heavy-ion collision. Due to this possible loss of nucleons to other sources, it is proposed that approaching a specific value or quantity of an isospin dependent observable may not be sufficient for obtaining isospin equilibration. Rather, convergence of the quasi-projectile and quasi-target asymmetries (or alternatively quasi-projectiles of mirror asymmetric reactions) to each other is a better indication that equilibration between the two sources has occurred. The interaction term used in the model did not show any appreciable difference between reactions that had a Coulomb gradient present between projectile and target and reactions that did not.

Many different surrogates for the experimental impact parameter were examined. Each surrogate was tested via the CoMD simulation to see how well the observable tracked with the actual event impact parameter from CoMD. The observables were then double-checked by examining their proposed binning that was designed to be linearly dependent on the impact parameter to the actual impact parameter distribution in each bin. It was found that the $V_{z,QP}$ observable had the cleanest correlation with impact parameter from the CoMD model and was a large improvement over the fixed-width excitation energy binning used in previous analyses.

Experimental data taken on the NIMROD-ISiS (Neutron-Ion Multidetector for Reaction Oriented Dynamics with Indiana Silicon Sphere) 4π charged particle detector array coupled with the TAMU Neutron Ball at the Texas A&M University Cyclotron Institute were examined via three primary isospin dependent observables. The isoscaling observable was used in two ways, one as a comparison to the seminal work by Tsang *et al.* [12] in isospin diffusion and the other was as a probe of the equilibration as a function of impact parameter. The isoscaling analysis com-

paring to Tsang *et al.* was found to be in good agreement with those results and found an isospin equilibration of approximately 80% in both the ^{70}Zn,^{64}Zn+^{70}Zn,^{64}Zn and ^{64}Zn,^{64}Ni+^{64}Zn,^{64}Ni sets of reactions. No significant difference was seen between the sets of reactions under these conditions. Additionally, the isoscaling with respect to the centrality of the reaction was examined and a signature of partial equilibration was found in the ^{64}Zn,^{64}Ni+^{64}Zn,^{64}Ni set of reactions but not in the ^{70}Zn,^{64}Zn+^{70}Zn,^{64}Zn set of reactions. This difference is largely attributed to the poor experimental statistics of the ^{64}Zn+^{70}Zn reaction affecting the yield scaling measurements.

The second isospin dependent observable analyzed was the isobaric yield ratio for the A=3 isobar and an equilibration of approximately 80% was found for both the Zn and A=64 sets of reactions. The isobaric yield ratio was examined with respect to the centrality of the collision as in the isoscaling case and a similar result was found: a signature of partial equilibration in the ^{64}Zn,^{64}Ni+^{64}Zn,^{64}Ni set of reactions but not in the ^{70}Zn,^{64}Zn+^{70}Zn,^{64}Zn set of reactions as determined by the convergence of the cross systems in each reaction set. Again, this difference is largely attributed to the poor experimental statistics of the ^{64}Zn+^{70}Zn reaction affecting the isobaric yield scaling measurement.

The last isospin dependent observable examined was a new observable: the direct measurement of the source asymmetry via reconstructed quasi-projectiles. Using the source asymmetry value, the equilibration in both reaction sets was found to be approximately 90%, much higher than in the other observables. In this measurement a strong signal of isospin equilibration was observed for the ^{70}Zn,^{64}Zn+^{70}Zn,^{64}Zn set of reactions but not in the ^{64}Zn,^{64}Ni+^{64}Zn,^{64}Ni set of reactions via the convergence of the cross systems, opposite of the trends seen in the yield scaling methods. The reason for this change is not clear, but it is presumed that the Coulomb asymmetry

of the ^{64}Zn,^{64}Ni+^{64}Zn,^{64}Ni set of reactions may be partially responsible. In order to better examine this hypothesis, future work could improve the understanding of the models used and apply them with and without the Coulomb interaction present in order to see what effect that has. Other expansions of this work could entail efforts to quantify the isospin asymmetry of the neck region and/or the "gas" region experimentally to see how these are affected by the centrality of the reaction.

Finally, the CoMD model was software filtered to match the experimental setup and treated in such a way as to be directly comparable to the experimental data. Unfortunately the input parameters chosen for the model produced fragment distributions that proved difficult to analyze by yield scaling studies. This difficulty could have occurred due to the two-part nature of the model treatment: the CoMD processed the reaction dynamically to 600 fm/c and then resulting hot reaction state was cooled using the GEMINI statistical decay method. By combining this dynamical model to the statistical decay model, effects from secondary decays in the GEMINI model may have obscured any signals of isospin equilibration in the CoMD fragment yield results. The CoMD also did not show any significant difference in the equilibration between reactions with a Coulomb gradient between projectile and target and reactions without such a Coulomb gradient. A possible expansion of this work could be to run the CoMD model with improved parameterizations of its input in addition to running the code with and without the Coulomb force applied. While a reaction that has no Coulomb force is clearly un-physical, the comparison between this and a physical interpretation of the Coulomb force could yield insight into what isospin dependent observables in the CoMD output are sensitive to the Coulomb gradient found in the ^{64}Zn,^{64}Ni+^{64}Zn,^{64}Ni reactions.

In summary, signatures of equilibration were seen using three separate isospin asymmetry observables (isoscaling α, A=3 isobaric yield ratios and reconstructed QP

asymmetry) in both charge-symmetric mass-asymmetric (^{70}Zn,^{64}Zn+^{70}Zn,^{64}Zn) and mass-symmetric charge-asymmetric (^{64}Zn,^{64}Ni+^{64}Zn,^{64}Ni) sets of nuclear reactions. While signatures of equilibration were observed in the experimental and iBUU04 data both binned by impact parameter as well as integrated over impact parameter, the CoMD model was not sensitive to the examined observables under the conditions in which the simulation was calculated. Finally, no clear difference was determined in the experimental data that could be identified as an effect of the Coulomb gradient in the ^{64}Zn,^{64}Ni+^{64}Zn,^{64}Ni reactions, though small differences between the two sets of reactions were observed.

REFERENCES

[1] G. R. Choppin, J. O. Liljenzin, and J. Rydberg. Radiochemistry and Nuclear Chemistry. Butterworth-Heinemann, Woburn, 2002.

[2] C. F. v. Weizsacker. Zur Theorie der Kernmassen. Zeitschrift fur Physik, 96(7-8):431–458, July 1935.

[3] G. Friedlander, J. W. Kennedy, E. S. Macias, and J. M. Miller. Nuclear and Radiochemistry. John Wiley and Sons, New York, 1981.

[4] G. Audi and A.H. Wapstra. The 1995 update to the atomic mass evaluation. Nuclear Physics A, 595(4):409–480, December 1995.

[5] M. B. Tsang, Yingxun Zhang, P. Danielewicz, M. Famiano, Zhuxia Li, W. G. Lynch, and a. W. Steiner. Constraints on the Density Dependence of the Symmetry Energy. Physical Review Letters, 102(12):122701, March 2009.

[6] A. Bonasera, Z. Chen, R. Wada, K. Hagel, J. Natowitz, P. Sahu, L. Qin, S. Kowalski, Th. Keutgen, T. Materna, and T. Nakagawa. Quantum Nature of a Nuclear Phase Transition. Physical Review Letters, 101(12):122702, September 2008.

[7] R Tripathi, A Bonasera, S Wuenschel, L W May, Z Kohley, G A Souliotis, S Galanopoulos, K Hagel, D V Shetty, K Huseman, S N Soisson, B C Stein, and S J Yennello. Investigation of critical behaviour from nuclear fragment yield ratios. Journal of Physics: Conference Series, 312(8):082043, September 2011.

[8] A. B. McIntosh, J. Mabiala, A. Bonasera, P. Cammarata, K. Hagel, Z. Kohley, L. Heilborn, L. W. May, P. Marini, A. Raphelt, G. A. Souliotis, S. Wuenschel,

A. Zarrella, H. Zheng, and S. J. Yennello. How much cooler would it be with some more neutrons? The European Physical Journal A, 50(2):35, February 2014.

[9] M. Colonna and M. B. Tsang. Isotopic compositions and scalings. The European Physical Journal A, 30(1):165–182, October 2006.

[10] T. X. Liu, W. G. Lynch, M. B. Tsang, X. D. Liu, R. Shomin, W. P. Tan, G. Verde, A. Wagner, H. F. Xi, H. S. Xu, B. Davin, Y. Larochelle, R. T. DeSouza, R. J. Charity, and L. G. Sobotka. Isospin diffusion observables in heavy-ion reactions. Physical Review C, 76, September 2007.

[11] M. B. Tsang, C. K. Gelbke, X. D. Liu, W. G. Lynch, W. P. Tan, G. Verde, H. S. Xu, W. A. Friedman, R. Donangelo, S. R. de Souza, C. B. Das, S. Das Gupta, and D. Zhabinsky. Isoscaling in statistical models. Physical Review C, 64(5):054615, October 2001.

[12] M. B. Tsang, T. X. Liu, L. Shi, P. Danielewicz, C. K. Gelbke, X. D. Liu, W. G. Lynch, W. P. Tan, G. Verde, A. Wagner, H. S. Xu, W. A. Friedman, L. Beaulieu, B. Davin, R. T. de Souza, Y. Larochelle, T. Lefort, R. Yanez, V. E. Viola, R. J. Charity, and L. G. Sobotka. Isospin Diffusion and the Nuclear Symmetry Energy in Heavy Ion Reactions. Physical Review Letters, 92(6):062701, February 2004.

[13] B. A. Li and U. Schroder. Isospin Physics in Heavy-Ion Collisions at Intermediate Energies. NOVA Science, Huntington, 2001.

[14] Lie-Wen Chen, Che Ming Ko, Bao-An Li, Chang Xu, and Jun Xu. Probing isospin- and momentum-dependent nuclear effective interactions in neutron-rich matter. The European Physical Journal A, 50(2):29, February 2014.

[15] Maria Colonna, Virgil Baran, and Massimo Di Toro. Theoretical predictions of experimental observables sensitive to the symmetry energy. The European

Physical Journal A, 50(2):30, February 2014.

[16] C. Fuchs and H. H. Wolter. Modelization of the EOS. The European Physical Journal A, 30(1):5–21, September 2006.

[17] Kei Iida and Kazuhiro Oyamatsu. Symmetry energy, unstable nuclei and neutron star crusts. The European Physical Journal A, 50(2):42, February 2014.

[18] B Li, L Chen, and C Ko. Recent progress and new challenges in isospin physics with heavy-ion reactions. Physics Reports, 464(4-6):113–281, August 2008.

[19] V Baran, M Colonna, V Greco, and M Ditoro. Reaction dynamics with exotic nuclei. Physics Reports, 410(5-6):335–466, May 2005.

[20] Bao-An Li, Che Ming Ko, and Wolfgang Bauer. Isospin Physics in Heavy-Ion Collisions at Intermediate Energies. International Journal of Modern Physics E, 07(02):147–229, April 1998.

[21] Andrew Steiner and Bao-An Li. Isospin diffusion in heavy-ion collisions and the neutron skin thickness of lead. Physical Review C, 72(4):041601, October 2005.

[22] D. V. Shetty, S. J. Yennello, and G. A. Souliotis. Density dependence of the symmetry energy and the nuclear equation of state: A dynamical and statistical model perspective. Physical Review C, 76(2):024606, August 2007.

[23] J M Lattimer and M Prakash. The physics of neutron stars. Science, 304(5670):536–42, April 2004.

[24] Lie-Wen Chen, Che Ko, and Bao-An Li. Nuclear matter symmetry energy and the neutron skin thickness of heavy nuclei. Physical Review C, 72(6):064309, December 2005.

[25] Bao-An Li. High density behaviour of nuclear symmetry energy and high energy heavy-ion collisions. Nuclear Physics A, 708(3-4):365–390, October 2002.

[26] T. Klähn, D. Blaschke, S. Typel, E. N. E. van Dalen, a. Faessler, C. Fuchs,

T. Gaitanos, H. Grigorian, a. Ho, E. E. Kolomeitsev, M. C. Miller, G. Röpke, J. Trümper, D. N. Voskresensky, F. Weber, and H. H. Wolter. Constraints on the high-density nuclear equation of state from the phenomenology of compact stars and heavy-ion collisions. Physical Review C, 74(3):035802, September 2006.

[27] R.J. Furnstahl. Neutron radii in mean-field models. Nuclear Physics A, 706(1-2):85–110, July 2002.

[28] Andrew Steiner. High-density symmetry energy and direct Urca process. Physical Review C, 74(4):045808, October 2006.

[29] Constança Providência, Sidney S. Avancini, Rafael Cavagnoli, Silvia Chiacchiera, Camille Ducoin, Fabrizio Grill, Jérôme Margueron, Débora P. Menezes, Aziz Rabhi, and Isaac Vidaña. Imprint of the symmetry energy on the inner crust and strangeness content of neutron stars. The European Physical Journal A, 50(2):44, February 2014.

[30] A. W. Steiner and S. Gandolfi. Connecting Neutron Star Observations to Three-Body Forces in Neutron Matter and to the Nuclear Symmetry Energy. Physical Review Letters, 108(8):081102, February 2012.

[31] Tobias Fischer, Matthias Hempel, Irina Sagert, Yudai Suwa, and Jürgen Schaffner-Bielich. Symmetry energy impact in simulations of core-collapse supernovae. The European Physical Journal A, 50(2):46, February 2014.

[32] A. B. McIntosh, A. Bonasera, Z. Kohley, P. J. Cammarata, K. Hagel, L. Heilborn, J. Mabiala, L. W. May, P. Marini, A. Raphelt, G. A. Souliotis, S. Wuenschel, A. Zarrella, and S. J. Yennello. Using light charged particles to probe the asymmetry dependence of the nuclear caloric curve. Physical Review C, 87(3):034617, March 2013.

[33] V.V. Sagun, A.I. Ivanytskyi, K.A. Bugaev, and I.N. Mishustin. The statistical

multifragmentation model for liquidgas phase transition with a compressible nuclear liquid. Nuclear Physics A, 924:24–46, April 2014.

[34] X. Viñas, M. Centelles, X. Roca-Maza, and M. Warda. Density dependence of the symmetry energy from neutron skin thickness in finite nuclei. The European Physical Journal A, 50(2):27, February 2014.

[35] K. Hagel, J. B. Natowitz, and G. Röpke. The equation of state and symmetry energy of low-density nuclear matter. The European Physical Journal A, 50(2):39, February 2014.

[36] K. Hebeler and A. Schwenk. Symmetry energy, neutron skin, and neutron star radius from chiral effective field theory interactions. The European Physical Journal A, 50(2):11, February 2014.

[37] J. Rikovska Stone, J. C. Miller, R. Koncewicz, P. D. Stevenson, and M. R. Strayer. Nuclear matter and neutron-star properties calculated with the Skyrme interaction. Physical Review C, 68(3):034324, September 2003.

[38] Bao-An Li. Probing the High Density Behavior of the Nuclear Symmetry Energy with High Energy Heavy-Ion Collisions. Physical Review Letters, 88(19):192701, April 2002.

[39] James M. Lattimer and Andrew W. Steiner. Constraints on the symmetry energy using the mass-radius relation of neutron stars. The European Physical Journal A, 50(2):40, February 2014.

[40] William G. Newton, Joshua Hooker, Michael Gearheart, Kyleah Murphy, De-Hua Wen, Farrukh J. Fattoyev, and Bao-An Li. Constraints on the symmetry energy from observational probes of the neutron star crust. The European Physical Journal A, 50(2):41, February 2014.

[41] G. Colò, U. Garg, and H. Sagawa. Symmetry energy from the nuclear collective motion: constraints from dipole, quadrupole, monopole and spin-dipole

resonances. The European Physical Journal A, 50(2):26, February 2014.

[42] E. De Filippo and A. Pagano. Experimental effects of dynamics and thermodynamics in nuclear reactions on the symmetry energy as seen by the CHIMERA 4 pi detector. The European Physical Journal A, 50(2):32, February 2014.

[43] M. Dutra, O. Lourenço, J. S. Sá Martins, A. Delfino, J. R. Stone, and P. D. Stevenson. Skyrme interaction and nuclear matter constraints. Physical Review C, 85(3):035201, March 2012.

[44] S. Gandolfi, J. Carlson, and Sanjay Reddy. Maximum mass and radius of neutron stars, and the nuclear symmetry energy. Physical Review C, 85(3):032801, March 2012.

[45] Z. Kohley, L. W. May, S. Wuenschel, A. Bonasera, K. Hagel, R. Tripathi, R. Wada, G. A. Souliotis, D. V. Shetty, S. Galanopoulos, M. Mehlman, W. B. Smith, S. N. Soisson, B. C. Stein, and S. J. Yennello. Investigation of transverse collective flow of intermediate mass fragments. Physical Review C, 82(6):064601, December 2010.

[46] Z. Kohley, L. W. May, S. Wuenschel, M. Colonna, M. Di Toro, M. Zielinska-Pfabe, K. Hagel, R. Tripathi, A. Bonasera, G. A. Souliotis, D. V. Shetty, S. Galanopoulos, M. Mehlman, W. B. Smith, S. N. Soisson, B. C. Stein, and S. J. Yennello. Transverse collective flow and midrapidity emission of isotopically identified light charged particles. Physical Review C, 83(4):044601, April 2011.

[47] James M. Lattimer and Yeunhwan Lim. CONSTRAINING THE SYMMETRY PARAMETERS OF THE NUCLEAR INTERACTION. The Astrophysical Journal, 771(1):51, July 2013.

[48] W. Lin, X. Liu, M. R. D. Rodrigues, S. Kowalski, R. Wada, M. Huang, S. Zhang, Z. Chen, J. Wang, G. Q. Xiao, R. Han, Z. Jin, J. Liu, F. Shi,

T. Keutgen, K. Hagel, M. Barbui, C. Bottosso, A. Bonasera, J. B. Natowitz, E. J. Kim, T. Materna, L. Qin, P. K. Sahu, K. J. Schmidt, S. Wuenschel, and H. Zheng. Novel determination of density, temperature, and symmetry energy for nuclear multifragmentation through primary fragment-yield reconstruction. Physical Review C, 89(2):021601, February 2014.

[49] W Lin, J Wang, and G Q Xiao. Experimental reconstruction of primary hot isotopes and characteristic properties of the fragmenting source in heavy-ion reactions near the Fermi energy. Physical Review C, 044603:1–11, 2014.

[50] P. Marini, A. Bonasera, A. McIntosh, R. Tripathi, S. Galanopoulos, K. Hagel, L. Heilborn, Z. Kohley, L. W. May, M. Mehlman, S. N. Soisson, G. A. Souliotis, D. V. Shetty, W. B. Smith, B. C. Stein, S. Wuenschel, and S. J. Yennello. Constraining the symmetry term in the nuclear equation of state at subsaturation densities and finite temperatures. Physical Review C, 85(3):034617, March 2012.

[51] J. B. Natowitz, G. Röpke, S. Typel, D. Blaschke, A. Bonasera, K. Hagel, T. Klähn, S. Kowalski, L. Qin, S. Shlomo, R. Wada, and H. H. Wolter. Symmetry Energy of Dilute Warm Nuclear Matter. Physical Review Letters, 104(20):202501, May 2010.

[52] J. Piekarewicz. Symmetry energy constraints from giant resonances: A relativistic mean-field theory overview. The European Physical Journal A, 50(2):25, February 2014.

[53] P. Russotto, P.Z. Wu, M. Zoric, M. Chartier, Y. Leifels, R.C. Lemmon, Q. Li, J. ukasik, A. Pagano, P. Pawowski, and W. Trautmann. Symmetry energy from elliptic flow in 197Au+197Au. Physics Letters B, 697(5):471–476, March 2011.

[54] D. V. Shetty, S. J. Yennello, A. S. Botvina, G. A. Souliotis, M. Jandel, E. Bell,

A. Keksis, S. Soisson, B. Stein, and J. Iglio. Symmetry energy and the isospin dependent equation of state. Physical Review C, 70(1):011601, July 2004.

[55] D.V. Shetty, S.J. Yennello, and G.A. Souliotis. Constraining the density dependence of the symmetry energy in the nuclear equation of state using heavy ion beams. Nuclear Instruments and Methods in Physics Research Section B: Beam Interactions with Materials and Atoms, 261(1-2):990–992, August 2007.

[56] G. A. Souliotis, D. V. Shetty, A. Keksis, E. Bell, M. Jandel, M. Veselsky, and S. J. Yennello. Heavy-residue isoscaling as a probe of the symmetry energy of hot fragments. Physical Review C, 73(2):024606, February 2006.

[57] M. B. Tsang, J. R. Stone, F. Camera, P. Danielewicz, S. Gandolfi, K. Hebeler, C. J. Horowitz, Jenny Lee, W. G. Lynch, Z. Kohley, R. Lemmon, P. Möller, T. Murakami, S. Riordan, X. Roca-Maza, F. Sammarruca, A. W. Steiner, I. Vidaña, and S. J. Yennello. Constraints on the symmetry energy and neutron skins from experiments and theory. Physical Review C, 86(1):015803, July 2012.

[58] Yingxun Zhang, D. D. S. Coupland, P. Danielewicz, Zhuxia Li, Hang Liu, Fei Lu, W. G. Lynch, and M. B. Tsang. Influence of in-medium N N cross sections, symmetry potential, and impact parameter on isospin observables. Physical Review C, 85(2):024602, February 2012.

[59] M. A. Famiano, T. Liu, W. G. Lynch, M. Mocko, A. M. Rogers, M. B. Tsang, M. S. Wallace, R. J. Charity, S. Komarov, D. G. Sarantites, L. G. Sobotka, and G. Verde. Neutron and Proton Transverse Emission Ratio Measurements and the Density Dependence of the Asymmetry Term of the Nuclear Equation of State. Physical Review Letters, 97(5):052701, August 2006.

[60] He-lei Liu, Gao-Chan Yong, and De-Hua Wen. Decomposition of the sensitivity of the symmetry energy observables. Physical Review C, 91(4):044609, April

2015.

[61] C. W. Ma, J. Yu, X. M. Bai, Y. L. Zhang, H. L. Wei, and S. S. Wang. Isobaric yield ratio difference and neutron density difference in calcium isotopes. Physical Review C, 89(5):057602, May 2014.

[62] Swagata Mallik and Gargi Chaudhuri. Effect of particle fluctuation on isoscaling and isobaric yield ratio of nuclear multifragmentation. Physics Letters B, 727(1-3):282–286, November 2013.

[63] Li Ou, Min Liu, and Zhuxia Li. Sensitive dependence of isotope and isobar distributions of limiting temperatures on the symmetry energy. Physical Review C, 89(1):011001, January 2014.

[64] Gargi Chaudhuri and Swagata Mallik. Effect of secondary decay on isoscaling: Results from the canonical thermodynamical model. Nuclear Physics A, 849(1):190–202, January 2011.

[65] S. Galanopoulos, G.A. Souliotis, A.L. Keksis, M. Veselsky, Z. Kohley, L.W. May, D.V. Shetty, S.N. Soisson, B.C. Stein, S. Wuenschel, and S.J. Yennello. Isoscaling of mass reconstructed quasiprojectiles from collisions in the Fermi energy regime. Nuclear Physics A, 837(3-4):145–162, June 2010.

[66] S. Kowalski, J. B. Natowitz, S. Shlomo, R. Wada, K. Hagel, J. Wang, T. Materna, Z. Chen, Y. G. Ma, L. Qin, A. S. Botvina, D. Fabris, M. Lunardon, S. Moretto, G. Nebbia, S. Pesente, V. Rizzi, G. Viesti, M. Cinausero, G. Prete, T. Keutgen, Y. El Masri, Z. Majka, and A. Ono. Experimental determination of the symmetry energy of a low density nuclear gas. Physical Review C, 75(1):014601, January 2007.

[67] Akira Ono, P. Danielewicz, W. Friedman, W. Lynch, and M. Tsang. Isospin fractionation and isoscaling in dynamical simulations of nuclear collisions. Physical Review C, 68(5):051601, November 2003.

[68] G. A. Souliotis, P. N. Fountas, M. Veselsky, S. Galanopoulos, Z. Kohley, A. McIntosh, S. J. Yennello, and A. Bonasera. Isoscaling of heavy projectile residues and N / Z equilibration in peripheral heavy-ion collisions below the Fermi energy. Physical Review C, 90(6):064612, December 2014.

[69] M. Veselsky, G. Souliotis, and M. Jandel. Isoscaling studies of fission: A sensitive probe into the dynamics of scission. Physical Review C, 69(4):044607, April 2004.

[70] S. Wuenschel, R. Dienhoffer, G. a. Souliotis, S. Galanopoulos, Z. Kohley, K. Hagel, D. V. Shetty, K. Huseman, L. W. May, S. N. Soisson, B. C. Stein, a. L. Caraley, and S. J. Yennello. Isoscaling of fragments with Z=1-17 from reconstructed quasiprojectiles. Physical Review C, 79(6):061602, June 2009.

[71] Fu Yao, Fang De-Qing, Ma Yu-Gang, Cai Xiang-Zhou, Tian Wen-Dong, Wang Hong-Wei, and Guo Wei. Isoscaling Behavior in 48,40 Ca+ 9 Be Collisions at Intermediate Energy Investigated by the HIPSE Model. Chinese Physics Letters, 26(8):082503, August 2009.

[72] P. Zhou, W. D. Tian, Y. G. Ma, X. Z. Cai, D. Q. Fang, and H. W. Wang. Influence of statistical sequential decay on isoscaling and symmetry energy coefficient in a gemini simulation. Physical Review C, 84(3):037605, September 2011.

[73] V. Baran, M. Colonna, and M. Di Toro. Neck fragmentation reaction mechanism. Nuclear Physics A, 730(3-4):329–354, January 2004.

[74] Lie-Wen Chen, Che Ming Ko, and Bao-An Li. Determination of the Stiffness of the Nuclear Symmetry Energy from Isospin Diffusion. Physical Review Letters, 94(3):032701, January 2005.

[75] E. Galichet, M. Rivet, B. Borderie, M. Colonna, R. Bougault, A. Chbihi, R. Dayras, D. Durand, J. Frankland, D. Guinet, P. Lautesse, N. Neindre,

O. Lopez, L. Manduci, M. Pârlog, E. Rosato, B. Tamain, E. Vient, C. Volant, and J. Wieleczko. Isospin diffusion in Ni58-induced reactions at intermediate energies. I. Experimental results. Physical Review C, 79(6):064614, June 2009.

[76] Z. Y. Sun, M. B. Tsang, W. G. Lynch, G. Verde, F. Amorini, L. Andronenko, M. Andronenko, G. Cardella, M. Chatterje, P. Danielewicz, E. De Filippo, P. Dinh, E. Galichet, E. Geraci, H. Hua, E. La Guidara, G. Lanzalone, H. Liu, F. Lu, S. Lukyanov, C. Maiolino, A. Pagano, S. Piantelli, M. Papa, S. Pirrone, G. Politi, F. Porto, F. Rizzo, P. Russotto, D. Santonocito, and Y. X. Zhang. Isospin diffusion and equilibration for Sn+Sn collisions at E/A=35 MeV. Physical Review C, 82(5):051603, November 2010.

[77] Hs Xu, Mb Tsang, Tx Liu, Xd Liu, Wg Lynch, Wp Tan, Vander Molen A, G Verde, A Wagner, Hf Xi, Ck Gelbke, L Beaulieu, B Davin, Y Larochelle, T Lefort, de Souza RT, R Yanez, Ve Viola, Rj Charity, and Lg Sobotka. Isospin fractionation in nuclear multifragmentation. Physical review letters, 85(4):716–9, July 2000.

[78] Zachary Wayne Kohley. Transverse Collective Flow and Emission Order of Mid-Rapidity Fragments in Fermi Energy Heavy Ion Collisions. PhD thesis, Texas A&M University, 2010.

[79] X. Liu, W. Lin, R. Wada, M. Huang, Z. Chen, G. Q. Xiao, S. Zhang, R. Han, M. H. Zhao, P. Ren, Z. Jin, J. Liu, F. Shi, J. B. Natowitz, A. Bonasera, K. Hagel, H. Zheng, M. Barbui, and K. Schmidt. Mass dependence of transverse flow in heavy ion collisions at intermediate energies. Physical Review C, 90(1):014604, July 2014.

[80] P. Russotto, M. D. Cozma, A. Le Fèvre, Y. Leifels, R. Lemmon, Q. Li, J. ukasik, and W. Trautmann. Flow probe of symmetry energy in relativistic heavy-ion reactions. The European Physical Journal A, 50(2):38, February 2014.

[81] L. Scalone, M. Colonna, and M. Di Toro. Transverse flows in charge asymmetric collisions. Physics Letters B, 461(1-2):9–14, August 1999.

[82] M. Di Toro, A. Olmi, and R. Roy. Neck dynamics. The European Physical Journal A, 30(1):65–70, October 2006.

[83] S. Hudan, R. Alfaro, L. Beaulieu, B. Davin, Y. Larochelle, T. Lefort, V. E. Viola, H. Xu, R. Yanez, R. T. de Souza, R. J. Charity, L. G. Sobotka, T. X. Liu, X. D. Liu, W. G. Lynch, R. Shomin, W. P. Tan, M. B. Tsang, A. Vander Molen, A. Wagner, and H. F. Xi. Interplay of initial deformation and Coulomb proximity on nuclear decay. Physical Review C, 70(3):031601, September 2004.

[84] J. Lukasik, J. Benlliure, V. Métivier, E. Plagnol, B. Tamain, M. Assenard, G. Auger, Ch. O. Bacri, E. Bisquer, B. Borderie, R. Bougault, R. Brou, Ph. Buchet, J. L. Charvet, A. Chbihi, J. Colin, D. Cussol, R. Dayras, A. Demeyer, D. Doré, D. Durand, E. Gerlic, S. Germain, D. Gourio, D. Guinet, P. Lautesse, J. L. Laville, J. F. Lecolley, A. Le Fèvre, T. Lefort, R. Legrain, O. Lopez, M. Louvel, N. Marie, L. Nalpas, M. Parlog, J. Péter, O. Politi, A. Rahmani, T. Reposeur, M. F. Rivet, E. Rosato, F. Saint-Laurent, M. Squalli, J. C. Steckmeyer, M. Stern, L. Tassan-Got, E. Vient, C. Volant, J. P. Wieleczko, M. Colonna, F. Haddad, Ph. Eudes, T. Sami, and F. Sebille. Dynamical effects and intermediate mass fragment production in peripheral and semicentral collisions of Xe+Sn at 50 MeV/nucleon. Physical Review C, 55(4):1906–1916, April 1997.

[85] A. B. McIntosh, S. Hudan, J. Black, D. Mercier, C. J. Metelko, R. Yanez, R. T. de Souza, A. Chbihi, M. Famiano, M. O. Frégeau, J. Gauthier, J. Moisan, R. Roy, S. Bianchin, C. Schwarz, and W. Trautmann. Short-lived binary splits of an excited projectile-like fragment induced by transient deformation. Physical Review C, 81(3):034603, March 2010.

[86] C. P. Montoya, W. G. Lynch, D. R. Bowman, G. F. Peaslee, N. Carlin, R. T. de Souza, C. K. Gelbke, W. G. Gong, Y. D. Kim, M. A. Lisa, L. Phair, M. B. Tsang, J. B. Webster, C. Williams, N. Colonna, K. Hanold, M. A. McMahan, G. J. Wozniak, and L. G. Moretto. Fragmentation of Necklike Structures. Physical Review Letters, 73(23):3070–3073, December 1994.

[87] J. Tõke, B. Lott, S.P. Baldwin, B.M. Quednau, W.U. Schröder, L.G. Sobotka, J. Barreto, R.J. Charity, L Gallamore, D.G. Sarantites, D.W. Stracener, and R.T. De Souza. Dynamical production of intermediate-mass fragments in peripheral 209Bi+136Xe collisions at. Nuclear Physics A, 583:519–524, February 1995.

[88] V. Baran, M. Colonna, M. Di Toro, M. Zielinska-Pfabé, and H. H. Wolter. Isospin transport at Fermi energies. Physical Review C, 72(6):6, December 2005.

[89] M. DI TORO, M. COLONNA, C. RIZZO, and V. BARAN. THE DYNAMICAL DIPOLE RADIATION IN DISSIPATIVE COLLISIONS WITH EXOTIC BEAMS. International Journal of Modern Physics E, 17(01):110–119, January 2008.

[90] V. Baran, M. Colonna, M. Di Toro, V. Greco, M. Zielinska-Pfabé, and H.H. Wolter. Isospin effects in nuclear fragmentation. Nuclear Physics A, 703(3-4):603–632, June 2002.

[91] E. Galichet, M. Colonna, B. Borderie, and M. Rivet. Isospin diffusion in Ni58-induced reactions at intermediate energies. II. Dynamical simulations. Physical Review C, 79(6):064615, June 2009.

[92] Lie-Wen Chen, Che Ming Ko, Bao-an Li, and Gao-Chan Yong. Probing the Nuclear Symmetry Energy with Heavy-Ion Reactions Induced by Neutron-Rich Nuclei. Frontiers of Physics in China, 2(3):29, April 2007.

[93] D. Thériault, J. Gauthier, F. Grenier, F. Moisan, C. St-Pierre, R. Roy, B. Davin, S. Hudan, T. Paduszynski, R. T. de Souza, E. Bell, J. Garey, J. Iglio, A. L. Keksis, S. Parketon, C. Richers, D. V. Shetty, S. N. Soisson, G. A. Souliotis, B. C. Stein, and S. J. Yennello. Neutron-to-proton ratios of quasiprojectile and midrapidity emission in the Zn 64 + Zn 64 reaction at 45 MeV/nucleon. Physical Review C, 74(5):051602, November 2006.

[94] S. Hudan and R. T. DeSouza. Timescale for isospin equilibration in projectile breakup. The European Physical Journal A, 50(2):36, February 2014.

[95] S. Piantelli, P. R. Maurenzig, A. Olmi, L. Bardelli, M. Bini, G. Casini, A. Mangiarotti, G. Pasquali, G. Poggi, and A. A. Stefanini. Distinctive features of Coulomb-related emissions in peripheral heavy ion collisions at Fermi energies. Physical Review C, 76(6):061601, December 2007.

[96] S. Barlini, S. Piantelli, G. Casini, P. R. Maurenzig, A. Olmi, M. Bini, S. Carboni, G. Pasquali, G. Poggi, a. a. Stefanini, R. Bougault, E. Bonnet, B. Borderie, A. Chbihi, J. D. Frankland, D. Gruyer, O. Lopez, N. Le Neindre, M. Pârlog, M. F. Rivet, E. Vient, E. Rosato, G. Spadaccini, M. Vigilante, M. Bruno, T. Marchi, L. Morelli, M. Cinausero, M. Degerlier, F. Gramegna, T. Kozik, T. Twaróg, R. Alba, C. Maiolino, and D. Santonocito. Isospin transport in ˆ{84}Kr+ˆ{112,124}Sn collisions at Fermi energies. Physical Review C, 87(5):7, May 2013.

[97] S.J. Yennello, B. Young, J. Yee, J.A. Winger, J.S. Winfield, G.D. Westfall, A.Vander Molen, B.M. Sherrill, J. Shea, E. Norbeck, D.J. Morrissey, T. Li, E. Gualtieri, D. Craig, W. Benenson, and D. Bazin. The use of radioactive nuclear beams to study the equilibration of the degree of freedom in intermediate-energy heavy-ion reactions. Physics Letters B, 321(1-2):15–19, January 1994.

[98] Bao-An Li and Sherry J. Yennello. Isospin nonequilibrium in heavy-ion colli-

sions at intermediate energies. Physical Review C, 52(4):R1746–R1749, October 1995.

[99] H. Johnston, T. White, J. Winger, D. Rowland, B. Hurst, F. Gimeno-Nogues, D. O'Kelly, and S.J. Yennello. Isospin equilibration in the reaction 40Ar, 40Ca + 58Fe, 58Ni. Physics Letters B, 371(3-4):186–190, March 1996.

[100] H. Johnston, T. White, B. A. Li, E. Ramakrishnan, J. Winger, D. J. Rowland, B. Hurst, F. Gimeno-Nogues, D. O'Kelly, Y.-W. Lui, and S. J. Yennello. Isotopically resolved intermediate-mass fragment and light charged particle production from the reactions 40 Ar and 40 Ca with 58 Fe and 58 Ni at E beam = 33 and 45 MeV/nucleon. Physical Review C, 56(4):1972–1982, October 1997.

[101] F Rami, Y Leifels, de Schauenburg B, A Gobbi, B Hong, Jp Alard, A Andronic, R Averbeck, V Barret, Z Basrak, N Bastid, I Belyaev, A Bendarag, G Berek, R Caplar, N Cindro, P Crochet, A Devismes, P Dupieux, M Dzelalija, M Eskef, C Finck, Z Fodor, H Folger, L Fraysse, and A Genoux-Lubain. Isospin tracing: A probe of nonequilibrium in central heavy-Ion collisions. Physical review letters, 84(6):1120–3, February 2000.

[102] G. Ademard, B. Borderie, A. Chbihi, O. Lopez, P. Napolitani, M. F. Rivet, M. Boisjoli, E. Bonnet, R. Bougault, J. D. Frankland, E. Galichet, D. Guinet, M. Kabtoul, G. Lehaut, P. Lautesse, M La Commara, N Le Neindre, P. Marini, P Pawlowski, E. Rosato, R. Roy, E Spadaccini, E. Vient, M. Vigilante, J. P. Wieleczko, D. Gruyer, M. La Commara, N. Le Neindre, M. Pârlog, P. Pawowski, and G. Spadaccini. Isospin effects and symmetry energy studies with INDRA. The European Physical Journal A, 50(2):33, February 2014.

[103] Z. Kohley and S. J. Yennello. Heavy-ion collisions: Direct and indirect probes of the density and temperature dependence of Esym. The European Physical Journal A, 50(2):31, February 2014.

[104] R. Planeta, S. H. Zhou, K. Kwiatkowski, W. G. Wilson, V. E. Viola, H. Breuer, D. Benton, F. Khazaie, R. J. McDonald, A. C. Mignerey, A. Weston-Dawkes, R. T. de Souza, J. R. Huizenga, and W. U. Schroder. N/Z equilibration in damped collisions induced by EA = 8.5 MeV 58Ni and 64 Ni on 238U. Physical Review C, 1988.

[105] W. U. Schroder and J. R. Huizenga. DAMPED HEAVY-ION COLLISIONS. Annual Review of Nuclear Science, 1977.

[106] W. U. Schröder, J. R. Birkelund, J. R. Huizenga, K. L. Wolf, and V. E. Viola. Interaction times for damped heavy-ion collisions. Physical Review C, 1977.

[107] M. B. Tsang, W. a. Friedman, C. K. Gelbke, W. G. Lynch, G. Verde, and H. S. Xu. Isotopic Scaling in Nuclear Reactions. Physical Review Letters, 86(22):5023–5026, May 2001.

[108] A. L. Keksis, L. W. May, G. a. Souliotis, M. Veselsky, S. Galanopoulos, Z. Kohley, D. V. Shetty, S. N. Soisson, B. C. Stein, R. Tripathi, S. Wuenschel, S. J. Yennello, and B. a. Li. Experimental studies of N/Z equilibration in peripheral collisions using fragment yield ratios. Physical Review C, 81(5):054602, May 2010.

[109] Elizabeth Bell. N/Z Equilibration. PhD thesis, Texas A&M University, 2005.

[110] R. Ghetti and J. Helgesson. Isospin effects in two-particle correlation functions: A probe for the isospin dependence of the nuclear equation of state. Nuclear Physics A, 752:480–483, April 2005.

[111] B. Yilmaz, S. Ayik, D. Lacroix, and O. Yilmaz. Nucleon exchange in heavy-ion collisions within a stochastic mean-field approach. Physical Review C, 90(2):024613, August 2014.

[112] August Lawrence Keksis. N/Z EQUILIBRATION IN DEEP INELASTIC COLLISIONS AND THE FRAGMENTATION OF THE RESULTING

QUASIPROJECTILES. PhD thesis, Texas A&M University, 2007.

[113] Douglas John Rowland. A STUDY OF THE PROJECTILE FRAGMENTATION OF ISOBARIC NUCLEI. PhD thesis, Texas A&M University, 2000.

[114] S. Wuenschel, K. Hagel, R. Wada, J.B. Natowitz, S.J. Yennello, Z. Kohley, C. Bottosso, L.W. May, W.B. Smith, D.V. Shetty, B.C. Stein, S.N. Soisson, and G. Prete. NIMRODISiS, a versatile tool for studying the isotopic degree of freedom in heavy ion collisions. Nuclear Instruments and Methods in Physics Research Section A: Accelerators, Spectrometers, Detectors and Associated Equipment, 604(3):578–583, June 2009.

[115] Trace Sciences International Inc. www.tracesciences.com.

[116] Thanks to John Greene at the ANL Target Lab for fabriacation of the targets.

[117] R. Wada, T. Keutgen, K. Hagel, Y. Ma, J. Wang, M. Murray, L. Qin, P. Smith, J. Natowitz, R. Alfarro, J. Cibor, M. Cinausero, Y. Masri, D. Fabris, E. Fioretto, A. Keksis, S. Kowalski, M. Lunardon, A. Makeev, N. Marie, E. Martin, Z. Majka, A. Martinez-Davalos, A. Menchaca-Rocha, G. Nebbia, G. Prete, V. Rizzi, A. Ruangma, D. Shetty, G. Souliotis, P. Staszel, M. Veselsky, G. Viesti, E. Winchester, S. Yennello, W. Zipper, and A. Ono. Reaction dynamics and multifragmentation in Fermi energy heavy ion reactions. Physical Review C, 69(4):044610, April 2004.

[118] K Kwiatkowski, D.S Bracken, K.B Morley, J Brzychczyk, E Renshaw Foxford, K Komisarcik, V.E Viola, N.R Yoder, J Dorsett, J Poehlman, N Madden, and J Ottarson. The Indiana silicon sphere 4π charged-particle detector array. Nuclear Instruments and Methods in Physics Research Section A: Accelerators, Spectrometers, Detectors and Associated Equipment, 360(3):571–583, June 1995.

[119] R.P. Schmitt, L. Cooke, G. Derrig, D. Fabris, B. Hurst, J.B. Natowitz, G. Nebbia, D. O'Kelly, B.K. Srivastava, W. Turmel, D. Utley, H. Utsunomiya, and R. Wada. A flexible 4π neutron detector for in-beam studies: the Texas A&M neutron ball. Nuclear Instruments and Methods in Physics Research Section A: Accelerators, Spectrometers, Detectors and Associated Equipment, 354(2-3):487–495, January 1995.

[120] J. Pouthas, B. Borderie, R. Dayras, E. Plagnol, M.F. Rivet, F. Saint-Laurent, J.C. Steckmeyer, G. Auger, C.O. Bacri, S. Barbey, A. Barbier, A. Benkirane, J. Benlliure, B. Berthier, E. Bougamont, P. Bourgault, P. Box, R. Bzyl, B. Cahan, Y. Cassagnou, D. Charlet, J.L. Charvet, A. Chbihi, T. Clerc, N. Copinet, D. Cussol, M. Engrand, J.M. Gautier, Y. Huguet, O. Jouniaux, J.L. Laville, P. Le Botlan, A. Leconte, R. Legrain, P. Lelong, M. Le Guay, L. Martina, C. Mazur, P. Mosrin, L. Olivier, J.P. Passerieux, S. Pierre, B. Piquet, E. Plaige, E.C. Pollacco, B. Raine, A. Richard, J. Ropert, C. Spitaels, L. Stab, D. Sznajderman, L. Tassan-got, J. Tillier, M. Tripon, P. Vallerand, C. Volant, P. Volkov, J.P. Wieleczko, and G. Wittwer. INDRA, a 4π charged product detection array at GANIL. Nuclear Instruments and Methods in Physics Research Section A: Accelerators, Spectrometers, Detectors and Associated Equipment, 357(2-3):418–442, April 1995.

[121] B Davin, R.T de Souza, R Yanez, Y Larochelle, R Alfaro, H.S Xu, A Alexander, K Bastin, L Beaulieu, J Dorsett, G Fleener, L Gelovani, T Lefort, J Poehlman, R.J Charity, L.G Sobotka, J Elson, A Wagner, T.X Liu, X.D Liu, W.G Lynch, L Morris, R Shomin, W.P Tan, M.B Tsang, G Verde, and J Yurkon. LASSA: a large area silicon strip array for isotopic identification of charged particles. Nuclear Instruments and Methods in Physics Research Section A: Accelerators, Spectrometers, Detectors and Associated Equipment, 473(3):302–318, Novem-

ber 2001.

[122] Glenn F. Knoll. Radiation Detection and Measurement. John Wiley & Sons, Ann Arbor, 2000.

[123] William R. Leo. Techniques for Nuclear and Particle Physics Experiments. Spring-Verlag, New York, 1994.

[124] Pico Systems www.pico-systems.com.

[125] G.A. Souliotis, M. Veselsky, D.V. Shetty, L. Trache, and S.J. Yennello. Neutron-rich rare isotope production and studies of the N/Z degree of freedom in binary collisions at Fermi energies. Nuclear Physics A, 746:526–531, December 2004.

[126] Sara Katherine Wuenschel. Temperature and Scaling Studies from Projectile Fragmentation of 86,78Kr+64,58Ni at 35 MeV/A. PhD thesis, Texas A&M University, 2009.

[127] H. Hubert, F.; Bimbot, R.; Gauvin. Range and Stopping-Power Tables for 2.5-500 MeV/nucleon Heavy Ions in Solids. Atomic Data and Nuclear Data Tables, 46(1), 1990.

[128] L. Tassan-Got. A new functional for charge and mass identification in ΔEE telescopes. Nuclear Instruments and Methods in Physics Research Section B: Beam Interactions with Materials and Atoms, 194(4):503–512, October 2002.

[129] C. B. Das, S. Das Gupta, C. Gale, and Bao-An Li. Momentum dependence of symmetry potential in asymmetric nuclear matter for transport model calculations. Physical Review C, 67(3):034611, March 2003.

[130] Bao-An Li, Champak B. Das, Subal Das Gupta, and Charles Gale. Effects of momentum-dependent symmetry potential on heavy-ion collisions induced by neutron-rich nuclei. Nuclear Physics A, 735(3-4):563–584, May 2004.

[131] Bao-An Li and Lie-Wen Chen. Nucleon-nucleon cross sections in neutron-rich

matter and isospin transport in heavy-ion reactions at intermediate energies. Physical Review C, 72(6):064611, December 2005.

[132] P. Marini, A. Zarrella, A. Bonasera, G. Bonasera, P. Cammarata, L. Heilborn, Z. Kohley, J. Mabiala, L.W. May, A.B. McIntosh, A. Raphelt, G.a. Souliotis, and S.J. Yennello. Experimental determination of the quasi-projectile mass with measured neutrons. Nuclear Instruments and Methods in Physics Research Section A: Accelerators, Spectrometers, Detectors and Associated Equipment, 707:80–88, April 2013.

[133] R. Tripathi, A. Bonasera, S. Wuenschel, L. W. May, Z. Kohley, G. a. Souliotis, S. Galanopoulos, K. Hagel, D. V. Shetty, K. Huseman, S. N. Soisson, B. C. Stein, and S. J. Yennello. Analysis of fragment yield ratios in the nuclear phase transition. Physical Review C, 83(5):054609, May 2011.

[134] R. Tripathi, A. Bonasera, S. Wuenschel, L. W. May, Z. Kohley, P. Marini, A. Mcintosh, G. a. Souliotis, S. Galanopoulos, K. Hagel, D. V. Shetty, K. Huseman, S. N. Soisson, B. C. Stein, and S. J. Yennello. Role of Quasiprojectile Isospin Asymmetry in Nuclear Fragmentation. International Journal of Modern Physics E, 21(03):1250019, March 2012.

[135] A.B. McIntosh, A. Bonasera, P. Cammarata, K. Hagel, L. Heilborn, Z. Kohley, J. Mabiala, L.W. May, P. Marini, A. Raphelt, G.A. Souliotis, S. Wuenschel, A. Zarrella, and S.J. Yennello. Asymmetry dependence of the nuclear caloric curve. Physics Letters B, 719(4-5):337–340, February 2013.

[136] S. Wuenschel, A. Bonasera, L.W. May, G.a. Souliotis, R. Tripathi, S. Galanopoulos, Z. Kohley, K. Hagel, D.V. Shetty, K. Huseman, S.N. Soisson, B.C. Stein, and S.J. Yennello. Measuring the temperature of hot nuclear fragments. Nuclear Physics A, 843(1-4):1–13, October 2010.

[137] J.C. Steckmeyer, E. Genouin-Duhamel, E. Vient, J. Colin, D. Durand,

G. Auger, C.O. Bacri, N. Bellaize, B. Borderie, R. Bougault, B. Bouriquet, R. Brou, P. Buchet, J.L. Charvet, A. Chbihi, D. Cussol, R. Dayras, N. DeCesare, A. Demeyer, D. Doré, J.D. Frankland, E. Galichet, E. Gerlic, D. Guinet, S. Hudan, P. Lautesse, F. Lavaud, J.L. Laville, J.F. Lecolley, C. Leduc, R. Legrain, N. Le Neindre, O. Lopez, M. Louvel, A.M. Maskay, L. Nalpas, J. Normand, M. Pârlog, P. Pawowski, E. Plagnol, M.F. Rivet, E. Rosato, F. Saint-Laurent, G. Tbcaru, B. Tamain, L. Tassan-Got, O. Tirel, K. Turzo, M. Vigilante, C. Volant, and J.P. Wieleczko. Excitation energy and angular momentum of quasiprojectiles produced in the Xe+Sn collisions at incident energies between 25 and 50 MeV/nucleon. Nuclear Physics A, 686(1-4):537–567, April 2001.

[138] Massimo Papa, Toshiki Maruyama, and Aldo Bonasera. Constrained molecular dynamics approach to fermionic systems. Physical Review C, 64(2):024612, July 2001.

[139] M. Papa, G. Giuliani, and A. Bonasera. Constrained molecular dynamics II: An N-body approach to nuclear systems. Journal of Computational Physics, 208(2):403–415, September 2005.

[140] R.J. Charity, M.A. McMahan, G.J. Wozniak, R.J. McDonald, L.G. Moretto, D.G. Sarantites, L.G. Sobotka, G. Guarino, A. Pantaleo, L. Fiore, A. Gobbi, and K.D. Hildenbrand. Systematics of complex fragment emission in niobium-induced reactions. Nuclear Physics A, 483(2):371–405, June 1988.

[141] S N Soisson, A Botvina, G a Souliotis, B C Stein, L Heilborn, a L Keksis, Z Kohley, L W May, D V Shetty, S Wuenschel, and S J Yennello. Multifragmentation of reconstructed quasi-projectiles in the mass region A 30. Journal of Physics G: Nuclear and Particle Physics, 39(11):115104, November 2012.

[142] Y. G. Ma, K. Wang, Y. B. Wei, G. L. Ma, X. Z. Cai, J. G. Chen, D. Q Fang,

W. Guo, W. Q. Shen, W. D. Tian, and C. Zhong. Isoscaling in the lattice gas model. Physical Review C, 69(6):064610, June 2004.

[143] Akira Ono and Hisashi Horiuchi. Antisymmetrized molecular dynamics for heavy ion collisions. Progress in Particle and Nuclear Physics, 53(2):501–581, October 2004.

APPENDIX A

KINETIC ENERGY SPECTRA

Additional energy spectra similar to Figure 2.20 of Section 2.4. The kinetic energy spectra are shown for each ring of the NIMROD-ISiS array and each reaction system taken as part of this experiment (^{70}Zn,^{64}Ni+^{64}Zn and ^{64}Zn+^{70}Zn,^{64}Ni). The energy spectra for the ^{70}Zn+^{70}Zn, ^{64}Zn+^{64}Zn and ^{64}Ni+^{64}Ni systems taken by Z. Kohley can be found in Appendix B of his graduate thesis [78]. The energy spectra for the different elements are offset in order to allow each spectra to be viewed.

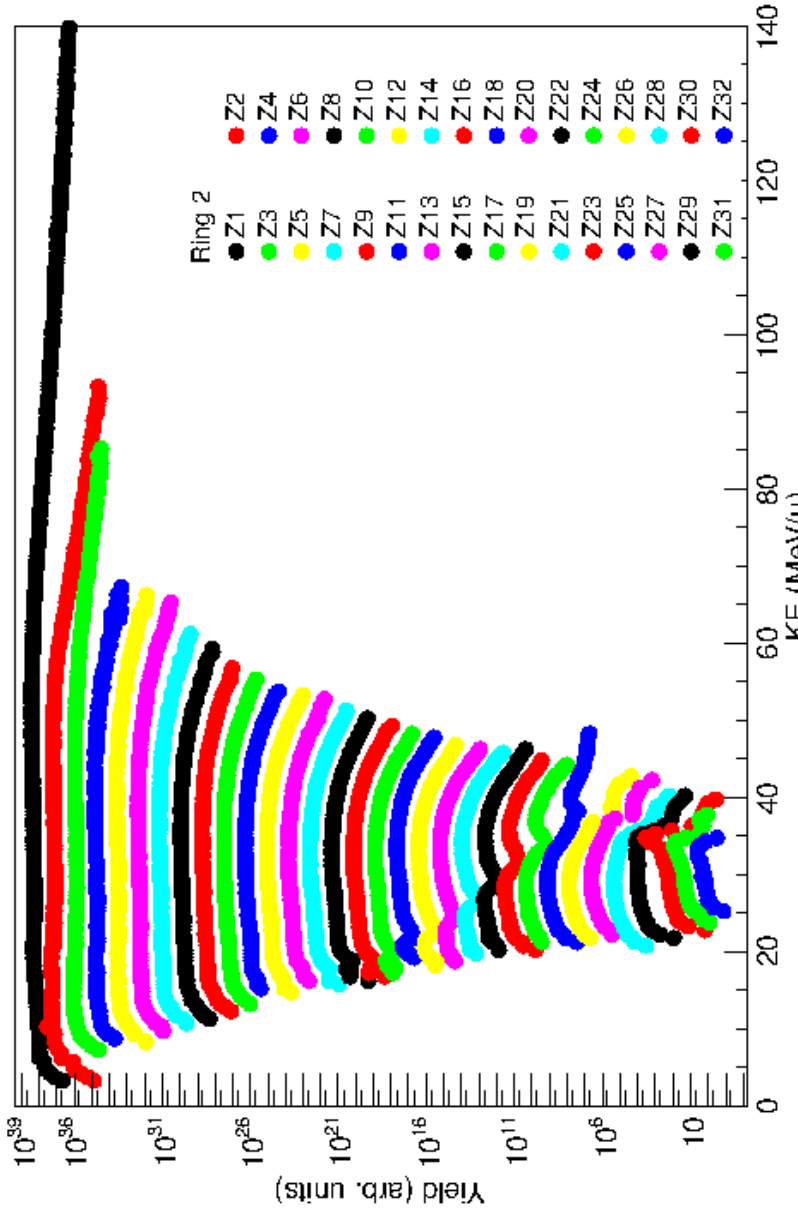

Figure A.1: Kinetic energy spectra for all elements in Ring 2 for the ^{70}Zn+^{64}Zn system.

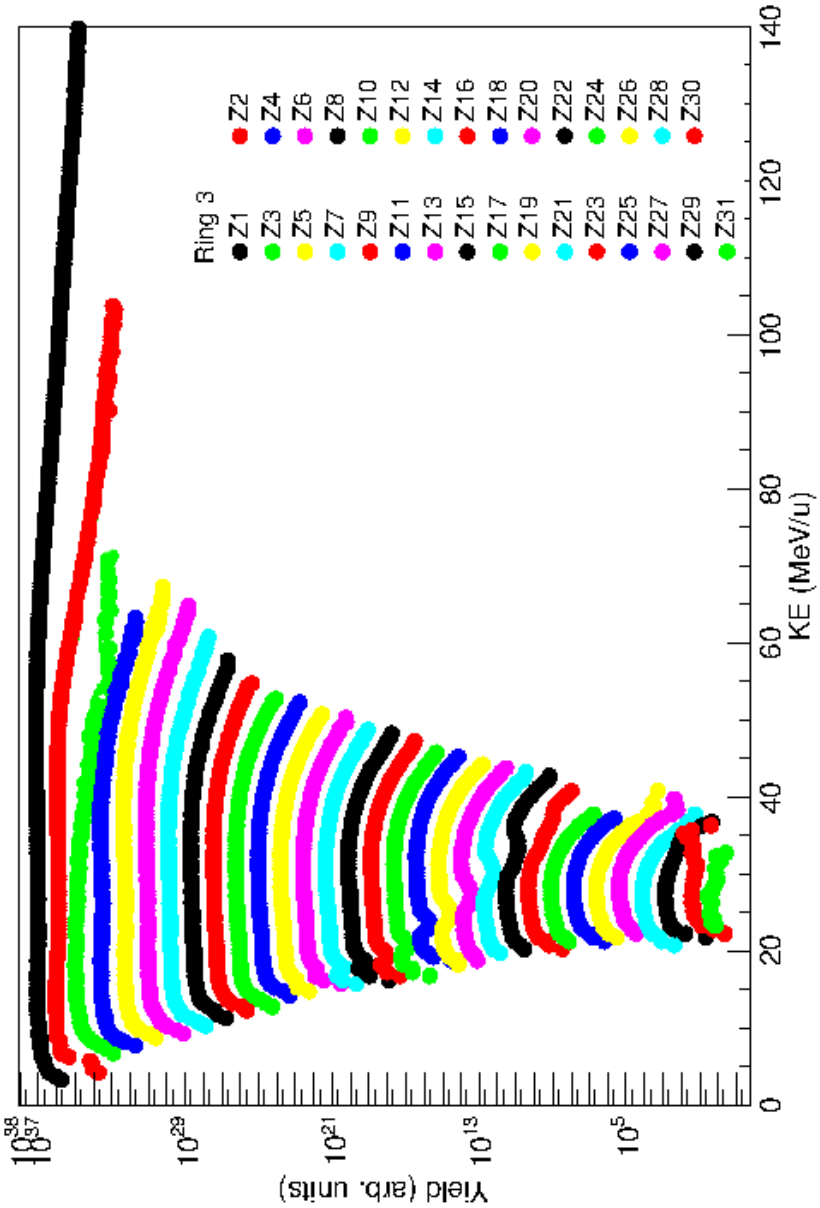

Figure A.2: Kinetic energy spectra for all elements in Ring 3 for the ^{70}Zn+^{64}Zn system.

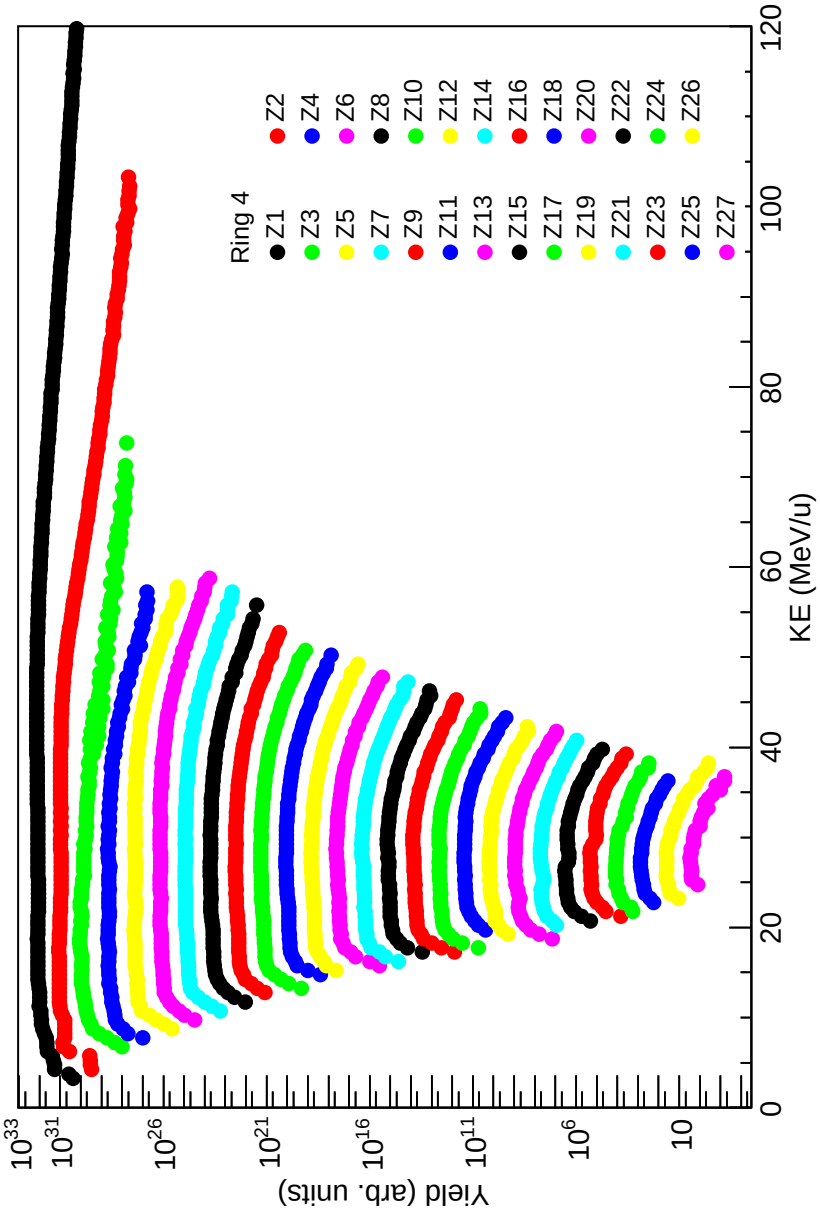

Figure A.3: Kinetic energy spectra for all elements in Ring 4 for the ^{70}Zn+^{64}Zn system.

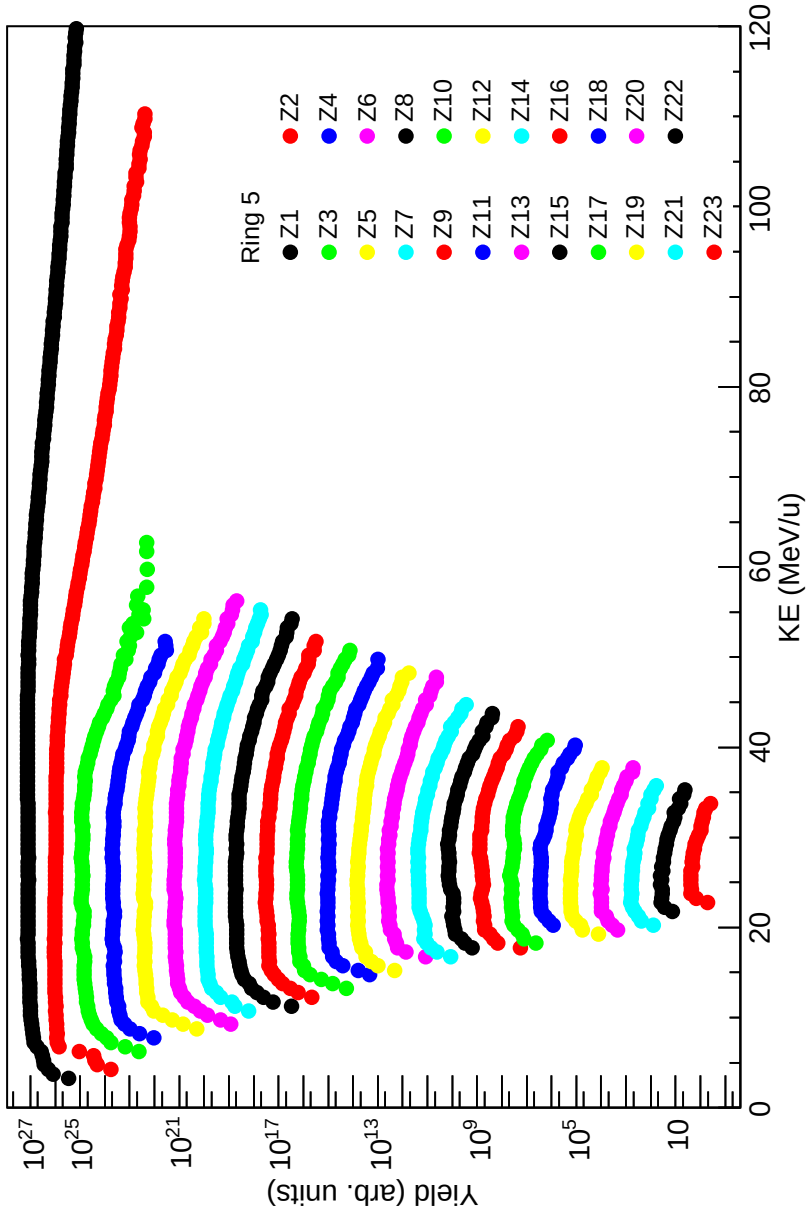

Figure A.4: Kinetic energy spectra for all elements in Ring 5 for the ^{70}Zn+^{64}Zn system.

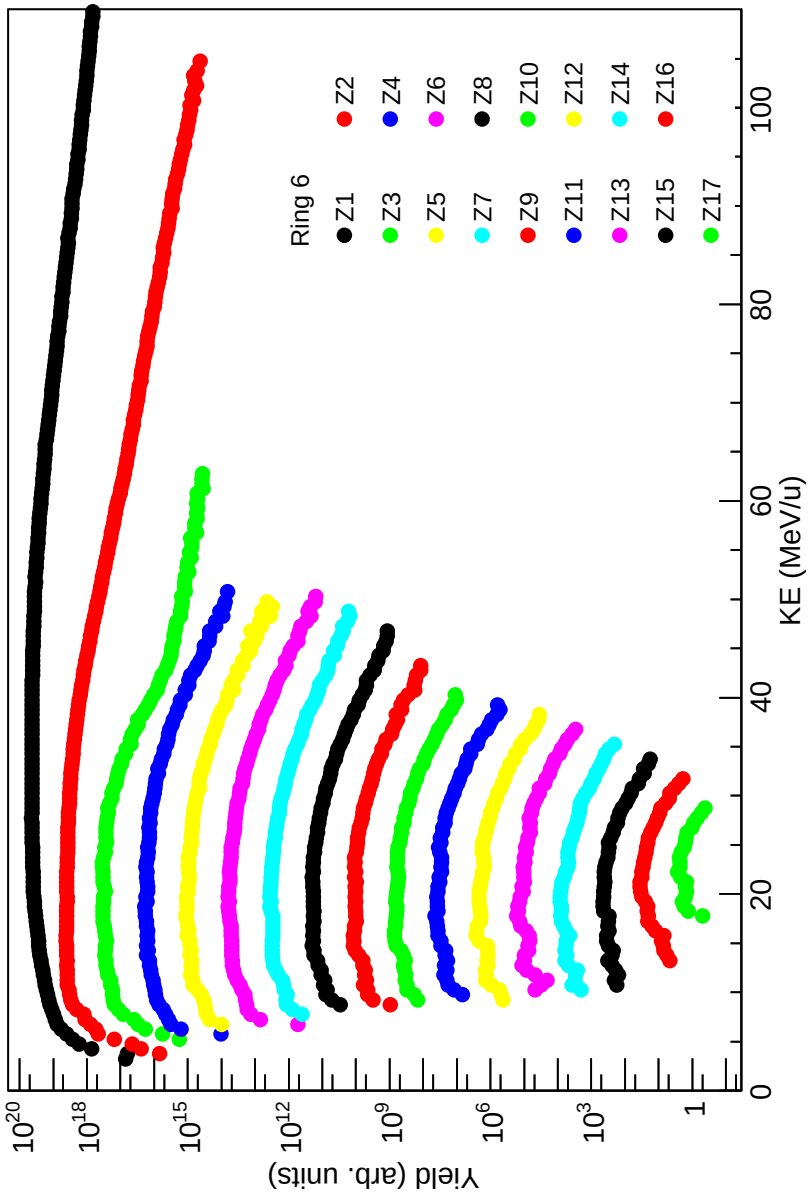

Figure A.5: Kinetic energy spectra for all elements in Ring 6 for the ^{70}Zn+^{64}Zn system.

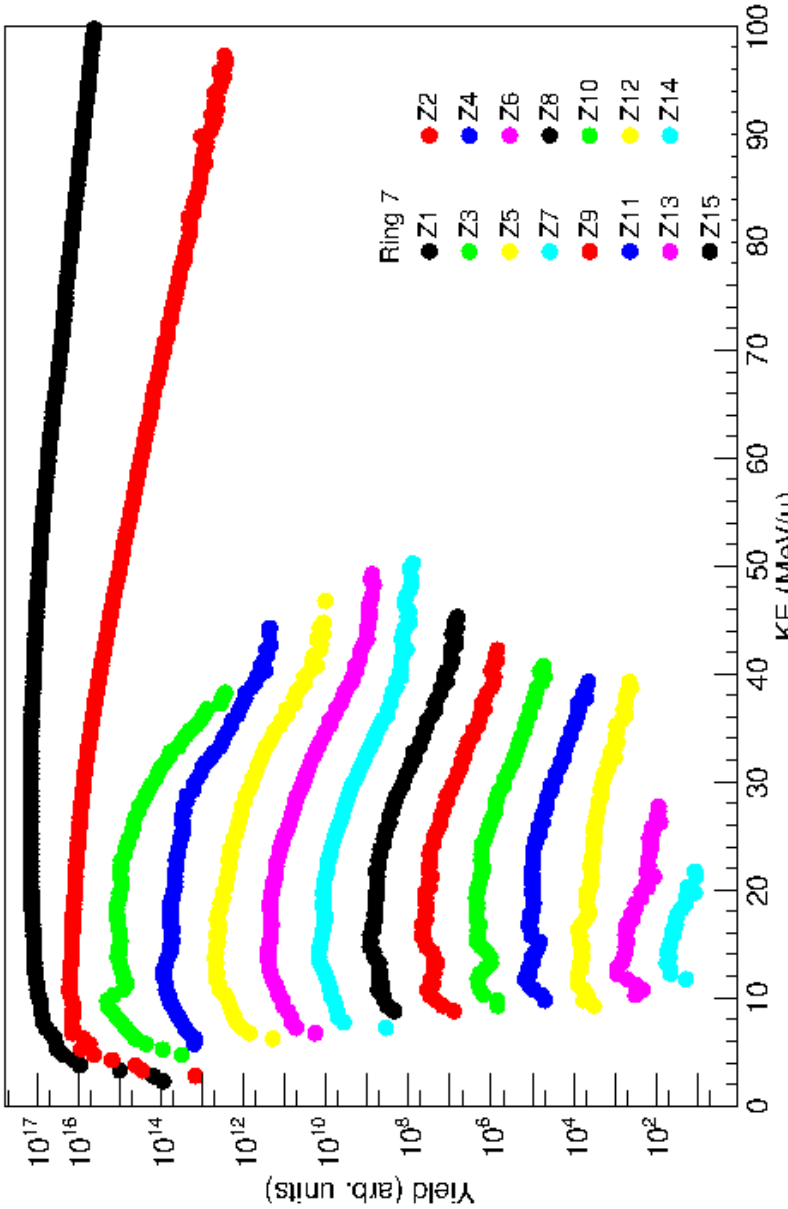

Figure A.6: Kinetic energy spectra for all elements in Ring 7 for the ^{70}Zn+^{64}Zn system.

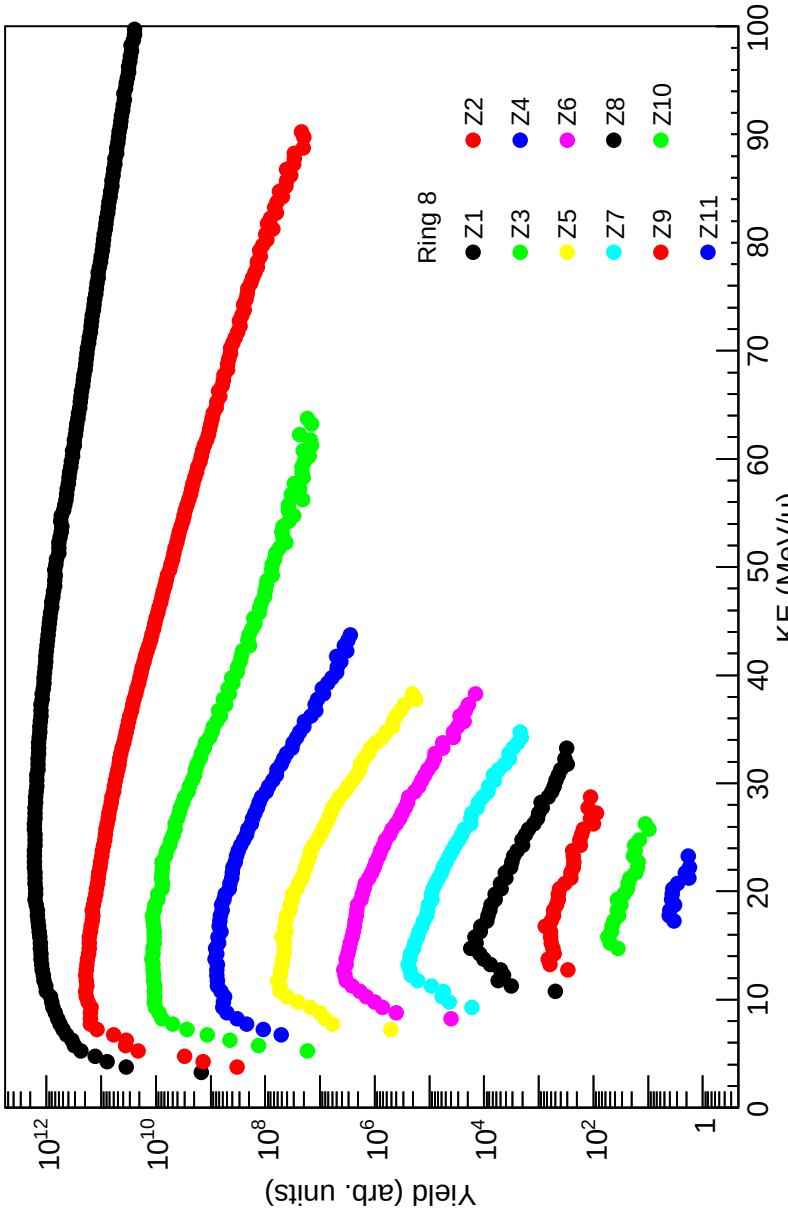

Figure A.7: Kinetic energy spectra for all elements in Ring 8 for the ^{70}Zn+^{64}Zn system.

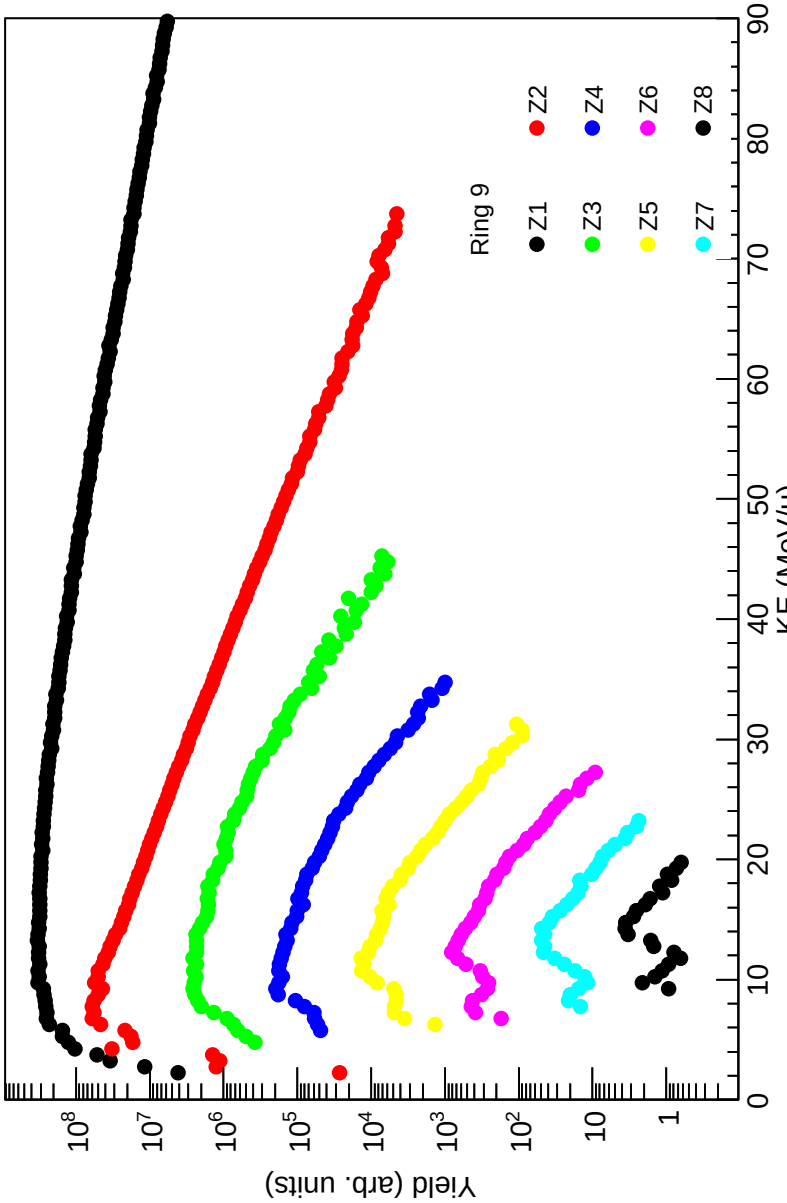

Figure A.8: Kinetic energy spectra for all elements in Ring 9 for the ^{70}Zn+^{64}Zn system.

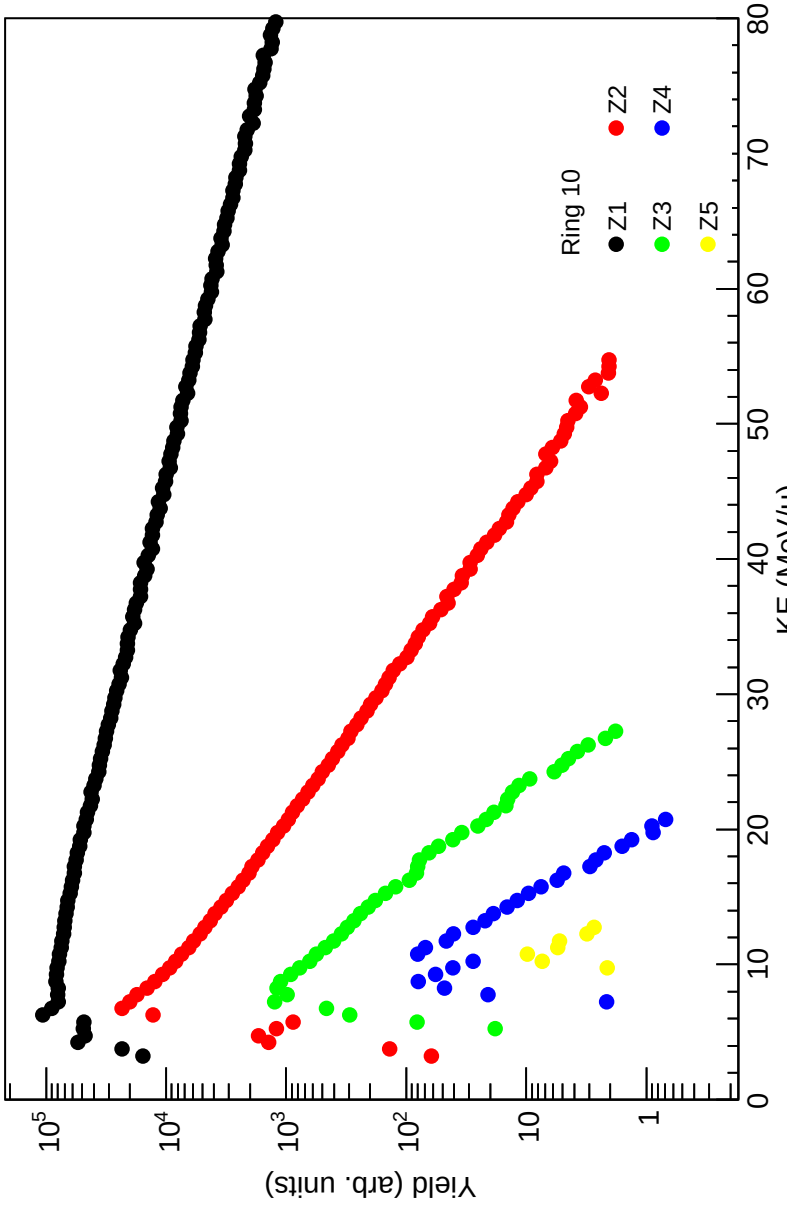

Figure A.9: Kinetic energy spectra for all elements in Ring 10 for the ^{70}Zn+^{64}Zn system.

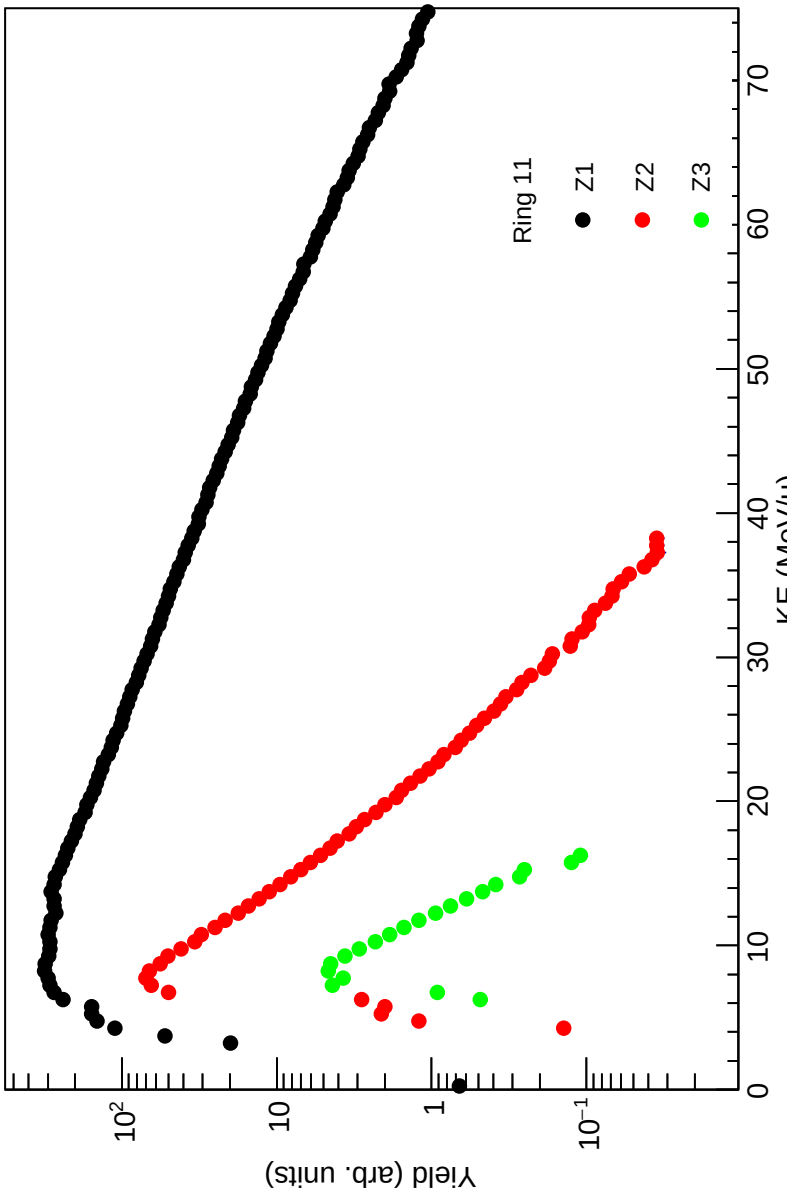

Figure A.10: Kinetic energy spectra for all elements in Ring 11 for the ^{70}Zn+^{64}Zn system.

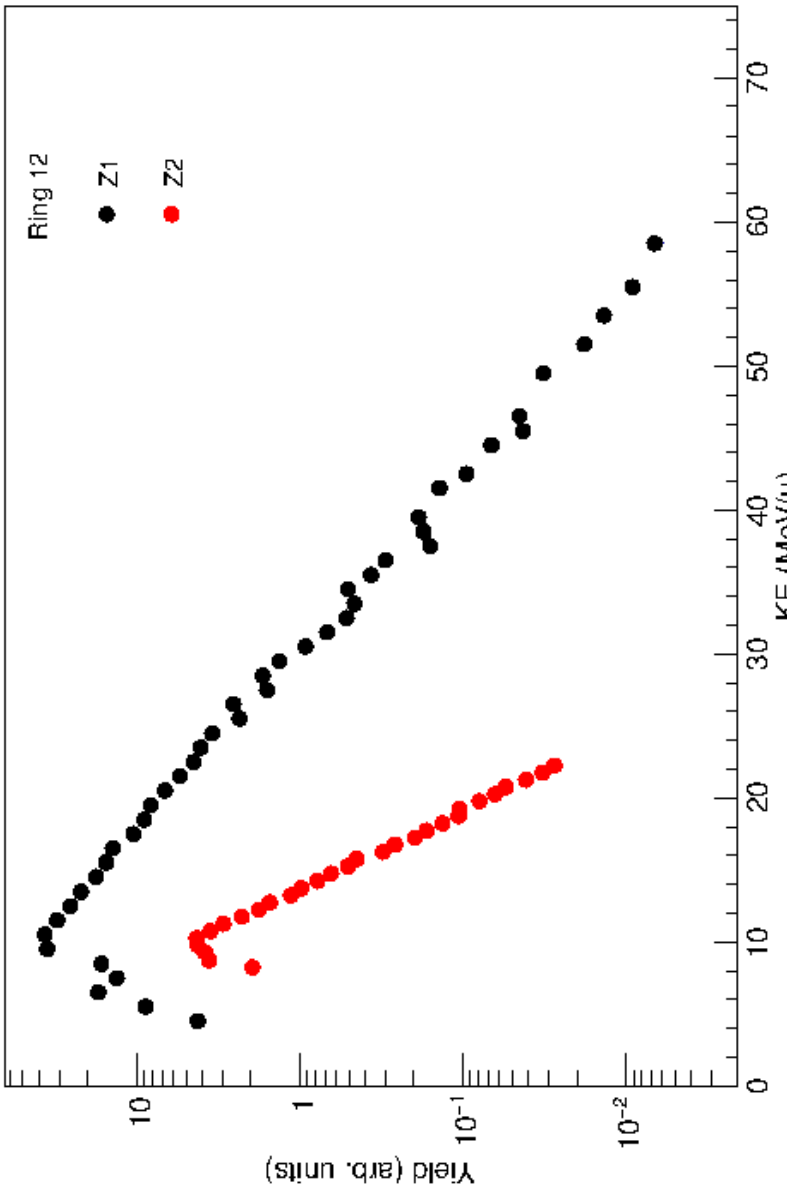

Figure A.11: Kinetic energy spectra for all elements in Ring 12 for the ^{70}Zn+^{64}Zn system.

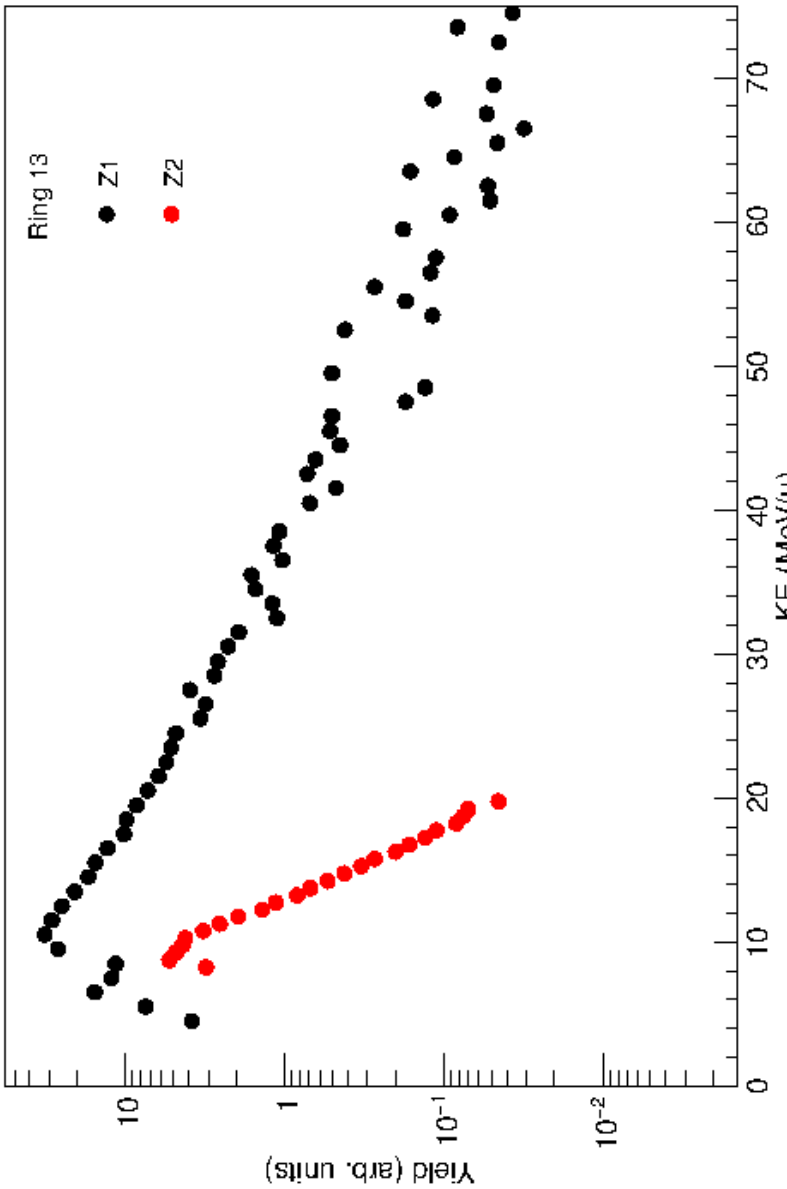

Figure A.12: Kinetic energy spectra for all elements in Ring 13 for the ^{70}Zn+^{64}Zn system.

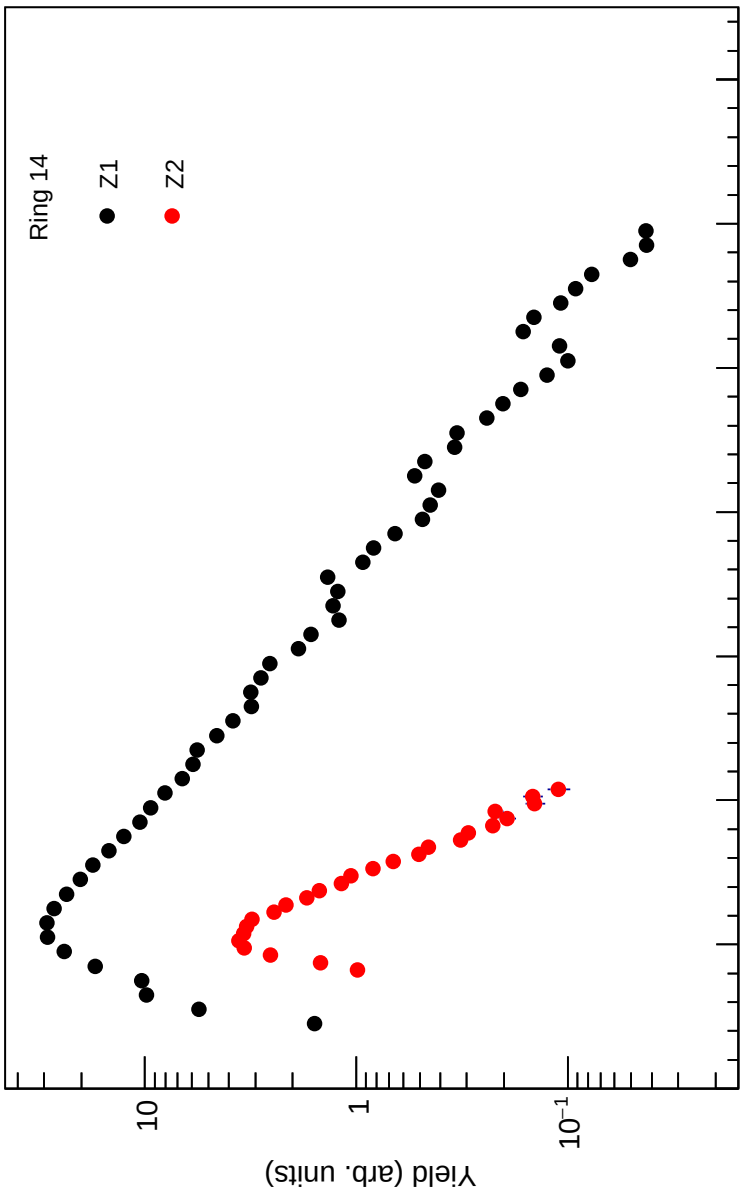

Figure A.13: Kinetic energy spectra for all elements in Ring 14 for the ^{70}Zn+^{64}Zn system.

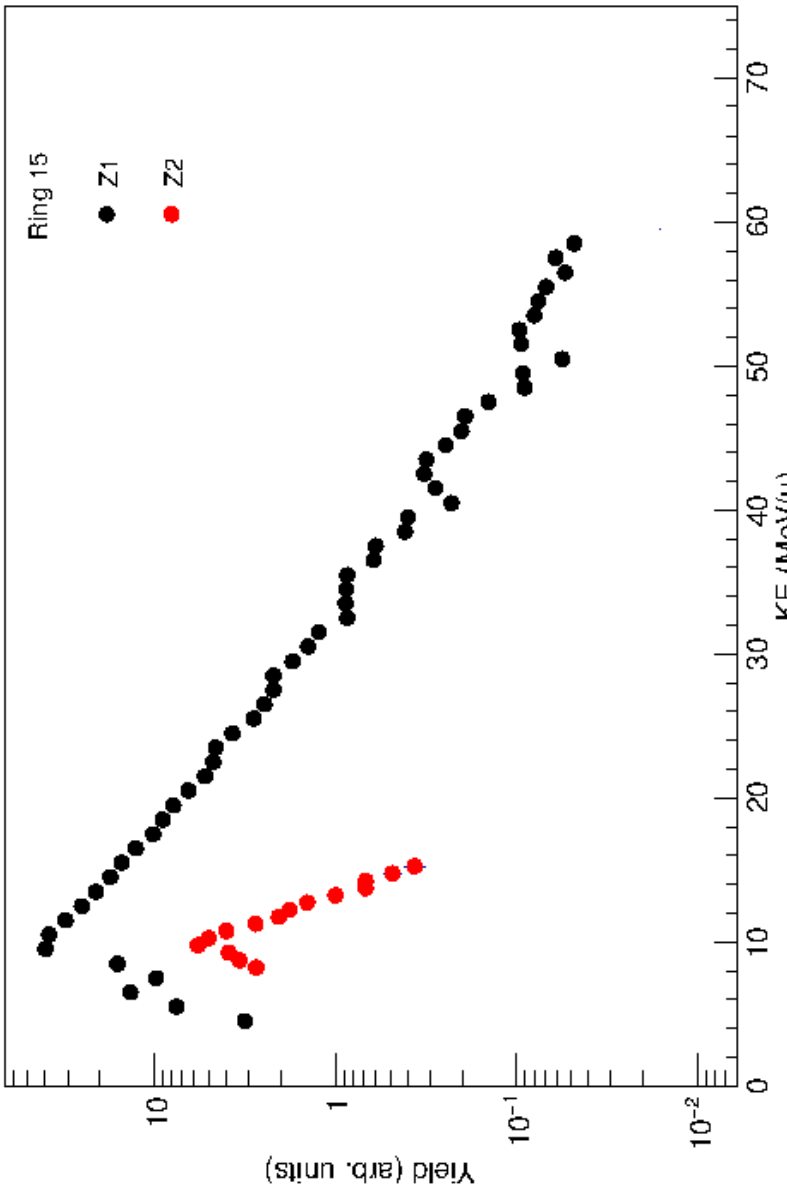

Figure A.14: Kinetic energy spectra for all elements in Ring 15 for the ^{70}Zn+^{64}Zn system.

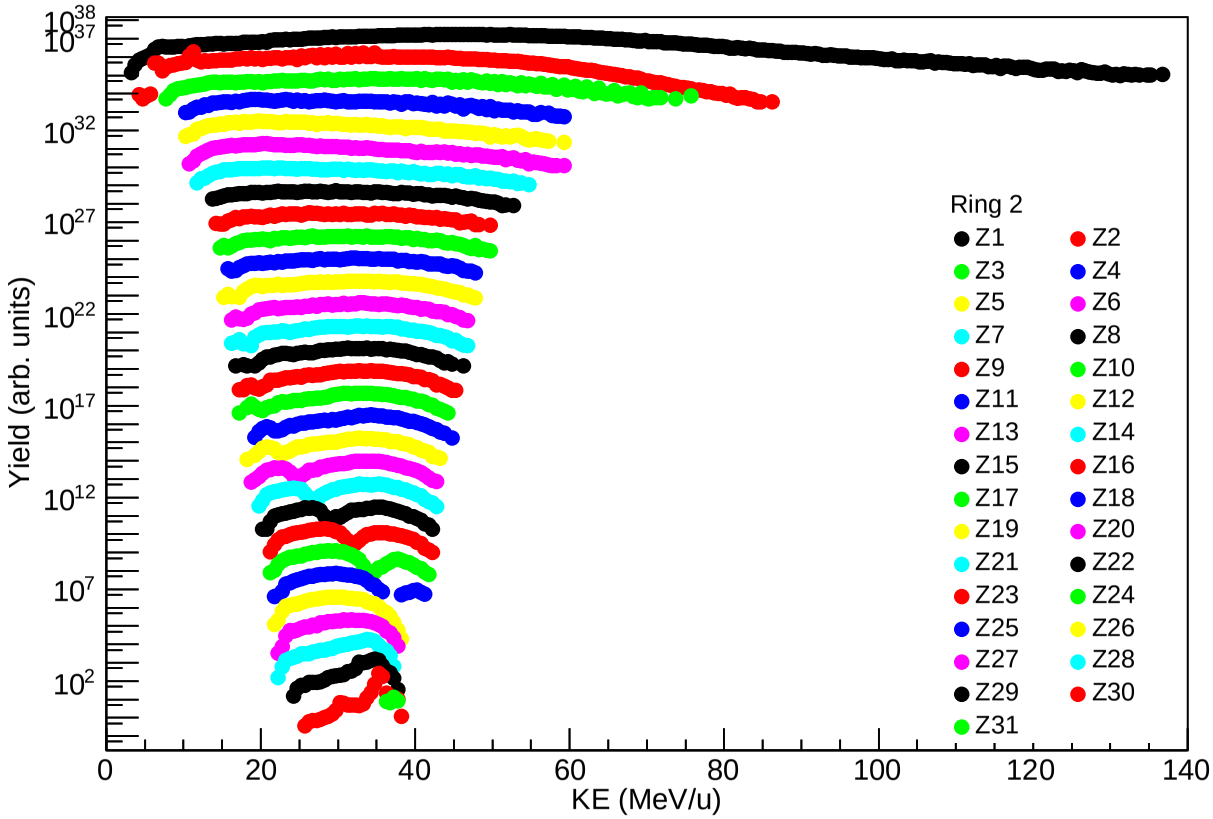

Figure A.15: Kinetic energy spectra for all elements in Ring 2 for the ^{64}Zn+^{70}Zn system.

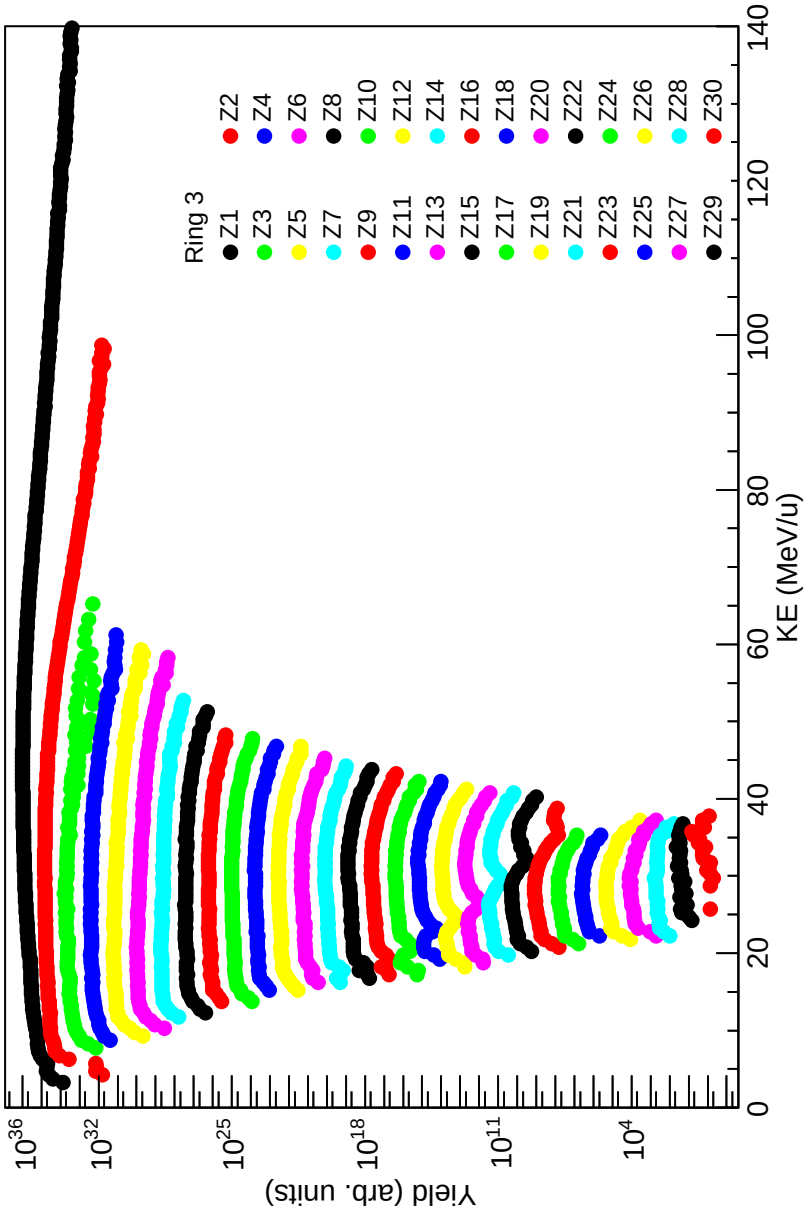

Figure A.16: Kinetic energy spectra for all elements in Ring 3 for the ^{64}Zn+^{70}Zn system.

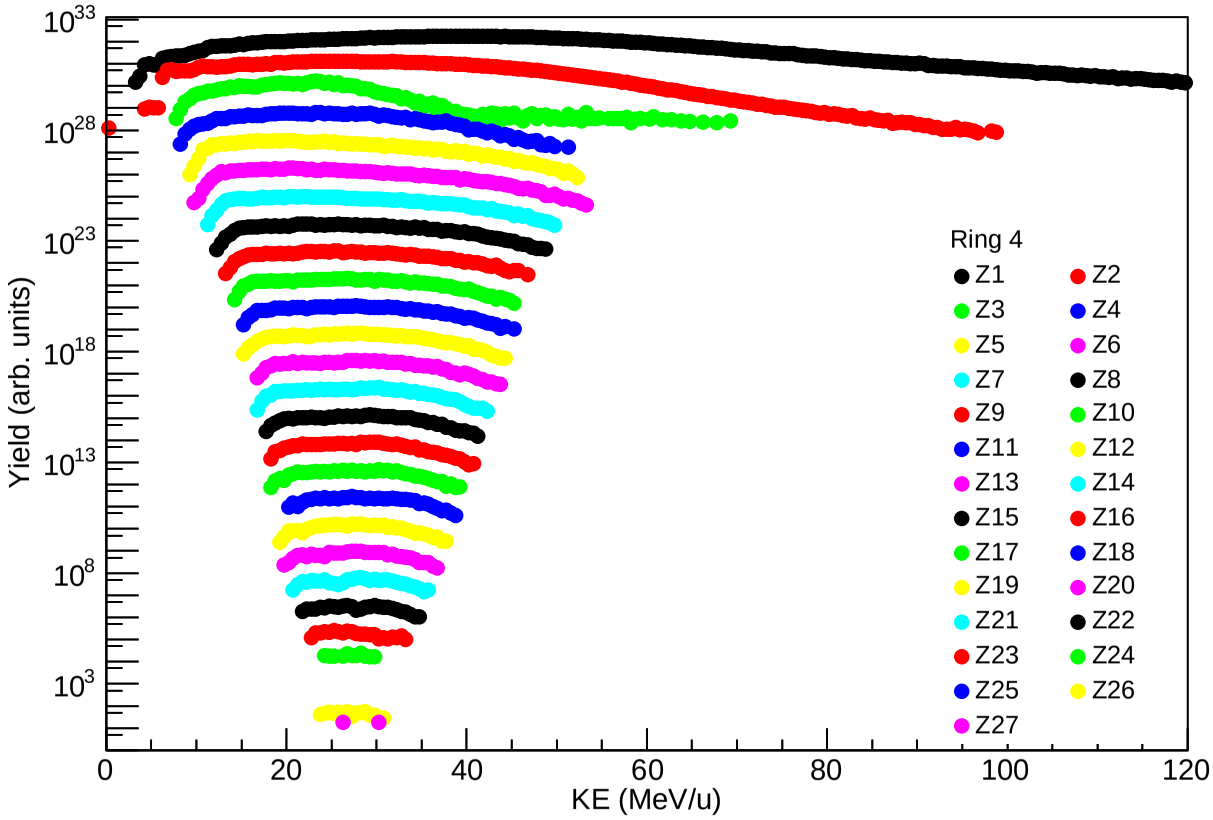

Figure A.17: Kinetic energy spectra for all elements in Ring 4 for the ^{64}Zn+^{70}Zn system.

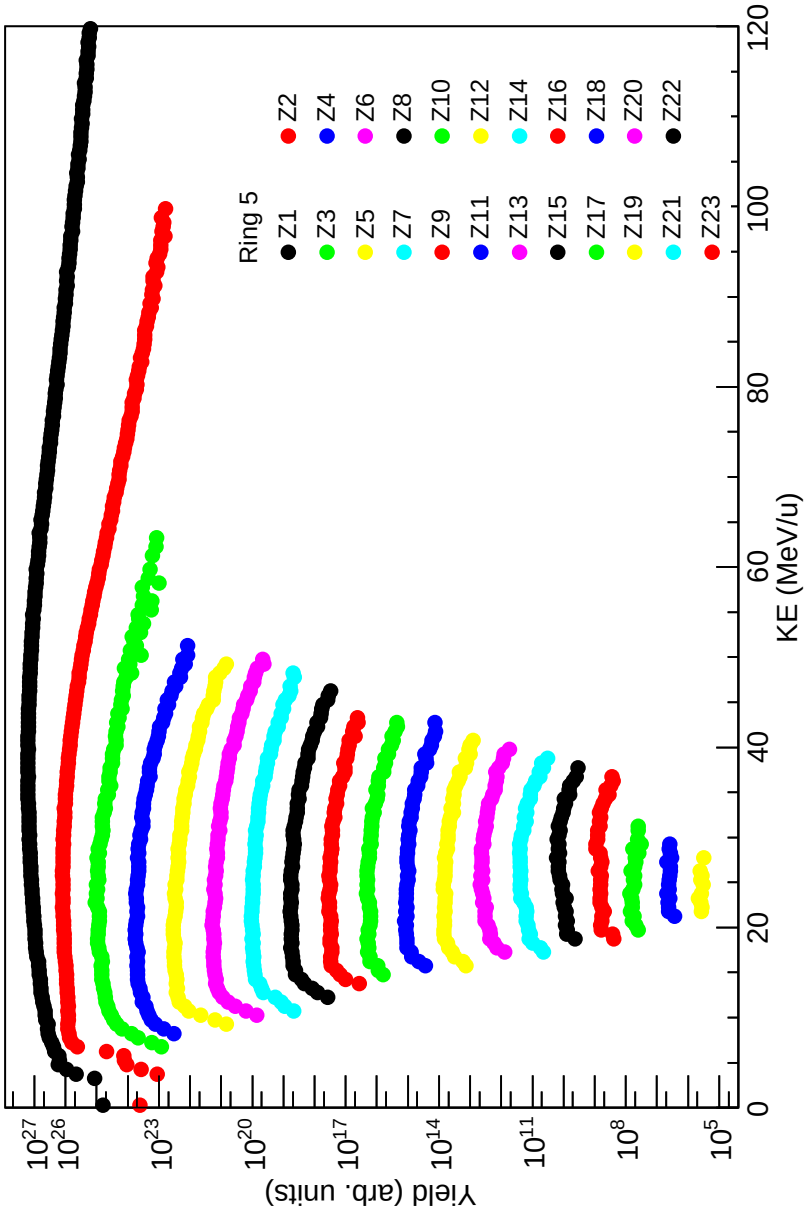

Figure A.18: Kinetic energy spectra for all elements in Ring 5 for the ^{64}Zn+^{70}Zn system.

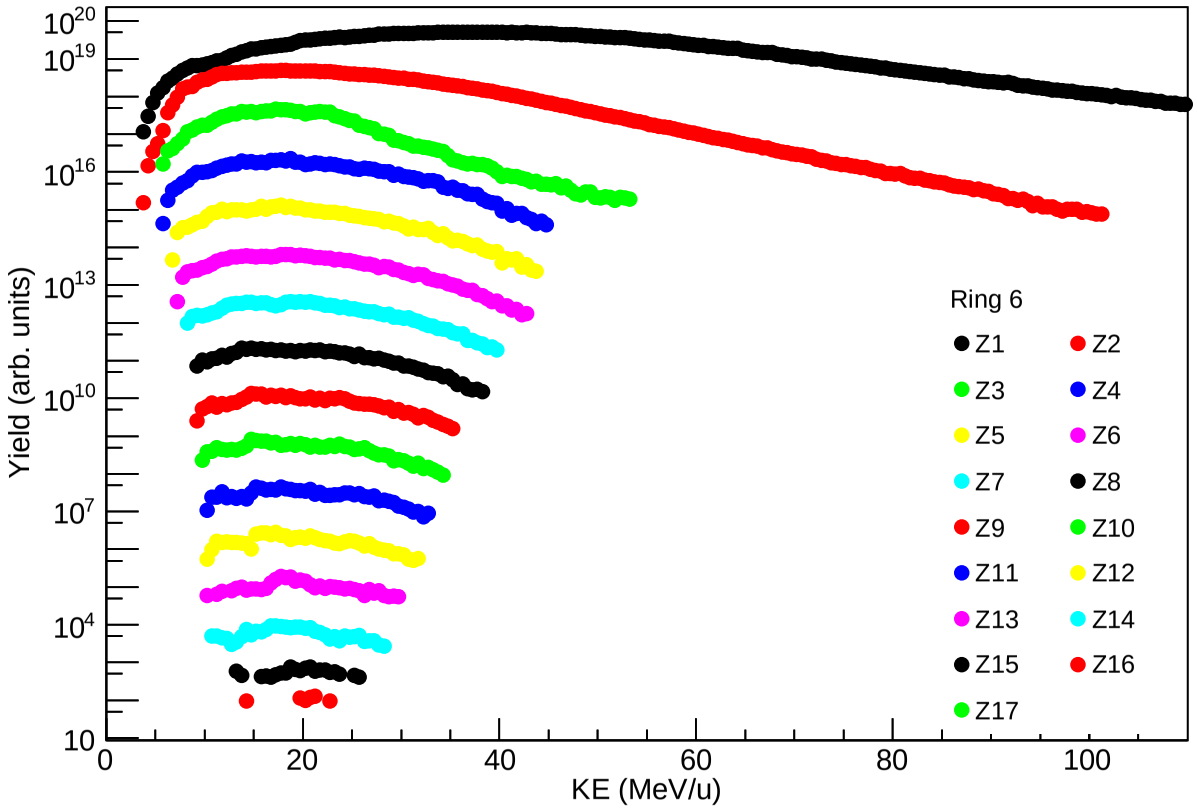

Figure A.19: Kinetic energy spectra for all elements in Ring 6 for the ^{64}Zn+^{70}Zn system.

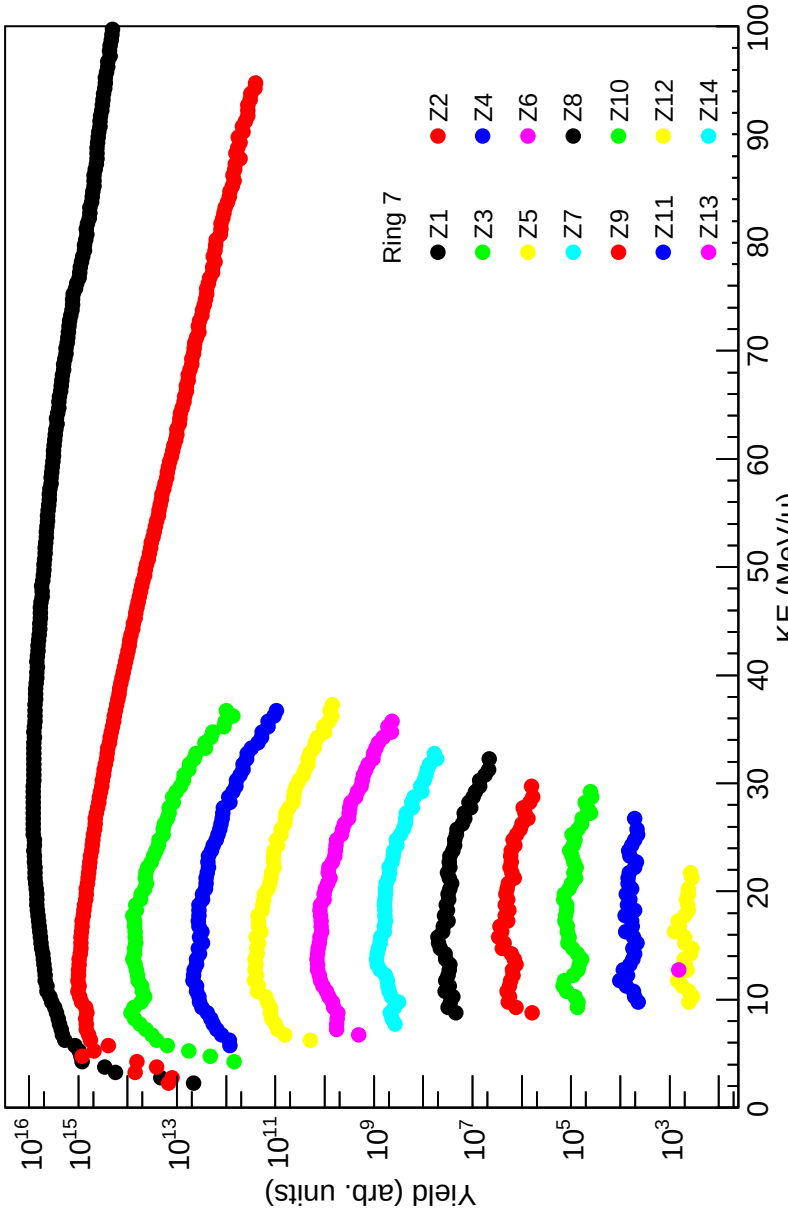

Figure A.20: Kinetic energy spectra for all elements in Ring 7 for the ^{64}Zn+^{70}Zn system.

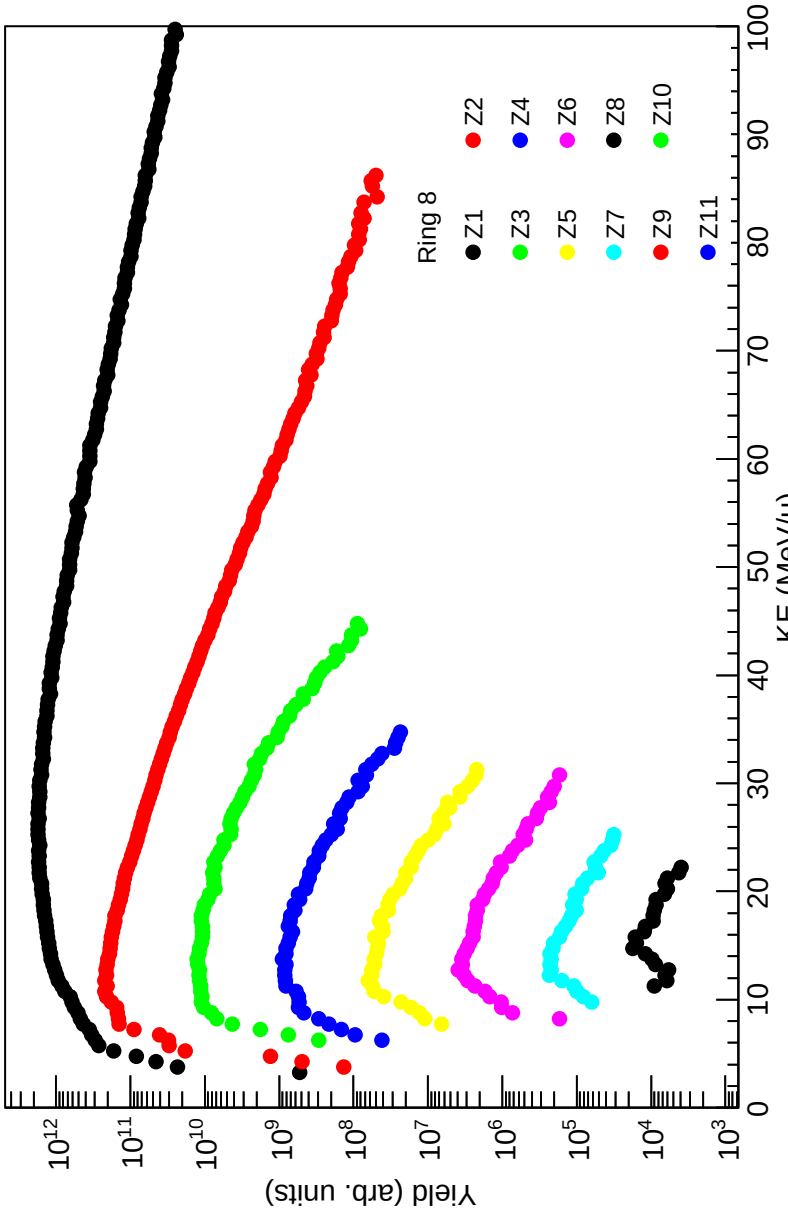

Figure A.21: Kinetic energy spectra for all elements in Ring 8 for the ^{64}Zn+^{70}Zn system.

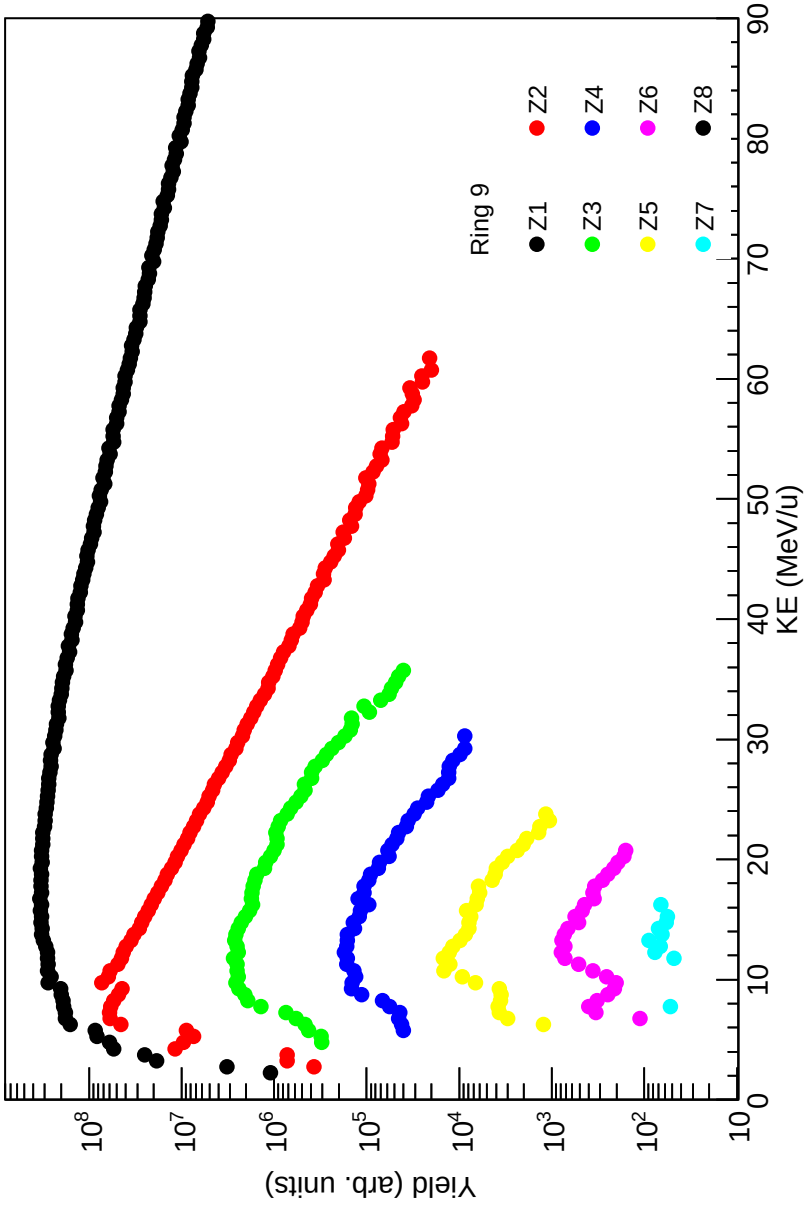

Figure A.22: Kinetic energy spectra for all elements in Ring 9 for the ^{64}Zn+^{70}Zn system.

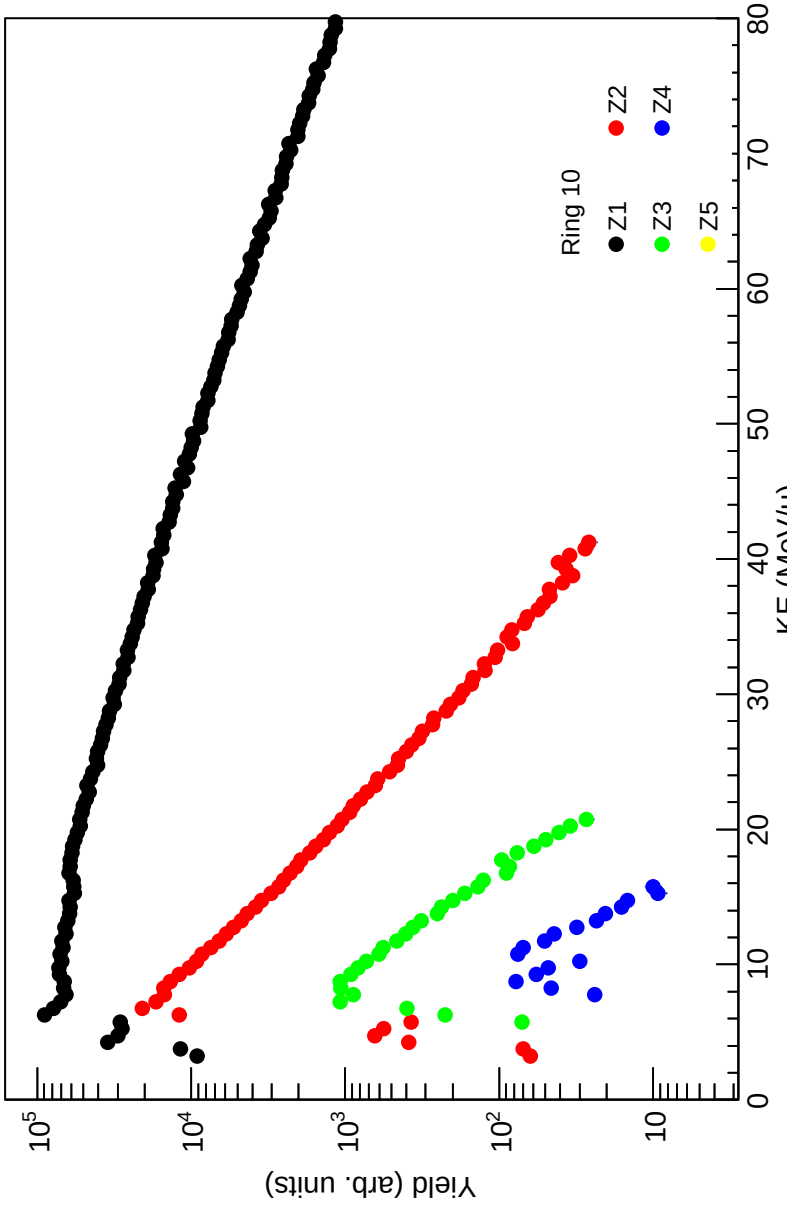

Figure A.23: Kinetic energy spectra for all elements in Ring 10 for the ^{64}Zn+^{70}Zn system.

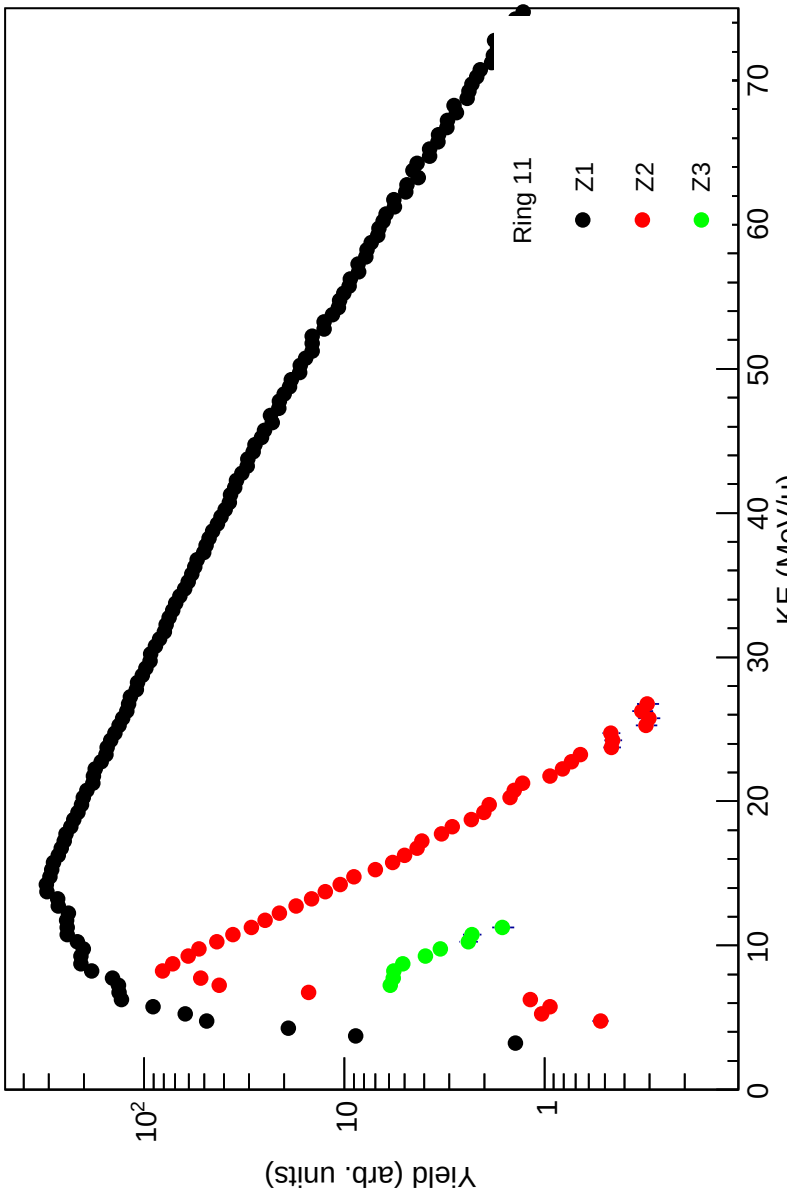

Figure A.24: Kinetic energy spectra for all elements in Ring 11 for the ^{64}Zn+^{70}Zn system.

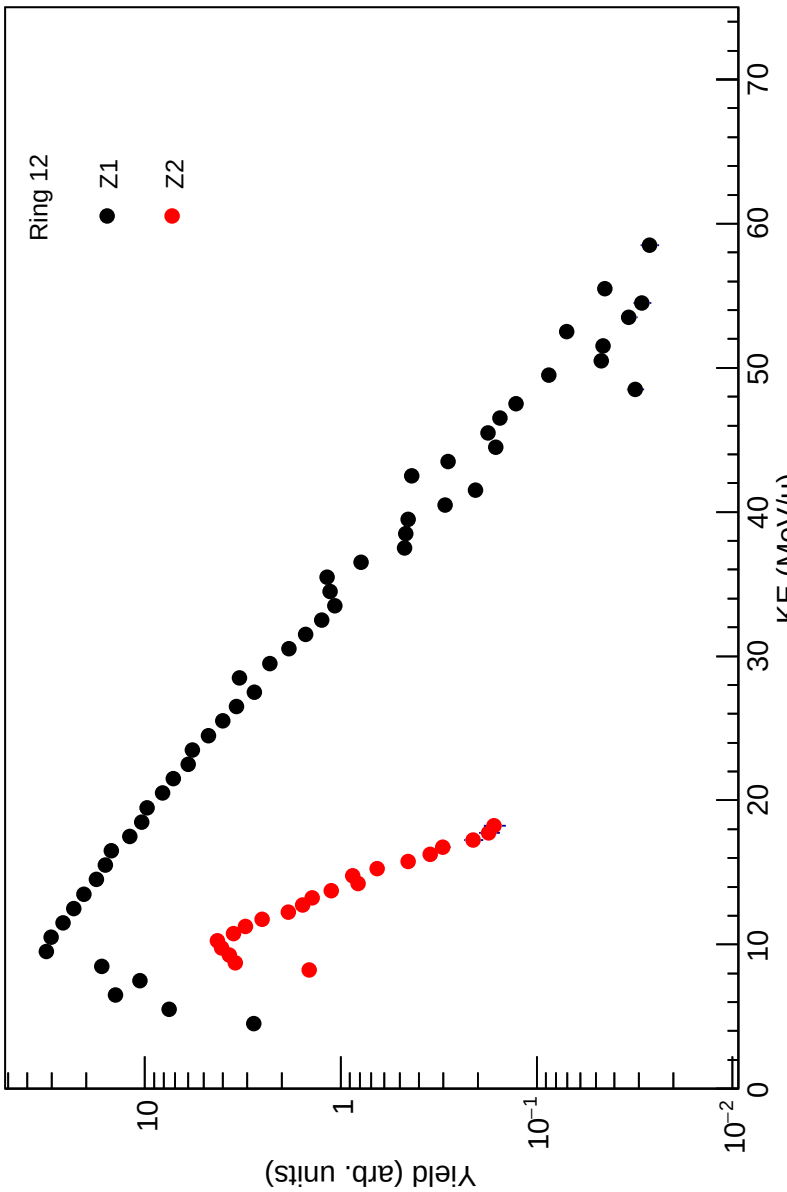

Figure A.25: Kinetic energy spectra for all elements in Ring 12 for the ^{64}Zn+^{70}Zn system.

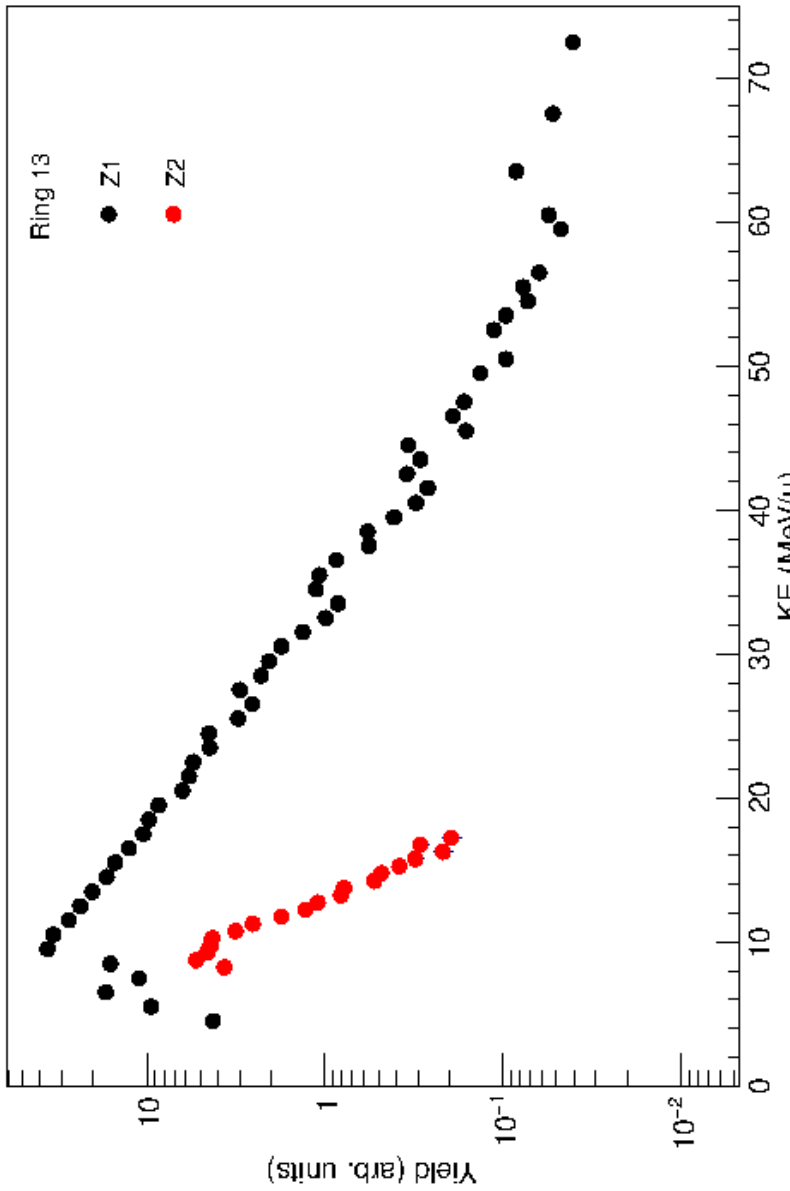

Figure A.26: Kinetic energy spectra for all elements in Ring 13 for the ^{64}Zn+^{70}Zn system.

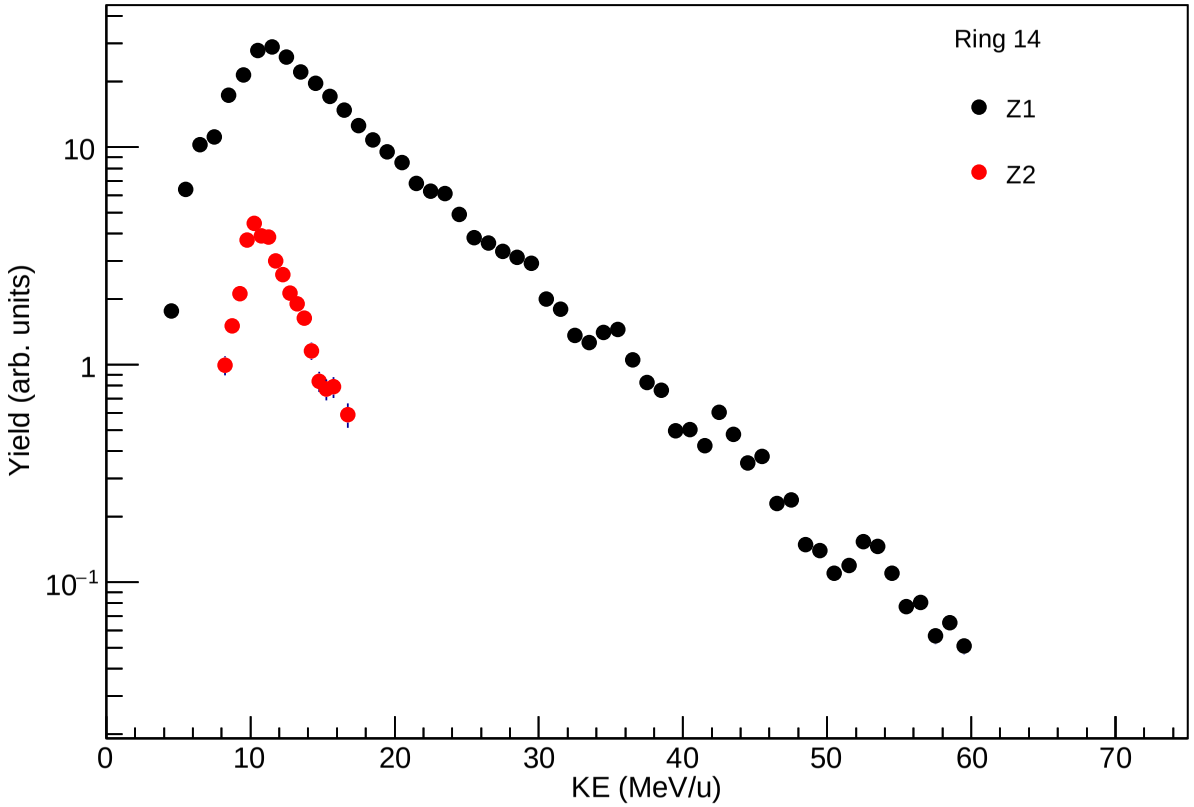

Figure A.27: Kinetic energy spectra for all elements in Ring 14 for the ^{64}Zn+^{70}Zn system.

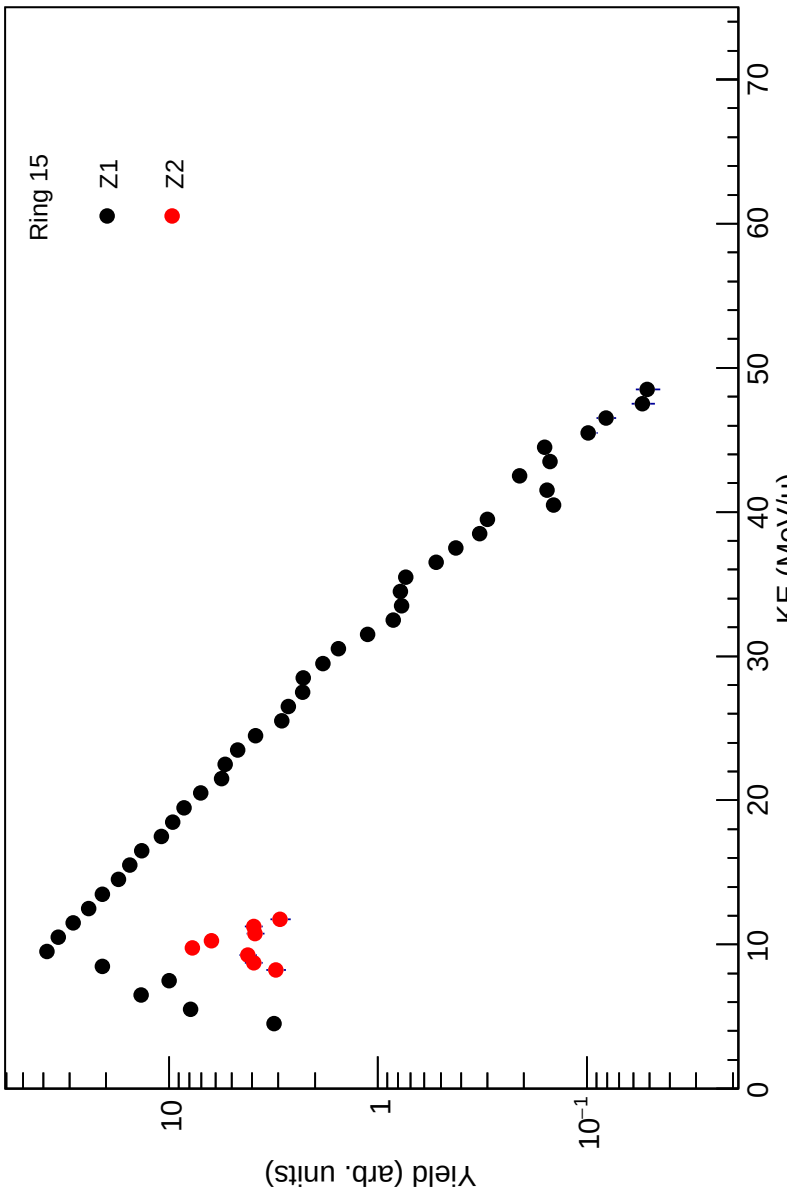

Figure A.28: Kinetic energy spectra for all elements in Ring 15 for the ^{64}Zn+^{70}Zn system.

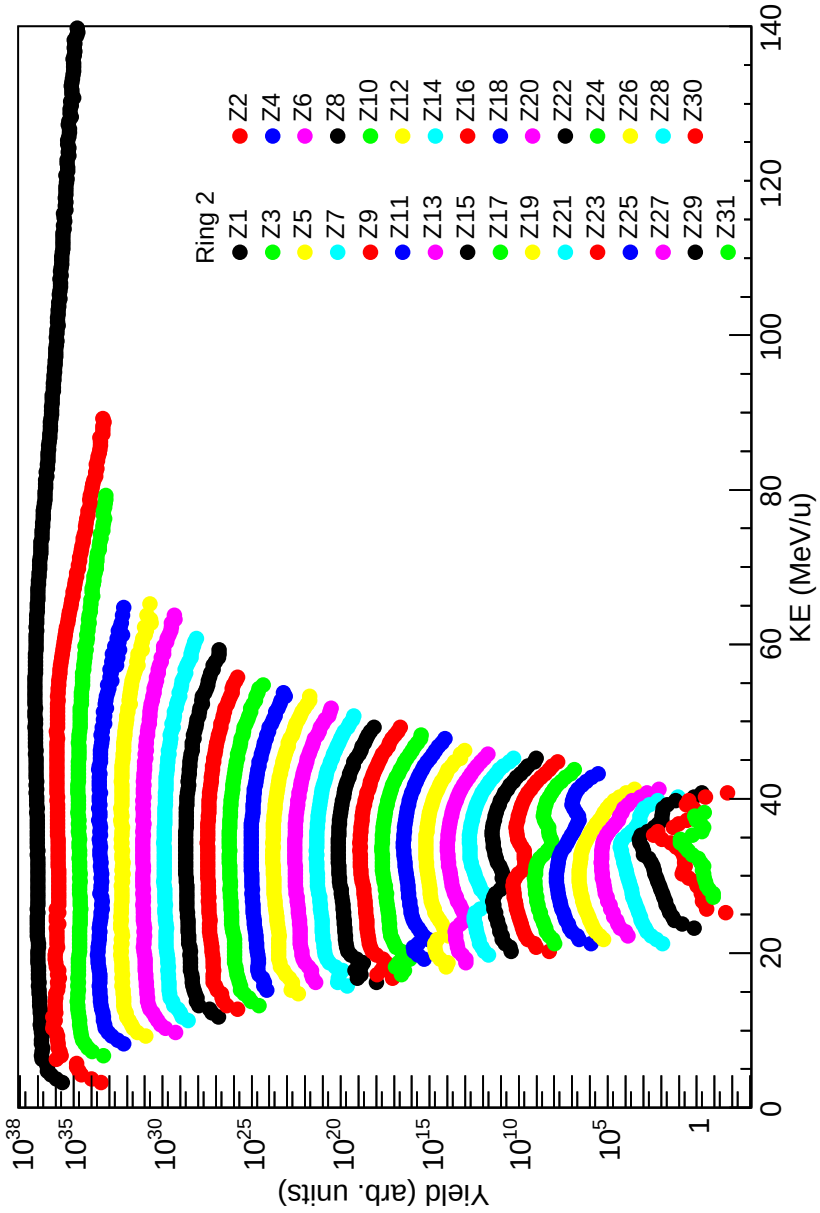

Figure A.29: Kinetic energy spectra for all elements in Ring 2 for the ^{64}Zn+^{64}Ni system.

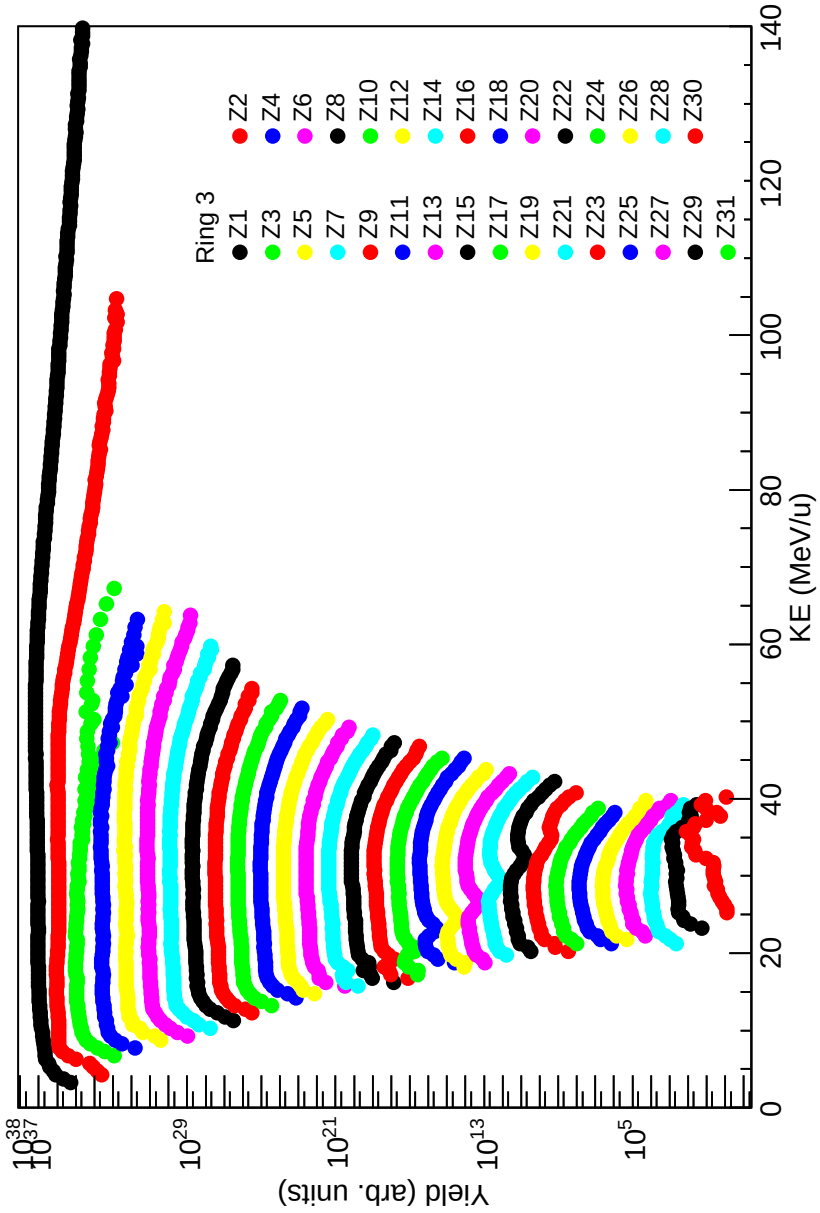

Figure A.30: Kinetic energy spectra for all elements in Ring 3 for the ^{64}Zn+^{64}Ni system.

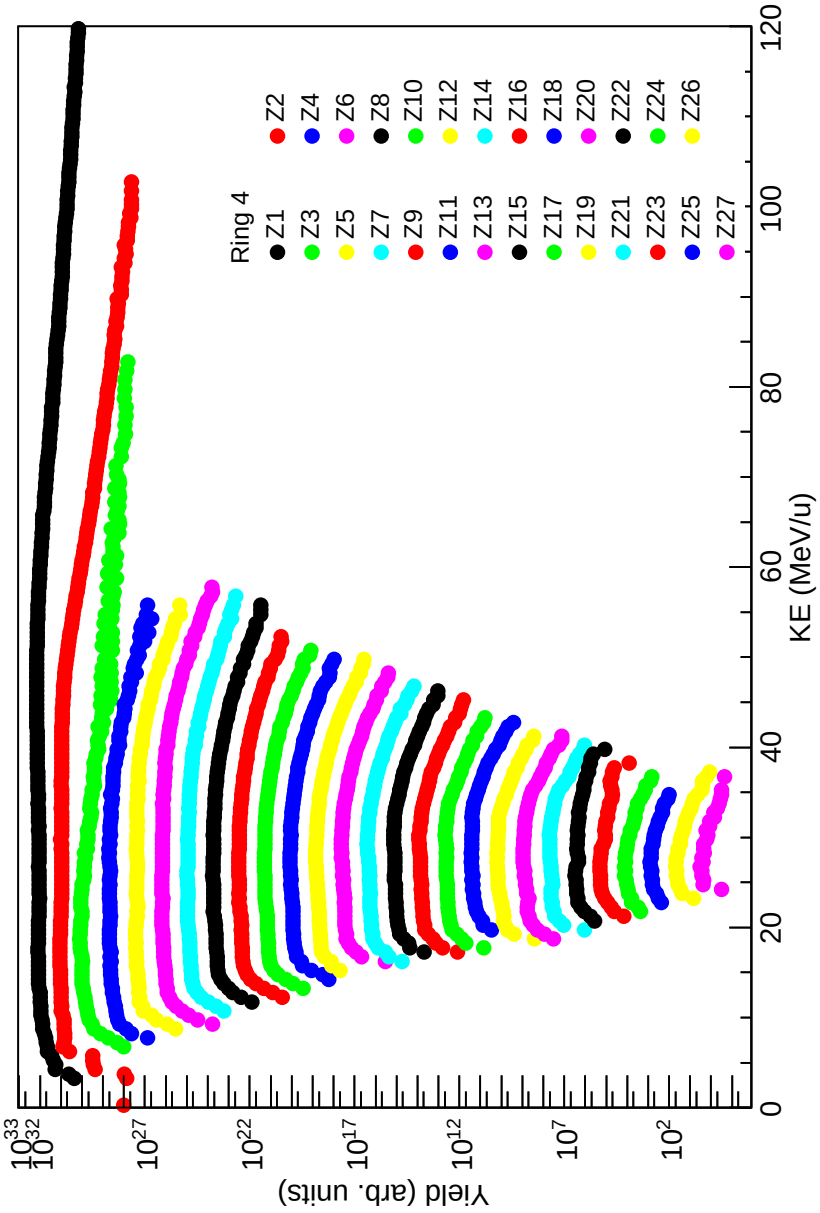

Figure A.31: Kinetic energy spectra for all elements in Ring 4 for the ^{64}Zn+^{64}Ni system.

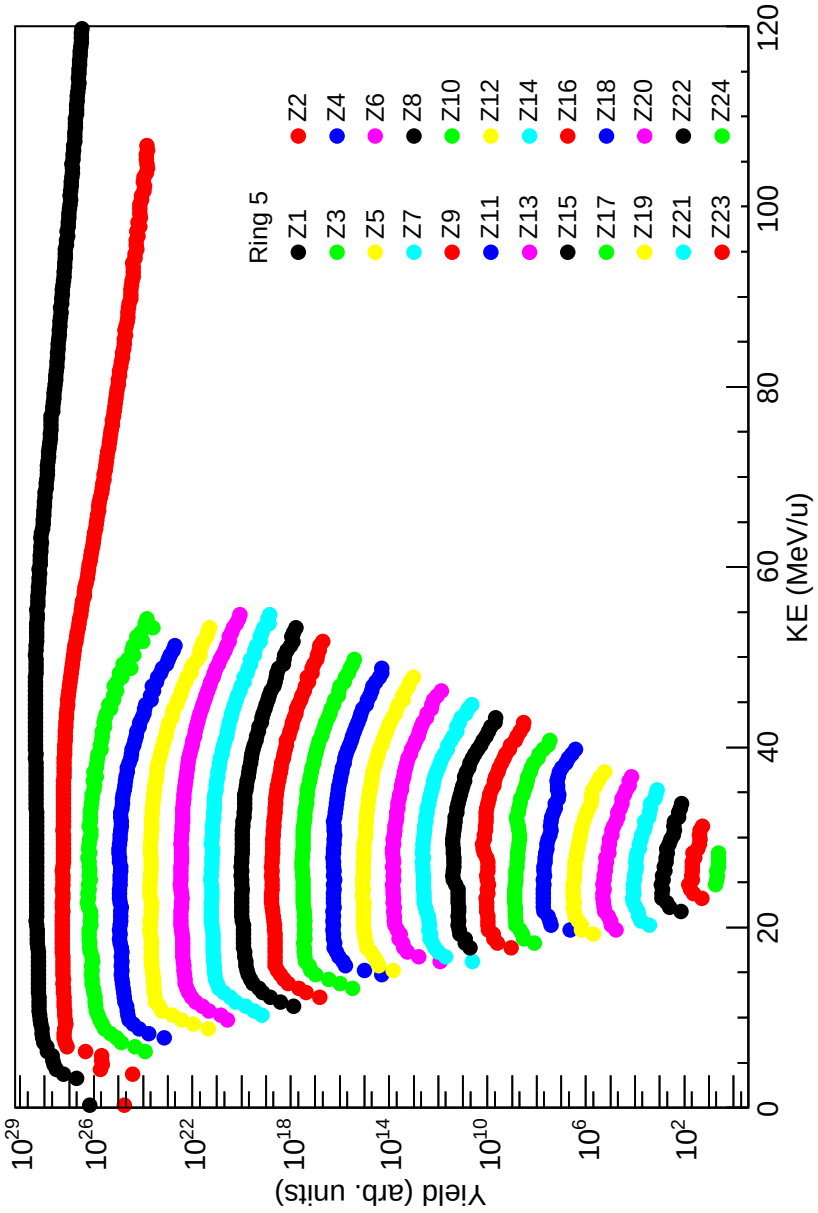

Figure A.32: Kinetic energy spectra for all elements in Ring 5 for the ^{64}Zn+^{64}Ni system.

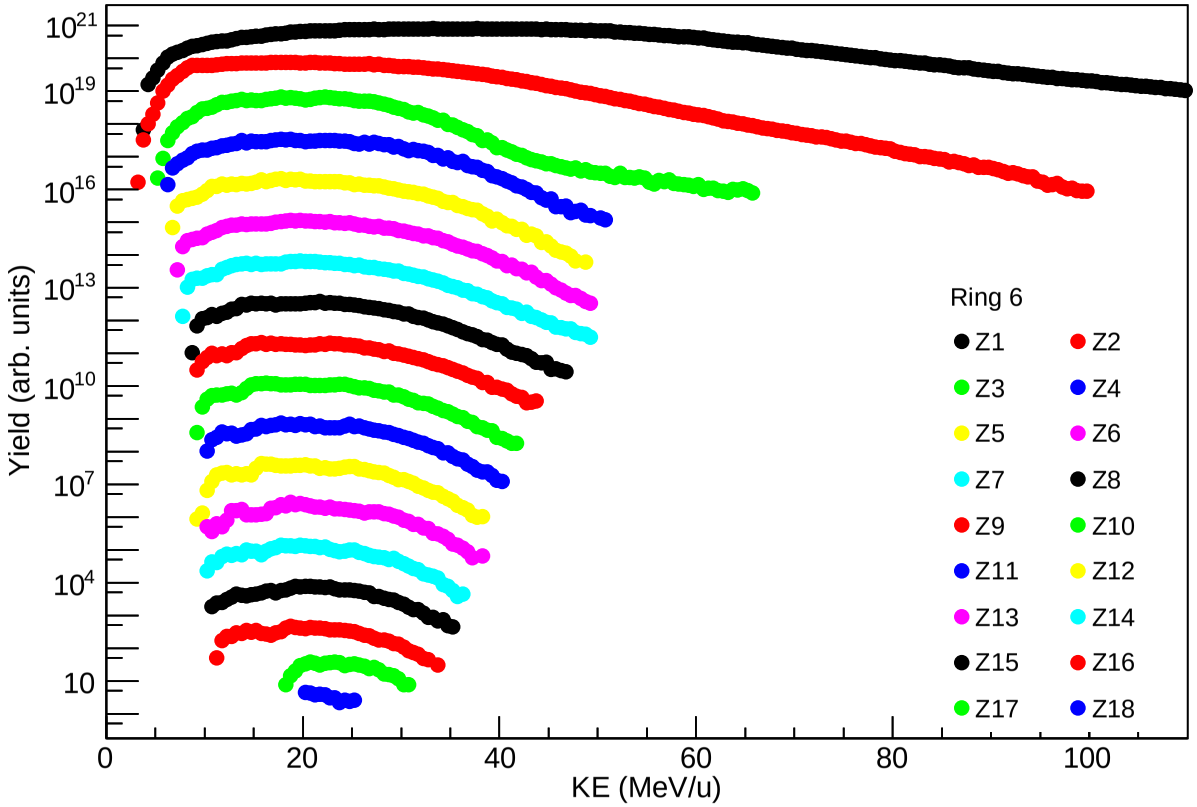

Figure A.33: Kinetic energy spectra for all elements in Ring 6 for the ^{64}Zn+^{64}Ni system.

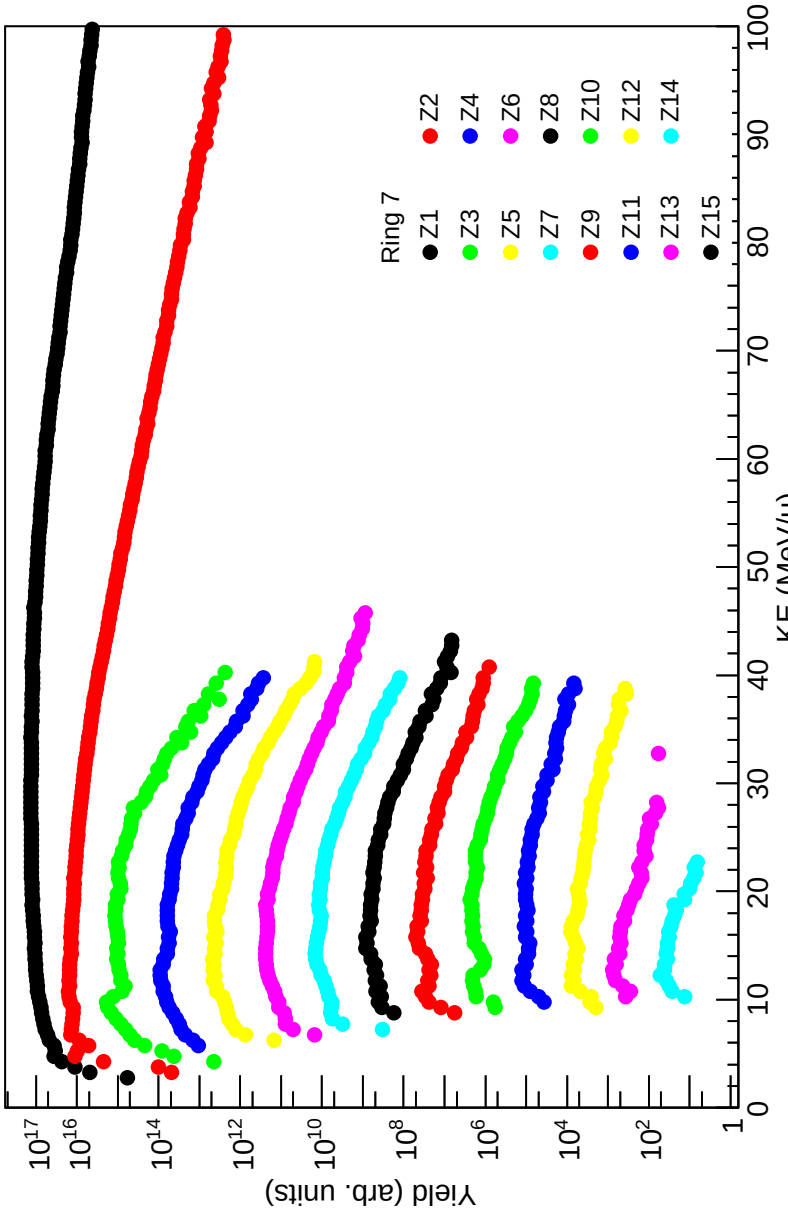

Figure A.34: Kinetic energy spectra for all elements in Ring 7 for the ^{64}Zn+^{64}Ni system.

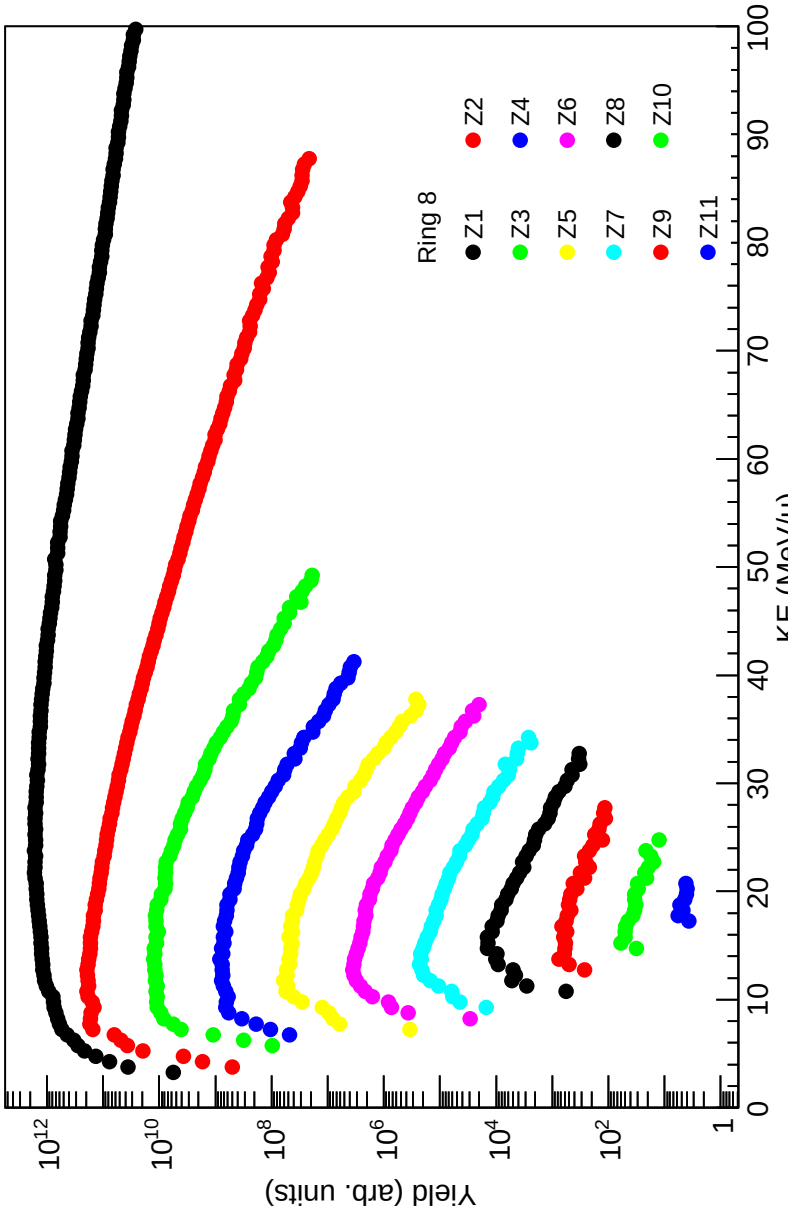

Figure A.35: Kinetic energy spectra for all elements in Ring 8 for the ^{64}Zn+^{64}Ni system.

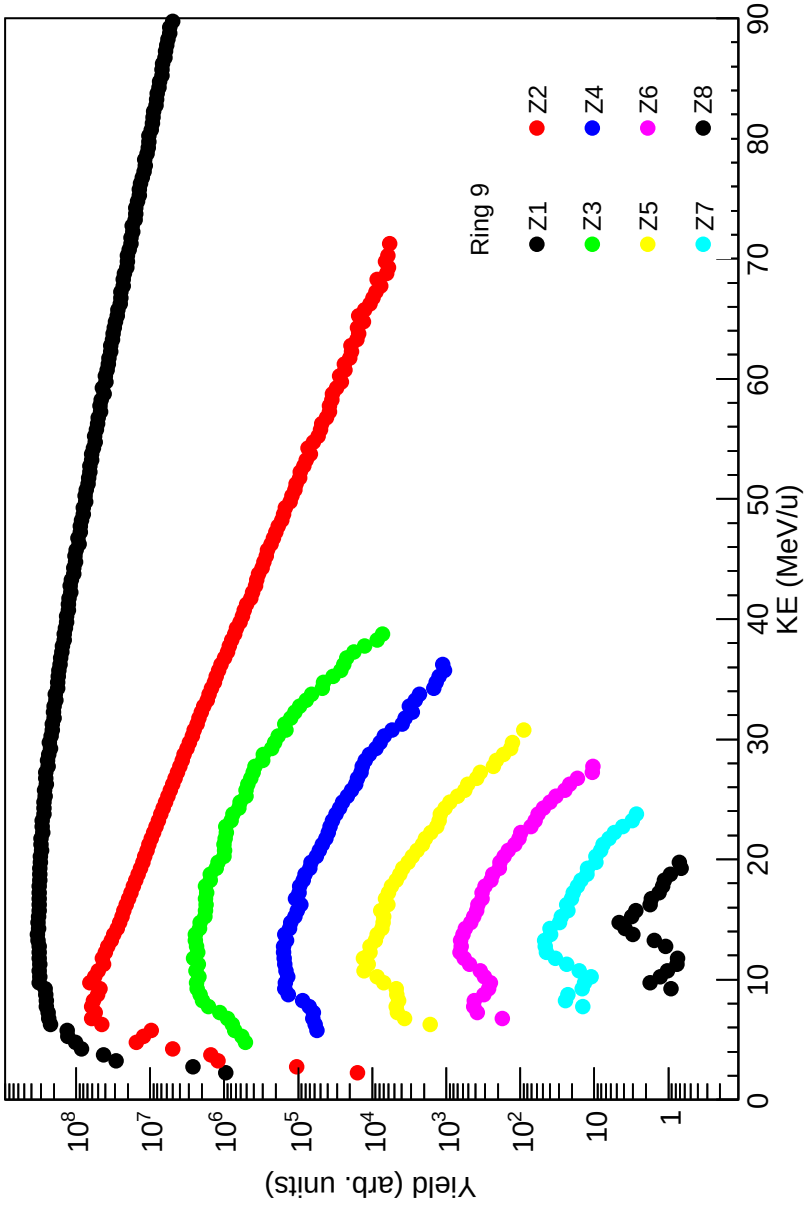

Figure A.36: Kinetic energy spectra for all elements in Ring 9 for the ^{64}Zn+^{64}Ni system.

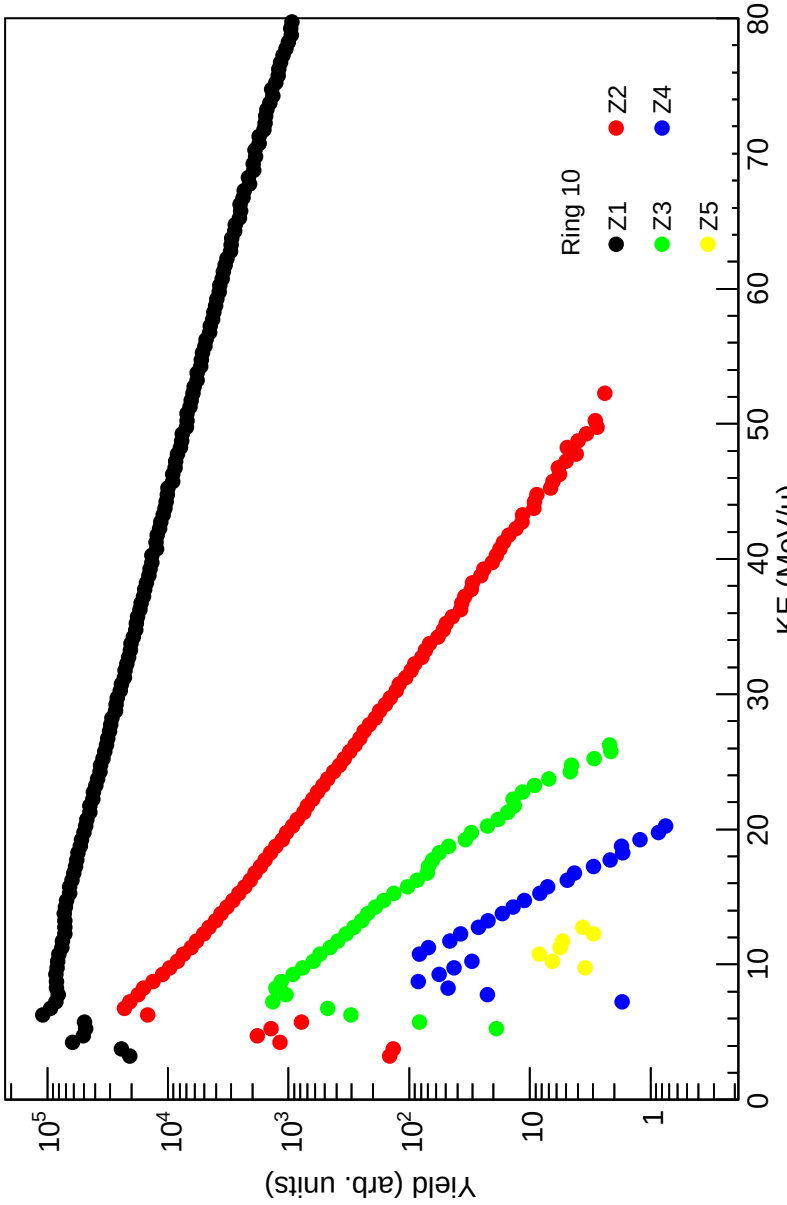

Figure A.37: Kinetic energy spectra for all elements in Ring 10 for the ^{64}Zn+^{64}Ni system.

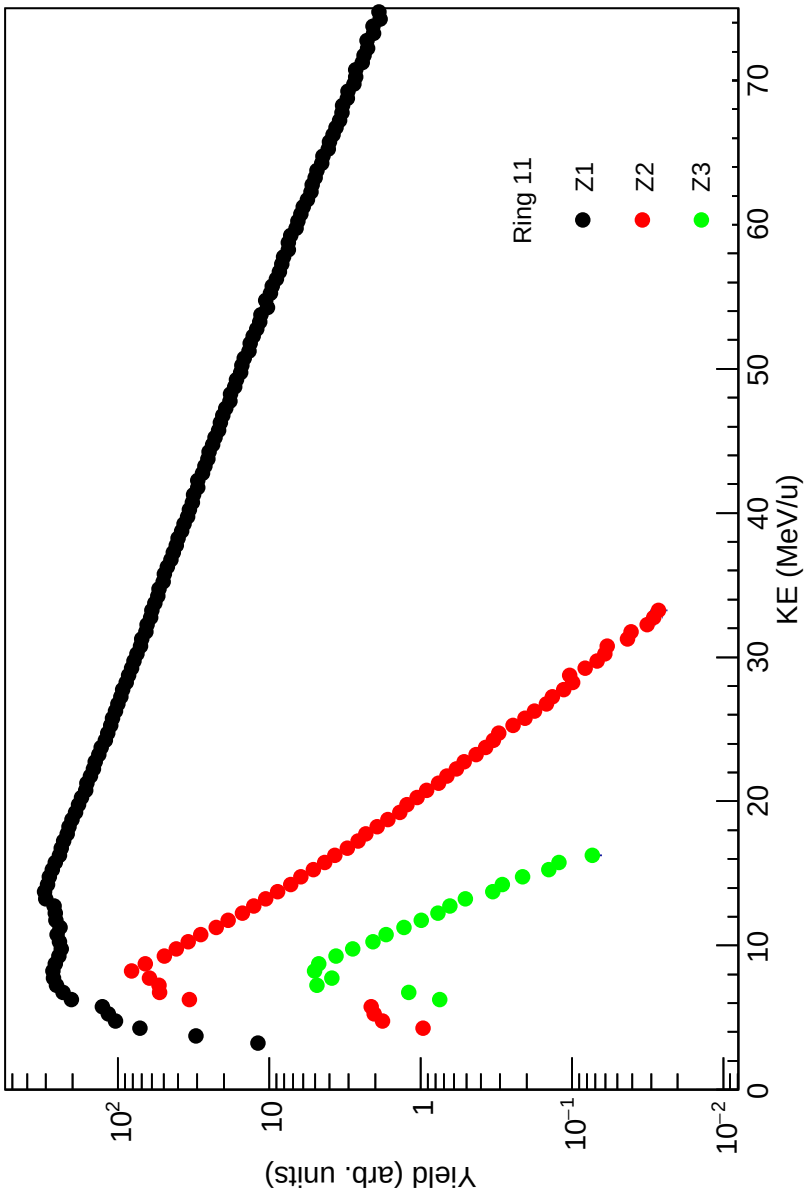

Figure A.38: Kinetic energy spectra for all elements in Ring 11 for the ^{64}Zn+^{64}Ni system.

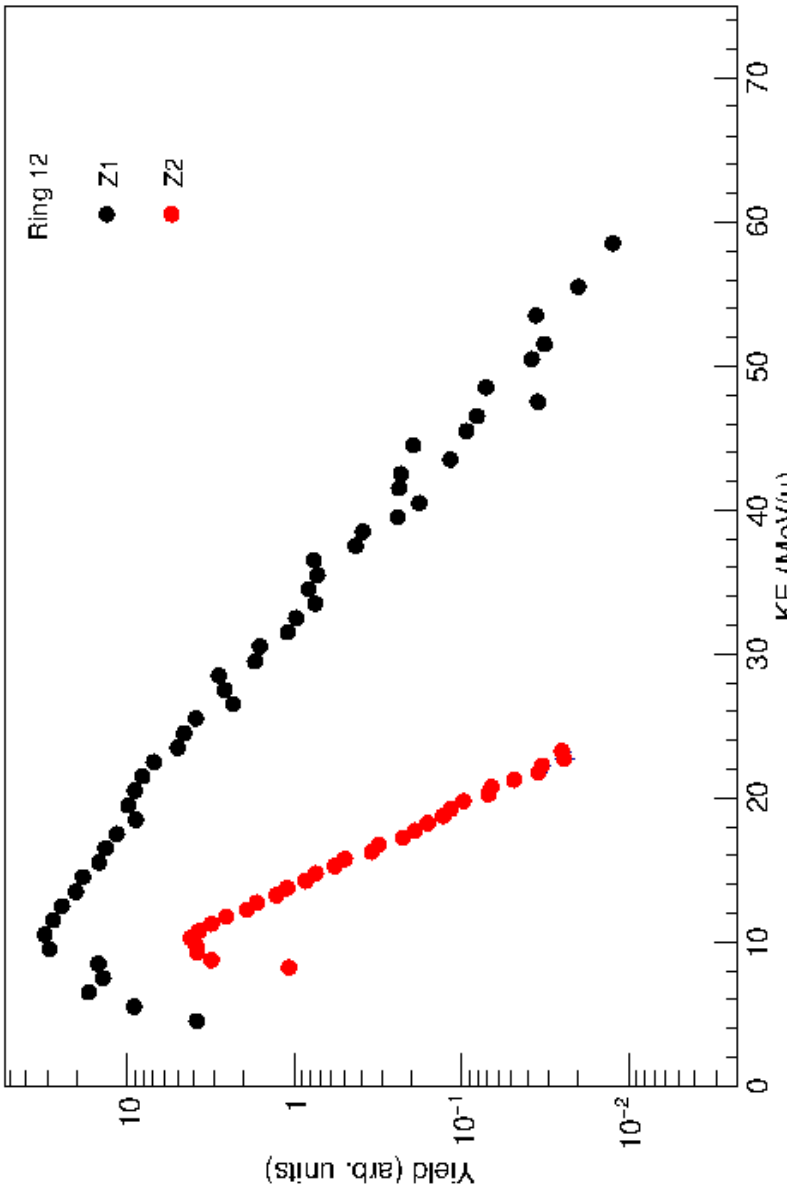

Figure A.39: Kinetic energy spectra for all elements in Ring 12 for the ^{64}Zn+^{64}Ni system.

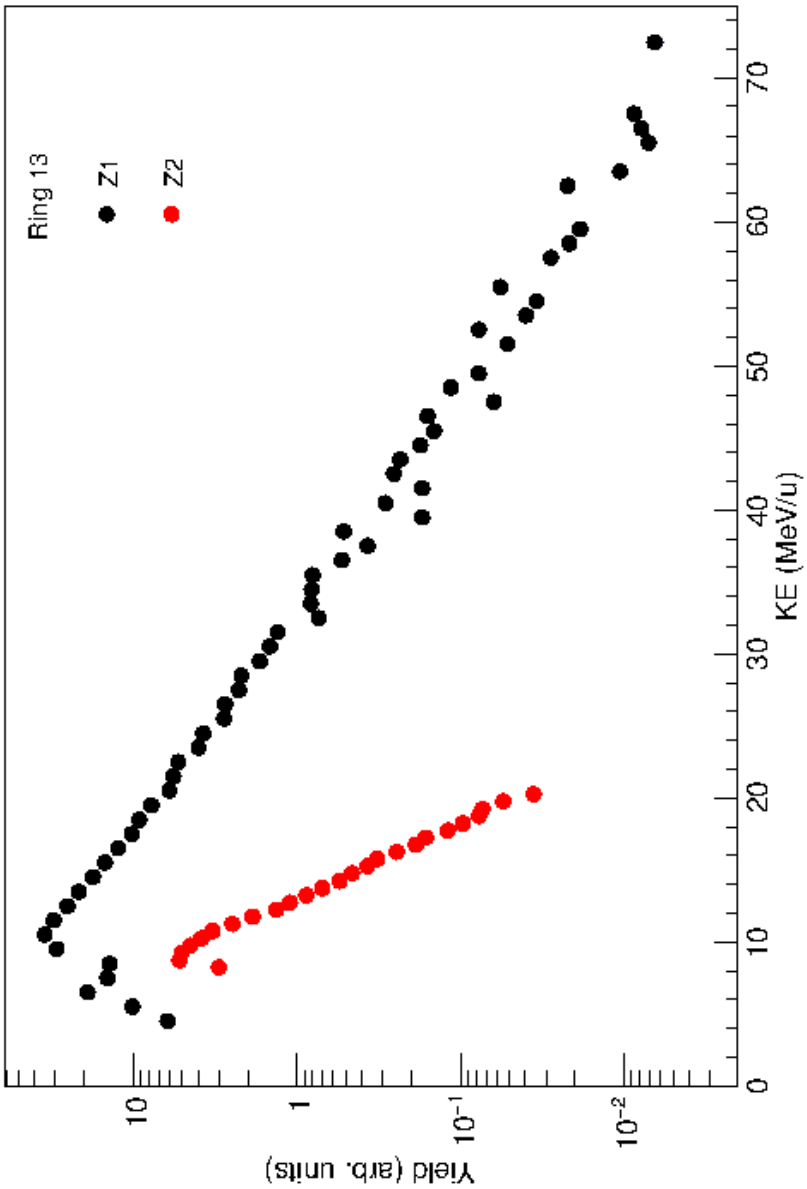

Figure A.40: Kinetic energy spectra for all elements in Ring 13 for the ^{64}Zn+^{64}Ni system.

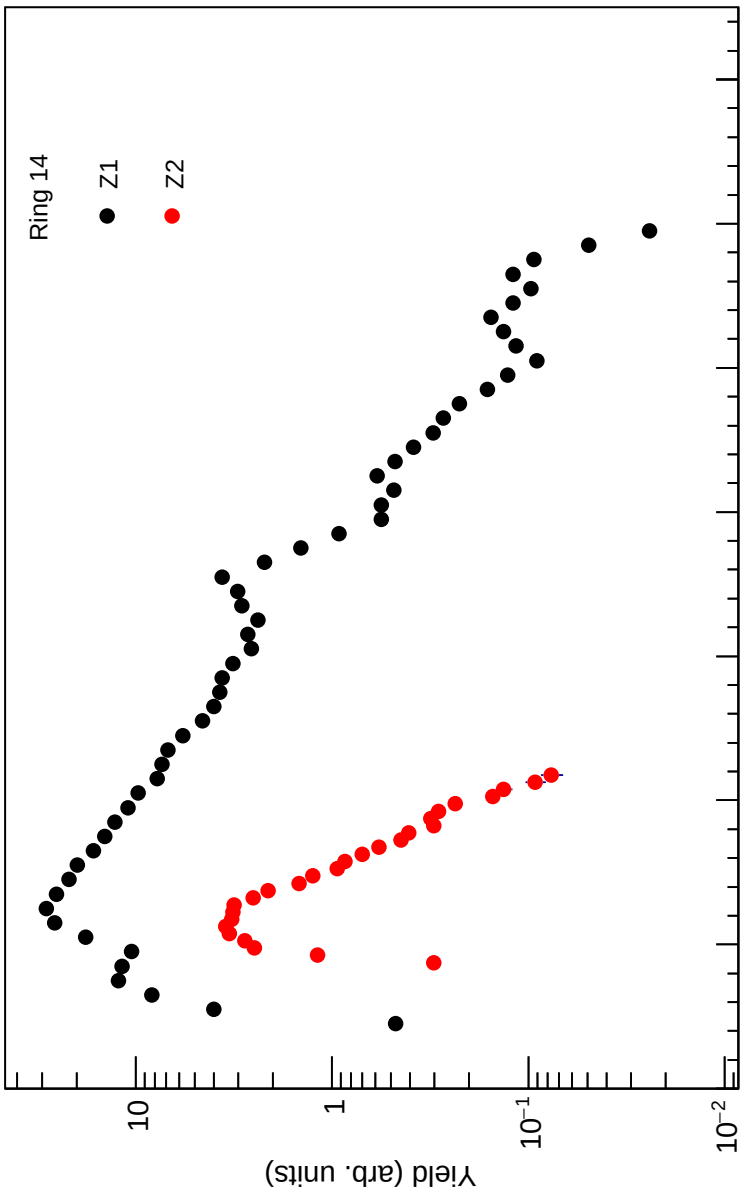

Figure A.41: Kinetic energy spectra for all elements in Ring 14 for the ^{64}Zn+^{64}Ni system.

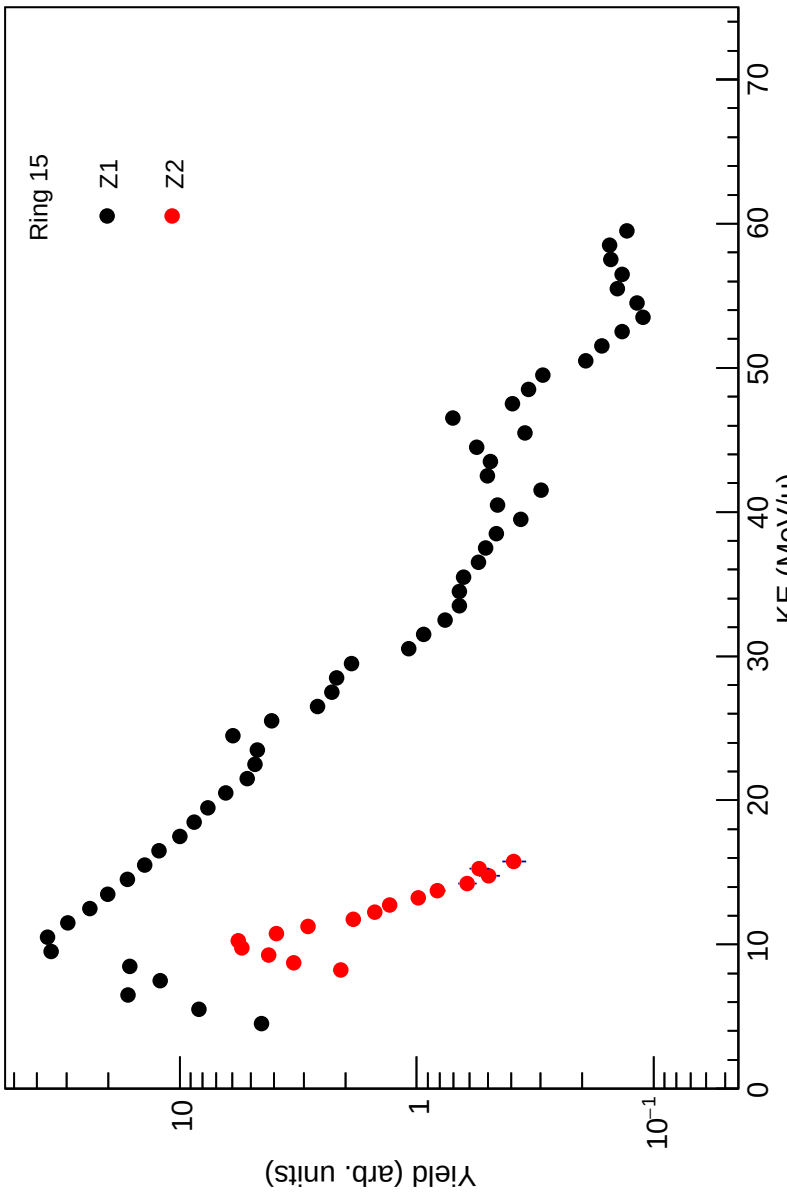

Figure A.42: Kinetic energy spectra for all elements in Ring 15 for the ^{64}Zn+^{64}Ni system.

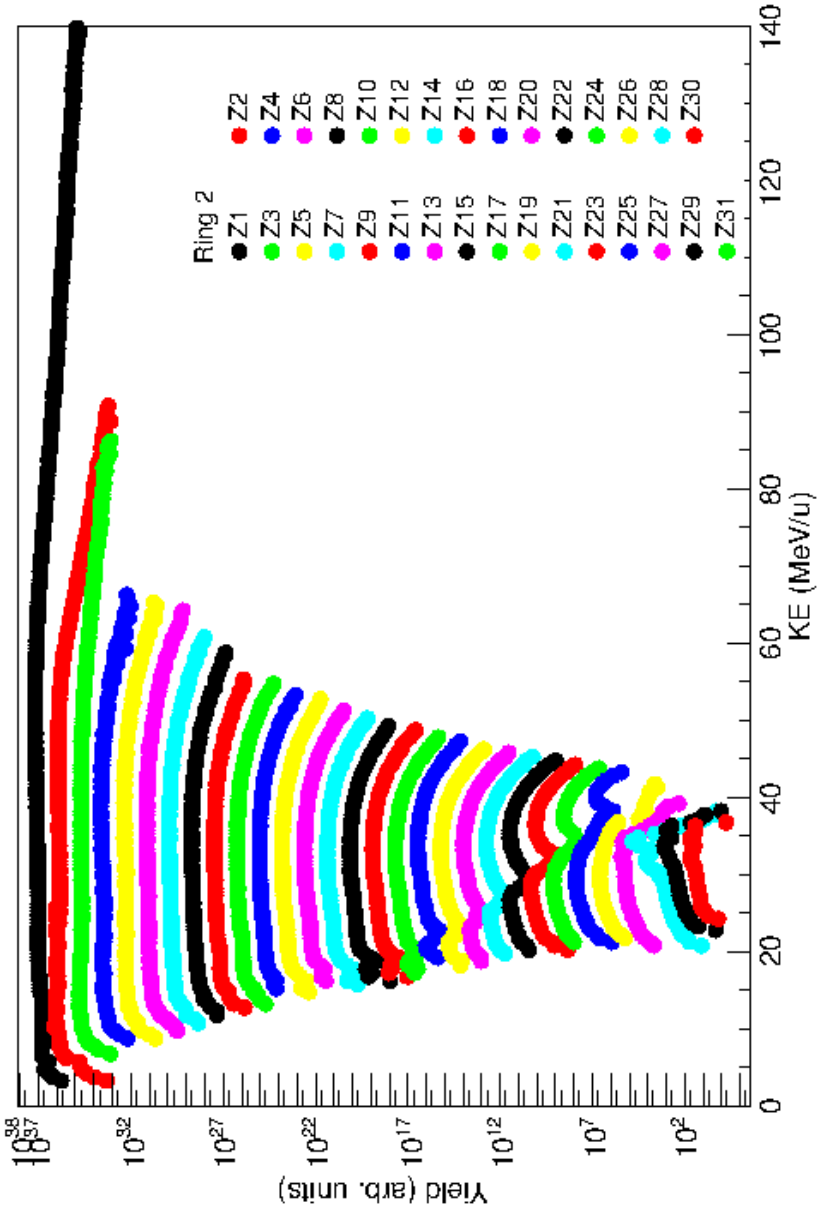

Figure A.43: Kinetic energy spectra for all elements in Ring 2 for the ^{64}Ni+^{64}Zn system.

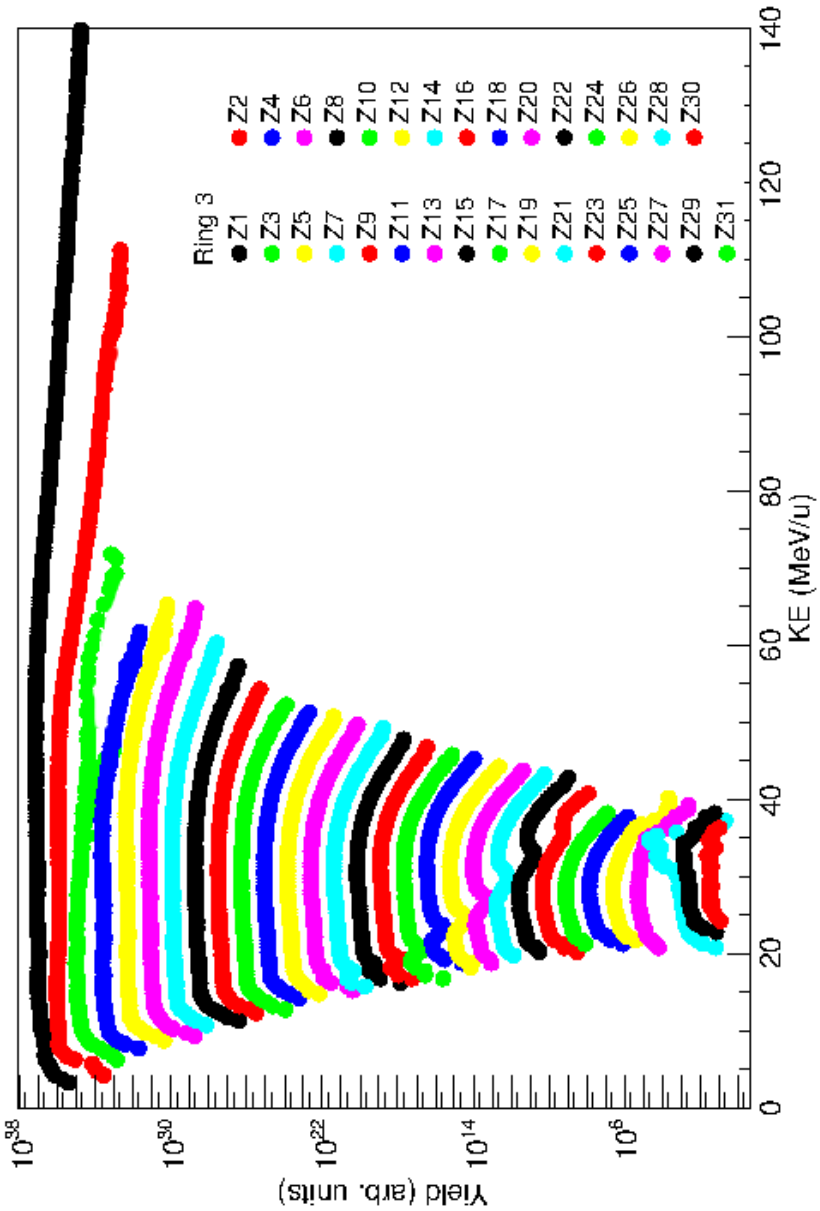

Figure A.44: Kinetic energy spectra for all elements in Ring 3 for the ^{64}Ni+^{64}Zn system.

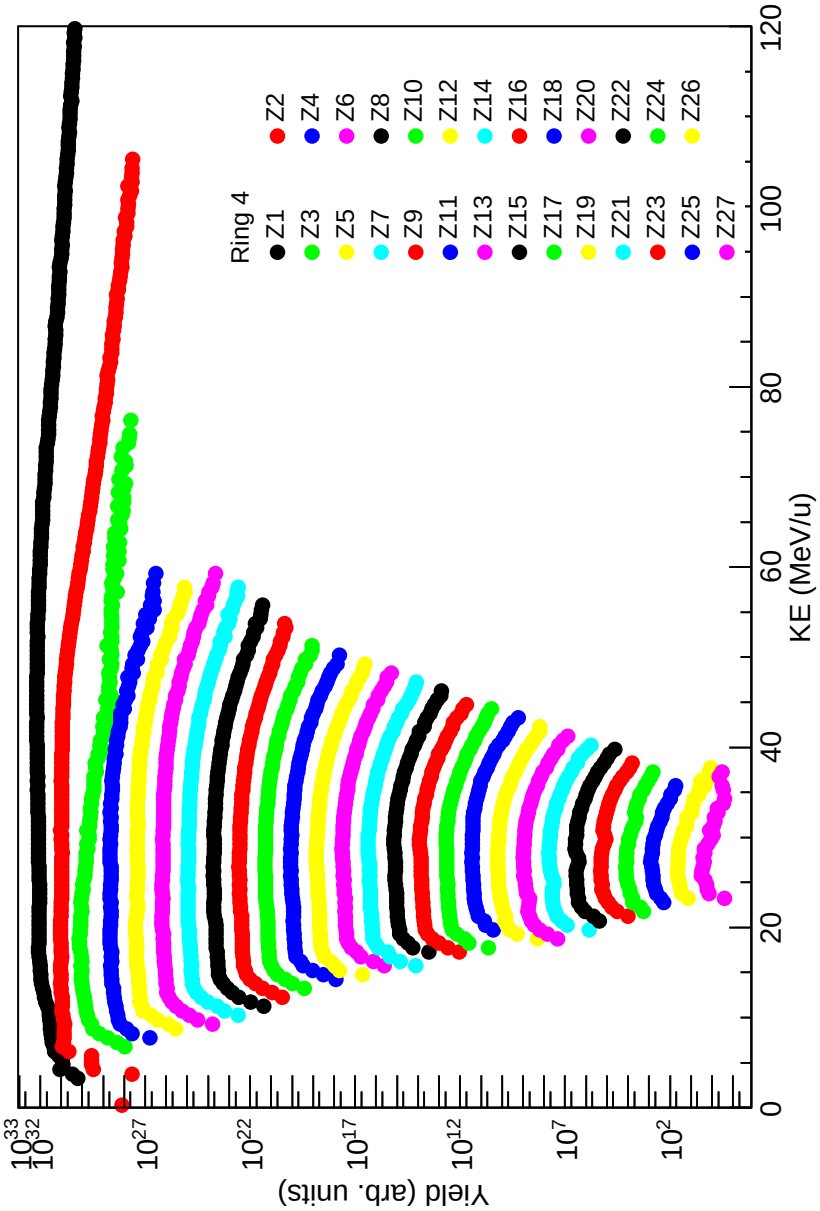

Figure A.45: Kinetic energy spectra for all elements in Ring 4 for the ^{64}Ni+^{64}Zn system.

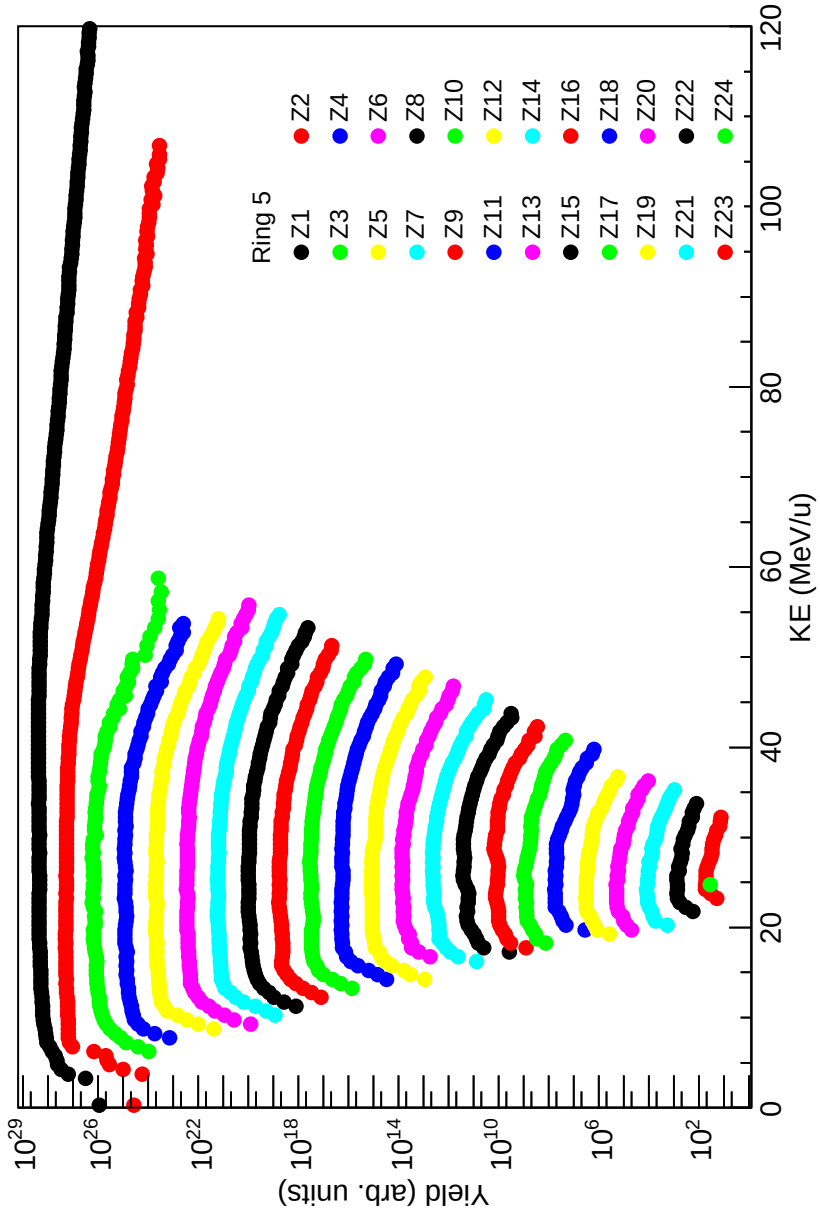

Figure A.46: Kinetic energy spectra for all elements in Ring 5 for the ^{64}Ni+^{64}Zn system.

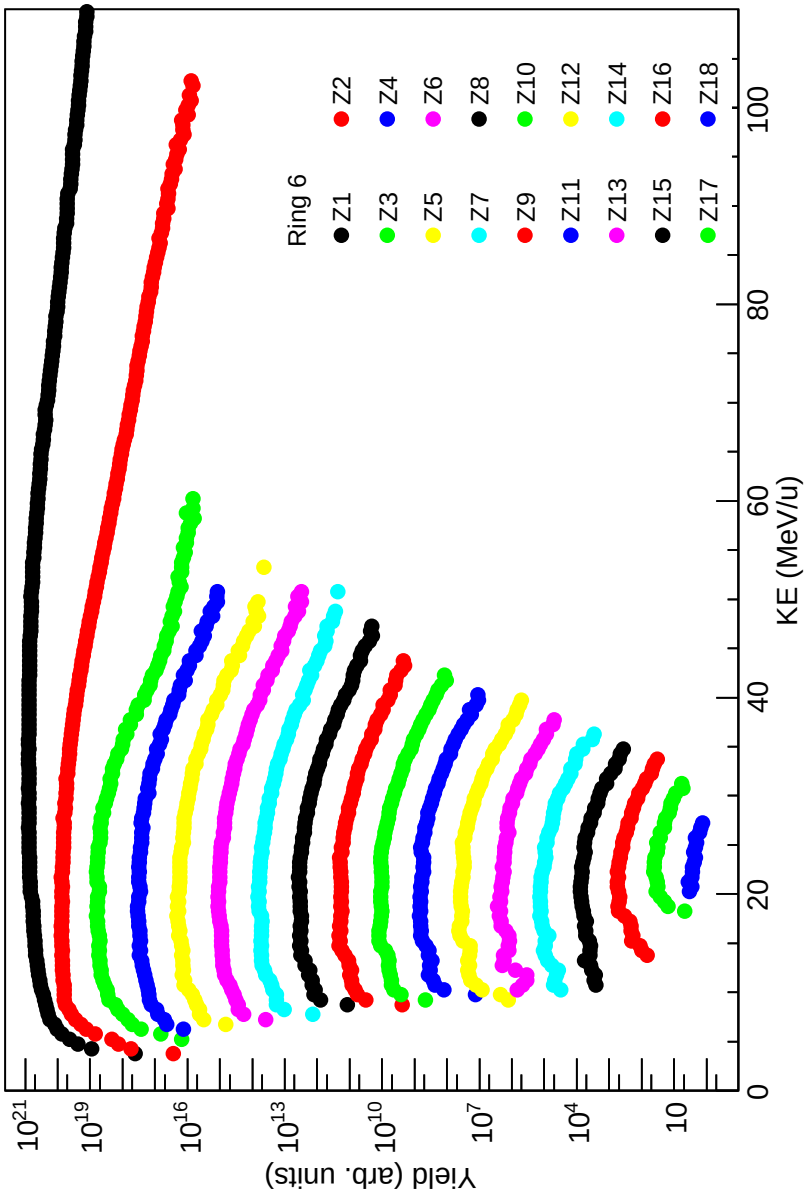

Figure A.47: Kinetic energy spectra for all elements in Ring 6 for the ^{64}Ni+^{64}Zn system.

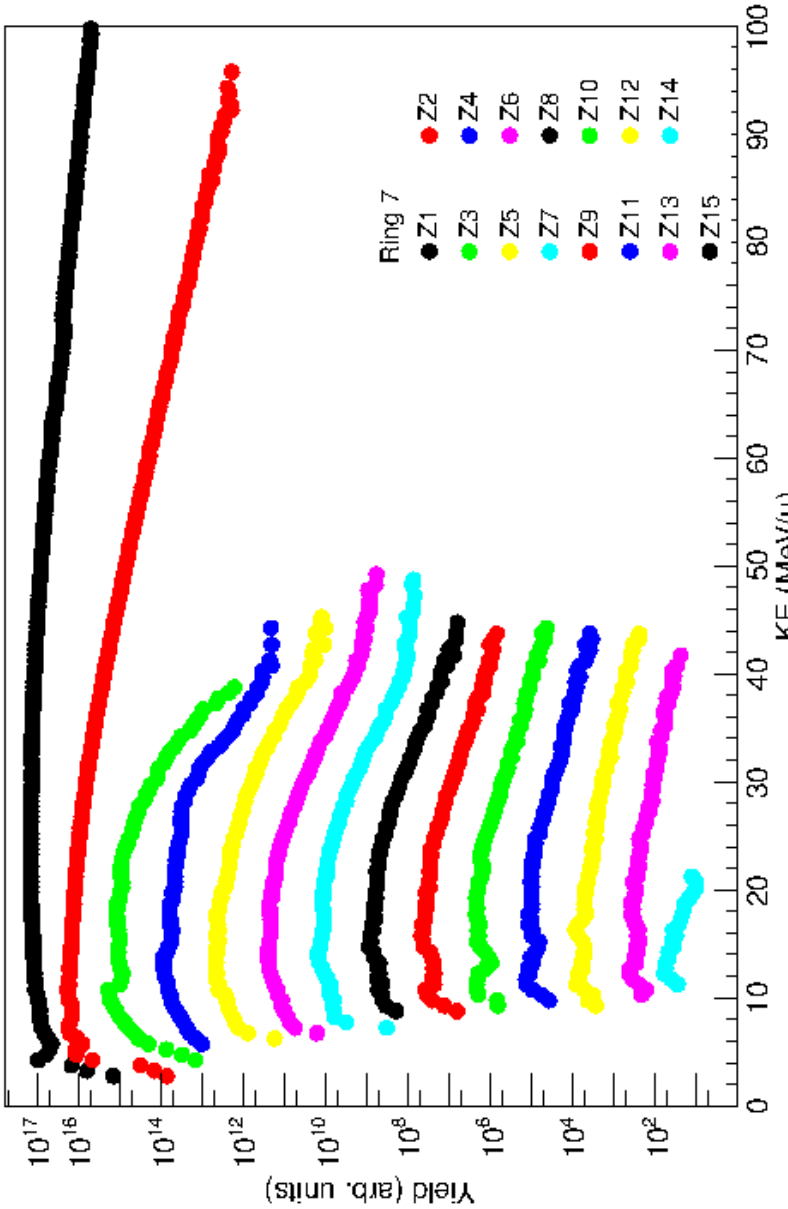

Figure A.48: Kinetic energy spectra for all elements in Ring 7 for the ^{64}Ni+^{64}Zn system.

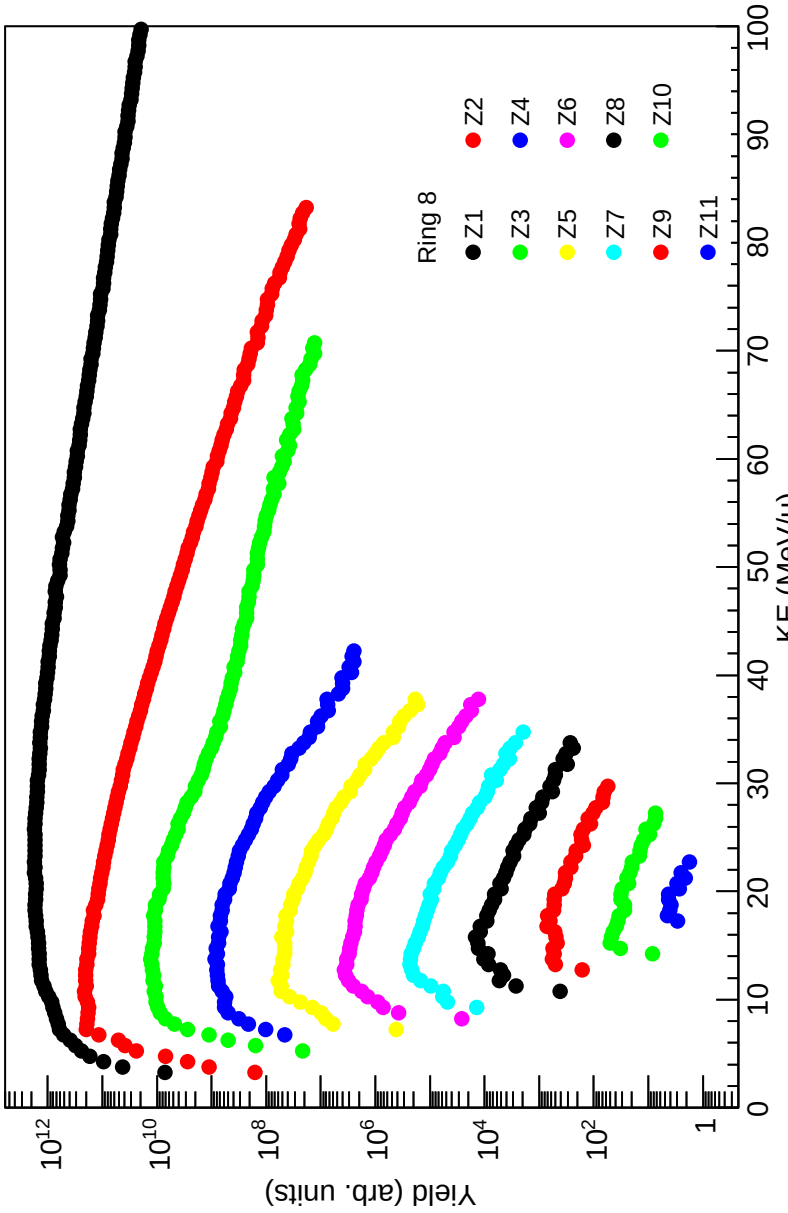

Figure A.49: Kinetic energy spectra for all elements in Ring 8 for the ^{64}Ni+^{64}Zn system.

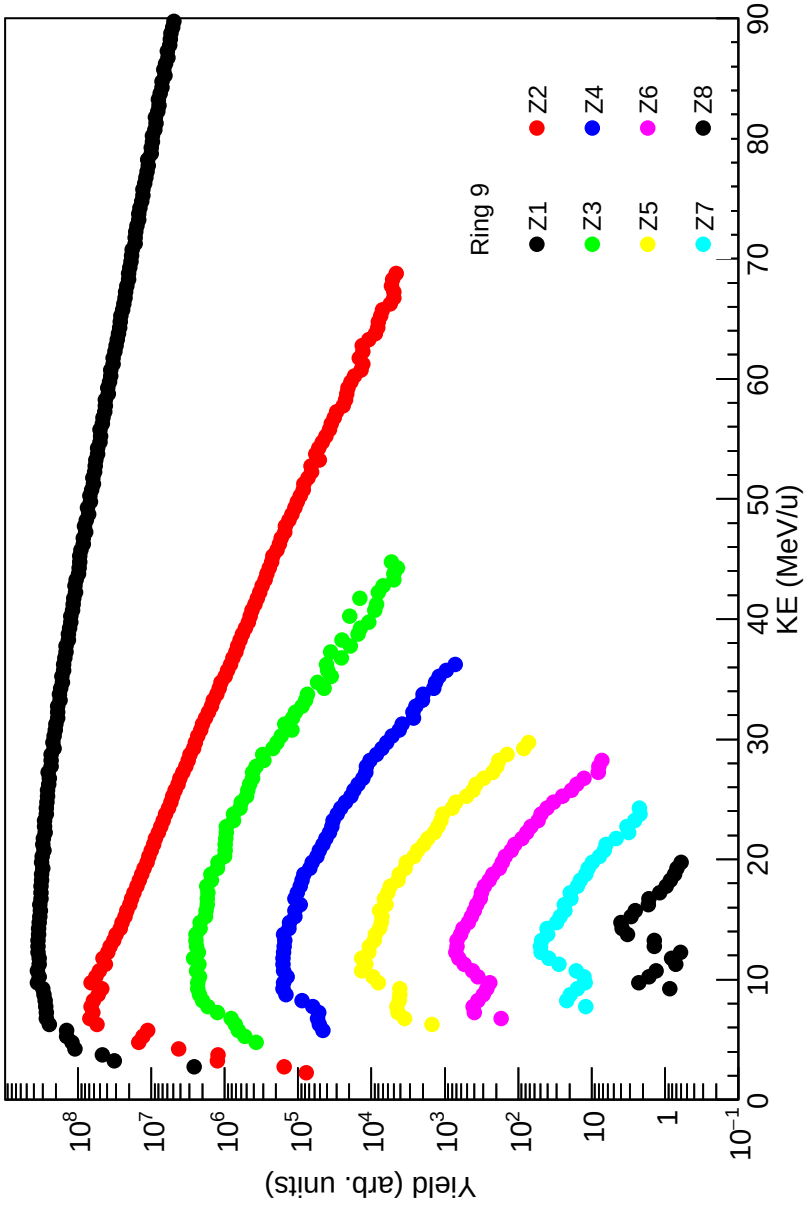

Figure A.50: Kinetic energy spectra for all elements in Ring 9 for the ^{64}Ni+^{64}Zn system.

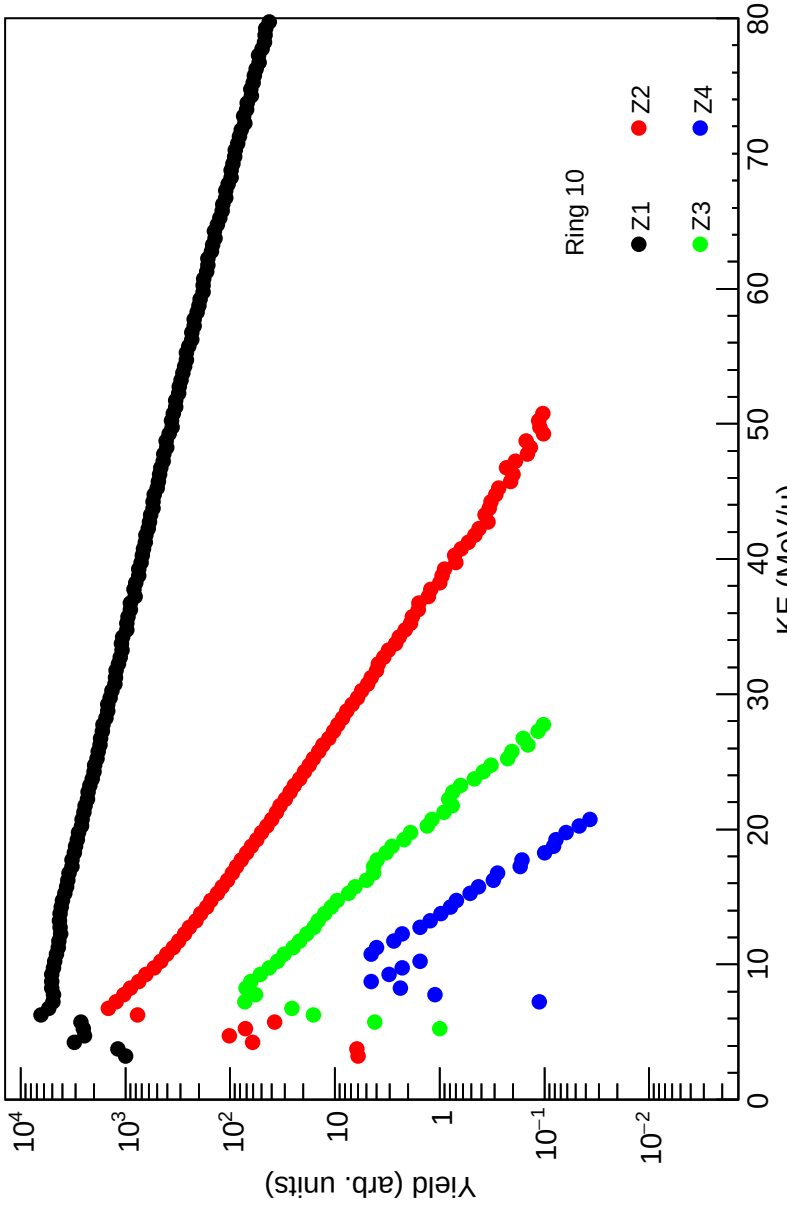

Figure A.51: Kinetic energy spectra for all elements in Ring 10 for the ^{64}Ni+^{64}Zn system.

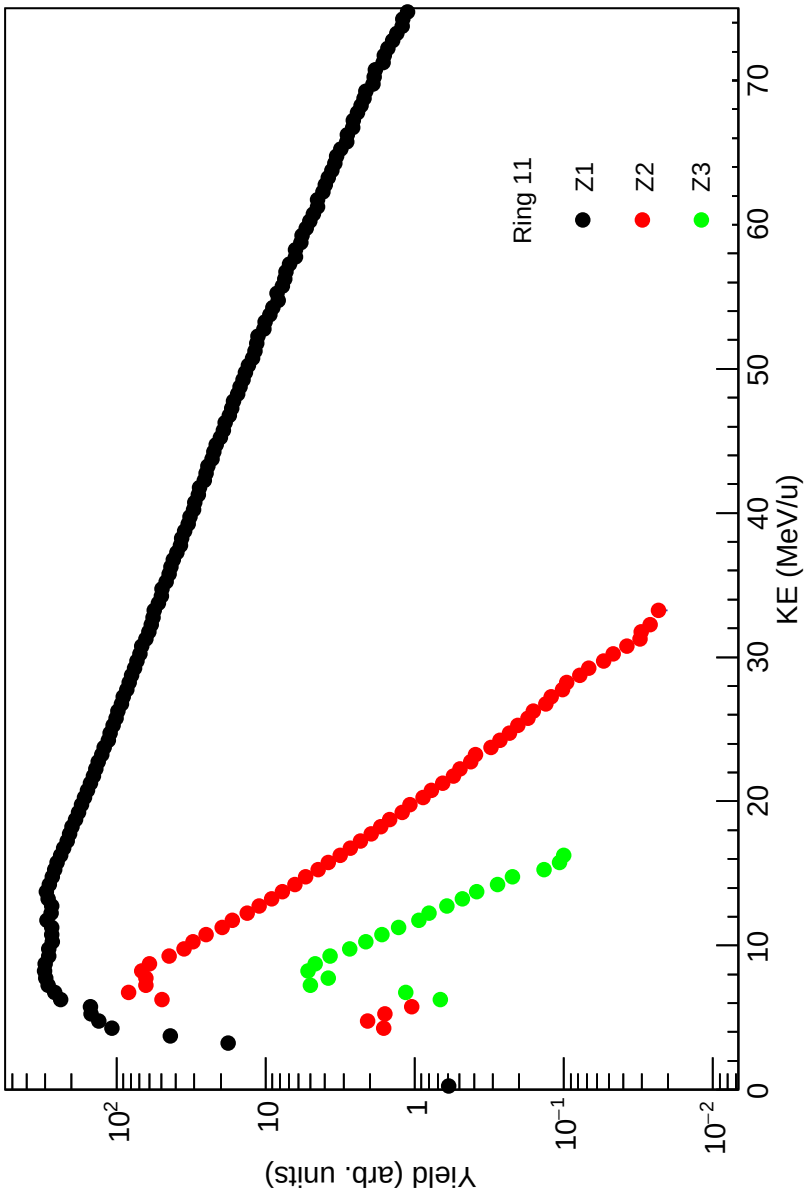

Figure A.52: Kinetic energy spectra for all elements in Ring 11 for the ^{64}Ni+^{64}Zn system.

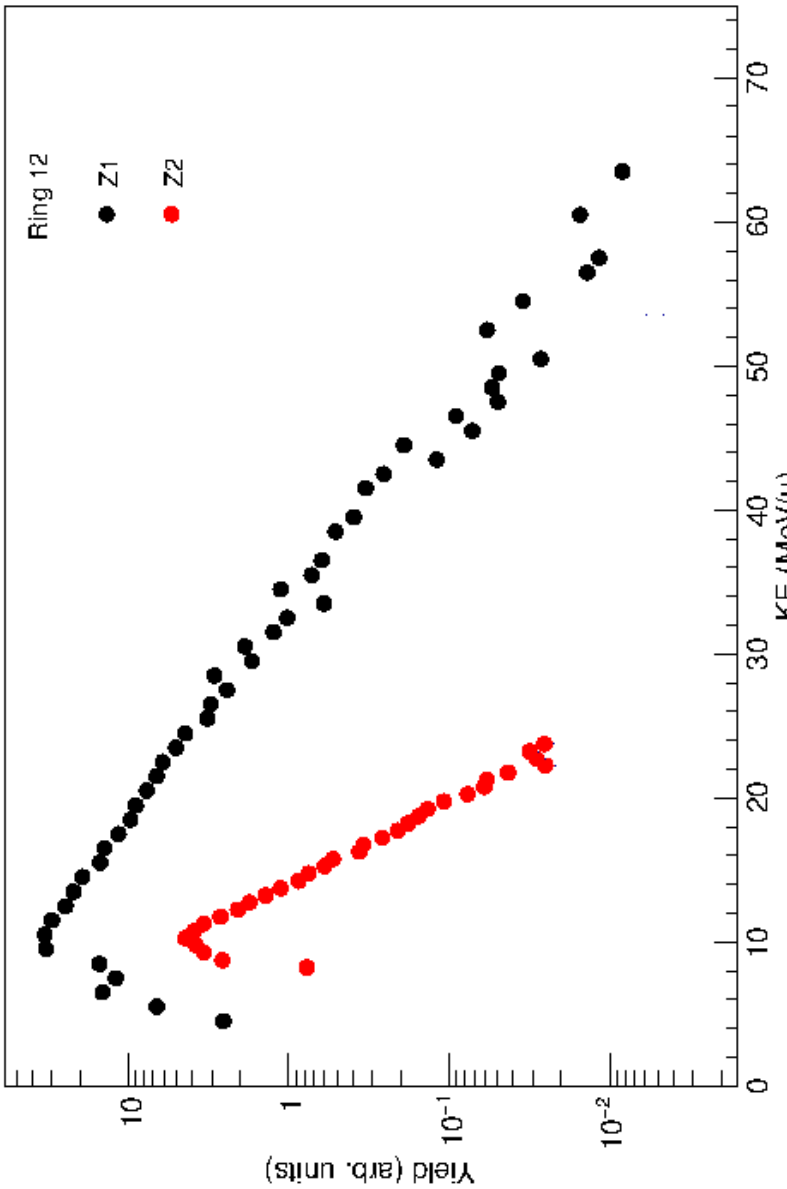

Figure A.53: Kinetic energy spectra for all elements in Ring 12 for the ^{64}Ni+^{64}Zn system.

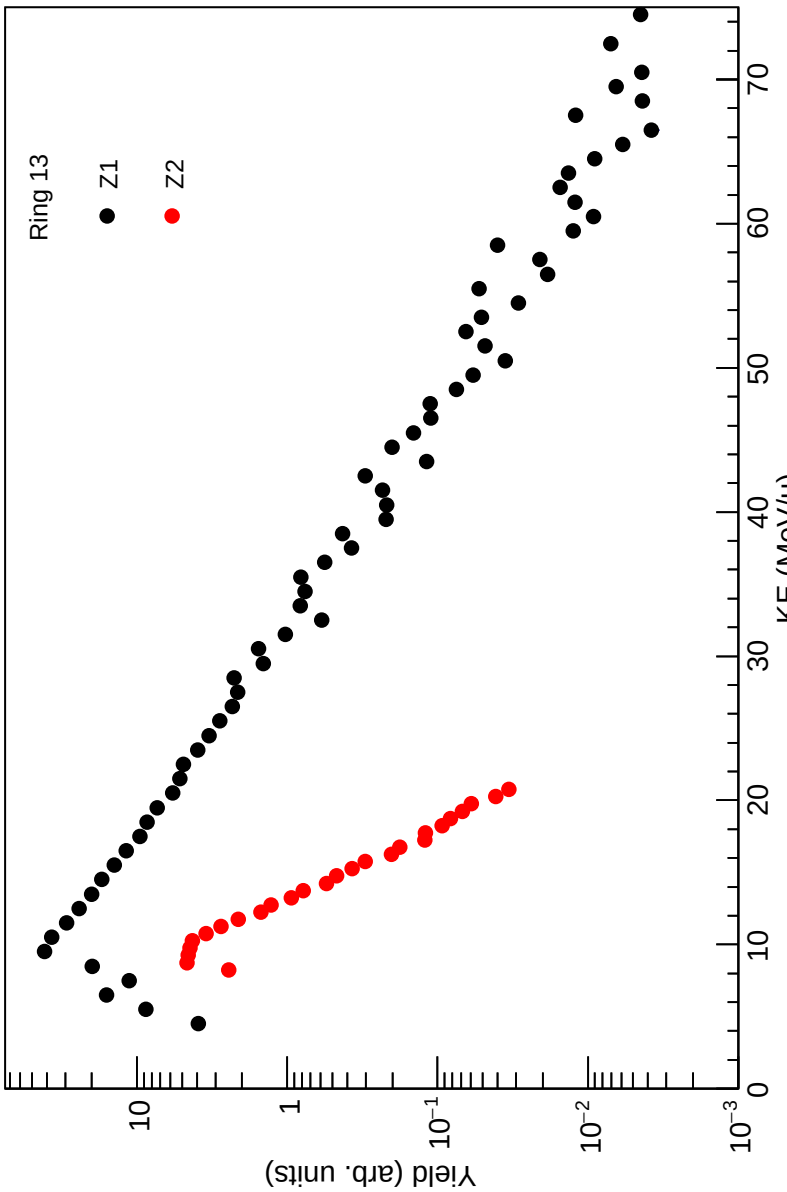

Figure A.54: Kinetic energy spectra for all elements in Ring 13 for the ^{64}Ni+^{64}Zn system.

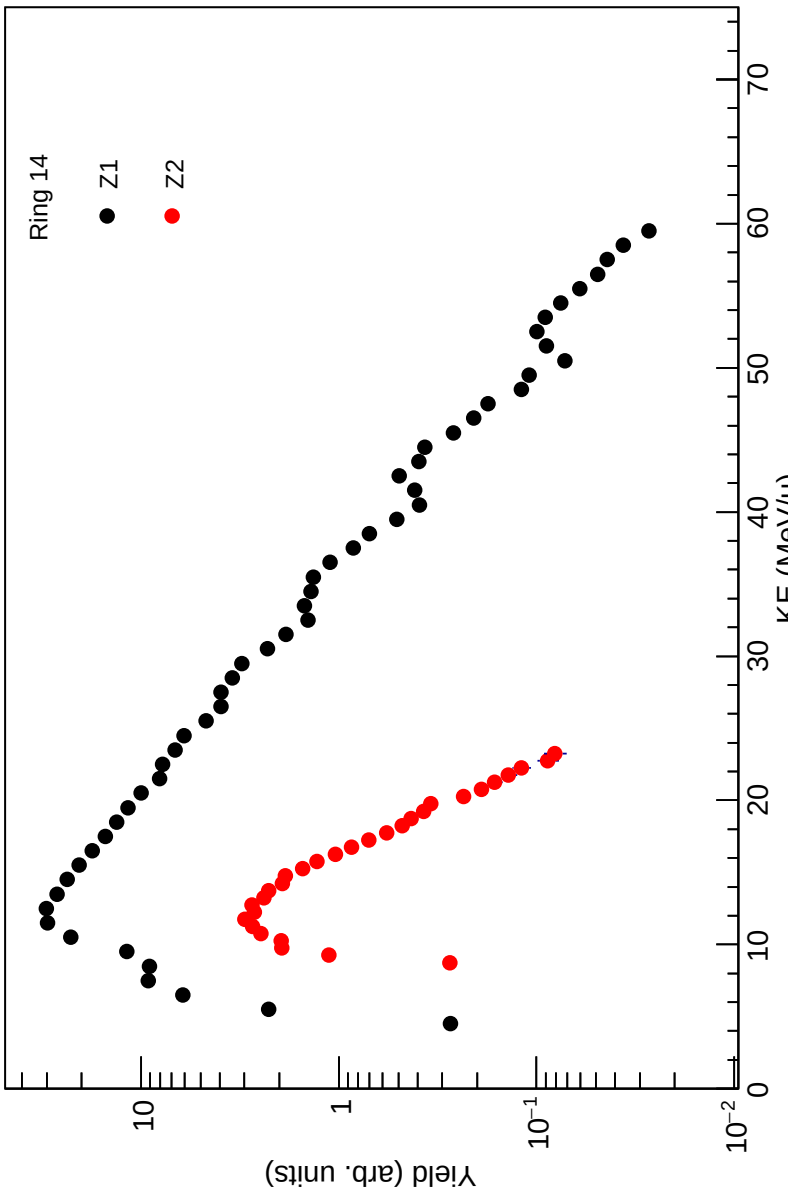

Figure A.55: Kinetic energy spectra for all elements in Ring 14 for the ^{64}Ni+^{64}Zn system.

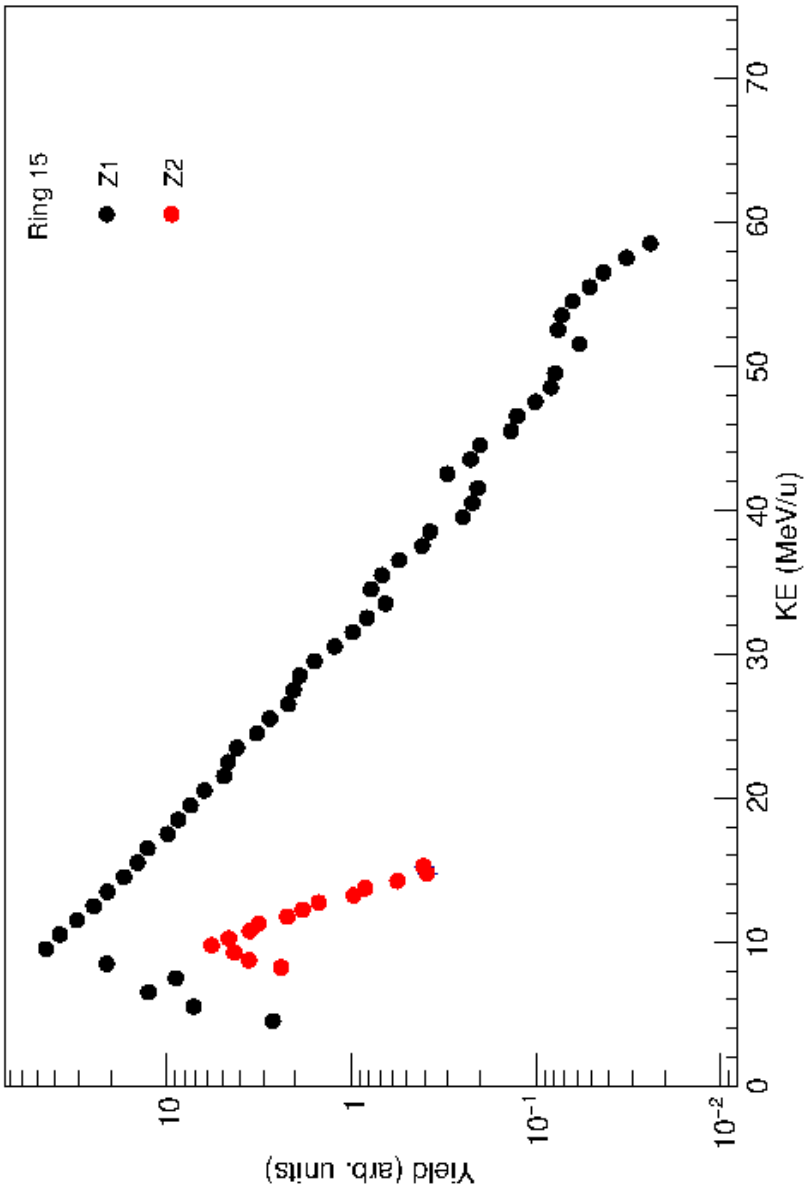

Figure A.56: Kinetic energy spectra for all elements in Ring 15 for the ^{64}Ni+^{64}Zn system.

APPENDIX B

IMPACT PARAMETER SURROGATE ANALYSIS

Additional and expanded plots from the impact parameter surrogate analysis found in Section 3.4.

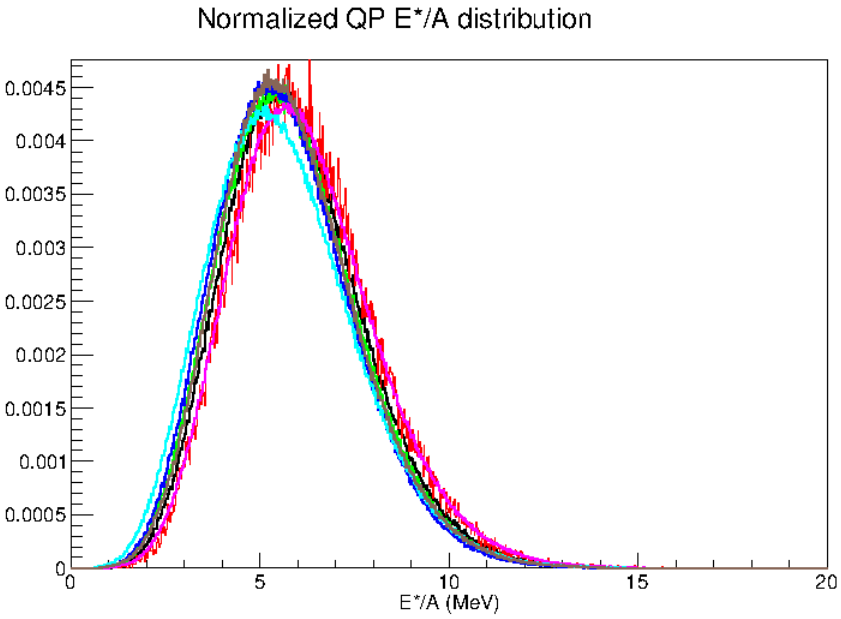

Figure B.1: The experimental E*/A distribution for all 7 reaction systems: black - ^{70}Zn+^{64}Zn, red - ^{64}Zn+^{70}Zn, green - ^{64}Zn+^{64}Ni, blue - ^{64}Ni+^{64}Zn, pink - ^{70}Zn+^{70}Zn, light blue - ^{64}Zn+^{64}Zn and brown - ^{64}Ni+^{64}Ni.

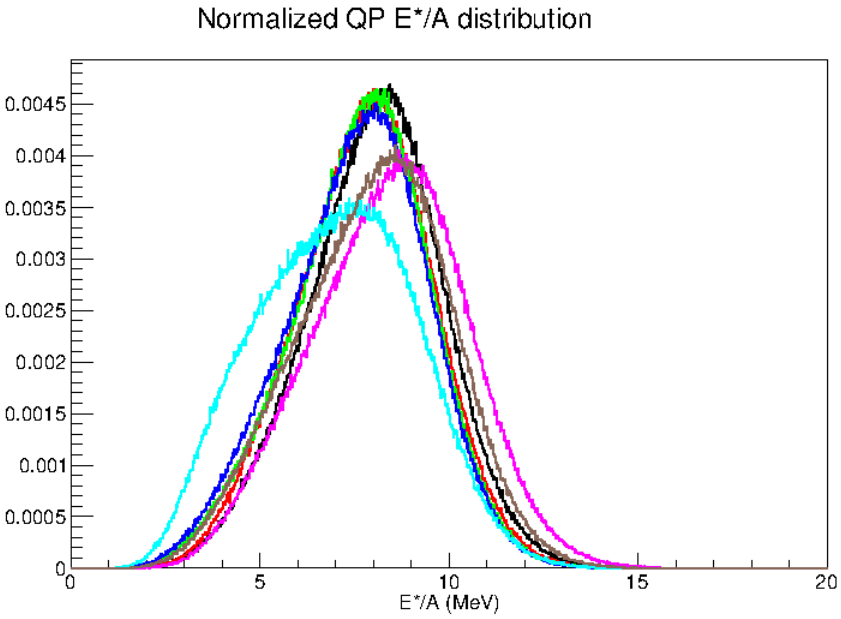

Figure B.2: The "asy-soft" CoMD E*/A distribution for all 7 reaction systems: black - ^{70}Zn+^{64}Zn, red - ^{64}Zn+^{70}Zn, green - ^{64}Zn+^{64}Ni, blue - ^{64}Ni+^{64}Zn, pink - ^{70}Zn+^{70}Zn, light blue - ^{64}Zn+^{64}Zn and brown - ^{64}Ni+^{64}Ni.

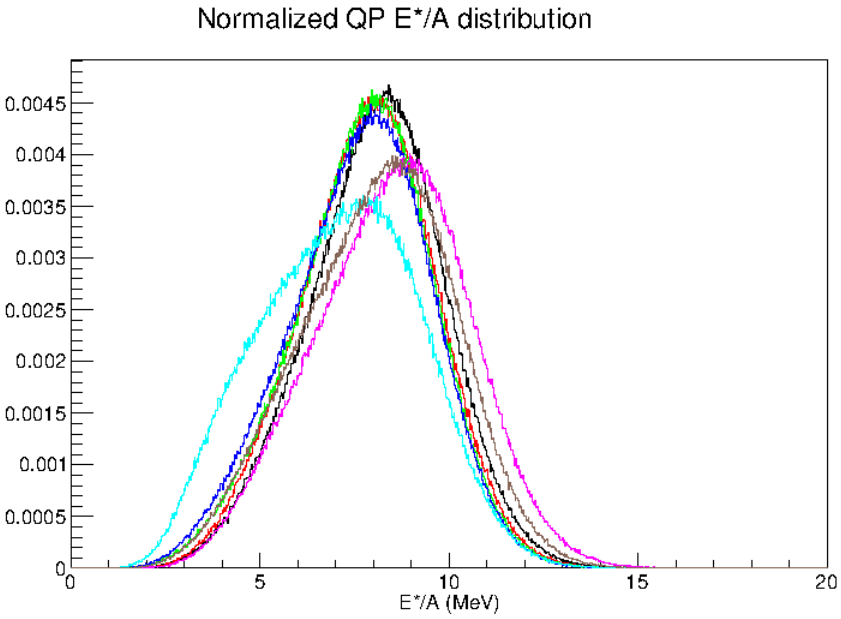

Figure B.3: The "asy-stiff" CoMD E*/A distribution for all 7 reaction systems: black - ^{70}Zn+^{64}Zn, red - ^{64}Zn+^{70}Zn, green - ^{64}Zn+^{64}Ni, blue - ^{64}Ni+^{64}Zn, pink - ^{70}Zn+^{70}Zn, light blue - ^{64}Zn+^{64}Zn and brown - ^{64}Ni+^{64}Ni.

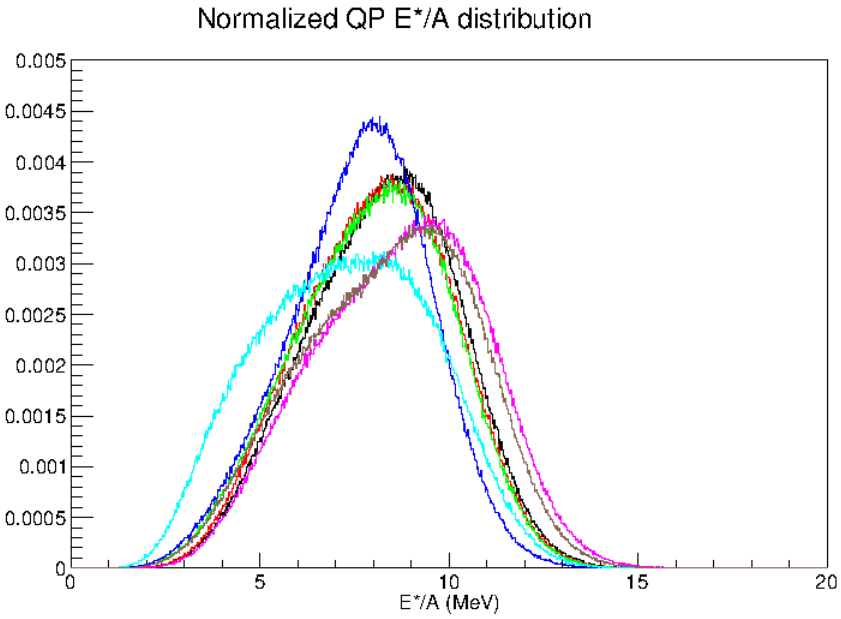

Figure B.4: The "asy-super-stiff" CoMD E*/A distribution for all 7 reaction systems: black - ^{70}Zn+^{64}Zn, red - ^{64}Zn+^{70}Zn, green - ^{64}Zn+^{64}Ni, blue - ^{64}Ni+^{64}Zn, pink - ^{70}Zn+^{70}Zn, light blue - ^{64}Zn+^{64}Zn and brown - ^{64}Ni+^{64}Ni.

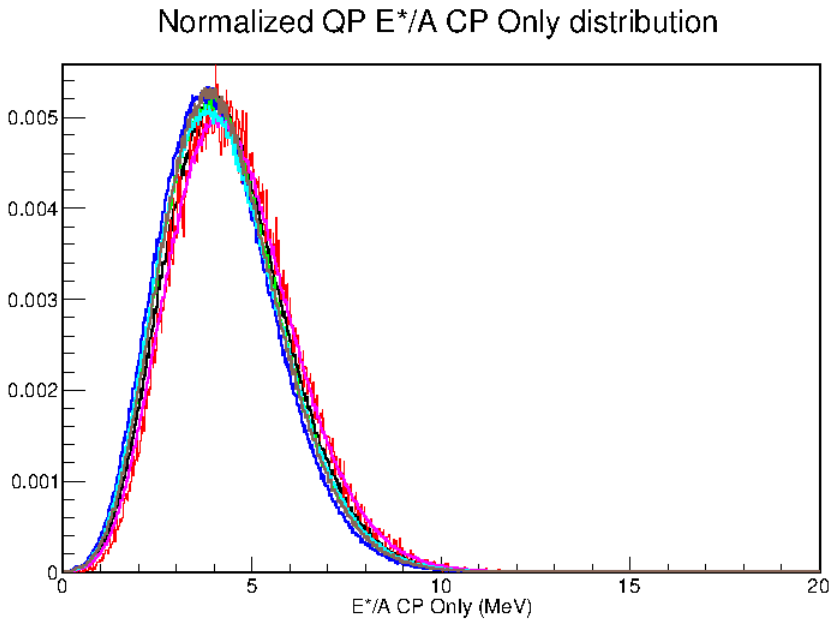

Figure B.5: The experimental E^*_{CP}/A distribution for all 7 reaction systems: black - ^{70}Zn+^{64}Zn, red - ^{64}Zn+^{70}Zn, green - ^{64}Zn+^{64}Ni, blue - ^{64}Ni+^{64}Zn, pink - ^{70}Zn+^{70}Zn, light blue - ^{64}Zn+^{64}Zn and brown - ^{64}Ni+^{64}Ni.

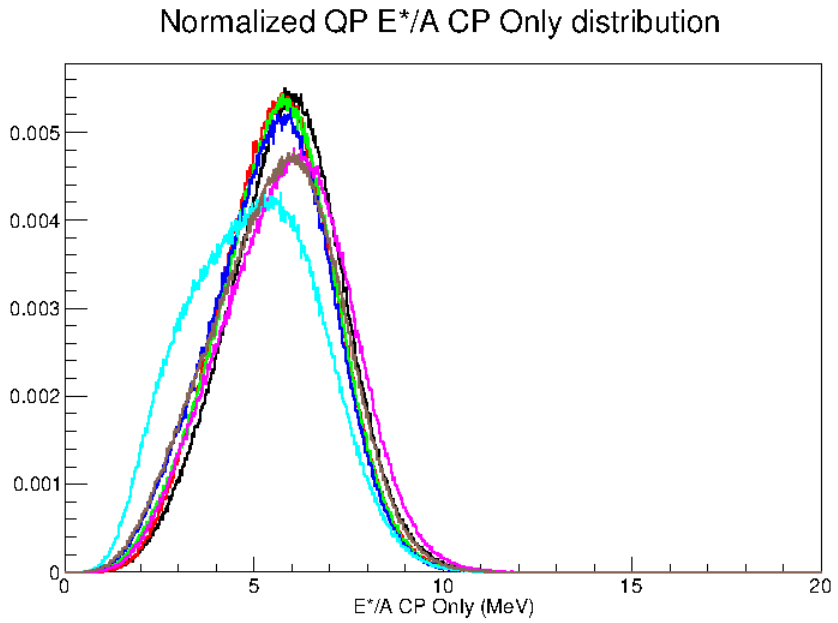

Figure B.6: The "asy-soft" CoMD E^*_{CP}/A distribution for all 7 reaction systems: black - ^{70}Zn+^{64}Zn, red - ^{64}Zn+^{70}Zn, green - ^{64}Zn+^{64}Ni, blue - ^{64}Ni+^{64}Zn, pink - ^{70}Zn+^{70}Zn, light blue - ^{64}Zn+^{64}Zn and brown - ^{64}Ni+^{64}Ni.

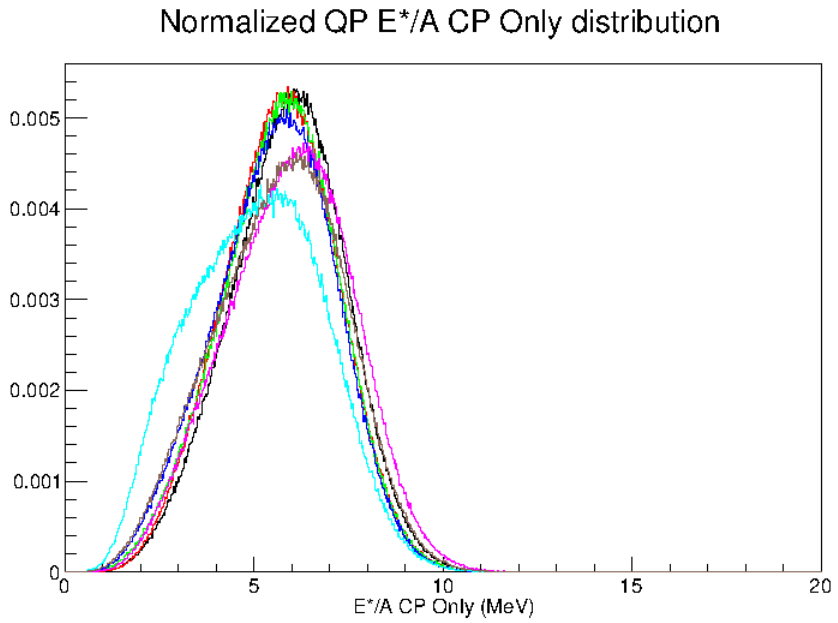

Figure B.7: The "asy-stiff" CoMD E^*_{CP}/A distribution for all 7 reaction systems: black - ^{70}Zn+^{64}Zn, red - ^{64}Zn+^{70}Zn, green - ^{64}Zn+^{64}Ni, blue - ^{64}Ni+^{64}Zn, pink - ^{70}Zn+^{70}Zn, light blue - ^{64}Zn+^{64}Zn and brown - ^{64}Ni+^{64}Ni.

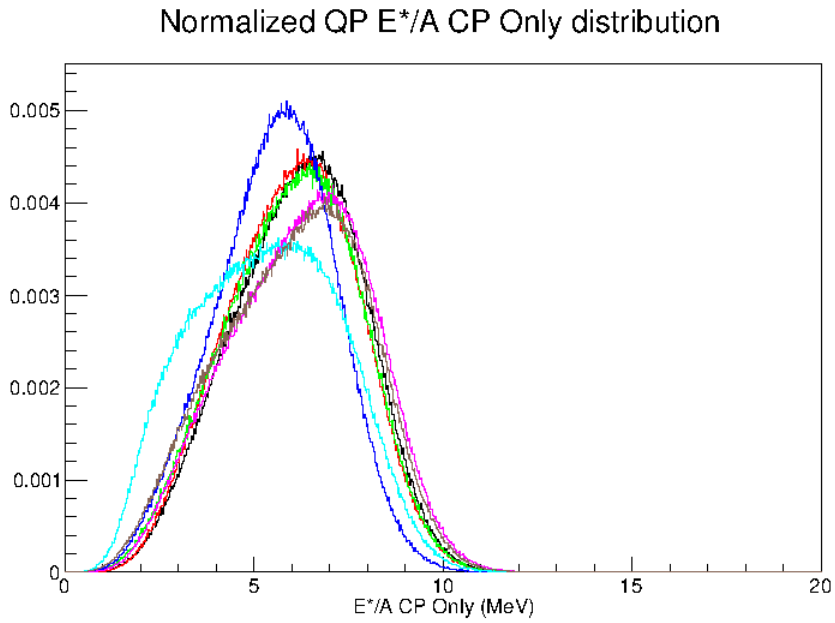

Figure B.8: The "asy-super-stiff" CoMD E^*_{CP}/A distribution for all 7 reaction systems: black - ^{70}Zn+^{64}Zn, red - ^{64}Zn+^{70}Zn, green - ^{64}Zn+^{64}Ni, blue - ^{64}Ni+^{64}Zn, pink - ^{70}Zn+^{70}Zn, light blue - ^{64}Zn+^{64}Zn and brown - ^{64}Ni+^{64}Ni.

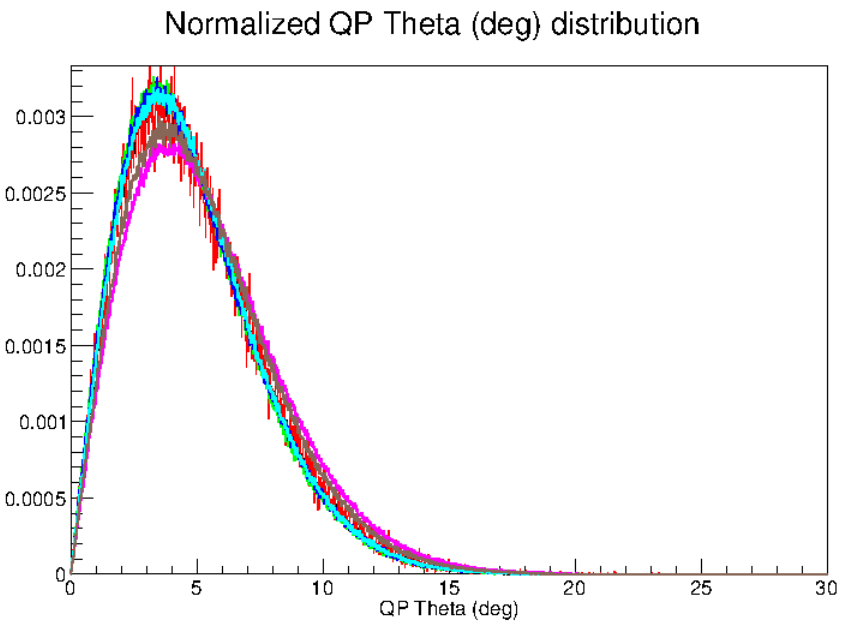

Figure B.9: The experimental θ_{QP} distribution for all 7 reaction systems: black - ^{70}Zn+^{64}Zn, red - ^{64}Zn+^{70}Zn, green - ^{64}Zn+^{64}Ni, blue - ^{64}Ni+^{64}Zn, pink - ^{70}Zn+^{70}Zn, light blue - ^{64}Zn+^{64}Zn and brown - ^{64}Ni+^{64}Ni.

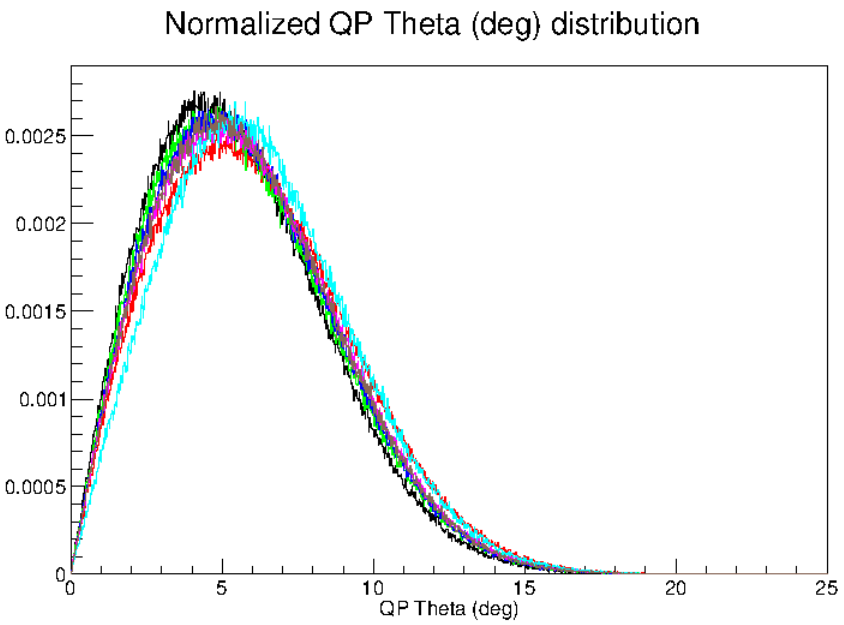

Figure B.10: The "asy-soft" CoMD θ_{QP} distribution for all 7 reaction systems: black - ^{70}Zn+^{64}Zn, red - ^{64}Zn+^{70}Zn, green - ^{64}Zn+^{64}Ni, blue - ^{64}Ni+^{64}Zn, pink - ^{70}Zn+^{70}Zn, light blue - ^{64}Zn+^{64}Zn and brown - ^{64}Ni+^{64}Ni.

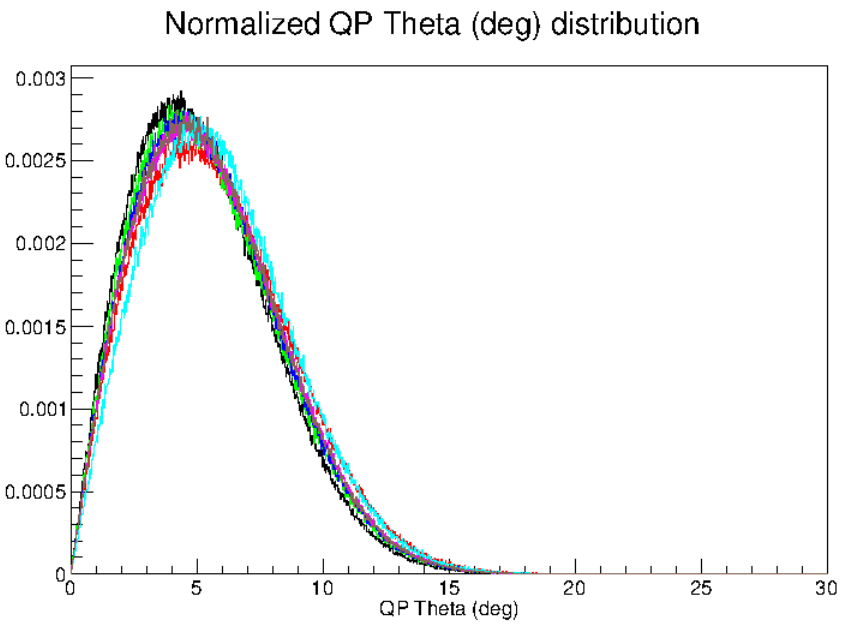

Figure B.11: The "asy-stiff" CoMD θ_{QP} distribution for all 7 reaction systems: black - ^{70}Zn+^{64}Zn, red - ^{64}Zn+^{70}Zn, green - ^{64}Zn+^{64}Ni, blue - ^{64}Ni+^{64}Zn, pink - ^{70}Zn+^{70}Zn, light blue - ^{64}Zn+^{64}Zn and brown - ^{64}Ni+^{64}Ni.

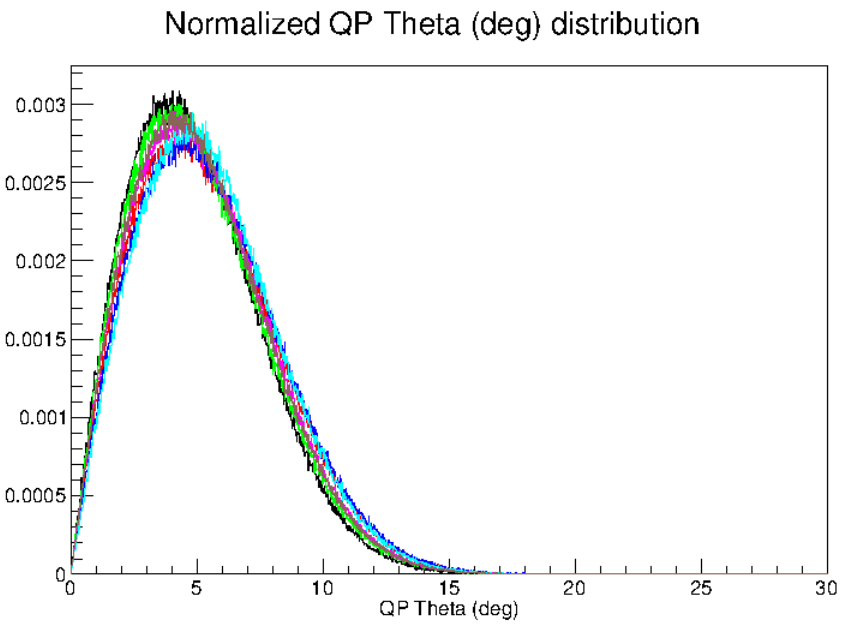

Figure B.12: The "asy-super-stiff" CoMD θ_{QP} distribution for all 7 reaction systems: black - ^{70}Zn+^{64}Zn, red - ^{64}Zn+^{70}Zn, green - ^{64}Zn+^{64}Ni, blue - ^{64}Ni+^{64}Zn, pink - ^{70}Zn+^{70}Zn, light blue - ^{64}Zn+^{64}Zn and brown - ^{64}Ni+^{64}Ni.

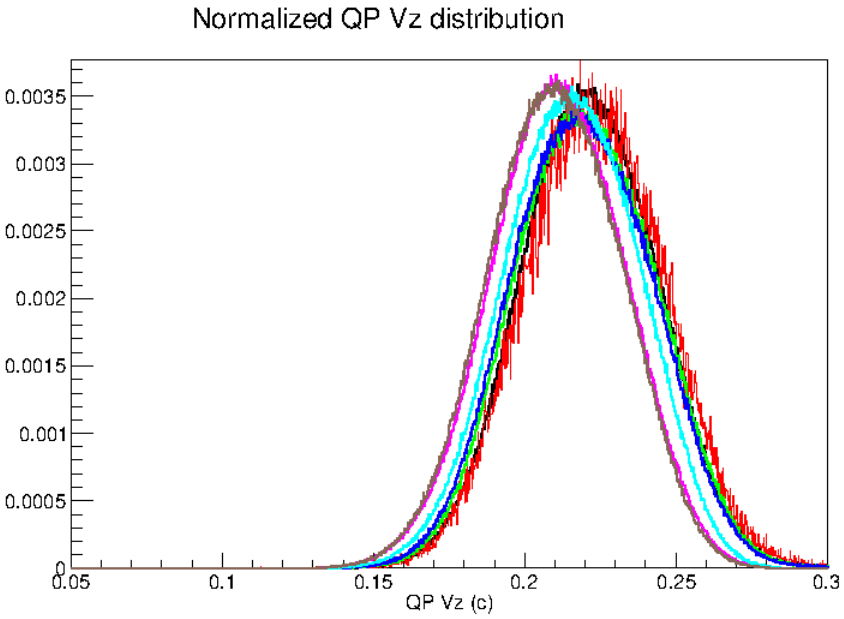

Figure B.13: The experimental $V_{z,QP}$ distribution for all 7 reaction systems: black - ^{70}Zn+^{64}Zn, red - ^{64}Zn+^{70}Zn, green - ^{64}Zn+^{64}Ni, blue - ^{64}Ni+^{64}Zn, pink - ^{70}Zn+^{70}Zn, light blue - ^{64}Zn+^{64}Zn and brown - ^{64}Ni+^{64}Ni.

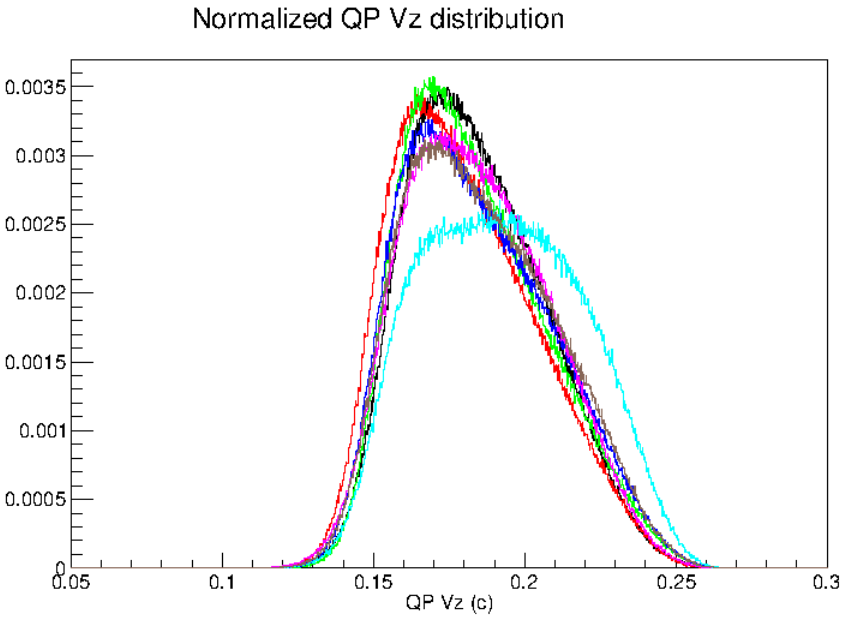

Figure B.14: The "asy-soft" CoMD $V_{z,QP}$ distribution for all 7 reaction systems: black - ^{70}Zn+^{64}Zn, red - ^{64}Zn+^{70}Zn, green - ^{64}Zn+^{64}Ni, blue - ^{64}Ni+^{64}Zn, pink - ^{70}Zn+^{70}Zn, light blue - ^{64}Zn+^{64}Zn and brown - ^{64}Ni+^{64}Ni.

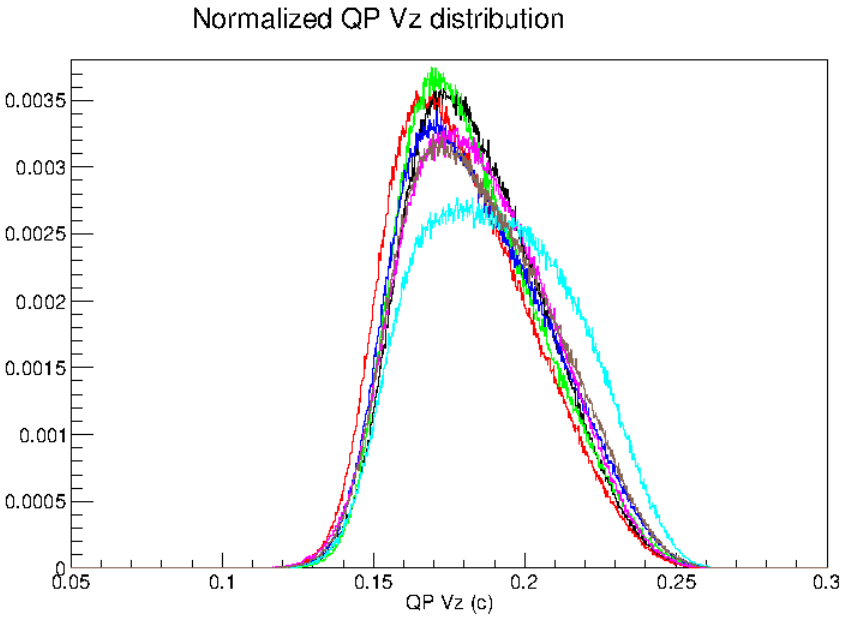

Figure B.15: The "asy-stiff" CoMD $V_{z,QP}$ distribution for all 7 reaction systems: black - ^{70}Zn+^{64}Zn, red - ^{64}Zn+^{70}Zn, green - ^{64}Zn+^{64}Ni, blue - ^{64}Ni+^{64}Zn, pink - ^{70}Zn+^{70}Zn, light blue - ^{64}Zn+^{64}Zn and brown - ^{64}Ni+^{64}Ni.

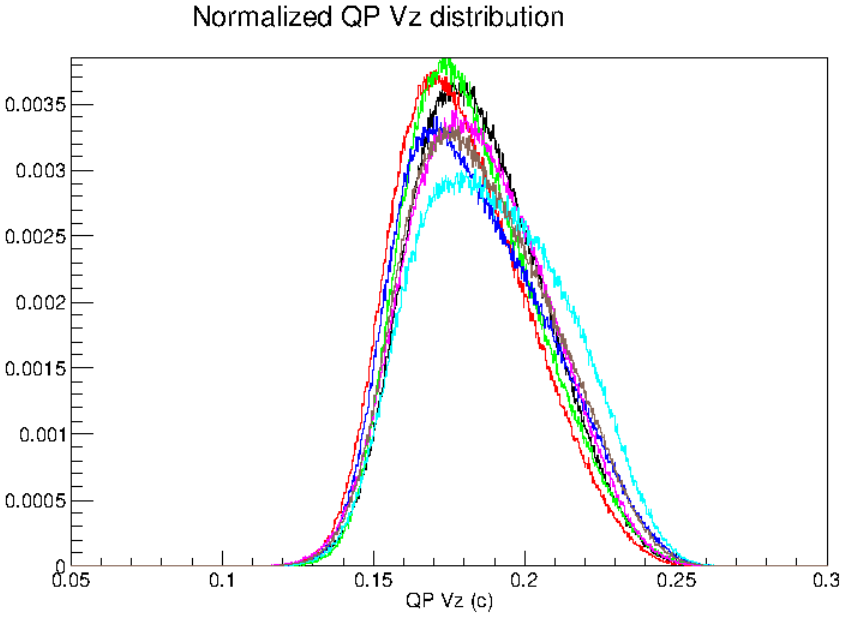

Figure B.16: The "asy-super-stiff" CoMD $V_{z,QP}$ distribution for all 7 reaction systems: black - ^{70}Zn+^{64}Zn, red - ^{64}Zn+^{70}Zn, green - ^{64}Zn+^{64}Ni, blue - ^{64}Ni+^{64}Zn, pink - ^{70}Zn+^{70}Zn, light blue - ^{64}Zn+^{64}Zn and brown - ^{64}Ni+^{64}Ni.

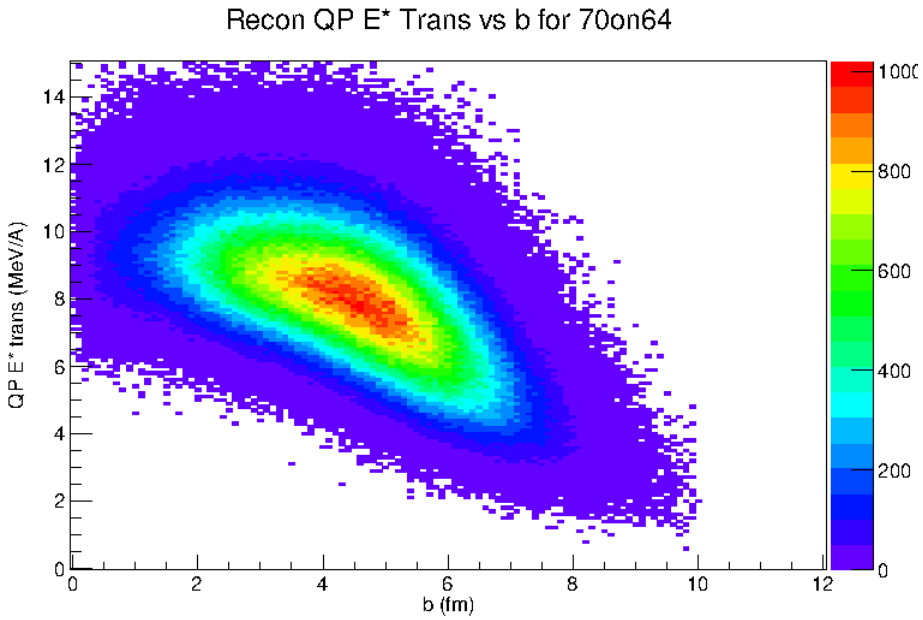

Figure B.17: The "asy-soft" CoMD E*/A as a function of impact parameter b for the ^{70}Zn+^{64}Zn reaction system.

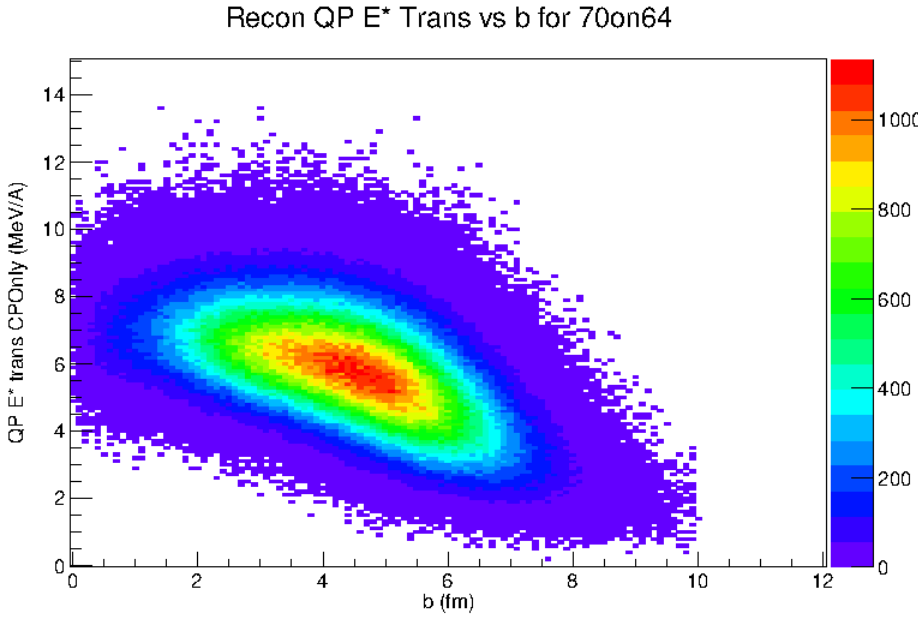

Figure B.18: The "asy-soft" CoMD E^*_{CP}/A as a function of impact parameter b for the ^{70}Zn+^{64}Zn reaction system.

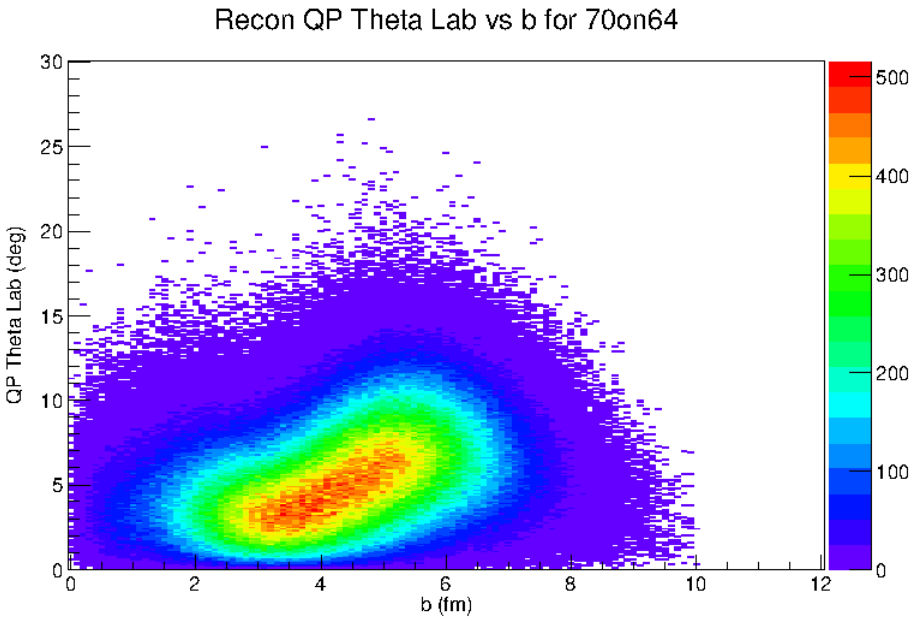

Figure B.19: The "asy-soft" CoMD θ_{QP} as a function of impact parameter b for the ^{70}Zn+^{64}Zn reaction system.

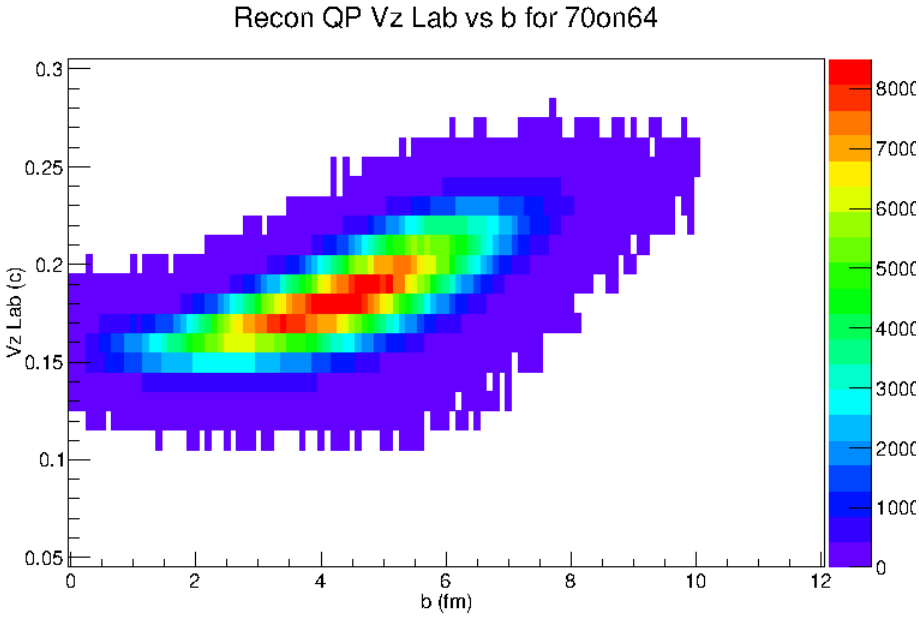

Figure B.20: The "asy-soft" CoMD $V_{z,QP}$ as a function of impact parameter b for the ^{70}Zn+^{64}Zn reaction system.

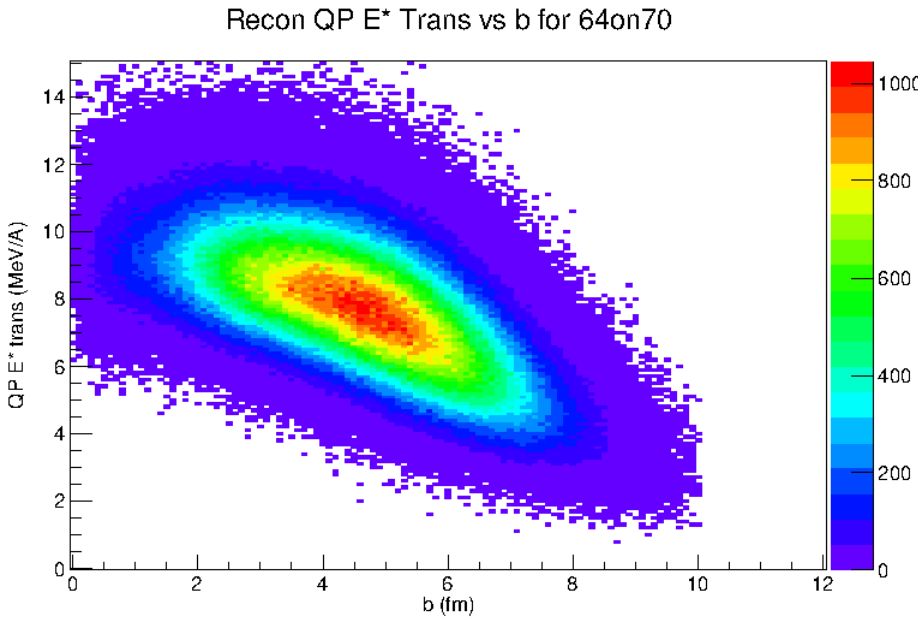

Figure B.21: The "asy-soft" CoMD E*/A as a function of impact parameter b for the ^{64}Zn+^{70}Zn reaction system.

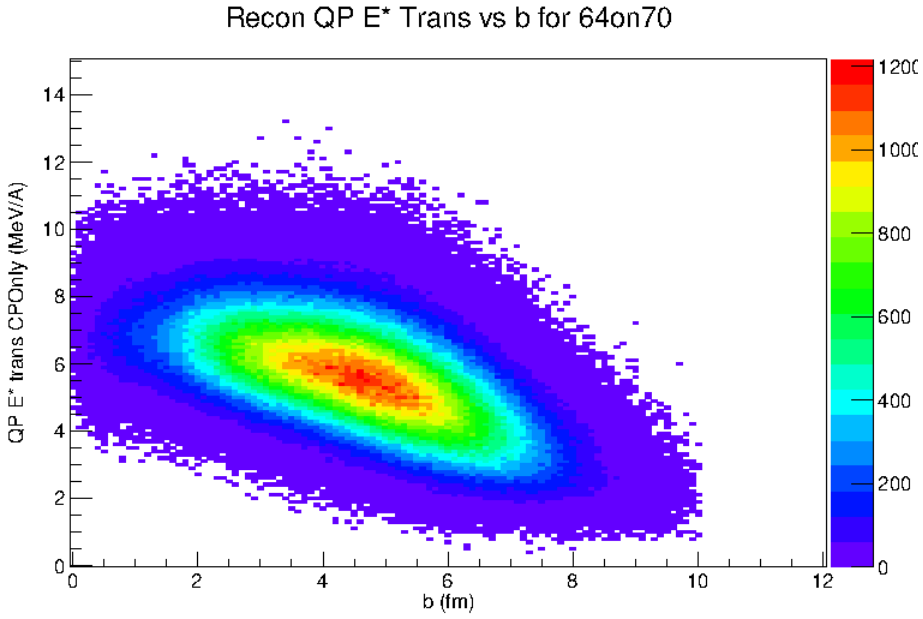

Figure B.22: The "asy-soft" CoMD E^*_{CP}/A as a function of impact parameter b for the ^{64}Zn+^{70}Zn reaction system.

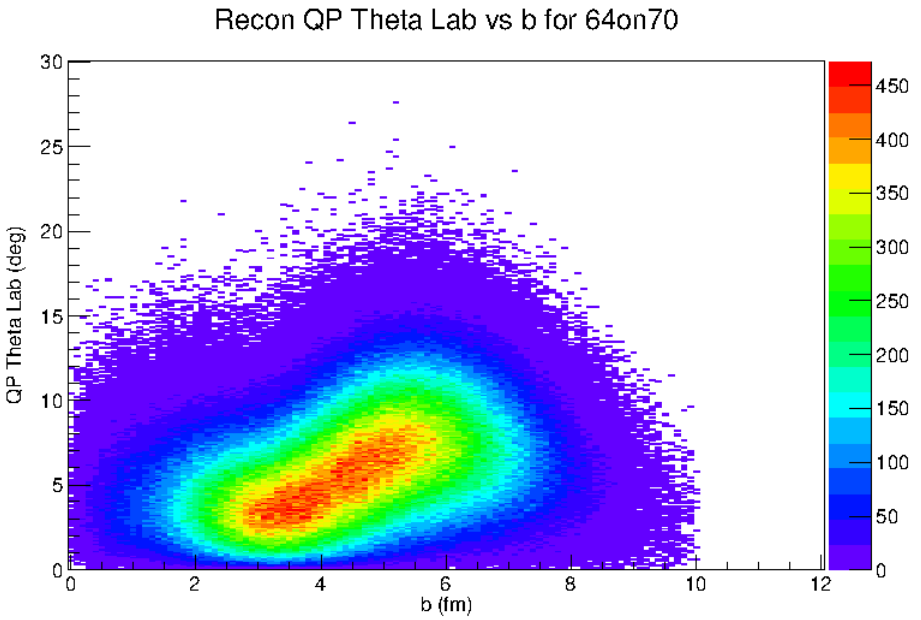

Figure B.23: The "asy-soft" CoMD θ_{QP} as a function of impact parameter b for the ^{64}Zn+^{70}Zn reaction system.

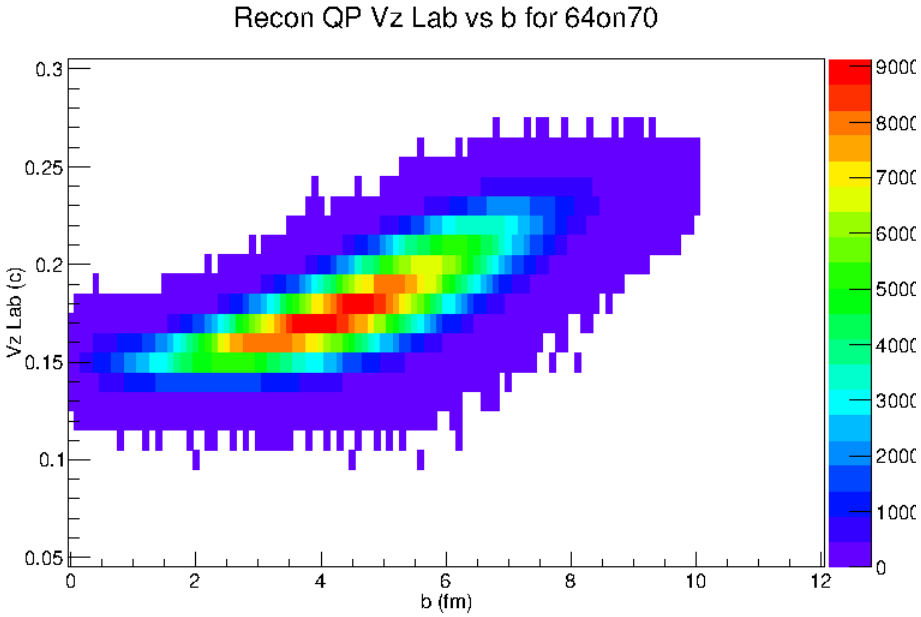

Figure B.24: The "asy-soft" CoMD $V_{z,QP}$ as a function of impact parameter b for the ^{64}Zn+^{70}Zn reaction system.

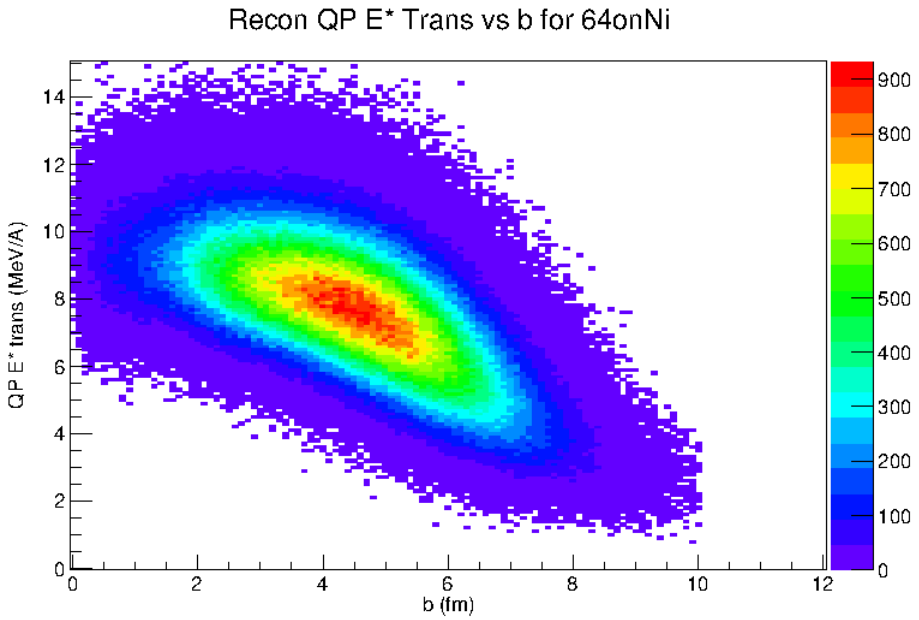

Figure B.25: The "asy-soft" CoMD E*/A as a function of impact parameter b for the ^{64}Zn+^{64}Ni reaction system.

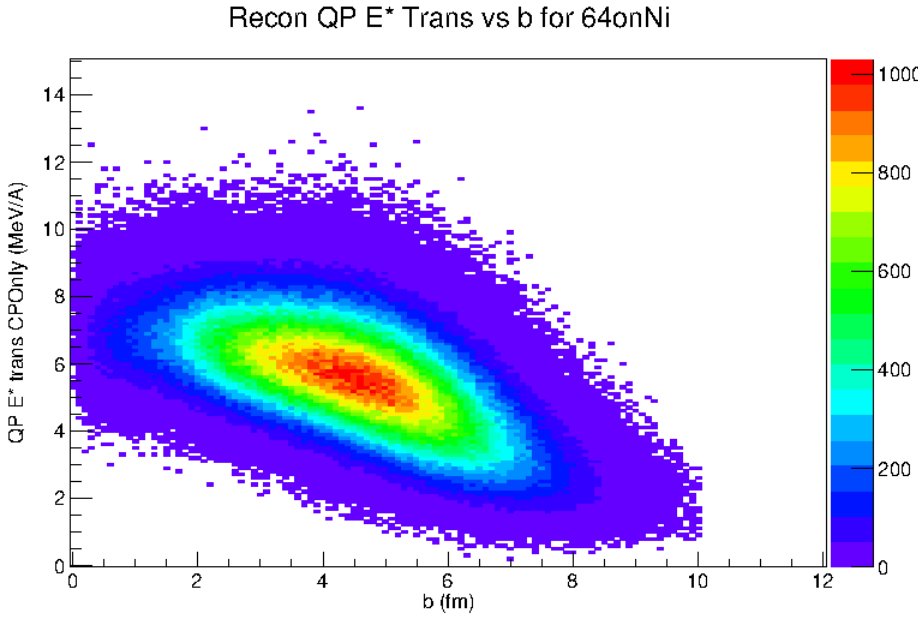

Figure B.26: The "asy-soft" CoMD E^*_{CP}/A as a function of impact parameter b for the ^{64}Zn+^{64}Ni reaction system.

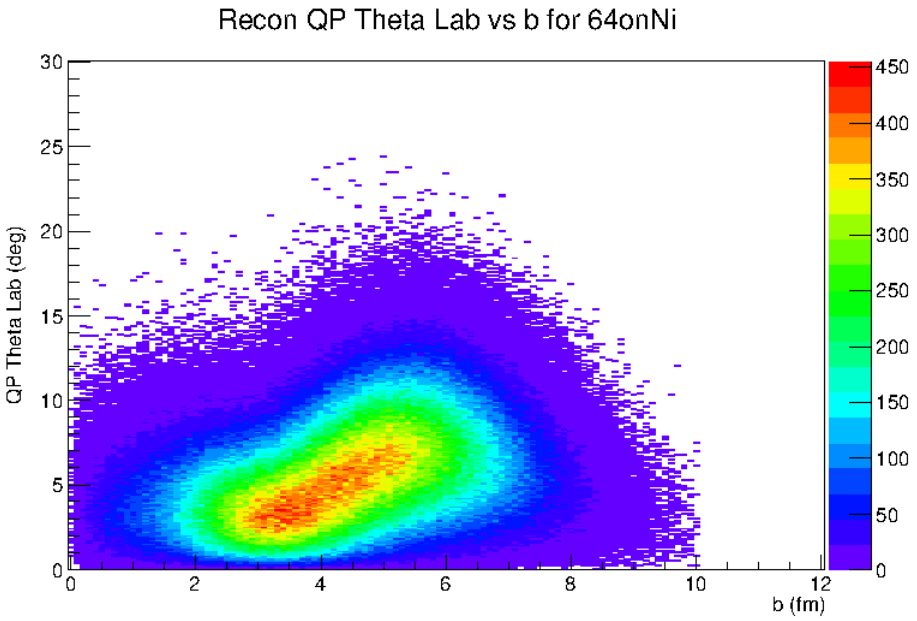

Figure B.27: The "asy-soft" CoMD θ_{QP} as a function of impact parameter b for the ^{64}Zn+^{64}Ni reaction system.

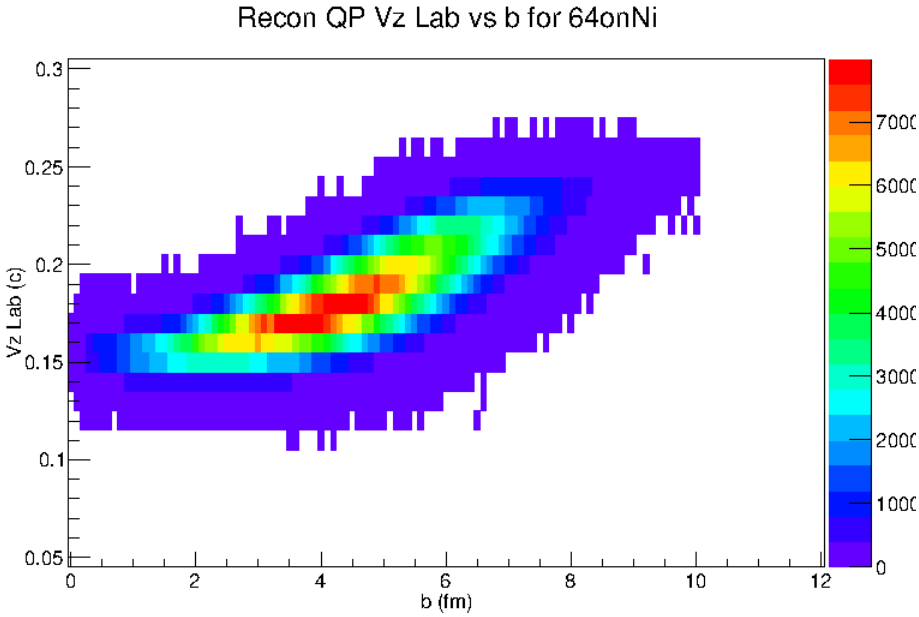

Figure B.28: The "asy-soft" CoMD $V_{z,QP}$ as a function of impact parameter b for the ^{64}Zn+^{64}Ni reaction system.

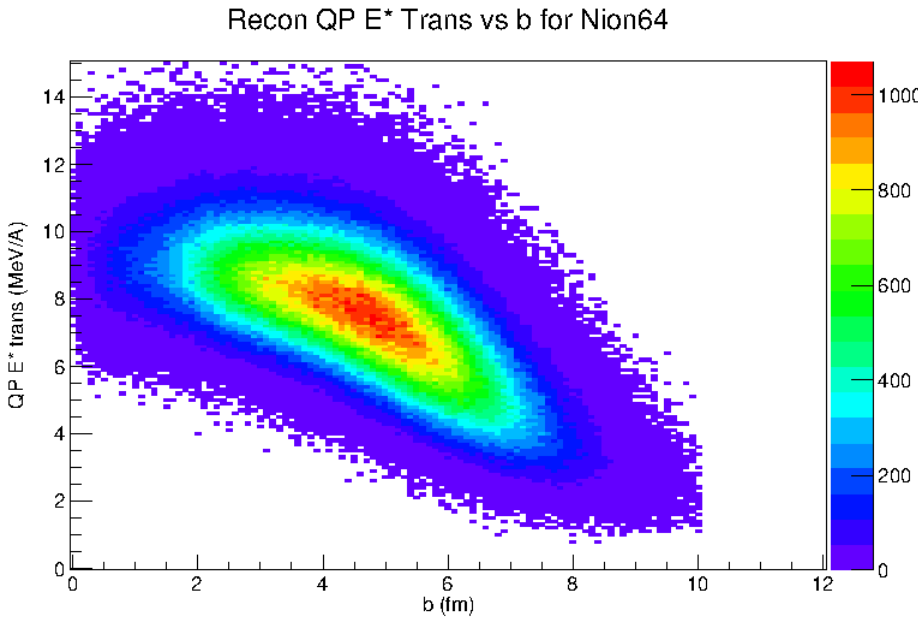

Figure B.29: The "asy-soft" CoMD E*/A as a function of impact parameter b for the ^{64}Ni+^{64}Zn reaction system.

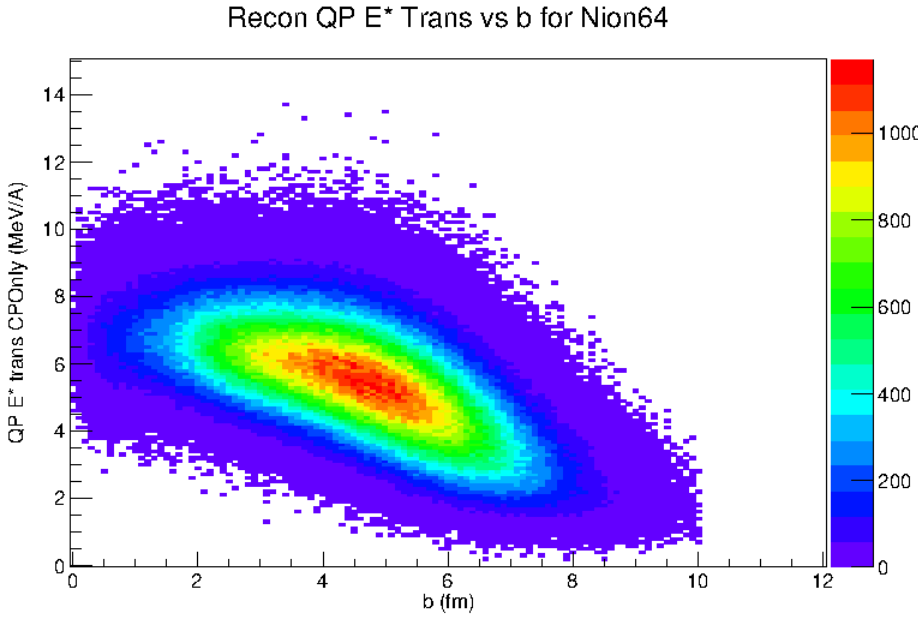

Figure B.30: The "asy-soft" CoMD E^*_{CP}/A as a function of impact parameter b for the ^{64}Ni+^{64}Zn reaction system.

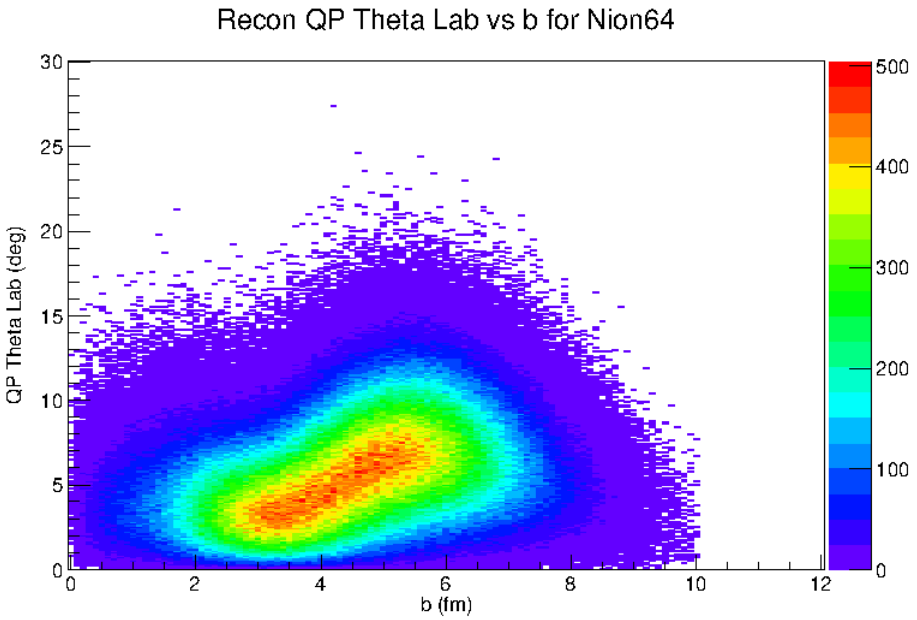

Figure B.31: The "asy-soft" CoMD θ_{QP} as a function of impact parameter b for the ^{64}Ni+^{64}Zn reaction system.

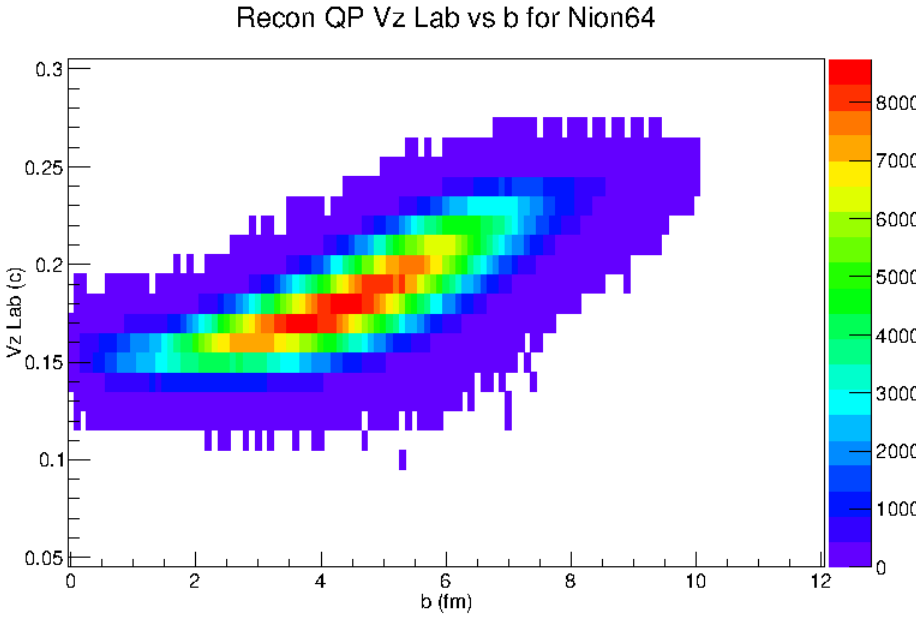

Figure B.32: The "asy-soft" CoMD $V_{z,QP}$ as a function of impact parameter b for the ^{64}Ni+^{64}Zn reaction system.

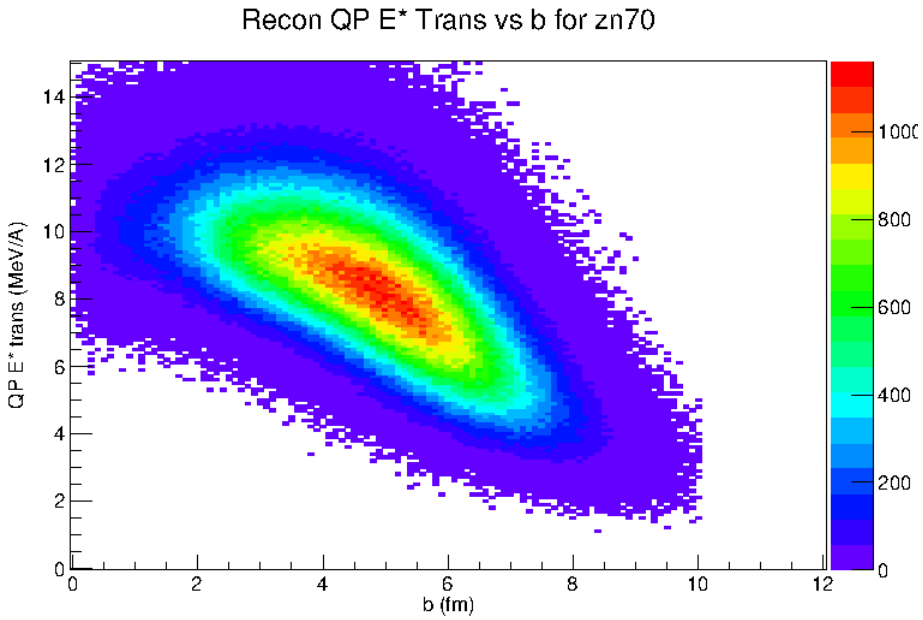

Figure B.33: The "asy-soft" CoMD E*/A as a function of impact parameter b for the ^{70}Zn+^{70}Zn reaction system.

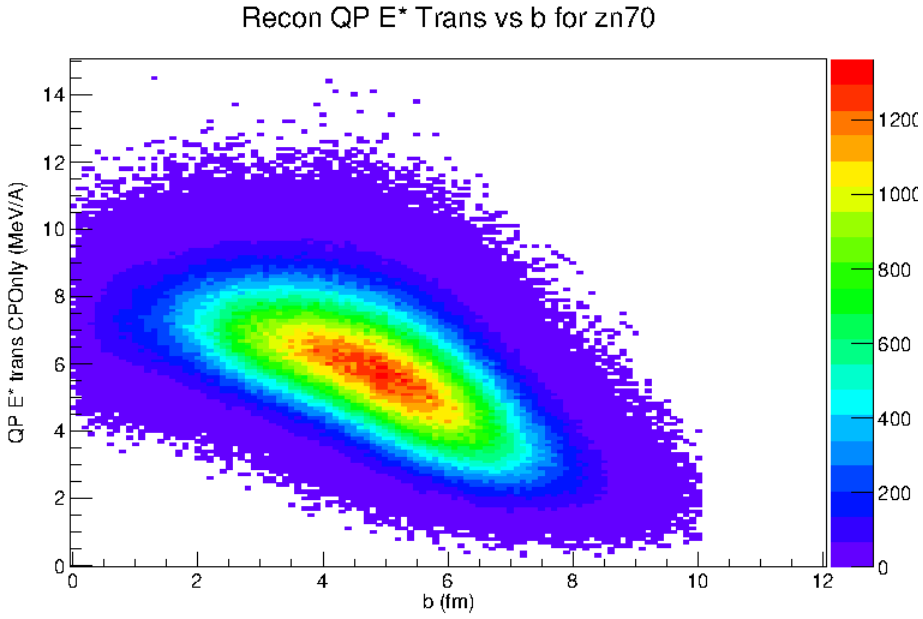

Figure B.34: The "asy-soft" CoMD E^*_{CP}/A as a function of impact parameter b for the ^{70}Zn+^{70}Zn reaction system.

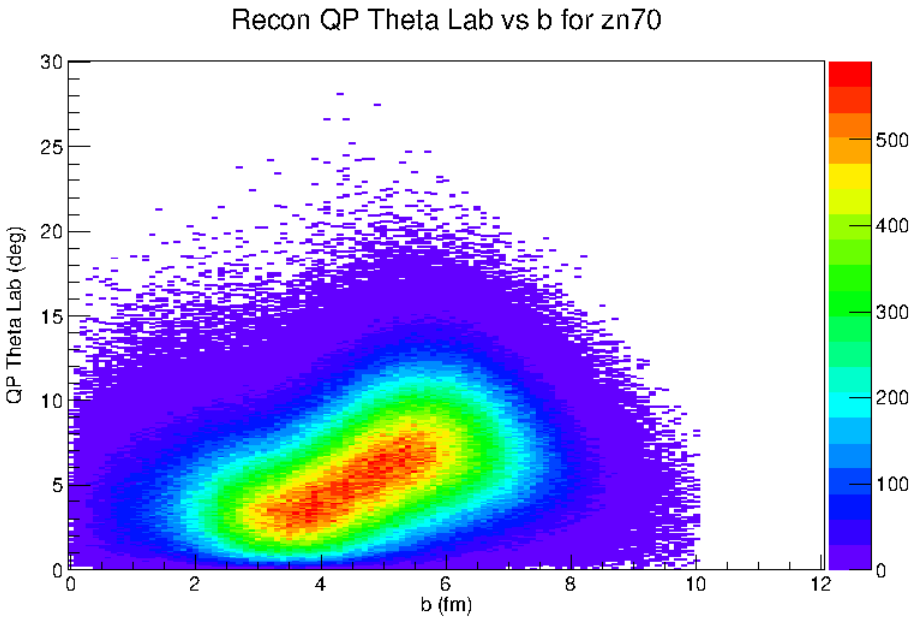

Figure B.35: The "asy-soft" CoMD θ_{QP} as a function of impact parameter b for the ^{70}Zn+^{70}Zn reaction system.

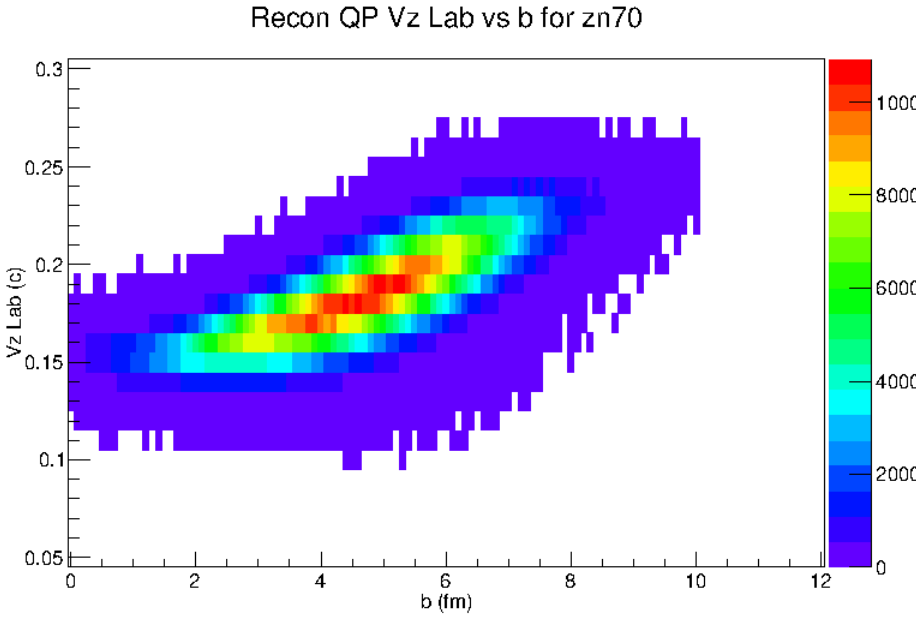

Figure B.36: The "asy-soft" CoMD $V_{z,QP}$ as a function of impact parameter b for the ^{70}Zn+^{70}Zn reaction system.

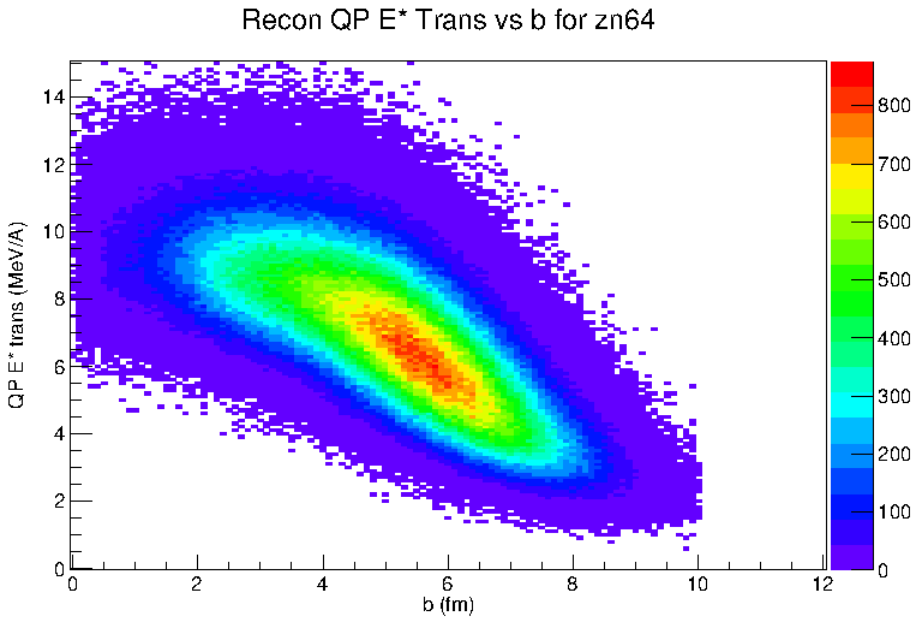

Figure B.37: The "asy-soft" CoMD E*/A as a function of impact parameter b for the ^{64}Zn+^{64}Zn reaction system.

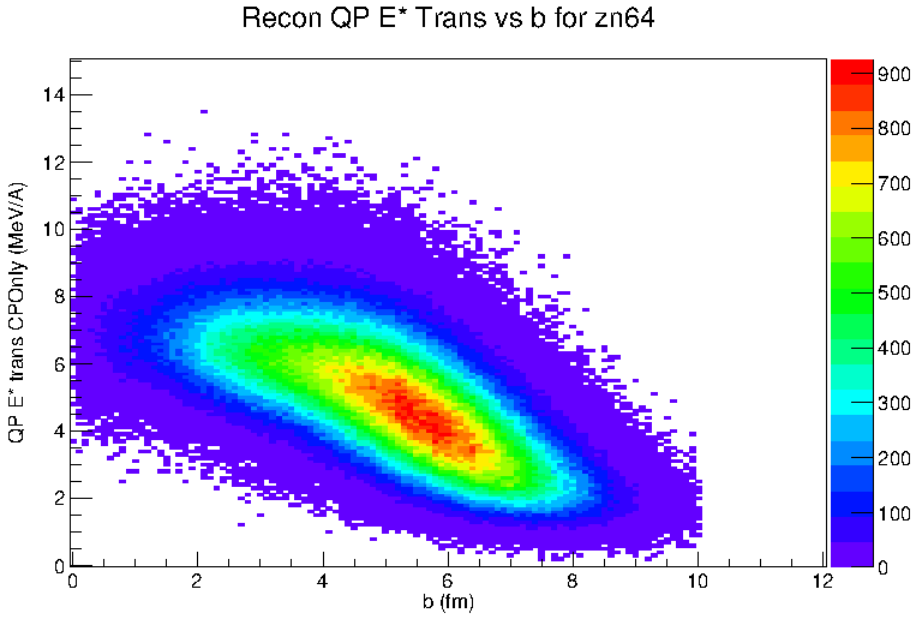

Figure B.38: The "asy-soft" CoMD E^*_{CP}/A as a function of impact parameter b for the ^{64}Zn+^{64}Zn reaction system.

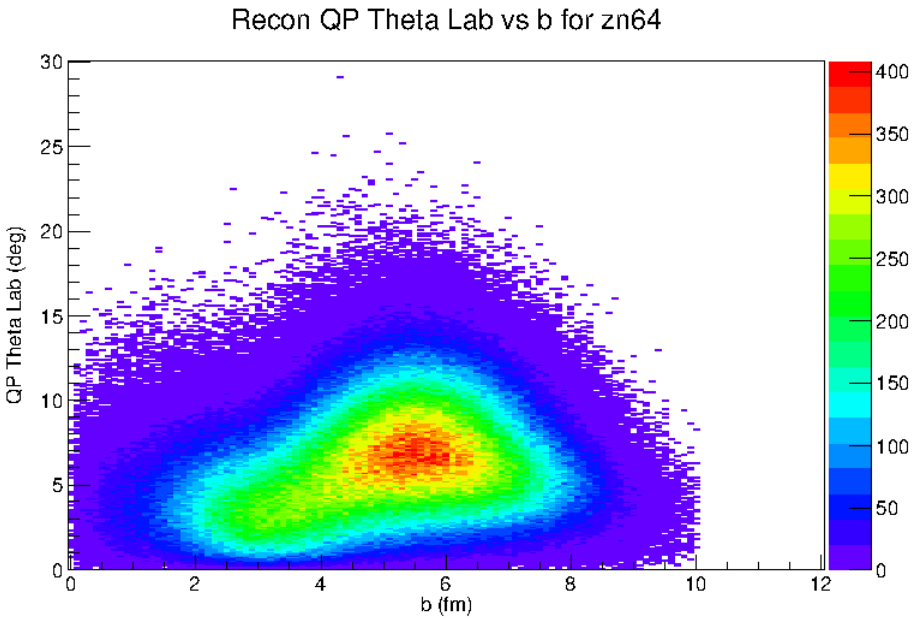

Figure B.39: The "asy-soft" CoMD θ_{QP} as a function of impact parameter b for the ^{64}Zn+^{64}Zn reaction system.

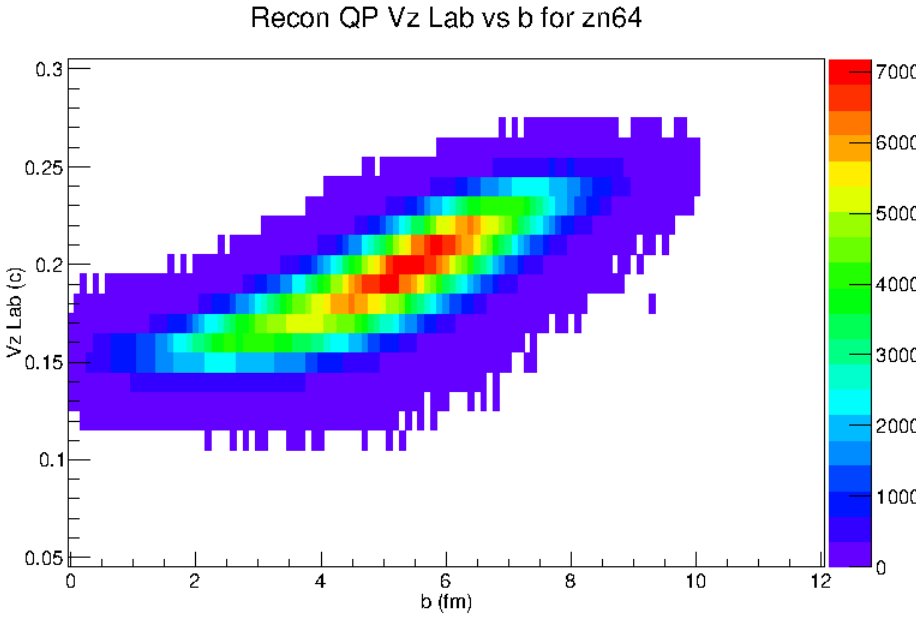

Figure B.40: The "asy-soft" CoMD $V_{z,QP}$ as a function of impact parameter b for the ^{64}Zn+^{64}Zn reaction system.

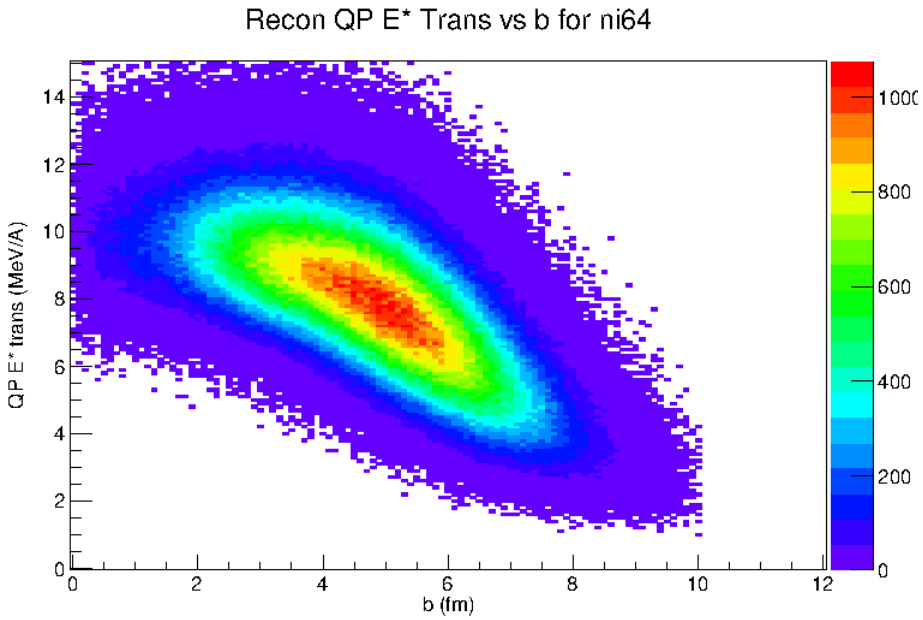

Figure B.41: The "asy-soft" CoMD E*/A as a function of impact parameter b for the ^{64}Ni+^{64}Ni reaction system.

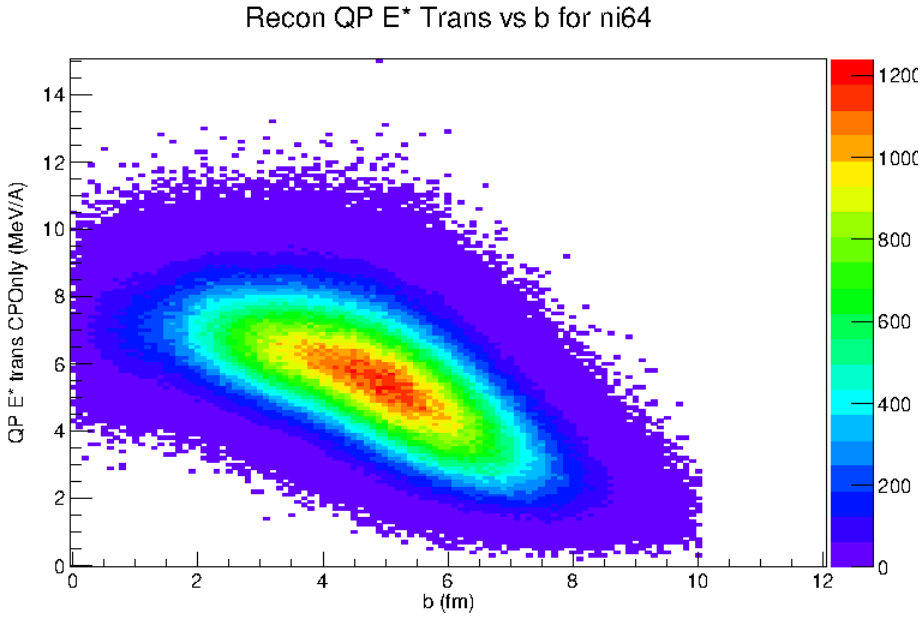

Figure B.42: The "asy-soft" CoMD E^*_{CP}/A as a function of impact parameter b for the ^{64}Ni+^{64}Ni reaction system.

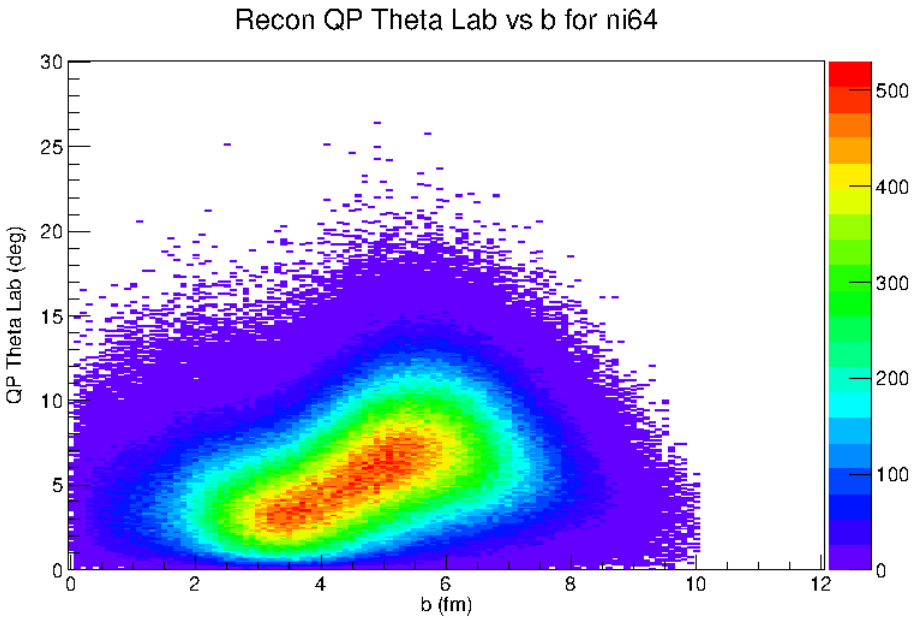

Figure B.43: The "asy-soft" CoMD θ_{QP} as a function of impact parameter b for the ^{64}Ni+^{64}Ni reaction system.

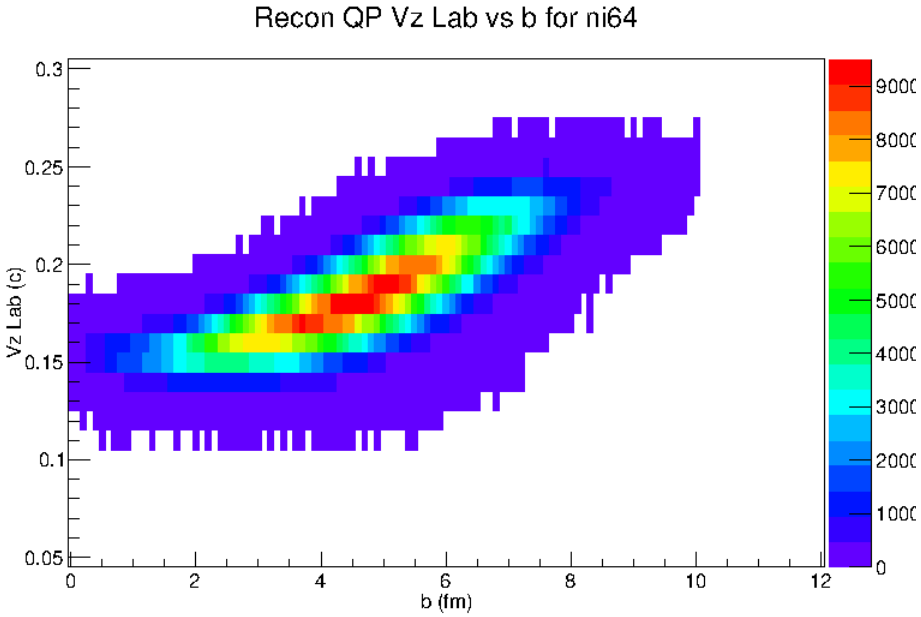

Figure B.44: The "asy-soft" CoMD $V_{z,QP}$ as a function of impact parameter b for the ^{64}Ni+^{64}Ni reaction system.

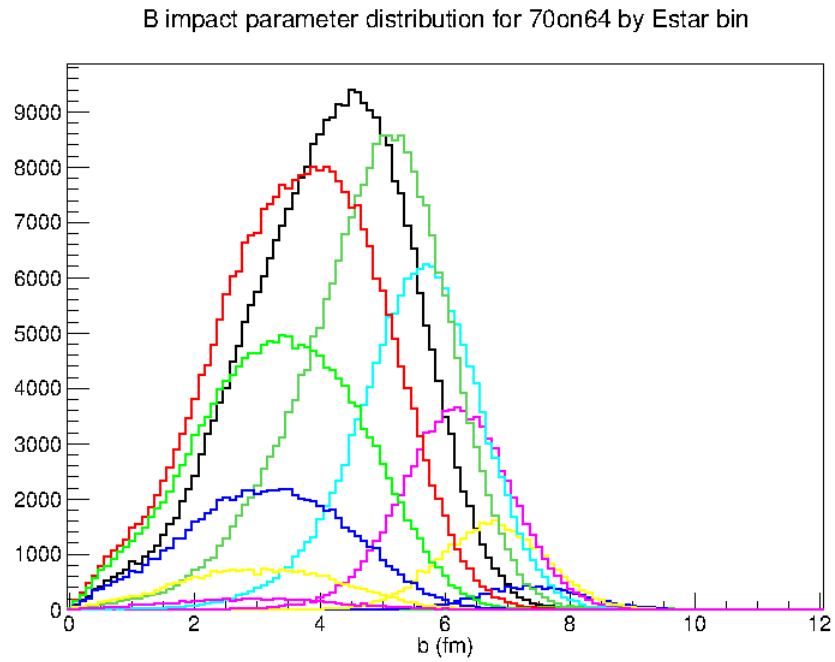

Figure B.45: The "asy-soft" CoMD impact parameter (b) distribution for each bin of the reconstructed QP E*/A surrogate for the ^{70}Zn+^{64}Zn reaction system.

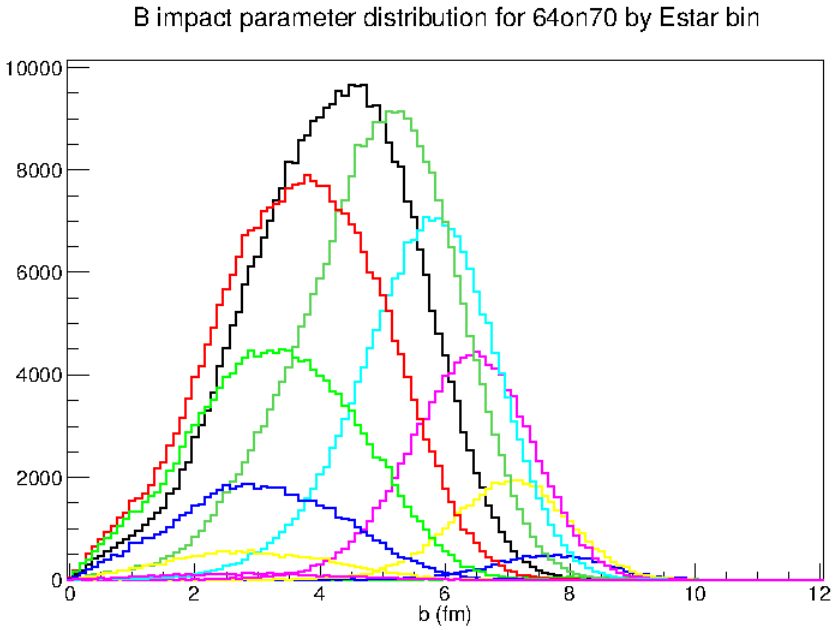

Figure B.46: The "asy-soft" CoMD impact parameter (b) distribution for each bin of the reconstructed QP E*/A surrogate for the ^{64}Zn+^{70}Zn reaction system.

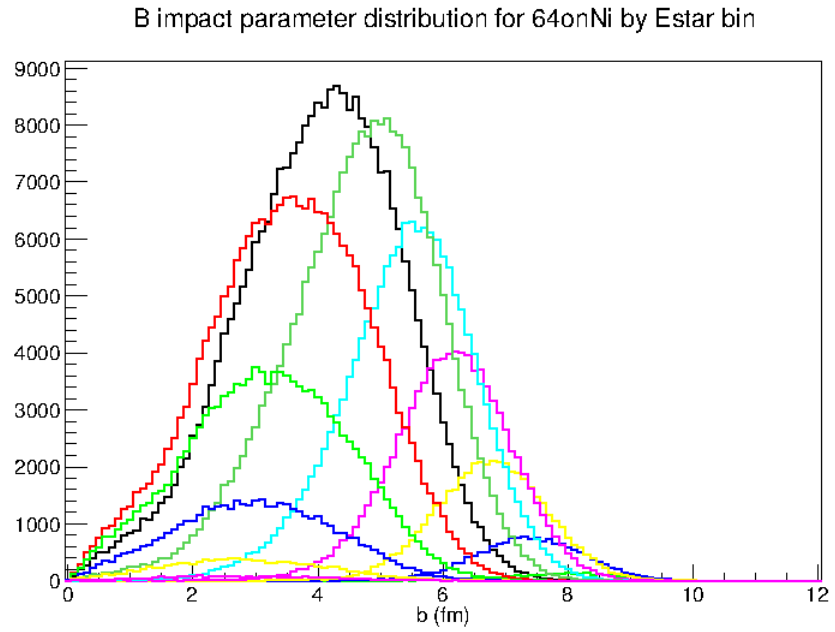

Figure B.47: The "asy-soft" CoMD impact parameter (b) distribution for each bin of the reconstructed QP E*/A surrogate for the ^{64}Zn+^{64}Ni reaction system.

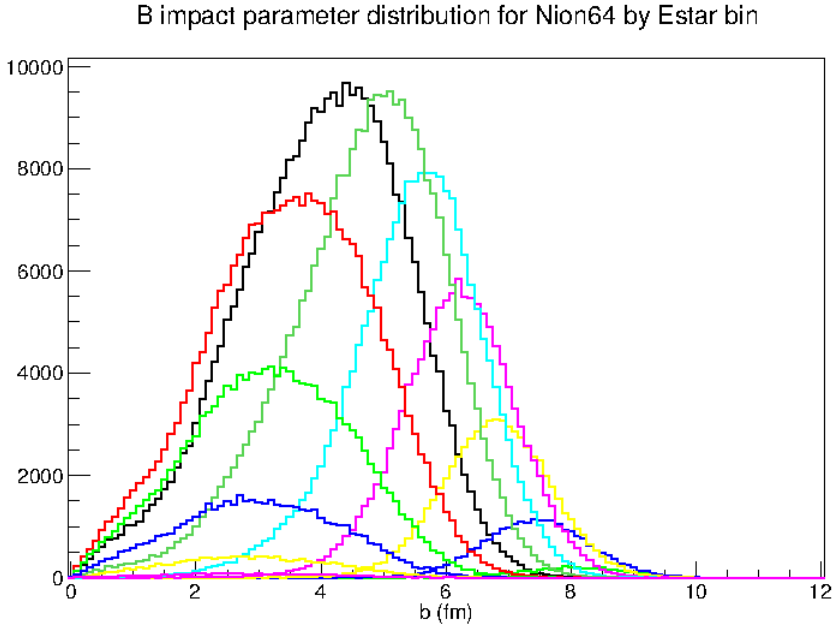

Figure B.48: The "asy-soft" CoMD impact parameter (b) distribution for each bin of the reconstructed QP E*/A surrogate for the ^{64}Ni+^{64}Zn reaction system.

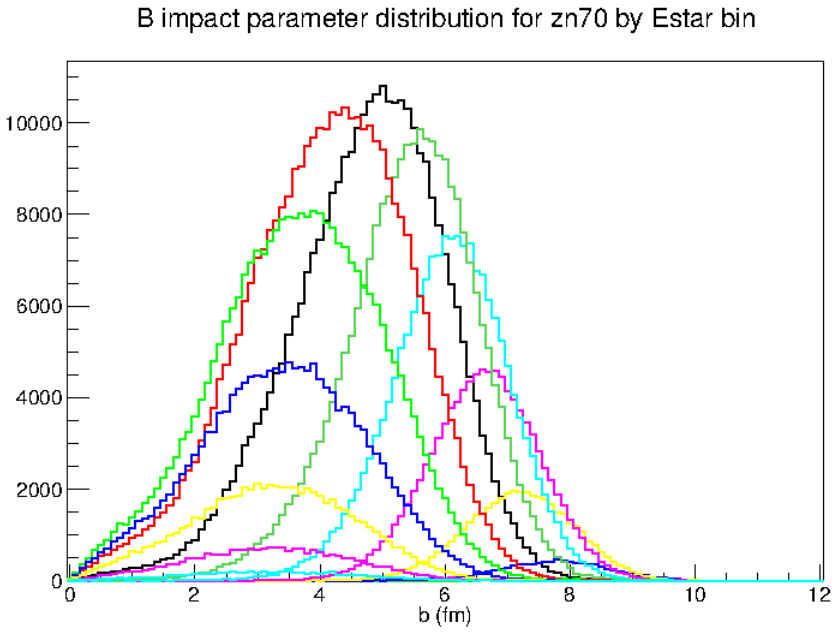

Figure B.49: The "asy-soft" CoMD impact parameter (b) distribution for each bin of the reconstructed QP E*/A surrogate for the ^{70}Zn+^{70}Zn reaction system.

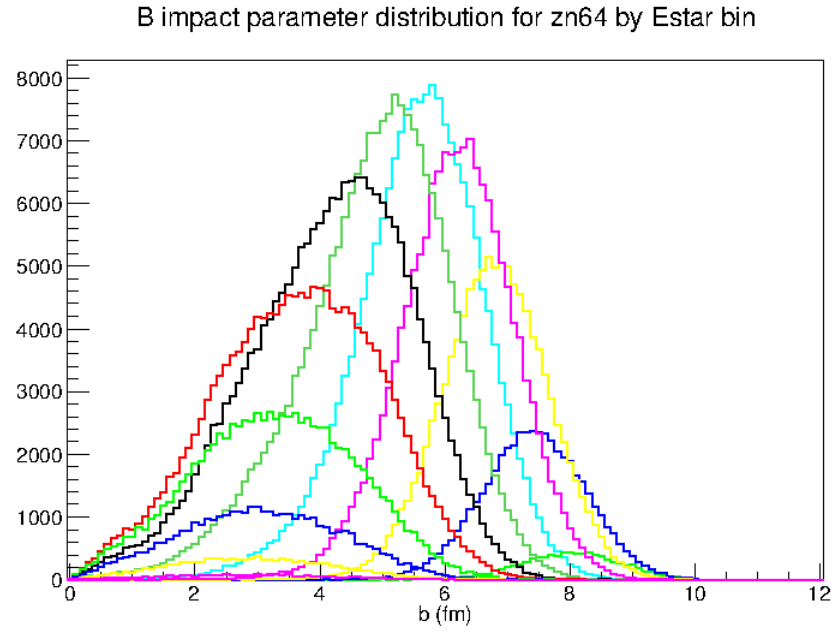

Figure B.50: The "asy-soft" CoMD impact parameter (b) distribution for each bin of the reconstructed QP E*/A surrogate for the ^{64}Zn+^{64}Zn reaction system.

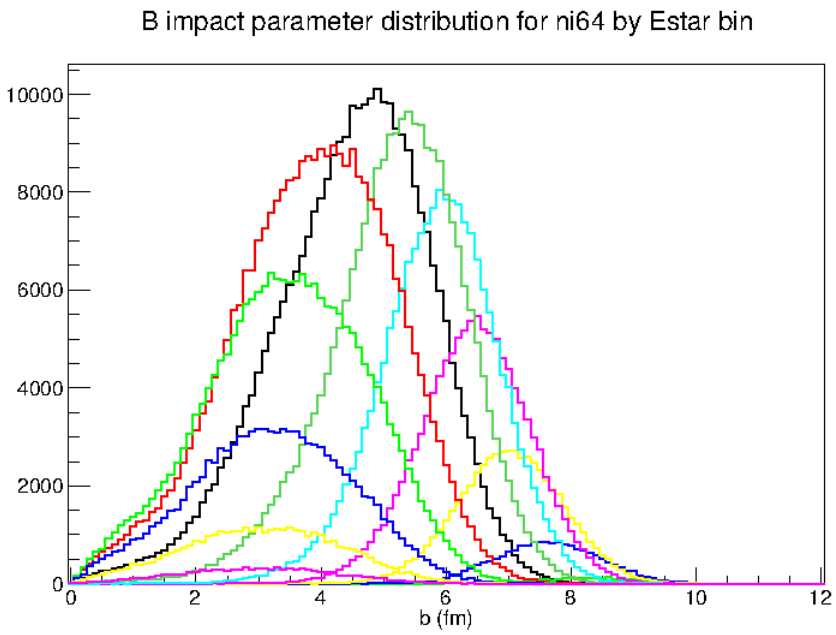

Figure B.51: The "asy-soft" CoMD impact parameter (b) distribution for each bin of the reconstructed QP E*/A surrogate for the ^{64}Ni+^{64}Ni reaction system.

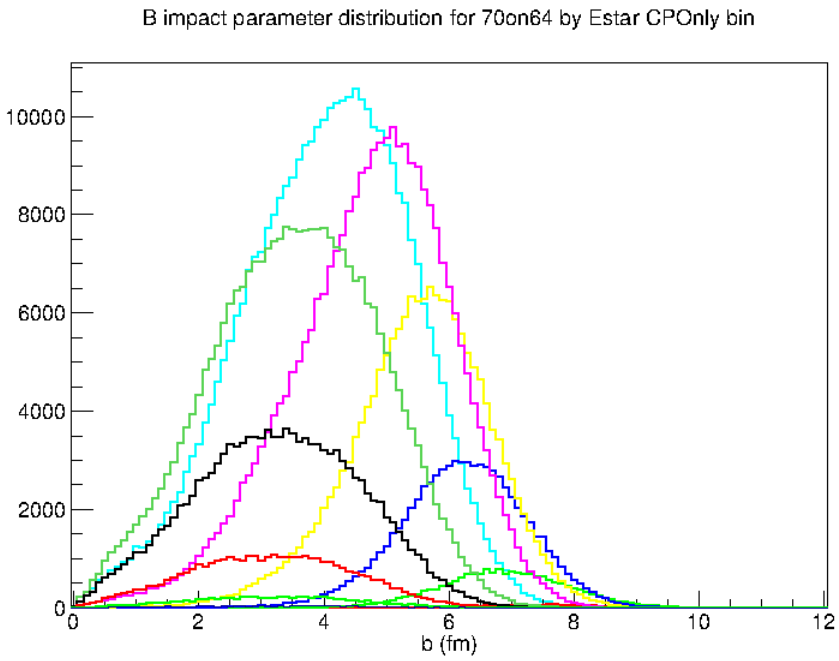

Figure B.52: The "asy-soft" CoMD impact parameter (b) distribution for each bin of the reconstructed QP E^*_{CP}/A surrogate for the ^{70}Zn+^{64}Zn reaction system.

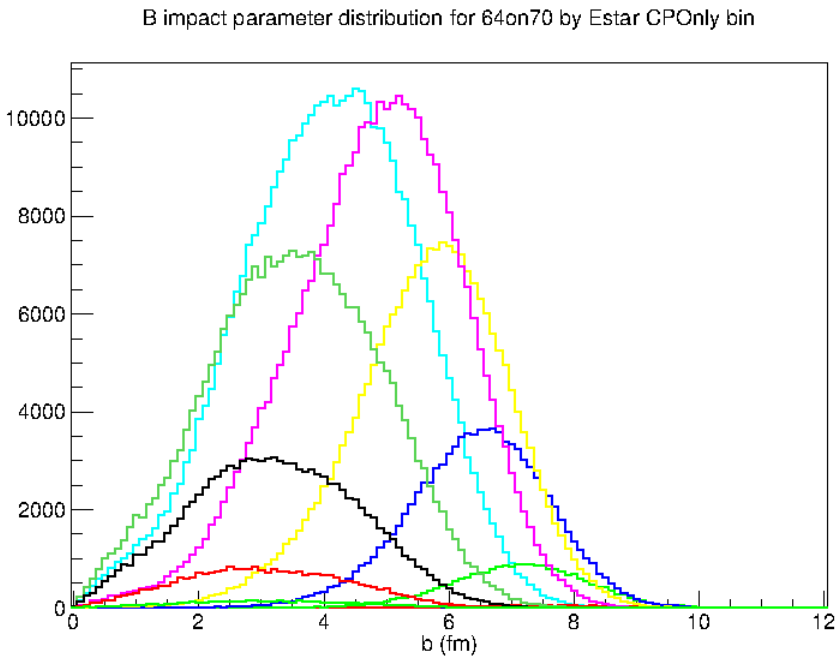

Figure B.53: The "asy-soft" CoMD impact parameter (b) distribution for each bin of the reconstructed QP E^*_{CP}/A surrogate for the ^{64}Zn+^{70}Zn reaction system.

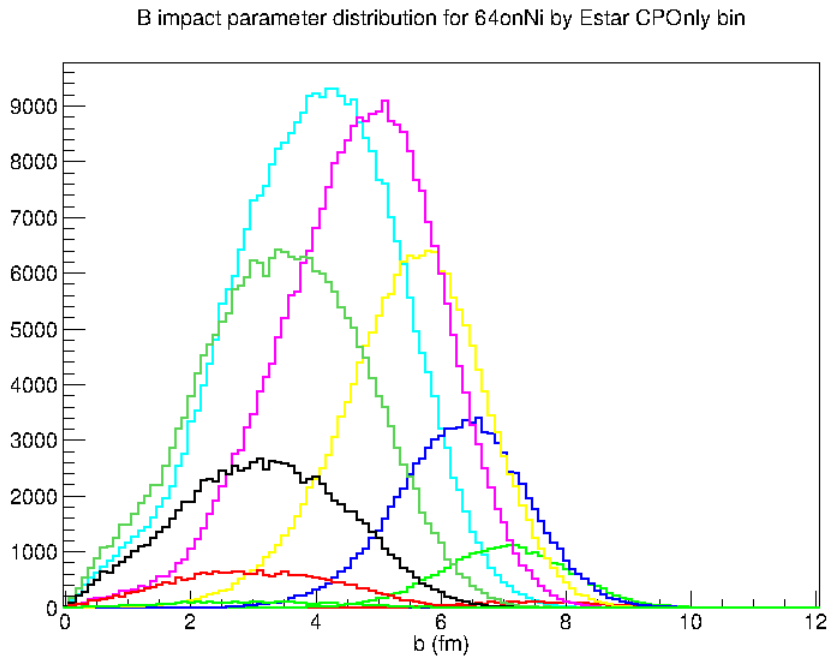

Figure B.54: The "asy-soft" CoMD impact parameter (b) distribution for each bin of the reconstructed QP E^*_{CP}/A surrogate for the ^{64}Zn+^{64}Ni reaction system.

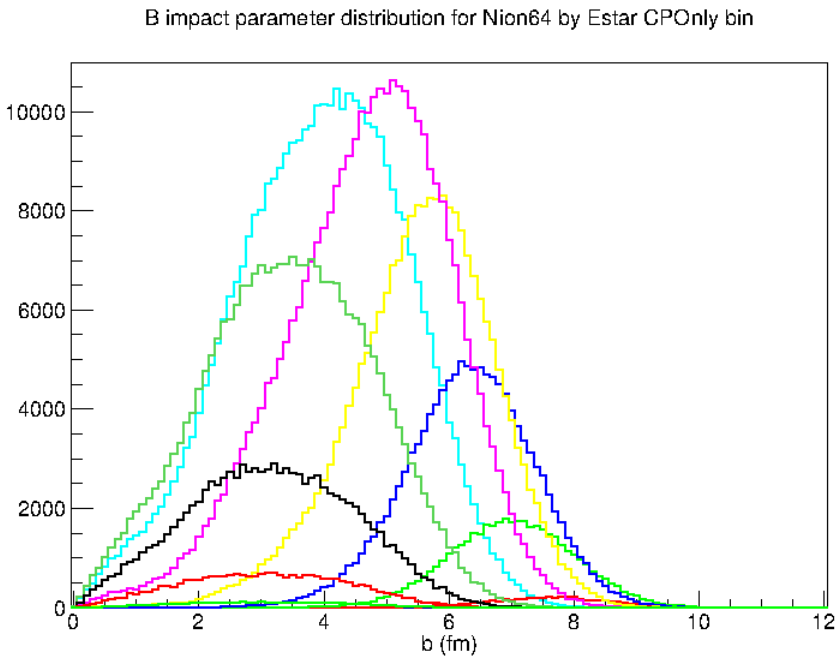

Figure B.55: The "asy-soft" CoMD impact parameter (b) distribution for each bin of the reconstructed QP E^*_{CP}/A surrogate for the ^{64}Ni+^{64}Zn reaction system.

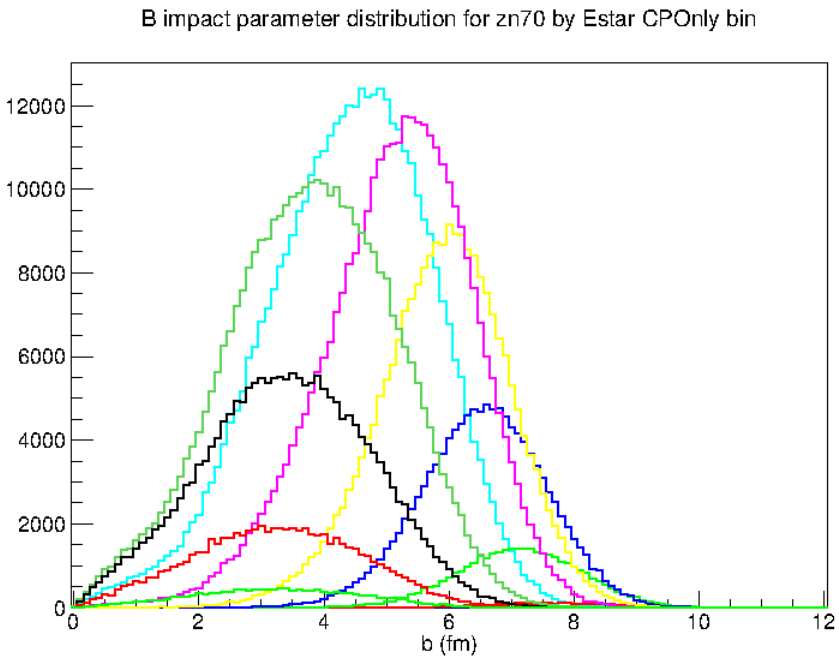

Figure B.56: The "asy-soft" CoMD impact parameter (b) distribution for each bin of the reconstructed QP E^*_{CP}/A surrogate for the ^{70}Zn+^{70}Zn reaction system.

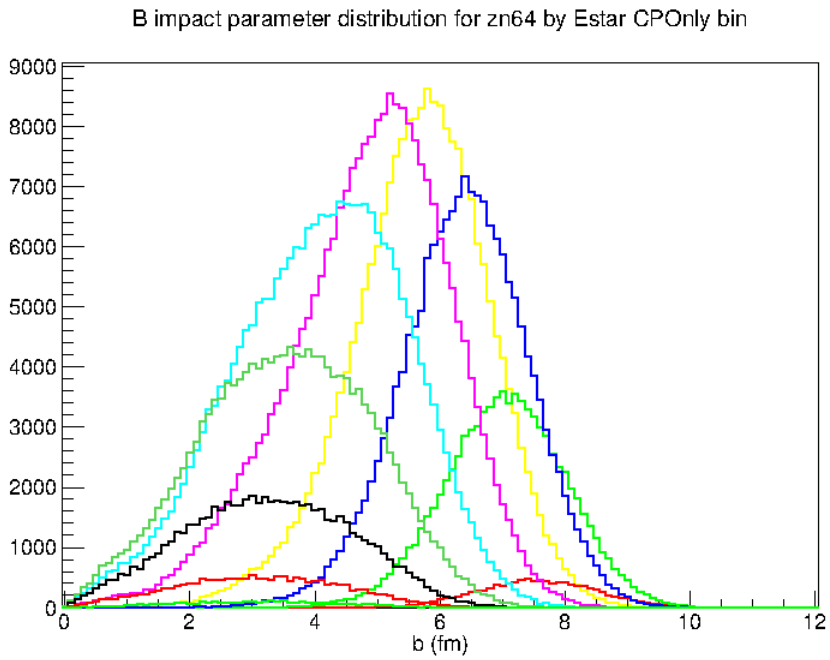

Figure B.57: The "asy-soft" CoMD impact parameter (b) distribution for each bin of the reconstructed QP E^*_{CP}/A surrogate for the ^{64}Zn+^{64}Zn reaction system.

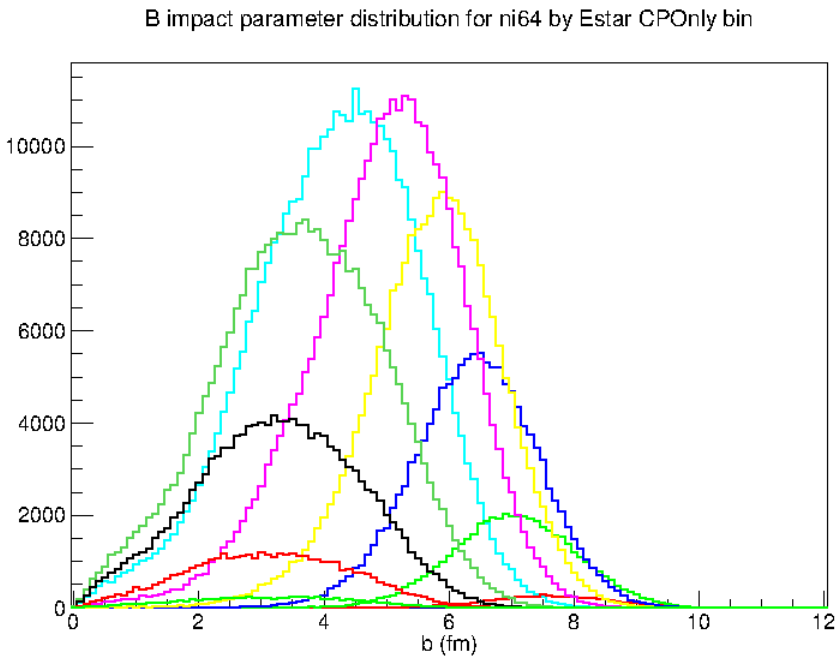

Figure B.58: The "asy-soft" CoMD impact parameter (b) distribution for each bin of the reconstructed QP E^*_{CP}/A surrogate for the ^{64}Ni+^{64}Ni reaction system.

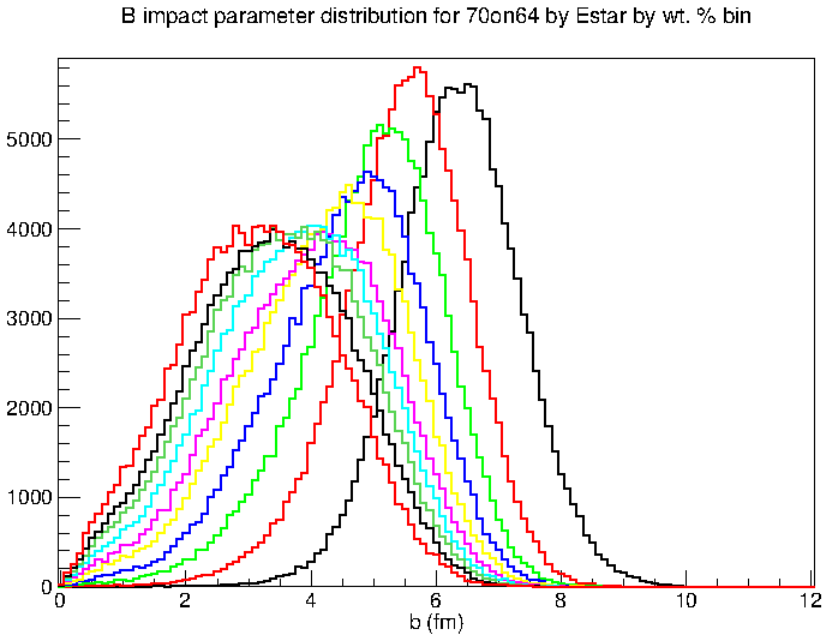

Figure B.59: The "asy-soft" CoMD impact parameter (b) distribution for each bin of the reconstructed QP E*/A surrogate cut by %wt. of the distribution for the ^{70}Zn+^{64}Zn reaction system.

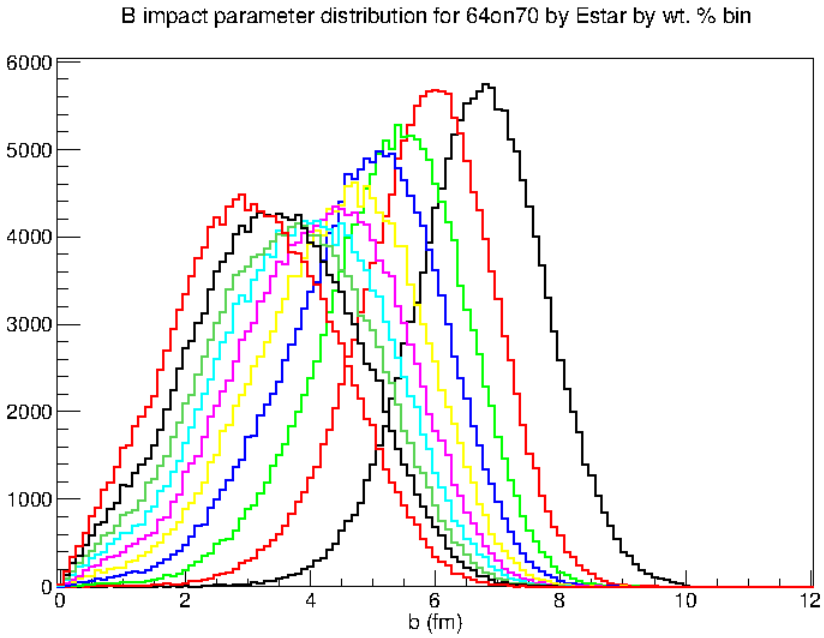

Figure B.60: The "asy-soft" CoMD impact parameter (b) distribution for each bin of the reconstructed QP E*/A surrogate cut by %wt. of the distribution for the ^{64}Zn+^{70}Zn reaction system.

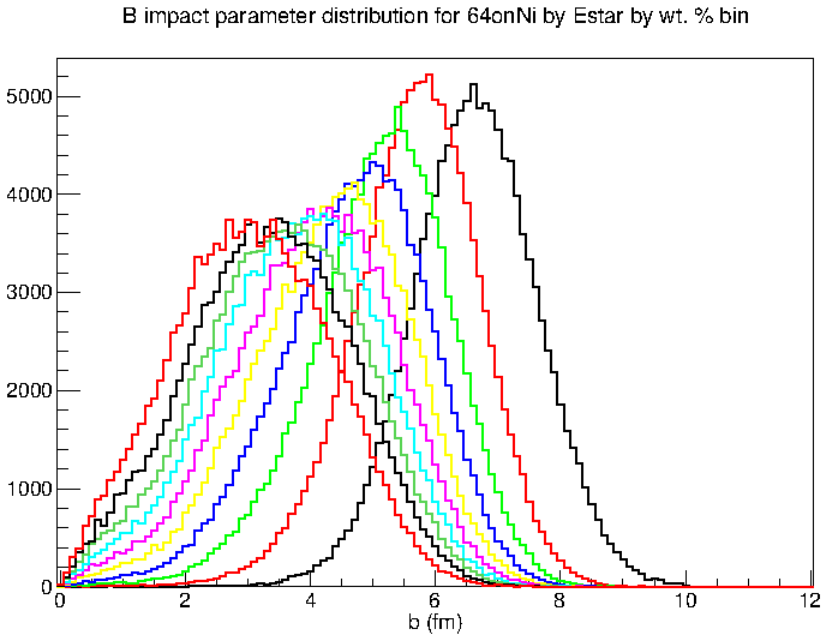

Figure B.61: The "asy-soft" CoMD impact parameter (b) distribution for each bin of the reconstructed QP E*/A surrogate cut by %wt. of the distribution for the ^{64}Zn+^{64}Ni reaction system.

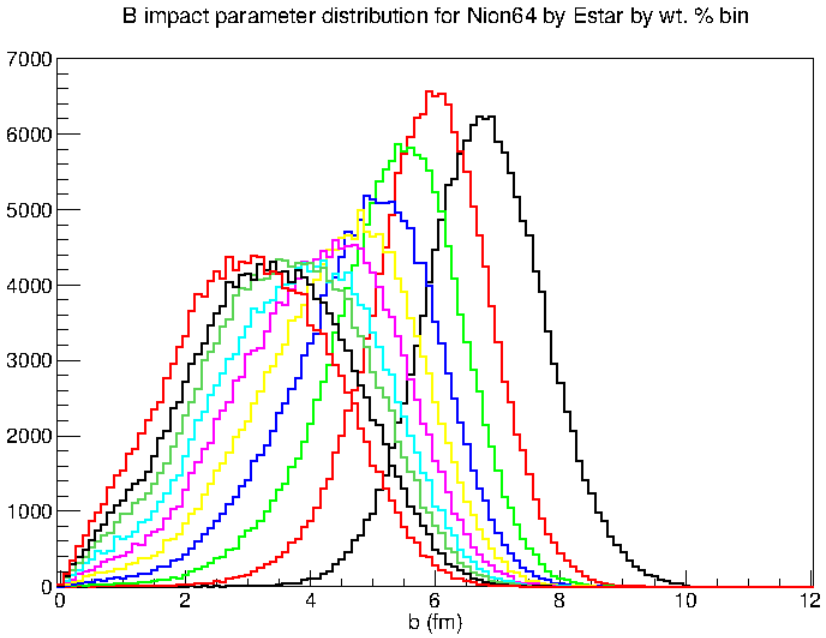

Figure B.62: The "asy-soft" CoMD impact parameter (b) distribution for each bin of the reconstructed QP E*/A surrogate cut by %wt. of the distribution for the ^{64}Ni+^{64}Zn reaction system.

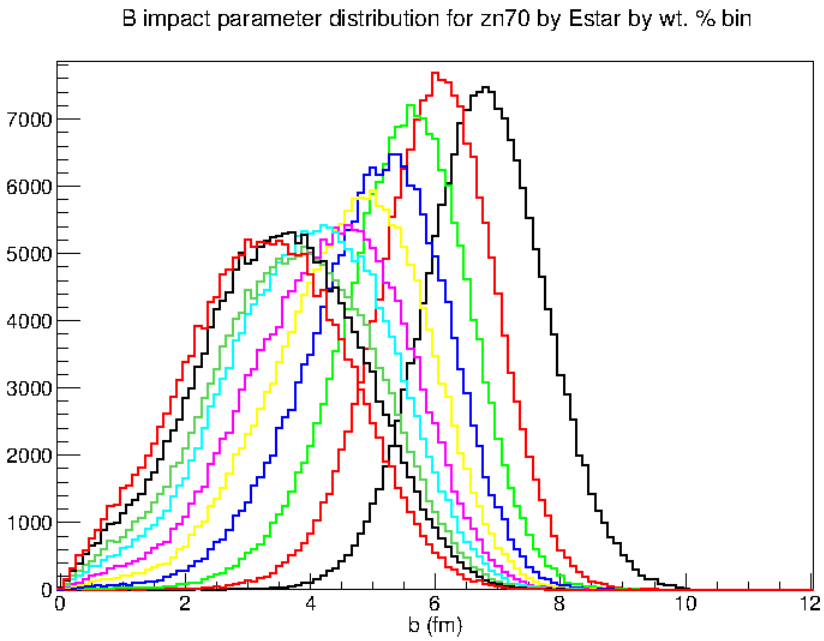

Figure B.63: The "asy-soft" CoMD impact parameter (b) distribution for each bin of the reconstructed QP E*/A surrogate cut by %wt. of the distribution for the ^{70}Zn+^{70}Zn reaction system.

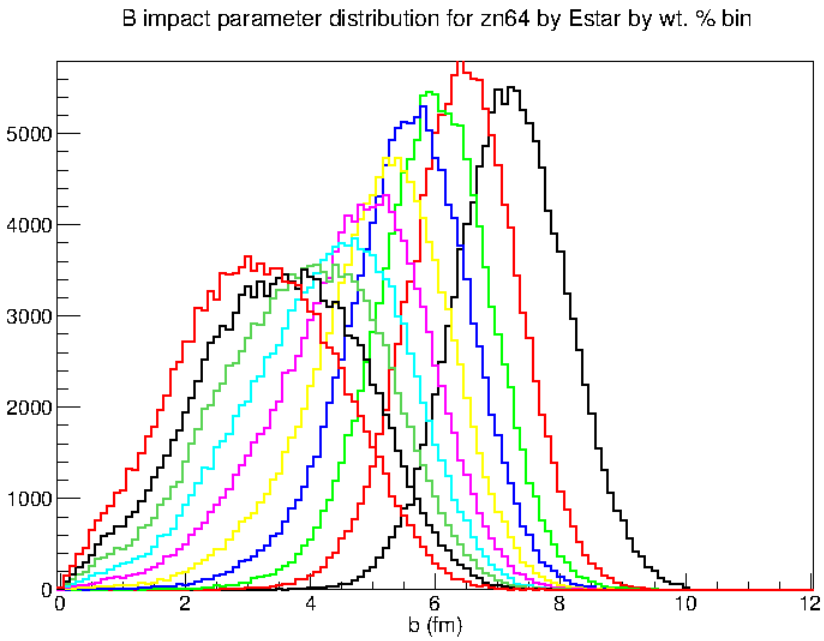

Figure B.64: The "asy-soft" CoMD impact parameter (b) distribution for each bin of the reconstructed QP E*/A surrogate cut by %wt. of the distribution for the ^{64}Zn+^{64}Zn reaction system.

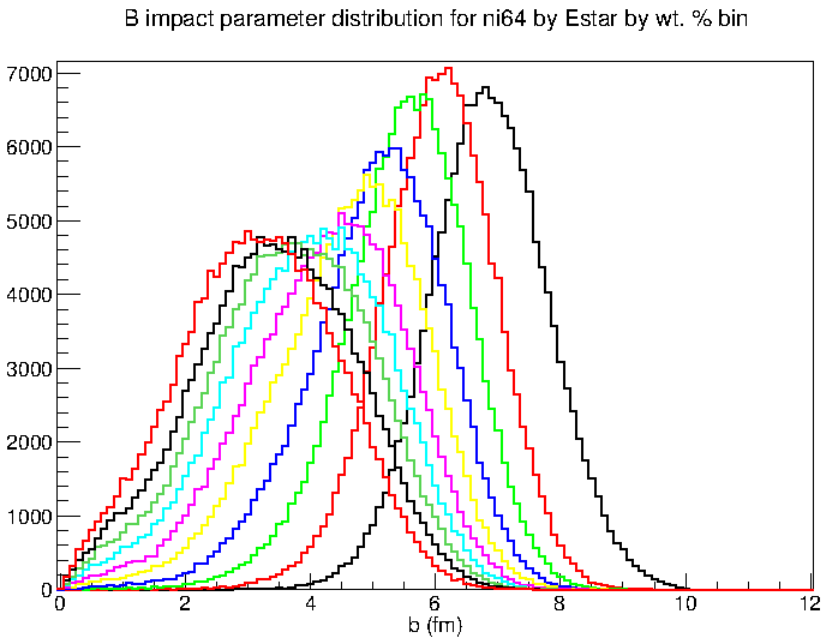

Figure B.65: The "asy-soft" CoMD impact parameter (b) distribution for each bin of the reconstructed QP E*/A surrogate cut by %wt. of the distribution for the ^{64}Ni+^{64}Ni reaction system.

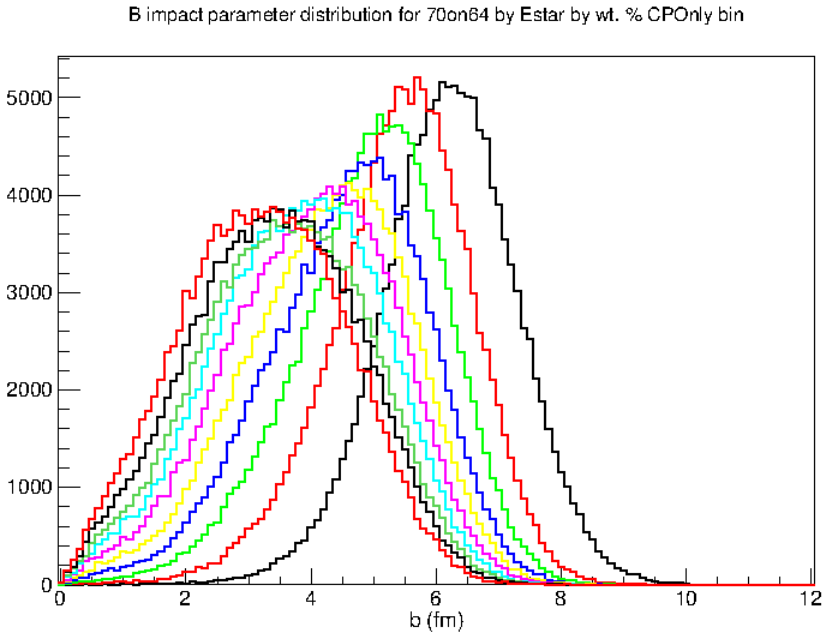

Figure B.66: The "asy-soft" CoMD impact parameter (b) distribution for each bin of the reconstructed QP E^*_{CP}/A surrogate cut by %wt. of the distribution for the ^{70}Zn+^{64}Zn reaction system.

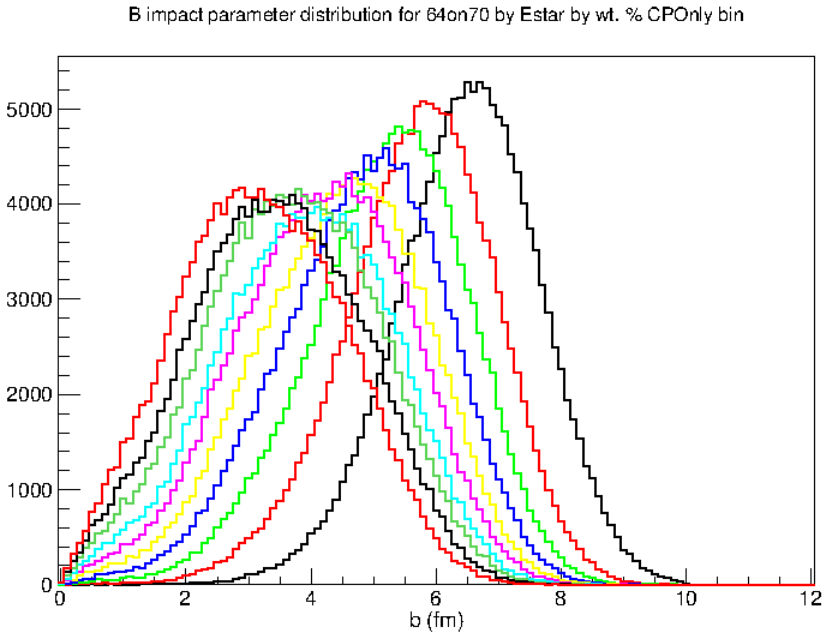

Figure B.67: The "asy-soft" CoMD impact parameter (b) distribution for each bin of the reconstructed QP E^*_{CP}/A surrogate cut by %wt. of the distribution for the ^{64}Zn+^{70}Zn reaction system.

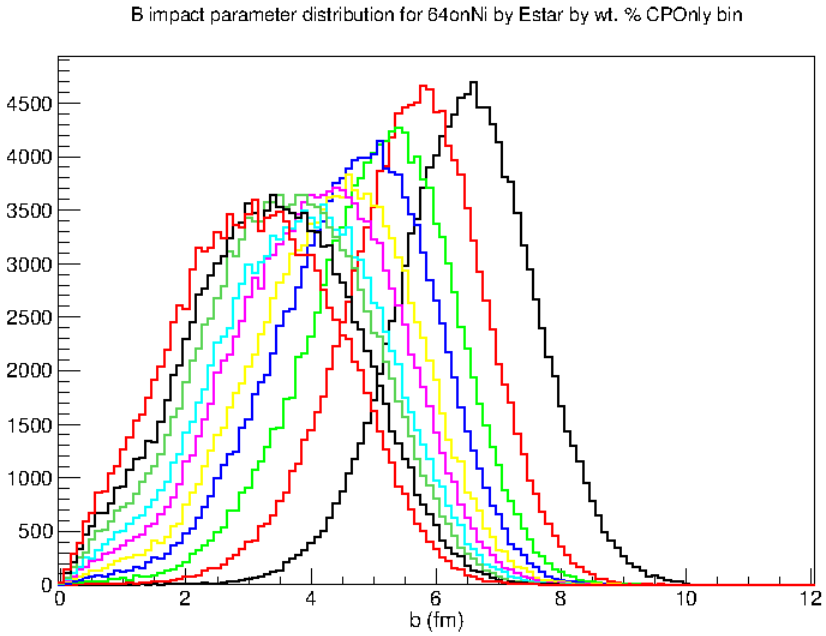

Figure B.68: The "asy-soft" CoMD impact parameter (b) distribution for each bin of the reconstructed QP E^*_{CP}/A surrogate cut by %wt. of the distribution for the ^{64}Zn+^{64}Ni reaction system.

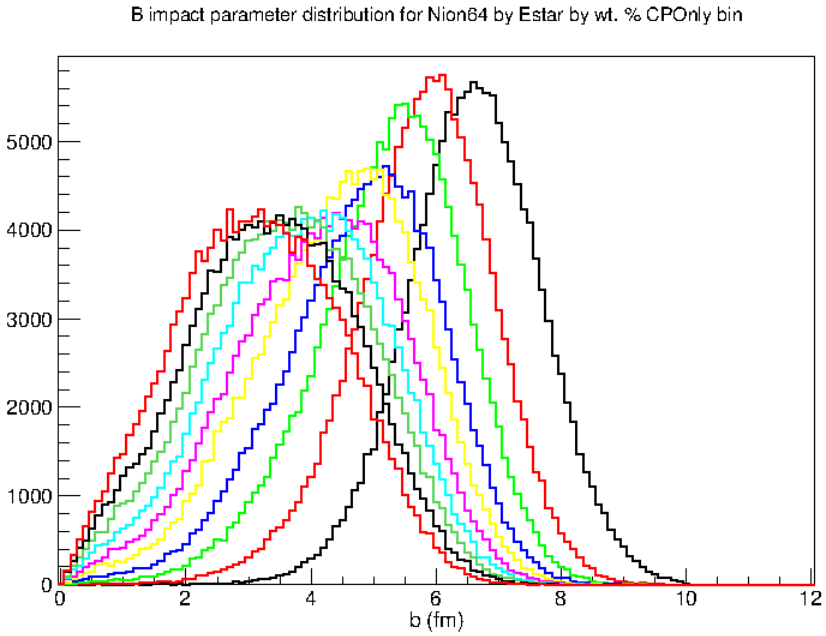

Figure B.69: The "asy-soft" CoMD impact parameter (b) distribution for each bin of the reconstructed QP E^*_{CP}/A surrogate cut by %wt. of the distribution for the ^{64}Ni+^{64}Zn reaction system.

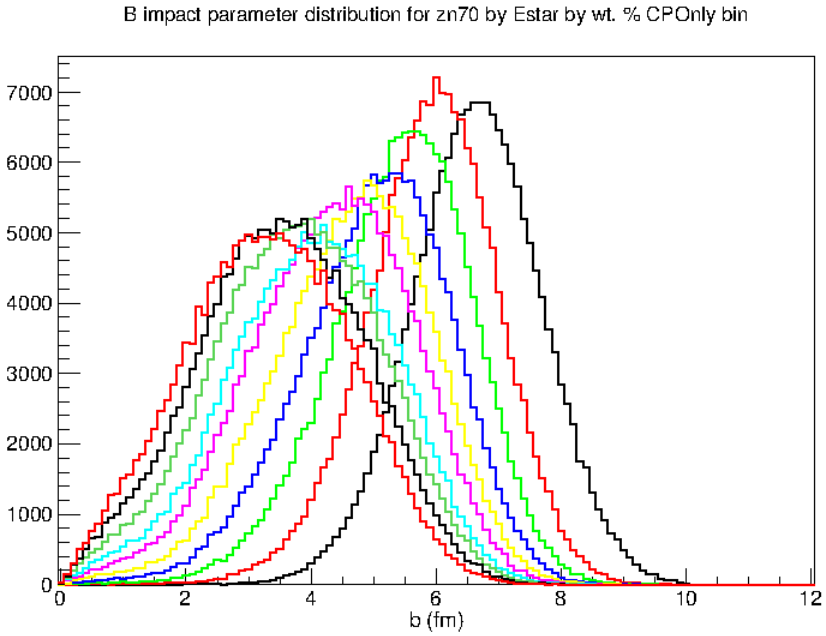

Figure B.70: The "asy-soft" CoMD impact parameter (b) distribution for each bin of the reconstructed QP E^*_{CP}/A surrogate cut by %wt. of the distribution for the ^{70}Zn+^{70}Zn reaction system.

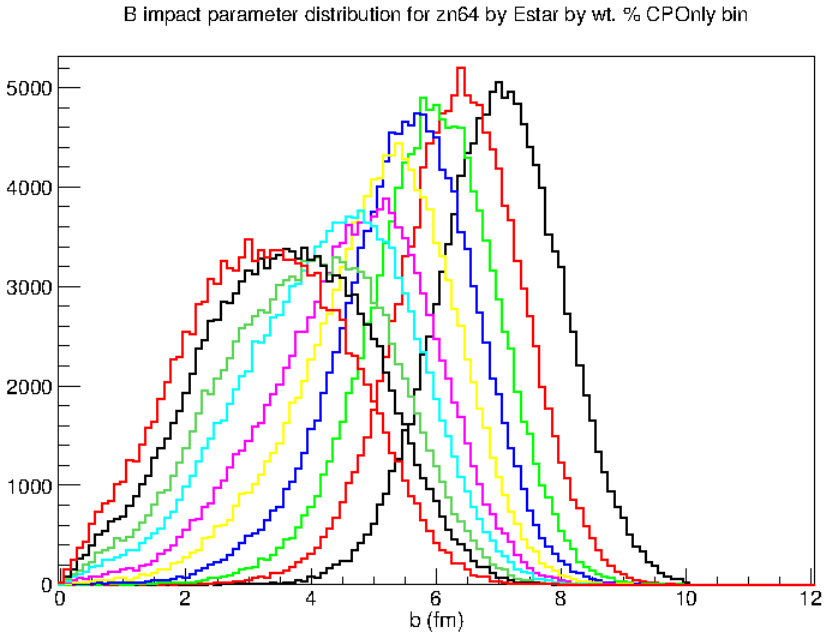

Figure B.71: The "asy-soft" CoMD impact parameter (b) distribution for each bin of the reconstructed QP E^*_{CP}/A surrogate cut by %wt. of the distribution for the ^{64}Zn+^{64}Zn reaction system.

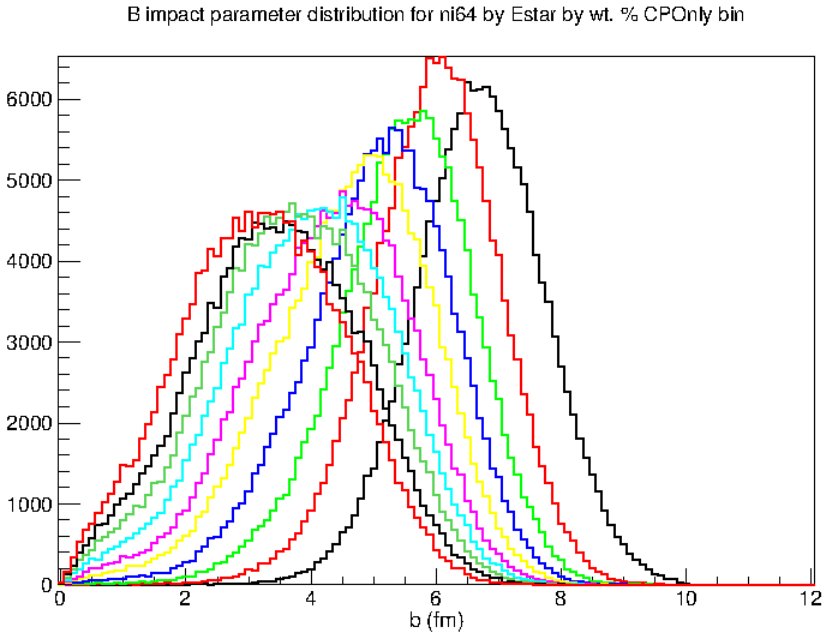

Figure B.72: The "asy-soft" CoMD impact parameter (b) distribution for each bin of the reconstructed QP E^*_{CP}/A surrogate cut by %wt. of the distribution for the ^{64}Ni+^{64}Ni reaction system.

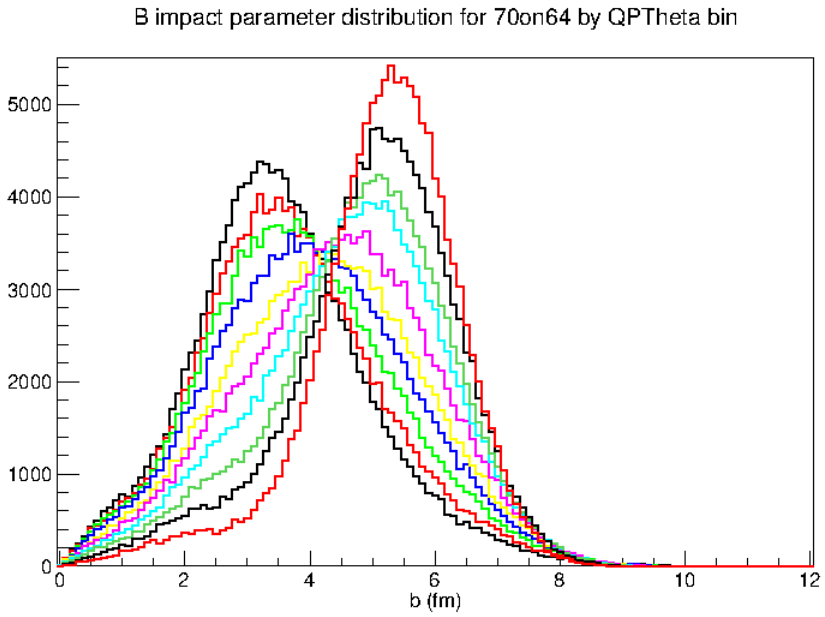

Figure B.73: The "asy-soft" CoMD impact parameter (b) distribution for each bin of the reconstructed θ_{QP} surrogate cut by %wt. of the distribution for the ^{70}Zn+^{64}Zn reaction system.

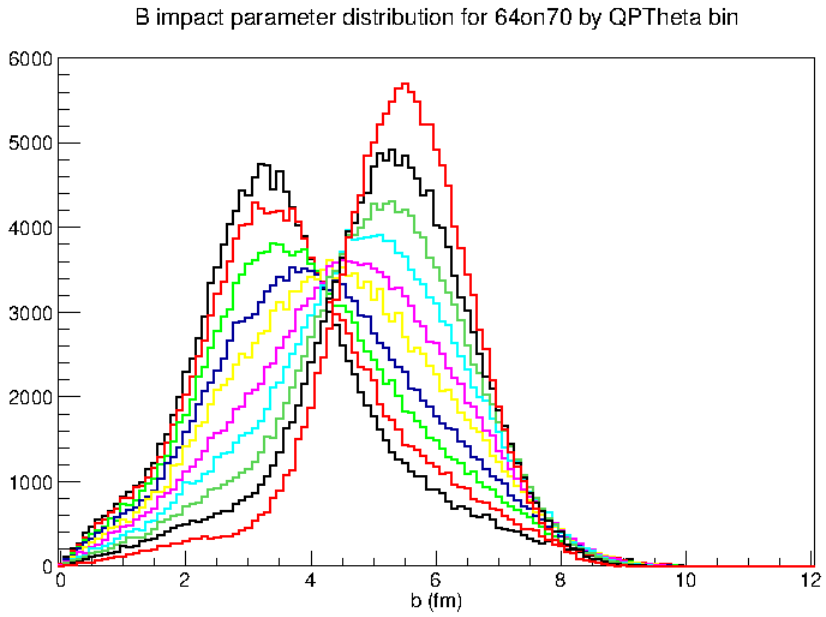

Figure B.74: The "asy-soft" CoMD impact parameter (b) distribution for each bin of the reconstructed θ_{QP} surrogate cut by %wt. of the distribution for the ^{64}Zn+^{70}Zn reaction system.

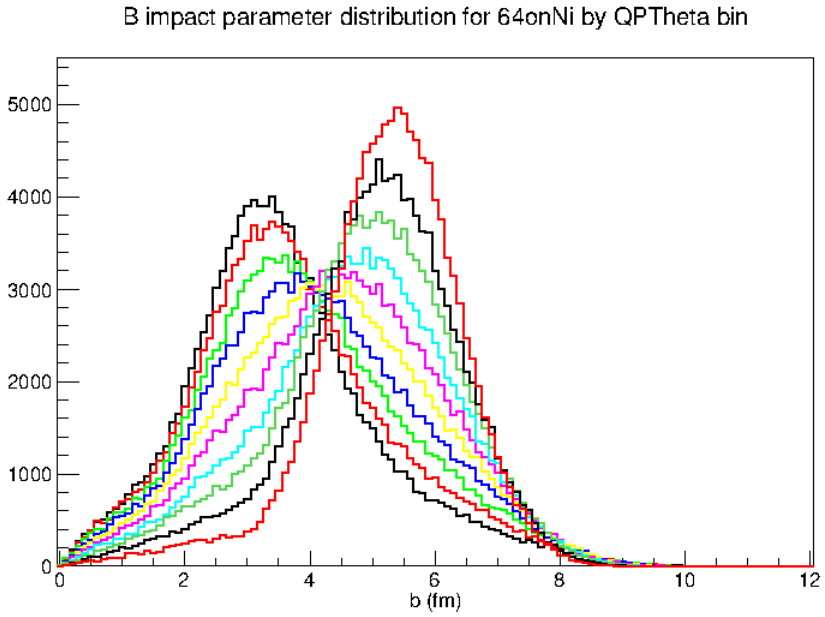

Figure B.75: The "asy-soft" CoMD impact parameter (b) distribution for each bin of the reconstructed θ_{QP} surrogate cut by %wt. of the distribution for the ^{64}Zn+^{64}Ni reaction system.

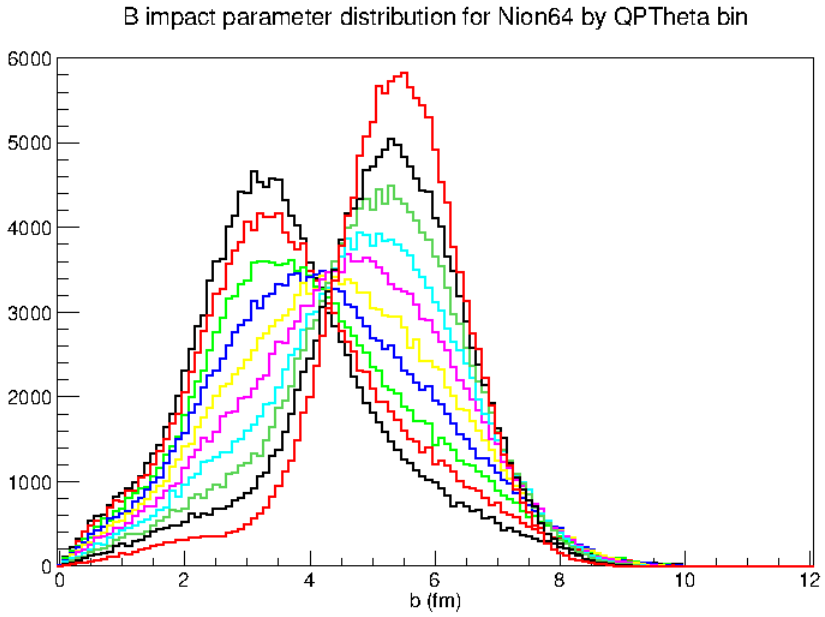

Figure B.76: The "asy-soft" CoMD impact parameter (b) distribution for each bin of the reconstructed θ_{QP} surrogate cut by %wt. of the distribution for the ^{64}Ni+^{64}Zn reaction system.

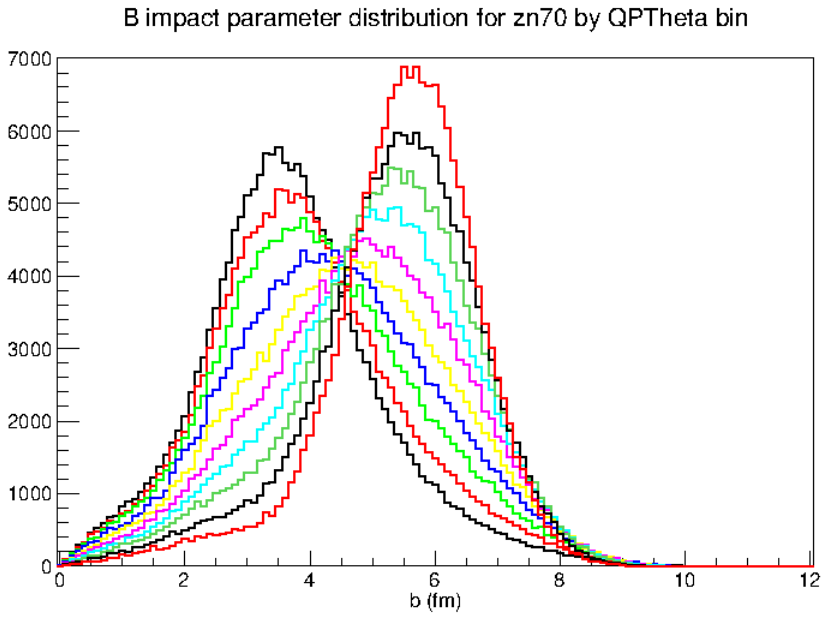

Figure B.77: The "asy-soft" CoMD impact parameter (b) distribution for each bin of the reconstructed θ_{QP} surrogate cut by %wt. of the distribution for the ^{70}Zn+^{70}Zn reaction system.

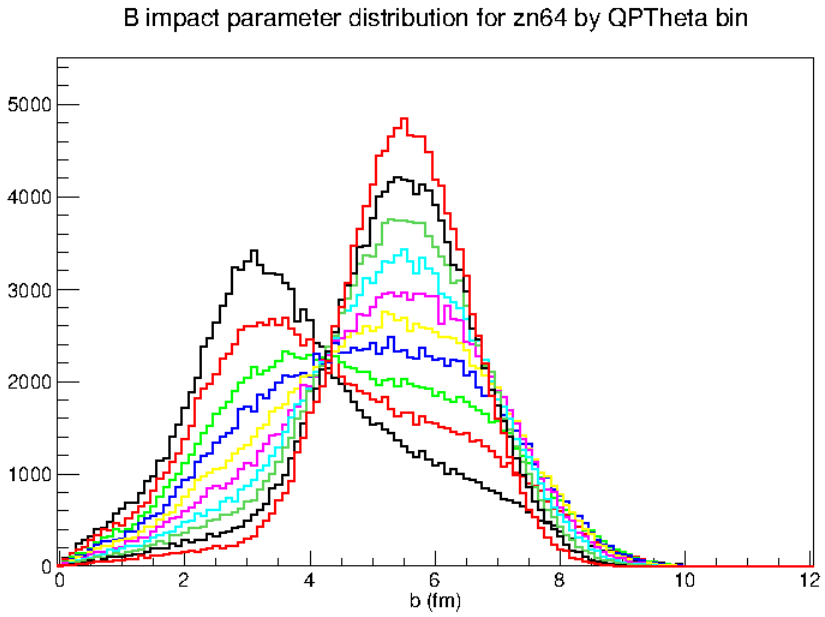

Figure B.78: The "asy-soft" CoMD impact parameter (b) distribution for each bin of the reconstructed θ_{QP} surrogate cut by %wt. of the distribution for the ^{64}Zn+^{64}Zn reaction system.

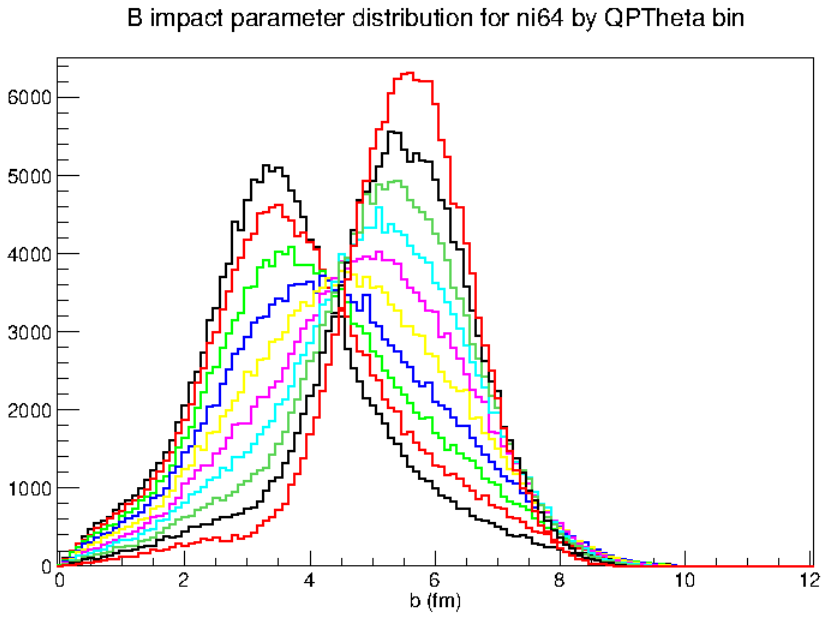

Figure B.79: The "asy-soft" CoMD impact parameter (b) distribution for each bin of the reconstructed θ_{QP} surrogate cut by %wt. of the distribution for the ^{64}Ni+^{64}Ni reaction system.

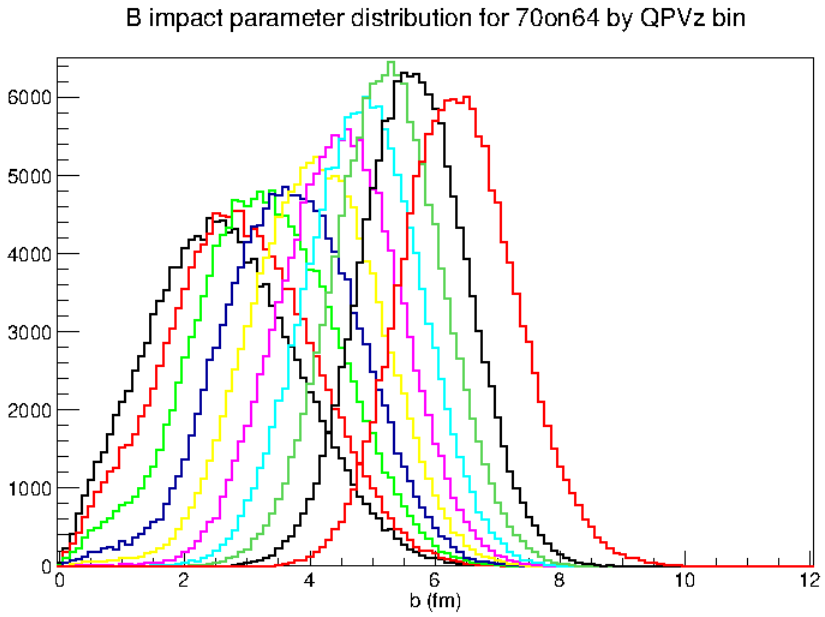

Figure B.80: The "asy-soft" CoMD impact parameter (b) distribution for each bin of the reconstructed $V_{z,QP}$ surrogate cut by %wt. of the distribution for the ^{70}Zn+^{64}Zn reaction system.

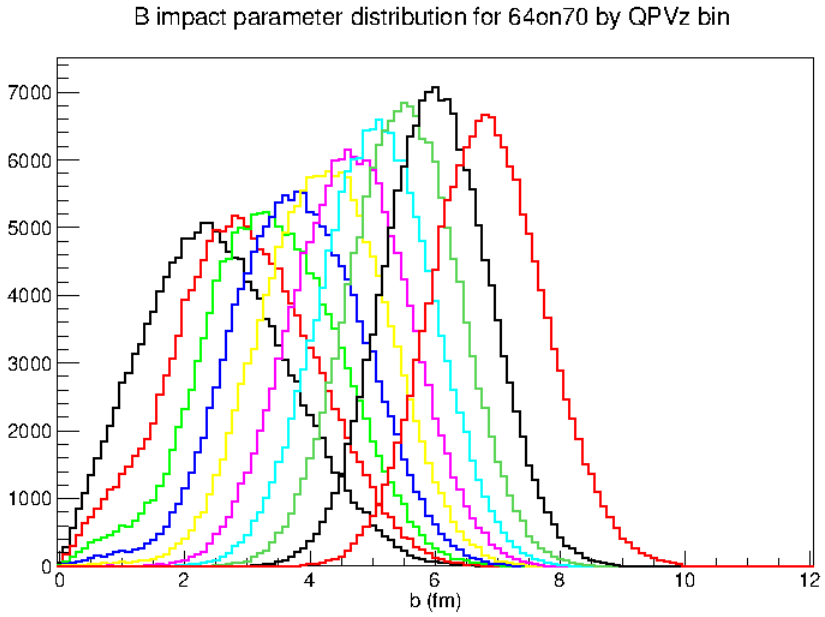

Figure B.81: The "asy-soft" CoMD impact parameter (b) distribution for each bin of the reconstructed $V_{z,QP}$ surrogate cut by %wt. of the distribution for the ^{64}Zn+^{70}Zn reaction system.

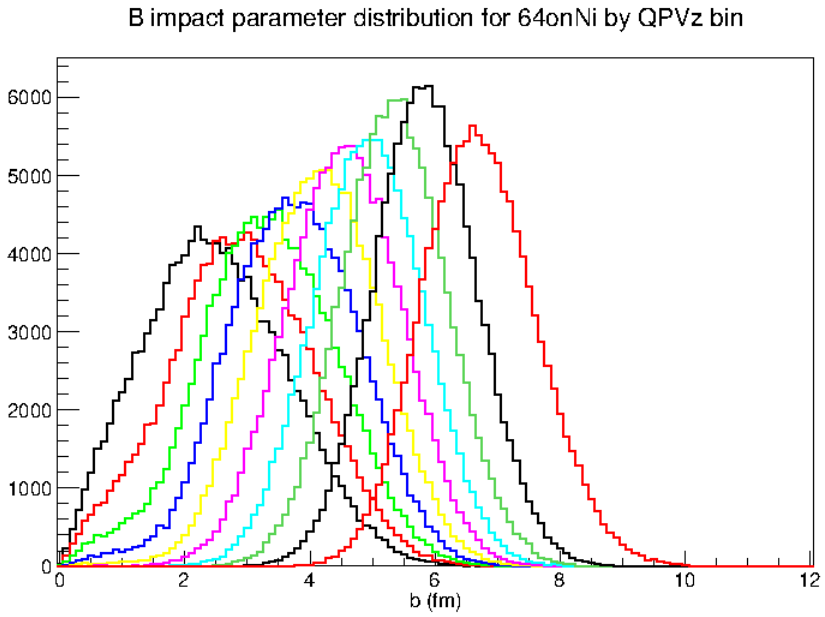

Figure B.82: The "asy-soft" CoMD impact parameter (b) distribution for each bin of the reconstructed $V_{z,QP}$ surrogate cut by %wt. of the distribution for the ^{64}Zn+^{64}Ni reaction system.

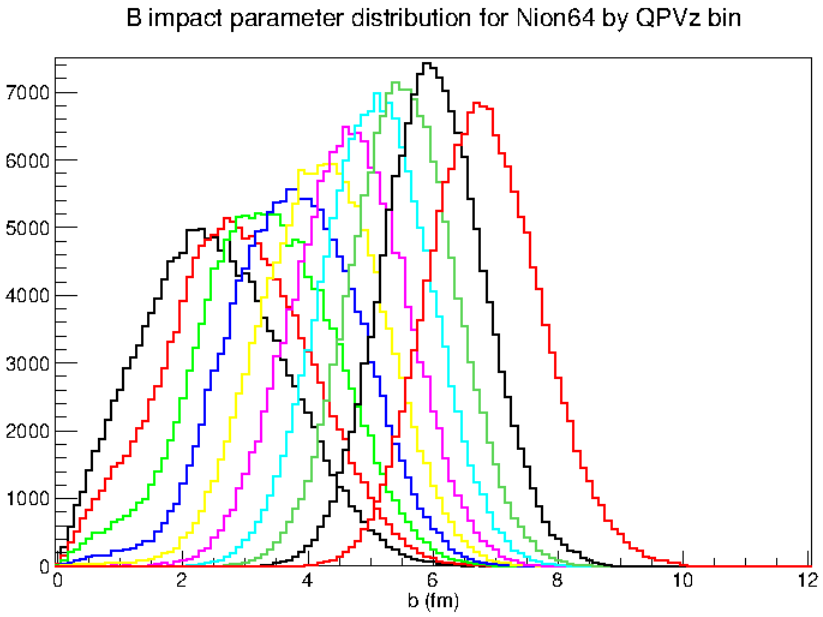

Figure B.83: The "asy-soft" CoMD impact parameter (b) distribution for each bin of the reconstructed $V_{z,QP}$ surrogate cut by %wt. of the distribution for the ^{64}Ni+^{64}Zn reaction system.

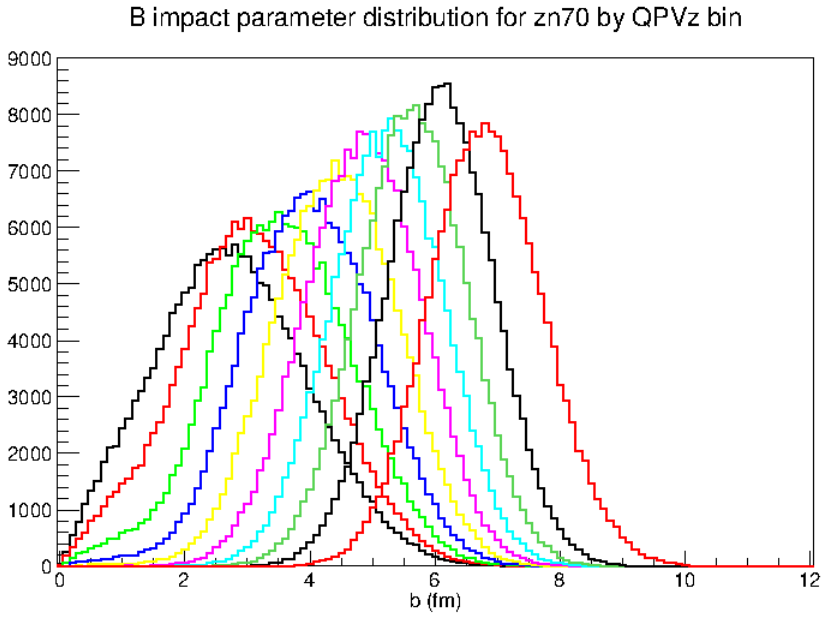

Figure B.84: The "asy-soft" CoMD impact parameter (b) distribution for each bin of the reconstructed $V_{z,QP}$ surrogate cut by %wt. of the distribution for the ^{70}Zn+^{70}Zn reaction system.

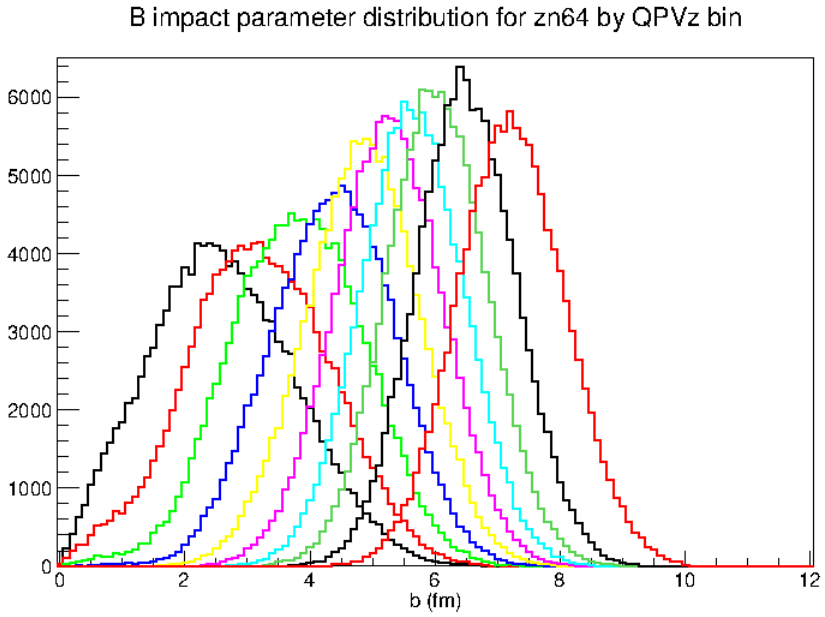

Figure B.85: The "asy-soft" CoMD impact parameter (b) distribution for each bin of the reconstructed $V_{z,QP}$ surrogate cut by %wt. of the distribution for the ^{64}Zn+^{64}Zn reaction system.

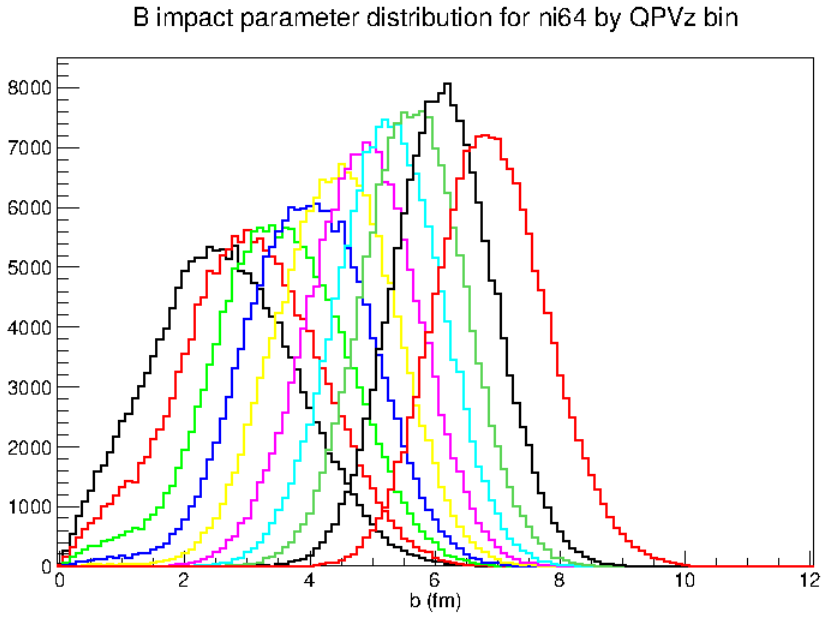

Figure B.86: The "asy-soft" CoMD impact parameter (b) distribution for each bin of the reconstructed $V_{z,QP}$ surrogate cut by %wt. of the distribution for the ^{64}Ni+^{64}Ni reaction system.

APPENDIX C

EQUILIBRATION ERROR CALCULATION

The following section describes in detail the analysis performed to estimate the errors on the values seen in Table 3.2 in Section 3.5.1.

The statistical errors on the yield ratio measurements seen in Table 3.2 are very small due to the large statistics from the experimental reaction systems. In order to better estimate the error on these calculations, the systematic error on the measurements were estimated. The two largest sources of error in the experiment could be attributed to the contamination between adjacent isotopes during the particle identification stage of the analysis detailed in Section 2.3.5 and the uncertainty in the neutron ball measurement and attribution of free neutrons, discussed in depth in reference [132].

Using the gaussian fits to the isotopes, the integral of the contamination in each isotope was calculated relative to the integral of the isotope gaussian and an average contamination value for each isotope was determined for each system. The total yields that were used in each yield scaling method were then adjusted by the amount of contamination calculated by taking the maximum possible effect on the yield from this contamination. For example, if we calculated that an isotope (Z,A) experienced a total of 10% of its identification was potentially contaminated, then the two extremes were determined: that all of the contamination came from the (Z,A+1) isotope and then that all the contamination came from the (Z,A-1) isotope. Once all the isotopic yields were calculated in this way, three values were left for each isotope: the experimental yield, the "maximum" yield and the "minimum" yield. The experimental yields were used to calculate all the values in the analysis

while the "maximum" and "minimum" yields were only used to calculate the errors.

In each ratio using yields, the four pair-wise combinations of "maximum" and "mimimum" yields were calculated and used through the analysis. The resulting values from the highest and lowest value for each observable were then used in the percent equilibration calculation (Eq. 3.5) to calculate the highest and lowest possible percent equilibration due to these errors. The calculated deviations that were farthest from the value calculated from the experimental yields were then used as the limits for the error estimation.

Since the neutrons were not contaminated by nearby isotopes, the width of the actual neutron distribution for each efficiency corrected QP-associated free neutron yield as seen in Reference [132] was used to estimate the error in the neutron values for inclusion in the QP m_s calculation. Therefore, the errors shown in Table 3.2 represent the limit of the maximum error on the equilibration due to the contamination in the particle identification and neutron uncertainties.

APPENDIX D

ISOSPIN EQUILIBRATION ANALYSIS

Additional and expanded plots from the isospin equilibration discussion found in Section 3.5.

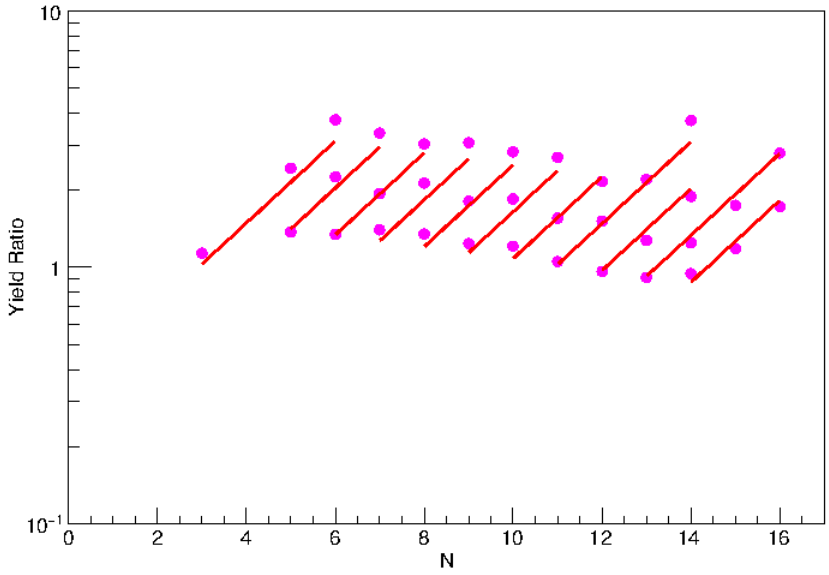

Figure D.1: An example isoscaling plot using an expanded range in fragments. The plot shows the isoscaling of abundant isotopes from Z=4-14 for the $^{70}Zn + ^{70}Zn$ system relative to the $^{64}Zn + ^{64}Zn$ system. The red fit lines correspond to the resulting global fit according to Eq. 1.8.

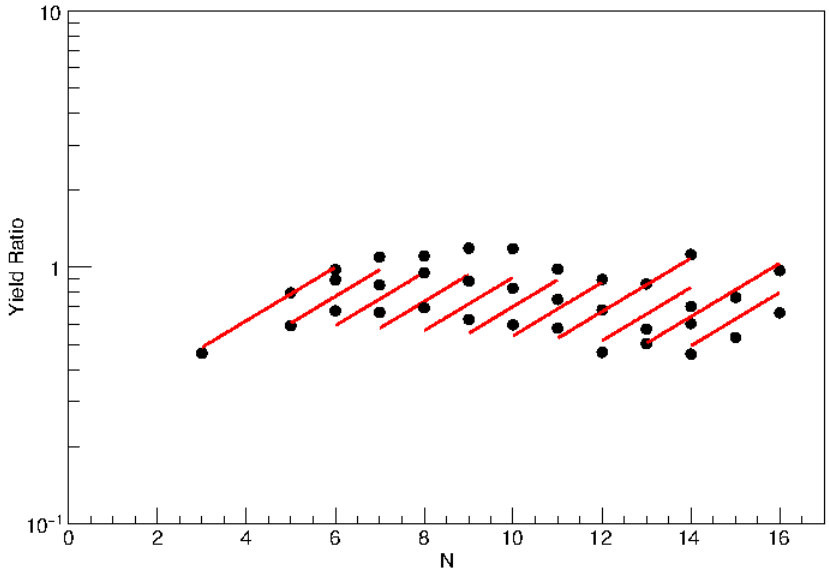

Figure D.2: An example isoscaling plot using an expanded range in fragments. The plot shows the isoscaling of abundant isotopes from Z=4-14 for the $^{70}Zn + ^{64}Zn$ system relative to the $^{64}Zn + ^{64}Zn$ system. The red fit lines correspond to the resulting global fit according to Eq. 1.8.

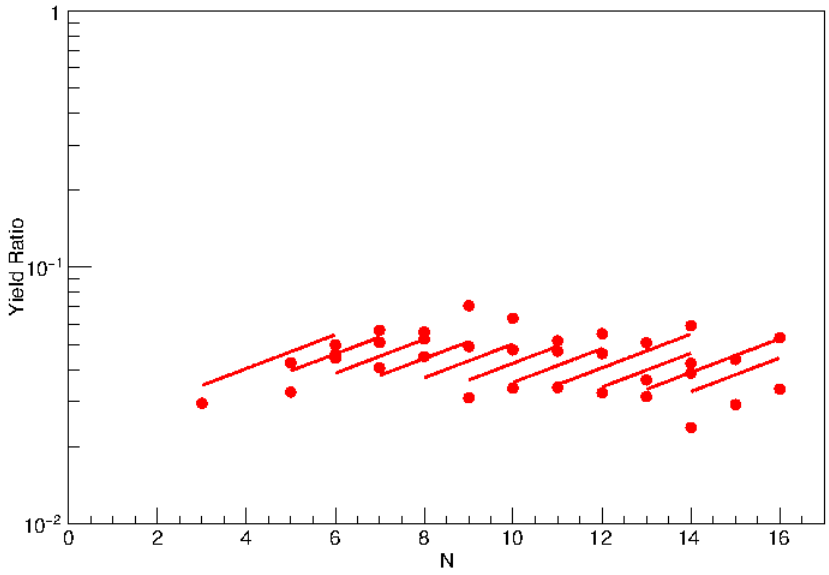

Figure D.3: An example isoscaling plot using an expanded range in fragments. The plot shows the isoscaling of abundant isotopes from Z=4-14 for the $^{64}Zn + ^{70}Zn$ system relative to the $^{64}Zn + ^{64}Zn$ system. The red fit lines correspond to the resulting global fit according to Eq. 1.8.

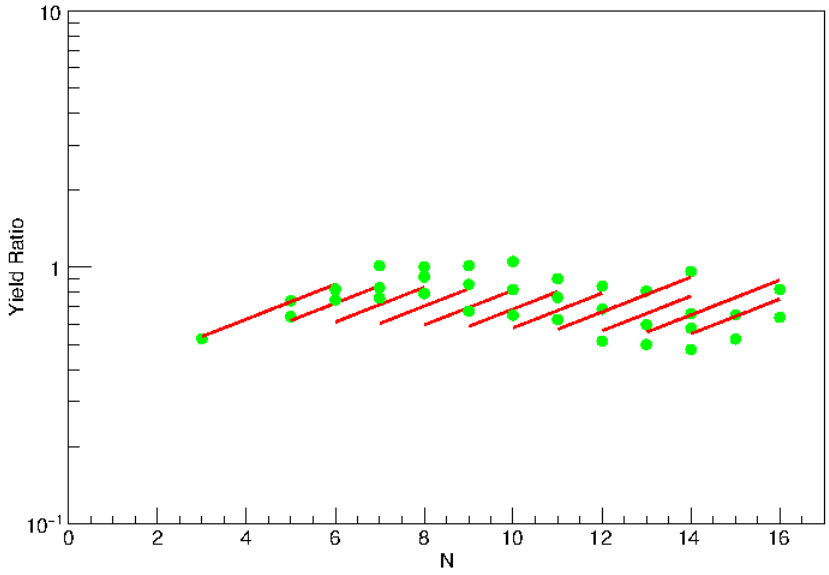

Figure D.4: An example isoscaling plot using an expanded range in fragments. The plot shows the isoscaling of abundant isotopes from Z=4-14 for the $^{64}Zn + ^{64}Ni$ system relative to the $^{64}Zn + ^{64}Zn$ system. The red fit lines correspond to the resulting global fit according to Eq. 1.8.

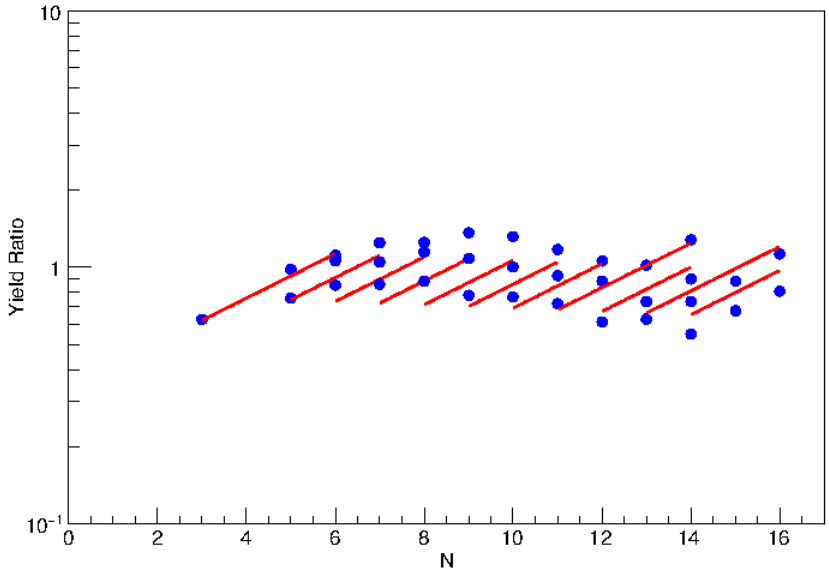

Figure D.5: An example isoscaling plot using an expanded range in fragments. The plot shows the isoscaling of abundant isotopes from Z=4-14 for the $^{64}Ni + ^{64}Zn$ system relative to the $^{64}Zn + ^{64}Zn$ system. The red fit lines correspond to the resulting global fit according to Eq. 1.8.

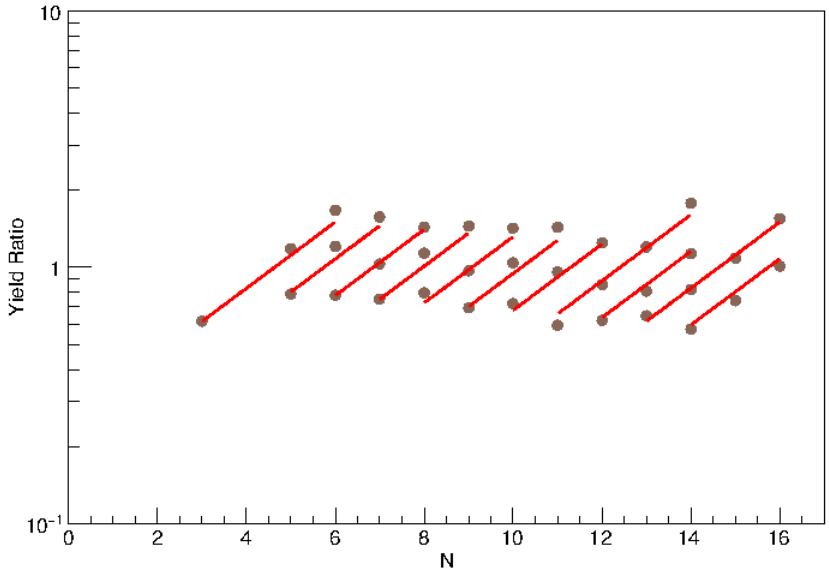

Figure D.6: An example isoscaling plot using an expanded range in fragments. The plot shows the isoscaling of abundant isotopes from Z=4-14 for the $^{64}Ni + ^{64}Ni$ system relative to the $^{64}Zn + ^{64}Zn$ system. The red fit lines correspond to the resulting global fit according to Eq. 1.8.

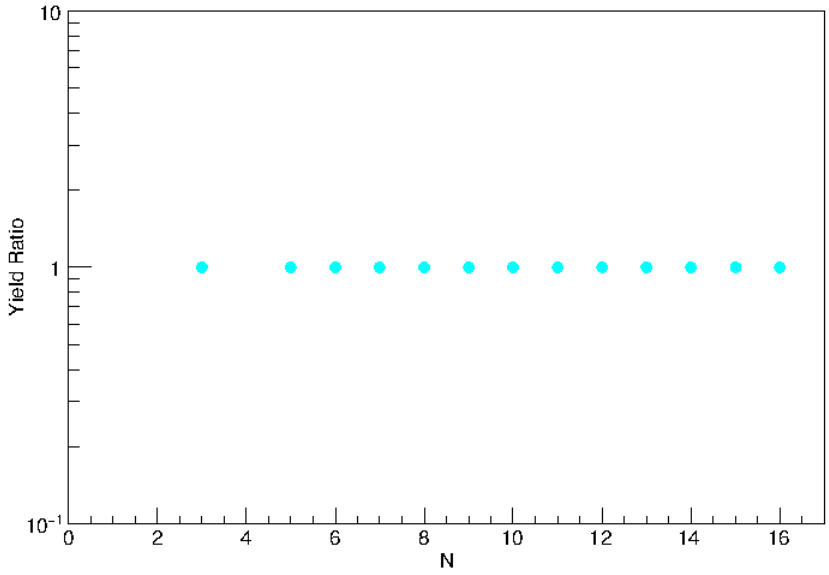

Figure D.7: An example isoscaling plot using an expanded range in fragments. The plot shows the isoscaling of abundant isotopes from Z=4-14 for the $^{64}Zn + ^{64}Zn$ system relative to the $^{64}Zn + ^{64}Zn$ system. Since this is the scaling of a system to itself, all yield ratio values are unity. This also demonstrates that since no fit can be applied in this case, the α and β parameters are definer as 0.

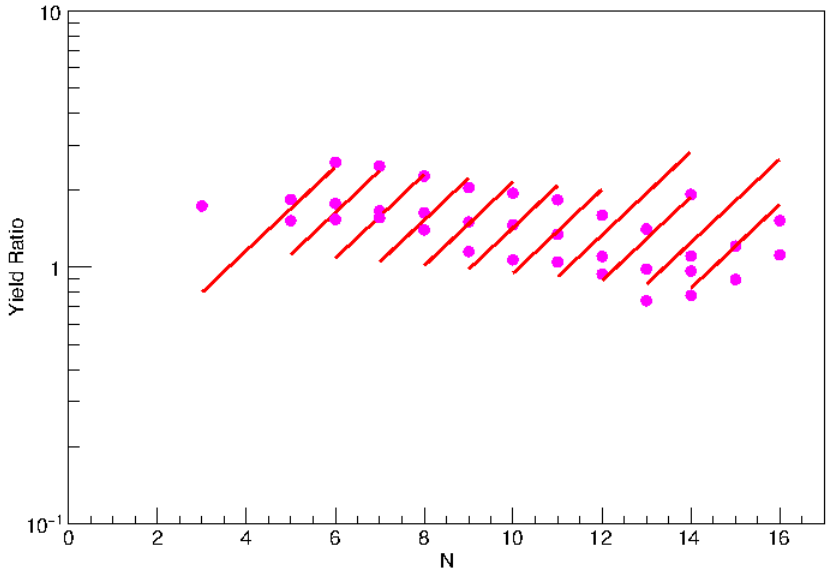

Figure D.8: An example isoscaling plot using an expanded range in fragments from the "asy-soft" CoMD. The plot shows the isoscaling of abundant isotopes from Z=4-14 for the $^{70}Zn + ^{70}Zn$ system relative to the $^{64}Zn + ^{64}Zn$ system. The red fit lines correspond to the resulting global fit according to Eq. 1.8, however due to the poor yield scaling from the CoMD data, the best fit lines represent a poor fit to the data.

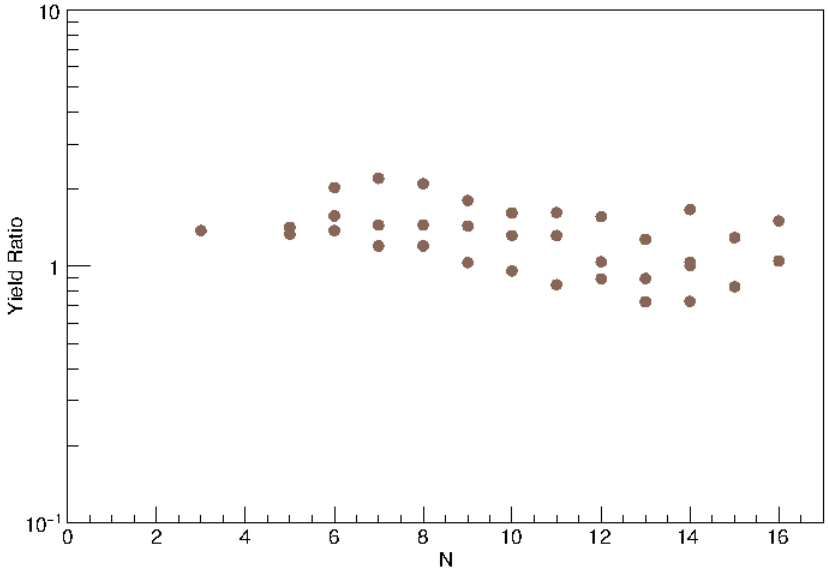

Figure D.9: An example isoscaling plot using an expanded range in fragments from the "asy-soft" CoMD. The plot shows the isoscaling of abundant isotopes from Z=4-14 for the $^{64}Ni + ^{64}Ni$ system relative to the $^{64}Zn + ^{64}Zn$ system. The red fit lines correspond to the resulting global fit according to Eq. 1.8, however due to the poor yield scaling from the CoMD data a best fit could not be constructed on this data set.

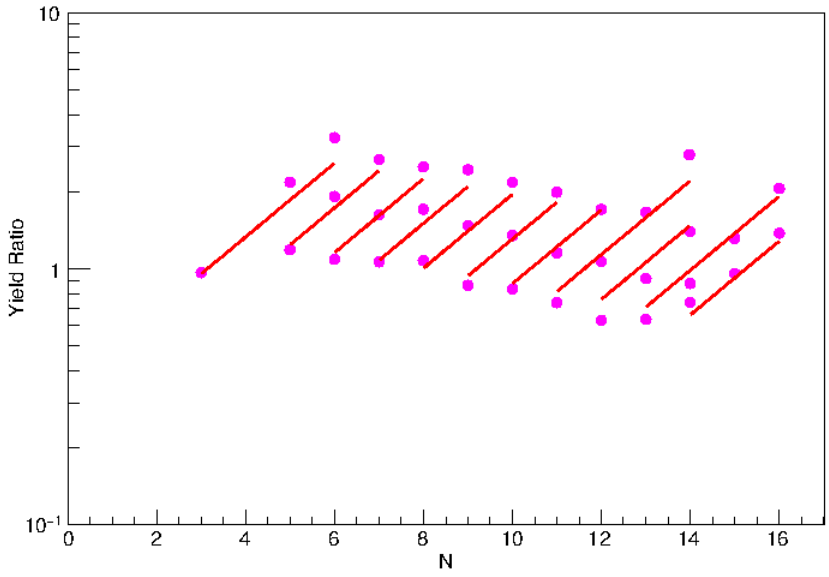

Figure D.10: An example isoscaling plot using an expanded range in fragments for an individual bin (bin # 0) in $V_{z,QP}$ for experimental data. The plot shows the isoscaling of abundant isotopes from Z=4-14 for the $^{70}Zn + ^{70}Zn$ system relative to the $^{64}Zn + ^{64}Zn$ system. The red fit lines correspond to the resulting global fit according to Eq. 1.8.

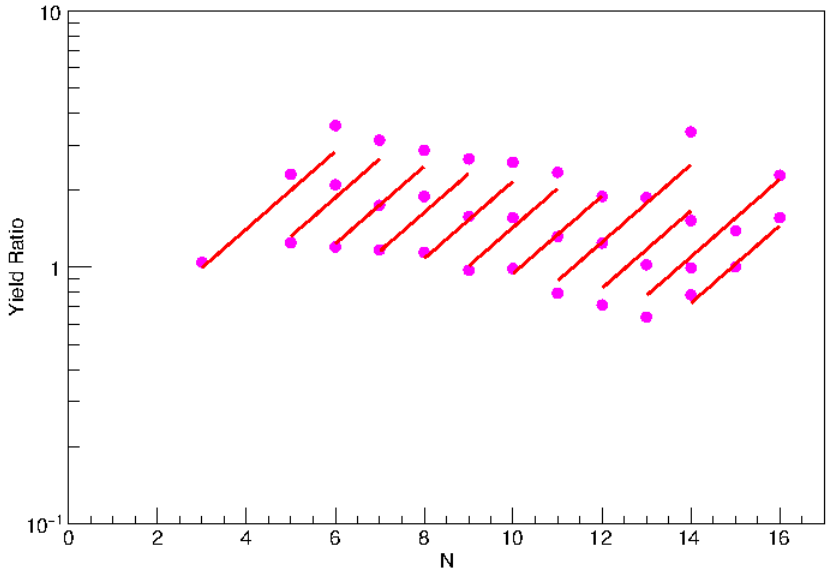

Figure D.11: An example isoscaling plot using an expanded range in fragments for an individual bin (bin # 1) in $V_{z,QP}$ for experimental data. The plot shows the isoscaling of abundant isotopes from Z=4-14 for the $^{70}Zn + ^{70}Zn$ system relative to the $^{64}Zn + ^{64}Zn$ system. The red fit lines correspond to the resulting global fit according to Eq. 1.8.

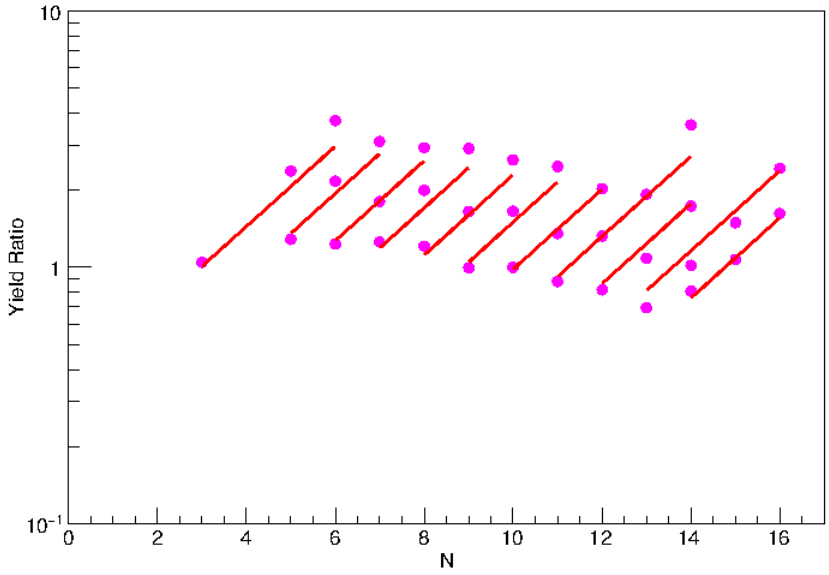

Figure D.12: An example isoscaling plot using an expanded range in fragments for an individual bin (bin # 2) in $V_{z,QP}$ for experimental data. The plot shows the isoscaling of abundant isotopes from Z=4-14 for the $^{70}Zn + ^{70}Zn$ system relative to the $^{64}Zn + ^{64}Zn$ system. The red fit lines correspond to the resulting global fit according to Eq. 1.8.

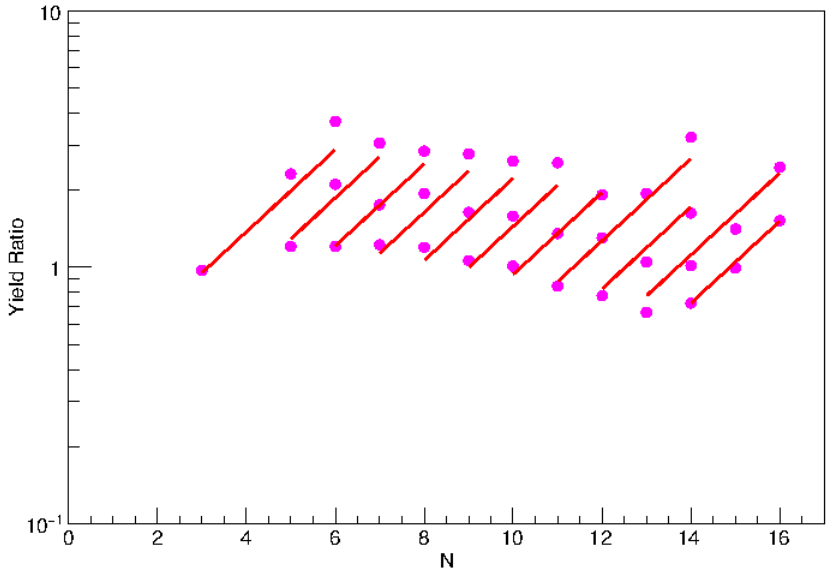

Figure D.13: An example isoscaling plot using an expanded range in fragments for an individual bin (bin # 3) in $V_{z,QP}$ for experimental data. The plot shows the isoscaling of abundant isotopes from Z=4-14 for the $^{70}Zn + ^{70}Zn$ system relative to the $^{64}Zn + ^{64}Zn$ system. The red fit lines correspond to the resulting global fit according to Eq. 1.8.

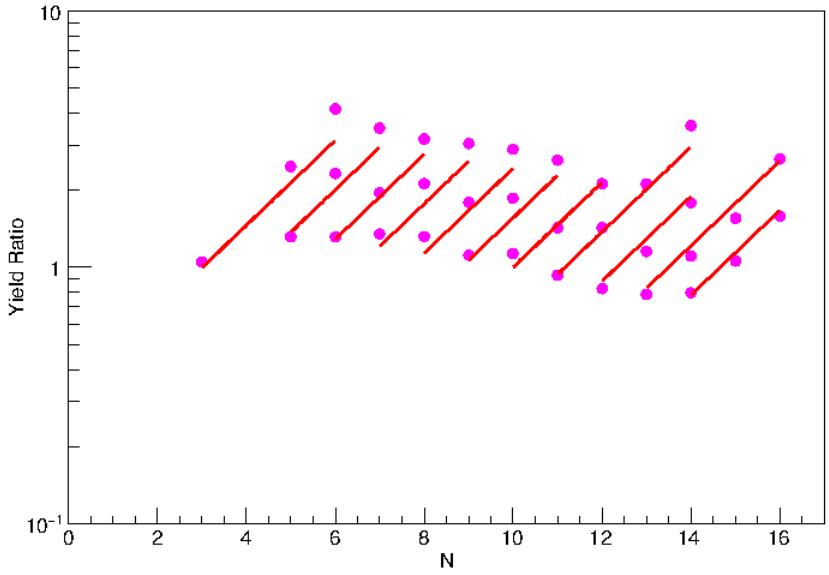

Figure D.14: An example isoscaling plot using an expanded range in fragments for an individual bin (bin # 4) in $V_{z,QP}$ for experimental data. The plot shows the isoscaling of abundant isotopes from Z=4-14 for the $^{70}Zn + ^{70}Zn$ system relative to the $^{64}Zn + ^{64}Zn$ system. The red fit lines correspond to the resulting global fit according to Eq. 1.8.

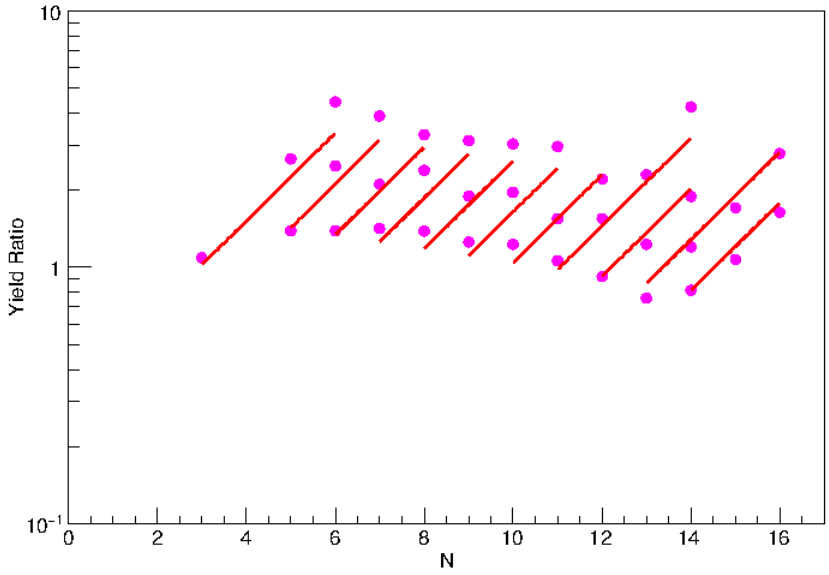

Figure D.15: An example isoscaling plot using an expanded range in fragments for an individual bin (bin # 5) in $V_{z,QP}$ for experimental data. The plot shows the isoscaling of abundant isotopes from Z=4-14 for the $^{70}Zn + ^{70}Zn$ system relative to the $^{64}Zn + ^{64}Zn$ system. The red fit lines correspond to the resulting global fit according to Eq. 1.8.

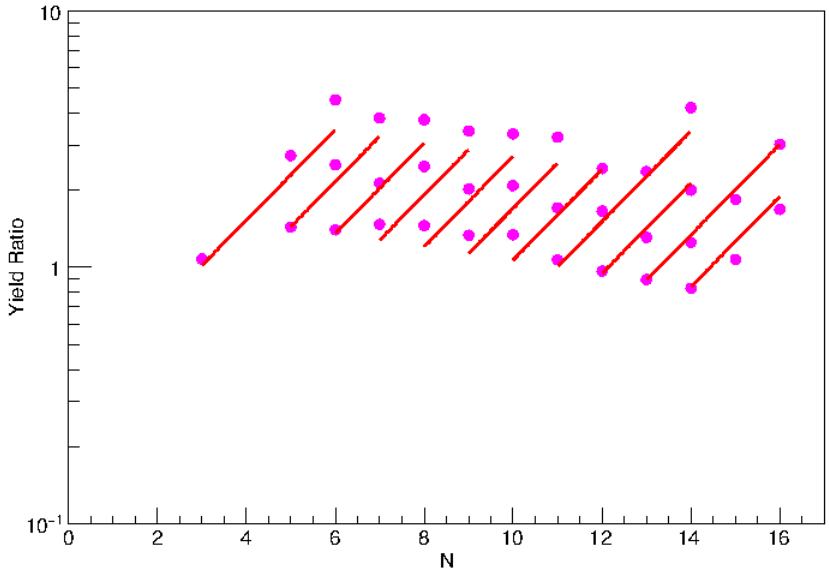

Figure D.16: An example isoscaling plot using an expanded range in fragments for an individual bin (bin # 6) in $V_{z,QP}$ for experimental data. The plot shows the isoscaling of abundant isotopes from Z=4-14 for the $^{70}Zn + ^{70}Zn$ system relative to the $^{64}Zn + ^{64}Zn$ system. The red fit lines correspond to the resulting global fit according to Eq. 1.8.

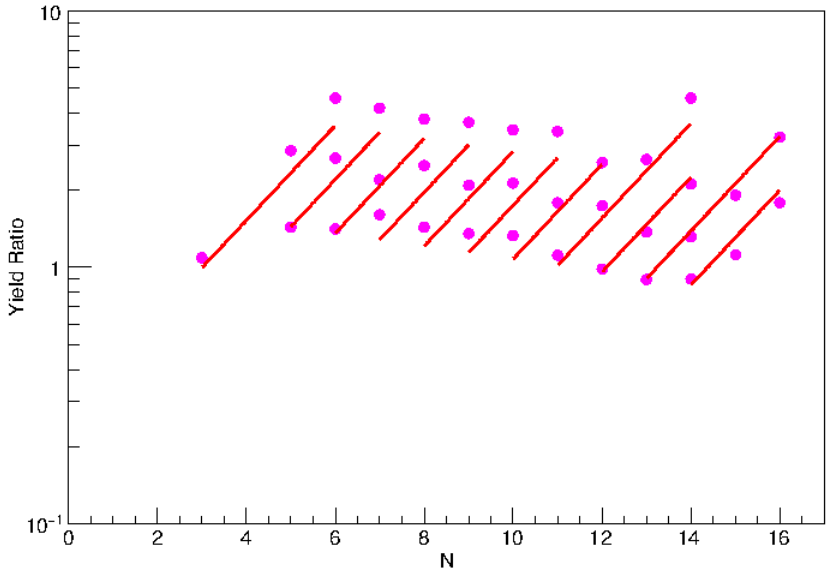

Figure D.17: An example isoscaling plot using an expanded range in fragments for an individual bin (bin # 7) in $V_{z,QP}$ for experimental data. The plot shows the isoscaling of abundant isotopes from Z=4-14 for the $^{70}Zn + ^{70}Zn$ system relative to the $^{64}Zn + ^{64}Zn$ system. The red fit lines correspond to the resulting global fit according to Eq. 1.8.

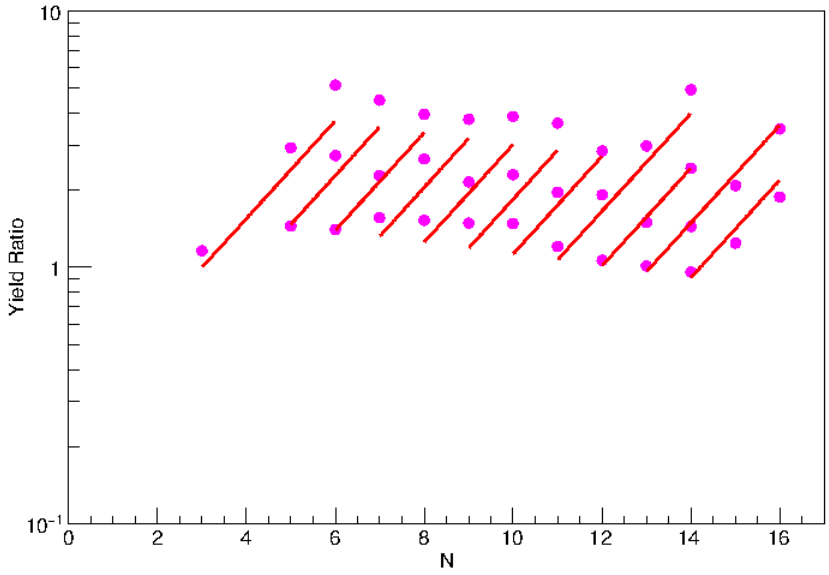

Figure D.18: An example isoscaling plot using an expanded range in fragments for an individual bin (bin # 8) in $V_{z,QP}$ for experimental data. The plot shows the isoscaling of abundant isotopes from Z=4-14 for the $^{70}Zn + ^{70}Zn$ system relative to the $^{64}Zn + ^{64}Zn$ system. The red fit lines correspond to the resulting global fit according to Eq. 1.8.

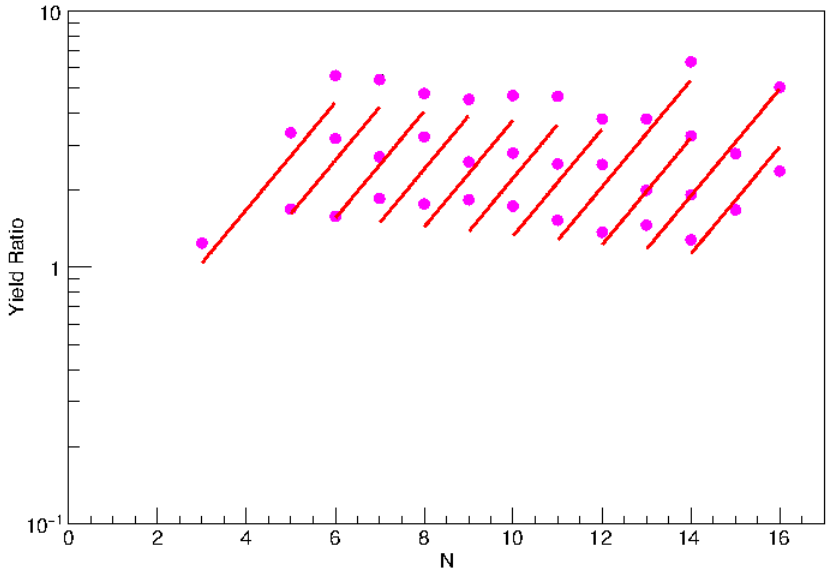

Figure D.19: An example isoscaling plot using an expanded range in fragments for an individual bin (bin # 9) in $V_{z,QP}$ for experimental data. The plot shows the isoscaling of abundant isotopes from Z=4-14 for the $^{70}Zn + ^{70}Zn$ system relative to the $^{64}Zn + ^{64}Zn$ system. The red fit lines correspond to the resulting global fit according to Eq. 1.8.

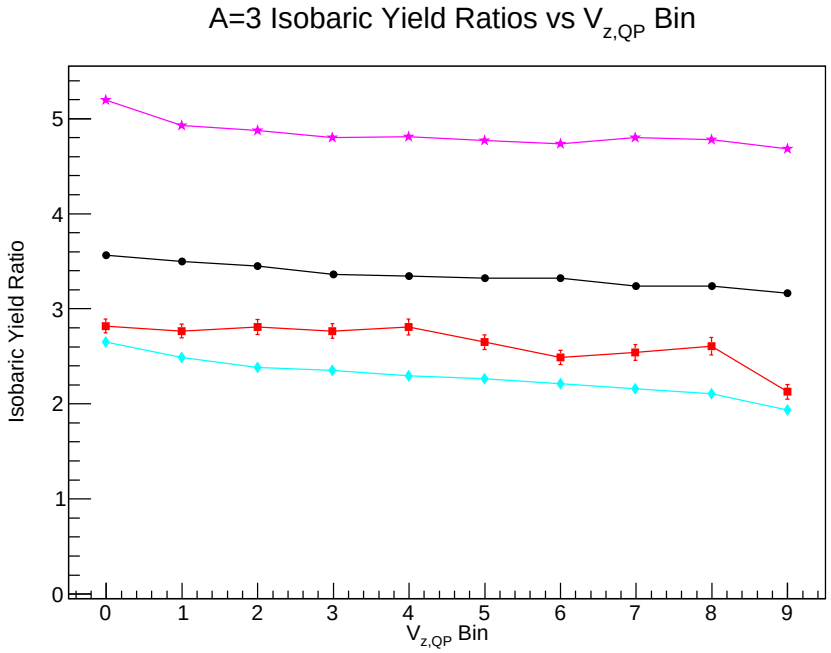

Figure D.20: Isobaric yield ratio for A=3 isobar as a function of $V_{z,QP}$ bin in the experimental data for the Zn set of reaction systems: $^{70}Zn + ^{70}Zn$ (pink stars), $^{70}Zn + ^{64}Zn$ (black circles), $^{64}Zn + ^{70}Zn$ (red squares) and $^{64}Zn + ^{64}Zn$ (light blue diamonds).

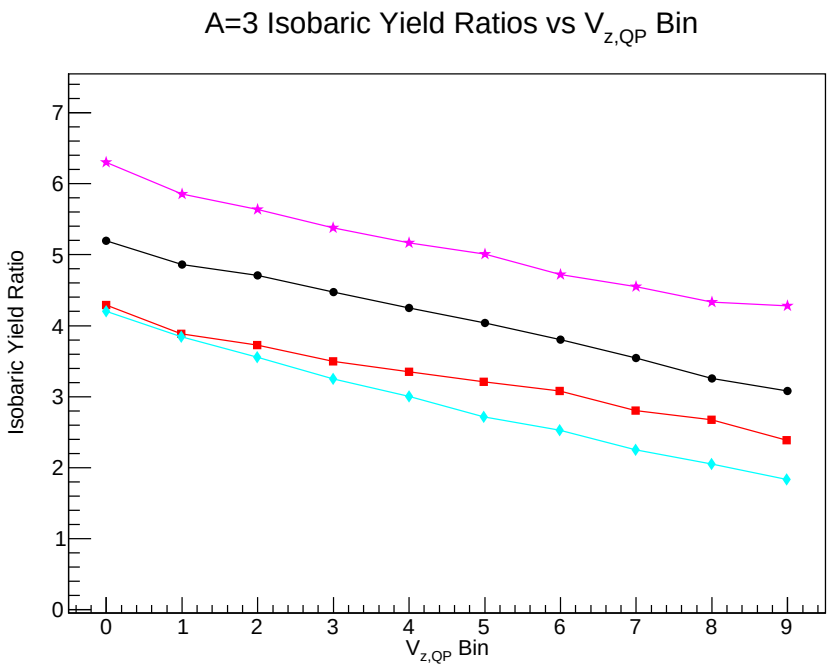

Figure D.21: Isobaric yield ratio for A=3 isobar as a function of $V_{z,QP}$ bin in the "asy-soft" CoMD data for the Zn set of reaction systems: $^{70}Zn + ^{70}Zn$ (pink stars), $^{70}Zn + ^{64}Zn$ (black circles), $^{64}Zn + ^{70}Zn$ (red squares) and $^{64}Zn + ^{64}Zn$ (light blue diamonds).

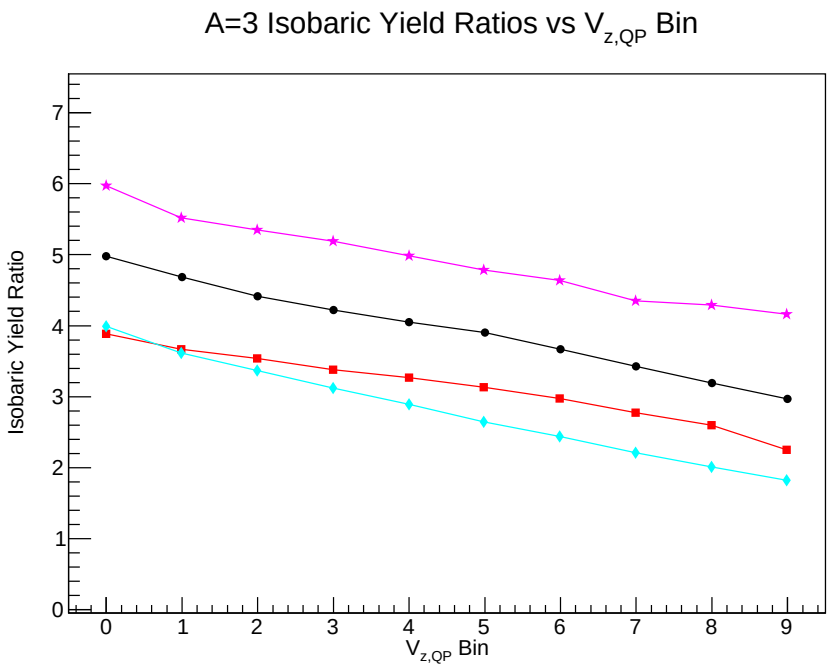

Figure D.22: Isobaric yield ratio for A=3 isobar as a function of $V_{z,QP}$ bin in the "asy-stiff" CoMD data for the Zn set of reaction systems: $^{70}Zn + ^{70}Zn$ (pink stars), $^{70}Zn + ^{64}Zn$ (black circles), $^{64}Zn + ^{70}Zn$ (red squares) and $^{64}Zn + ^{64}Zn$ (light blue diamonds).

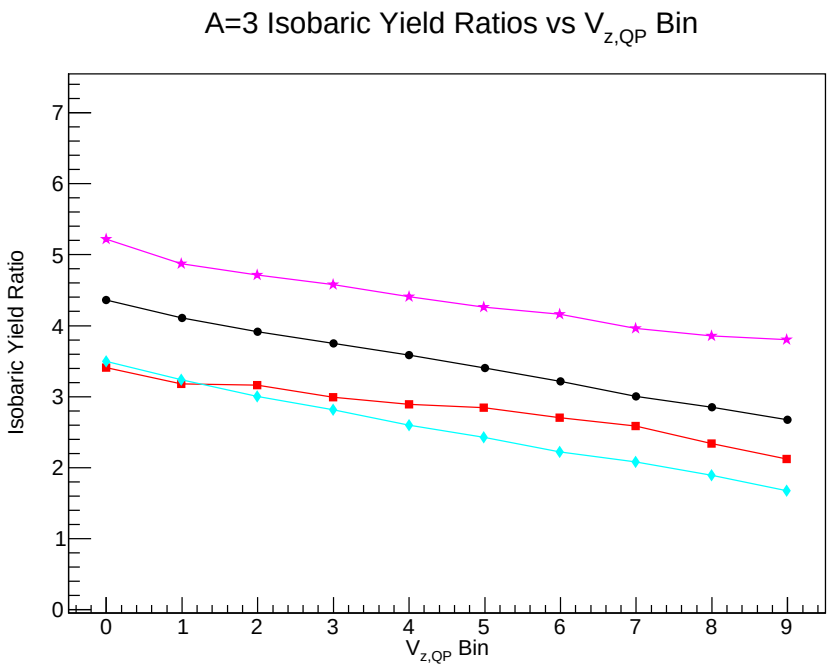

Figure D.23: Isobaric yield ratio for A=3 isobar as a function of $V_{z,QP}$ bin in the "asy-super-stiff" CoMD data for the Zn set of reaction systems: $^{70}Zn + ^{70}Zn$ (pink stars), $^{70}Zn + ^{64}Zn$ (black circles), $^{64}Zn + ^{70}Zn$ (red squares) and $^{64}Zn + ^{64}Zn$ (light blue diamonds).

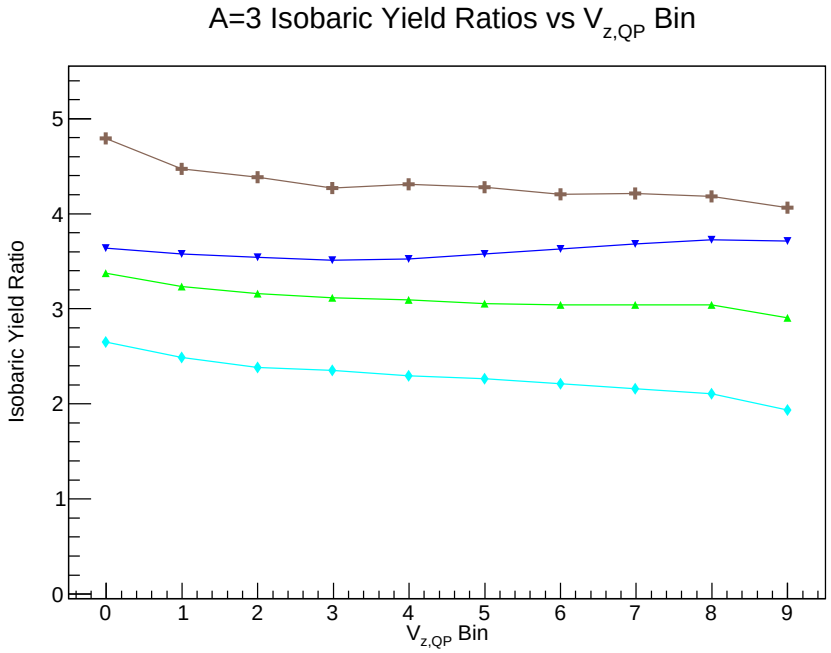

Figure D.24: Isobaric yield ratio for A=3 isobar as a function of $V_{z,QP}$ bin in the experimental data for the A=64 set of reaction systems: $^{64}Ni+^{64}Ni$ (brown crosses), $^{64}Ni+^{64}Zn$ (blue triangles), $^{64}Zn+^{64}Ni$ (green inverted triangles) and $^{64}Zn+^{64}Zn$ (light blue diamonds).

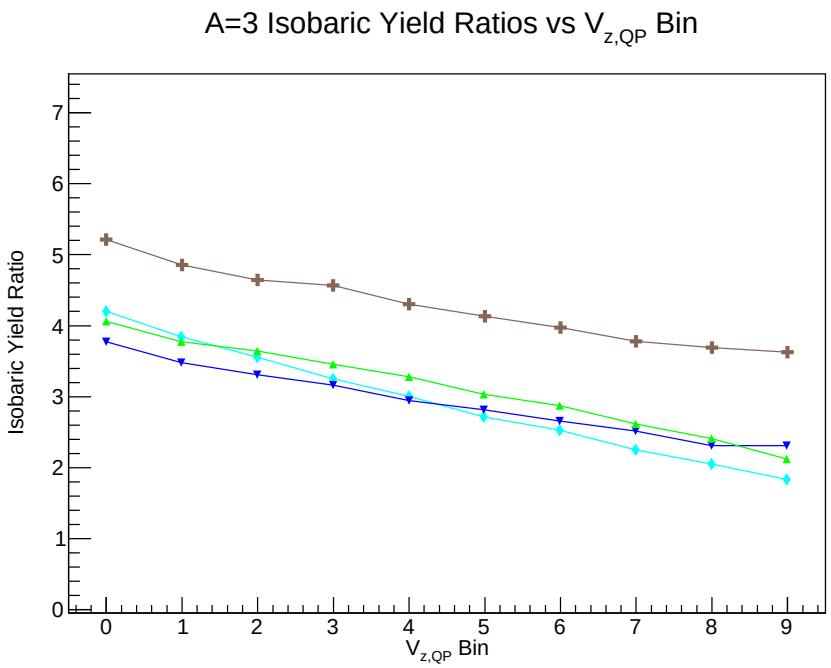

Figure D.25: Isobaric yield ratio for A=3 isobar as a function of $V_{z,QP}$ bin in the "asy-soft" CoMD data for the A=64 set of reaction systems: $^{64}Ni +^{64} Ni$ (brown crosses), $^{64}Ni +^{64} Zn$ (blue triangles), $^{64}Zn +^{64} Ni$ (green inverted triangles) and $^{64}Zn +^{64} Zn$ (light blue diamonds).

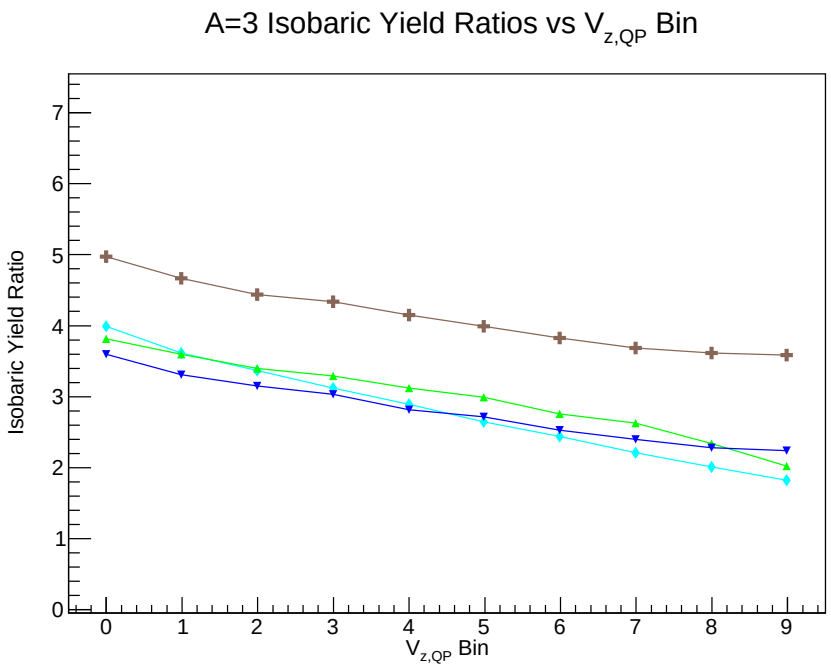

Figure D.26: Isobaric yield ratio for A=3 isobar as a function of $V_{z,QP}$ bin in the "asy-stiff" CoMD data for the A=64 set of reaction systems: $^{64}Ni + ^{64}Ni$ (brown crosses), $^{64}Ni + ^{64}Zn$ (blue triangles), $^{64}Zn + ^{64}Ni$ (green inverted triangles) and $^{64}Zn + ^{64}Zn$ (light blue diamonds).

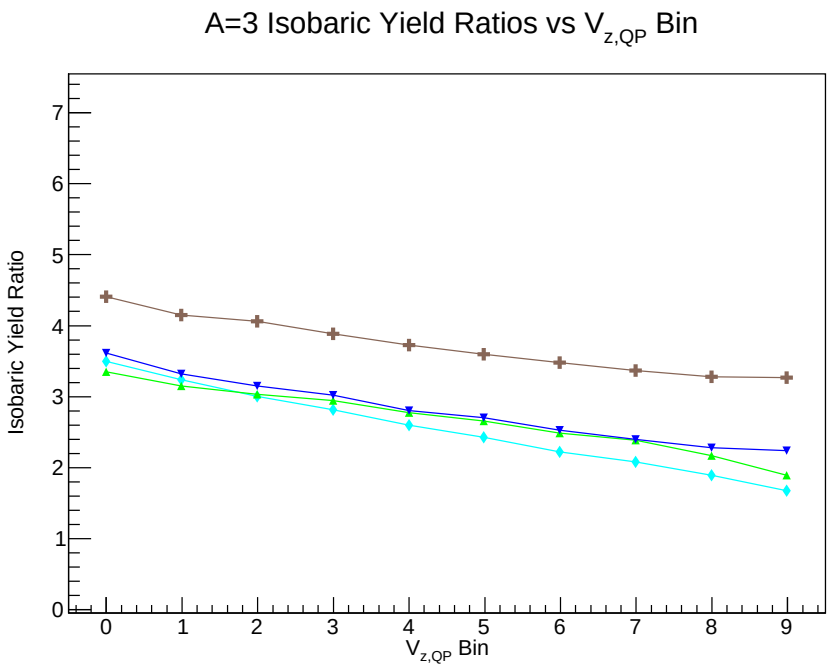

Figure D.27: Isobaric yield ratio for A=3 isobar as a function of $V_{z,QP}$ bin in the "asy-super-stiff" CoMD data for the A=64 set of reaction systems: $^{64}Ni + ^{64}Ni$ (brown crosses), $^{64}Ni + ^{64}Zn$ (blue triangles), $^{64}Zn + ^{64}Ni$ (green inverted triangles) and $^{64}Zn + ^{64}Zn$ (light blue diamonds).

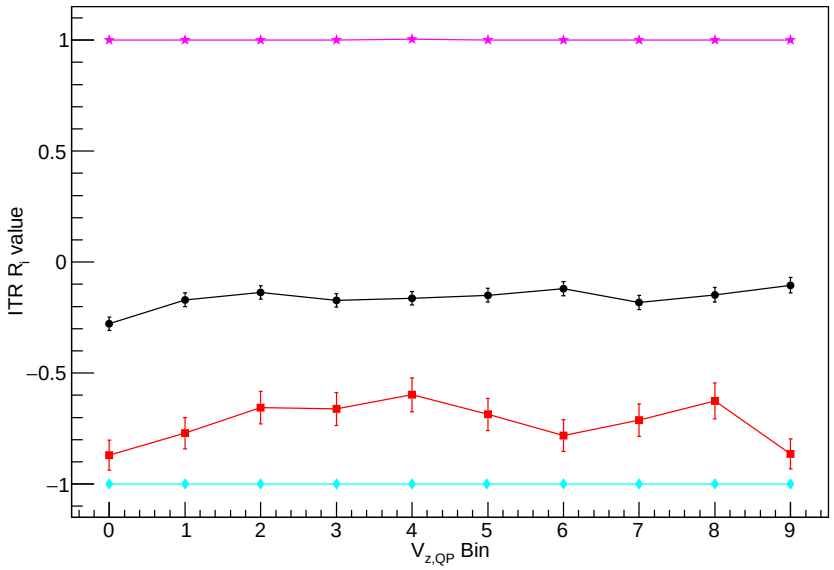

Figure D.28: Isospin Transport Ratio R_i for the A=3 isobar as a function of $V_{z,QP}$ bin in the experimental data for the Zn set of reaction systems: $^{70}Zn + ^{70}Zn$ (pink stars), $^{70}Zn + ^{64}Zn$ (black circles), $^{64}Zn + ^{70}Zn$ (red squares) and $^{64}Zn + ^{64}Zn$ (light blue diamonds).

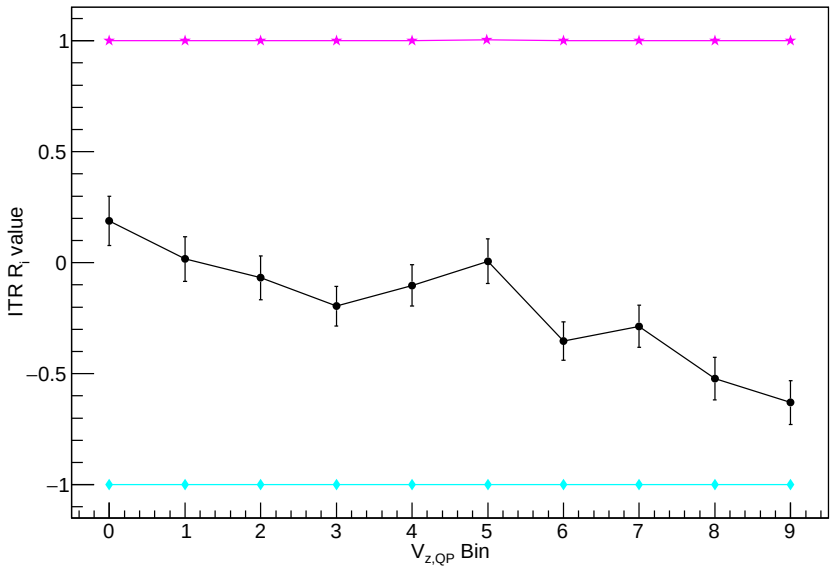

Figure D.29: Isospin Transport Ratio R_i for the A=7 isobar as a function of $V_{z,QP}$ bin in the experimental data for the Zn set of reaction systems: $^{70}Zn + ^{70}Zn$ (pink stars), $^{70}Zn + ^{64}Zn$ (black circles) and $^{64}Zn + ^{64}Zn$ (light blue diamonds). Due to poor statistics in the $^{64}Zn + ^{70}Zn$ (red squares) reaction system, the A=7 isobar in this system did not meet the minimum statistics requirement.

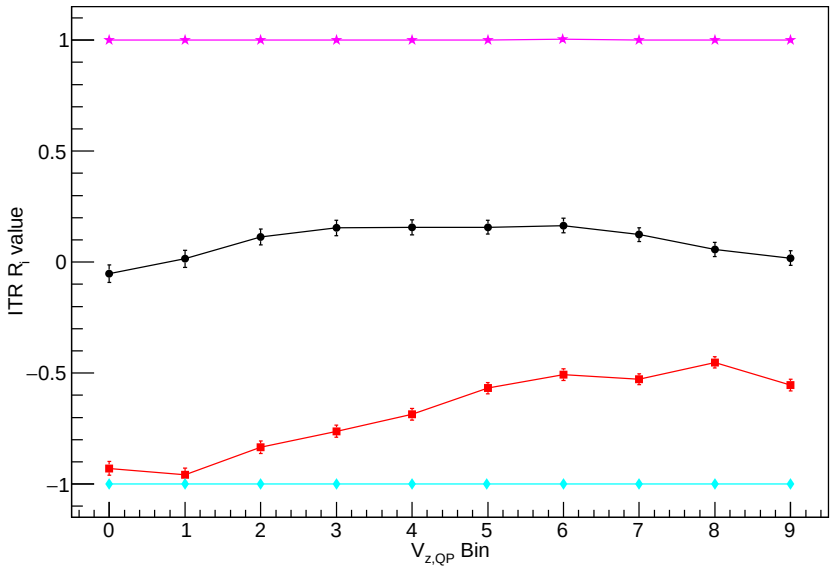

Figure D.30: Isospin Transport Ratio R_i for the A=3 isobar as a function of $V_{z,QP}$ bin in the "asy-soft" CoMD for the Zn set of reaction systems: $^{70}Zn + ^{70}Zn$ (pink stars), $^{70}Zn + ^{64}Zn$ (black circles), $^{64}Zn + ^{70}Zn$ (red squares) and $^{64}Zn + ^{64}Zn$ (light blue diamonds).

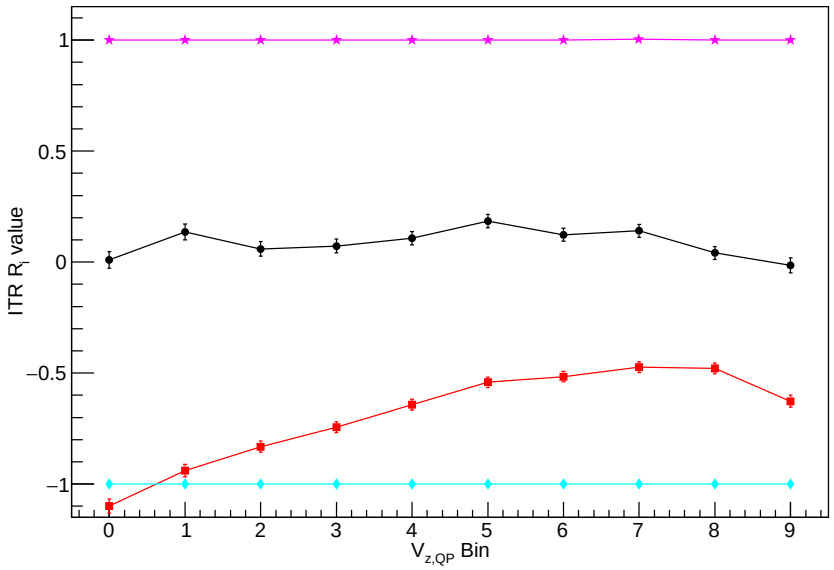

Figure D.31: Isospin Transport Ratio R_i for the A=3 isobar as a function of $V_{z,QP}$ bin in the "asy-stiff" CoMD for the Zn set of reaction systems: $^{70}Zn + ^{70}Zn$ (pink stars), $^{70}Zn + ^{64}Zn$ (black circles), $^{64}Zn + ^{70}Zn$ (red squares) and $^{64}Zn + ^{64}Zn$ (light blue diamonds).

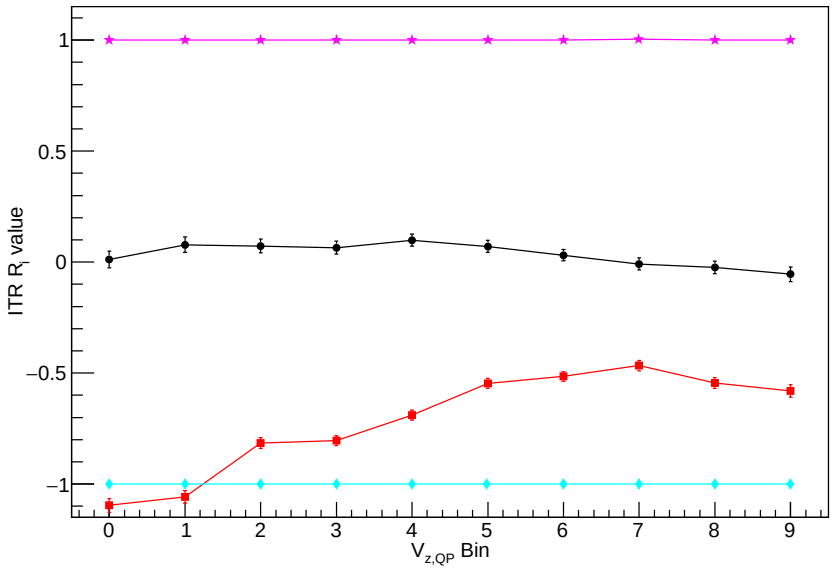

Figure D.32: Isospin Transport Ratio R_i for the A=3 isobar as a function of $V_{z,QP}$ bin in the "asy-super-stiff" CoMD for the Zn set of reaction systems: $^{70}Zn + ^{70}Zn$ (pink stars), $^{70}Zn + ^{64}Zn$ (black circles), $^{64}Zn + ^{70}Zn$ (red squares) and $^{64}Zn + ^{64}Zn$ (light blue diamonds).

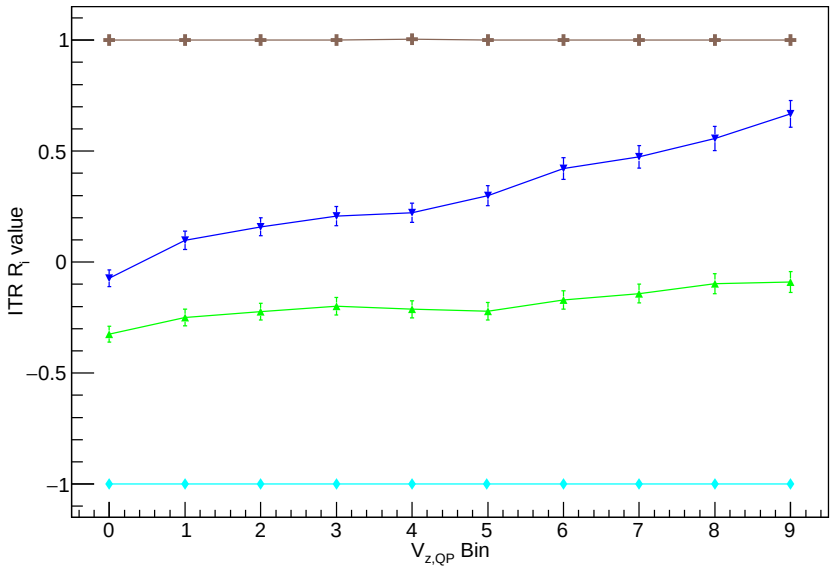

Figure D.33: Isospin Transport Ratio R_i for the A=3 isobar as a function of $V_{z,QP}$ bin in the experimental data for the A=64 set of reaction systems: $^{64}Ni + ^{64}Ni$ (brown crosses), $^{64}Ni + ^{64}Zn$ (blue triangles), $^{64}Zn + ^{64}Ni$ (green inverted triangles) and $^{64}Zn + ^{64}Zn$ (light blue diamonds).

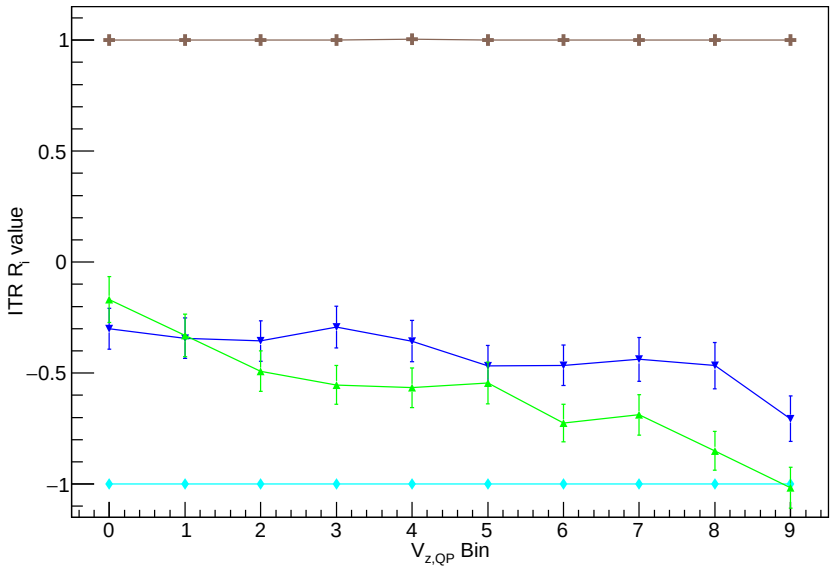

Figure D.34: Isospin Transport Ratio R_i for the A=7 isobar as a function of $V_{z,QP}$ bin in the experimental data for the A=64 set of reaction systems: $^{64}Ni + ^{64}Ni$ (brown crosses), $^{64}Ni + ^{64}Zn$ (blue triangles), $^{64}Zn + ^{64}Ni$ (green inverted triangles) and $^{64}Zn + ^{64}Zn$ (light blue diamonds).

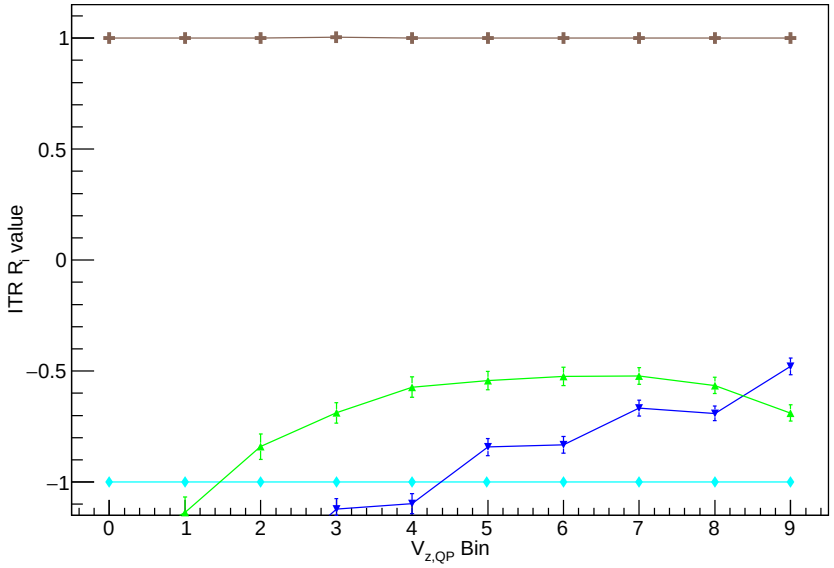

Figure D.35: Isospin Transport Ratio R_i for the A=3 isobar as a function of $V_{z,QP}$ bin in the "asy-soft" CoMD for the A=64 set of reaction systems: $^{64}Ni + ^{64}Ni$ (brown crosses), $^{64}Ni + ^{64}Zn$ (blue triangles), $^{64}Zn + ^{64}Ni$ (green inverted triangles) and $^{64}Zn + ^{64}Zn$ (light blue diamonds).

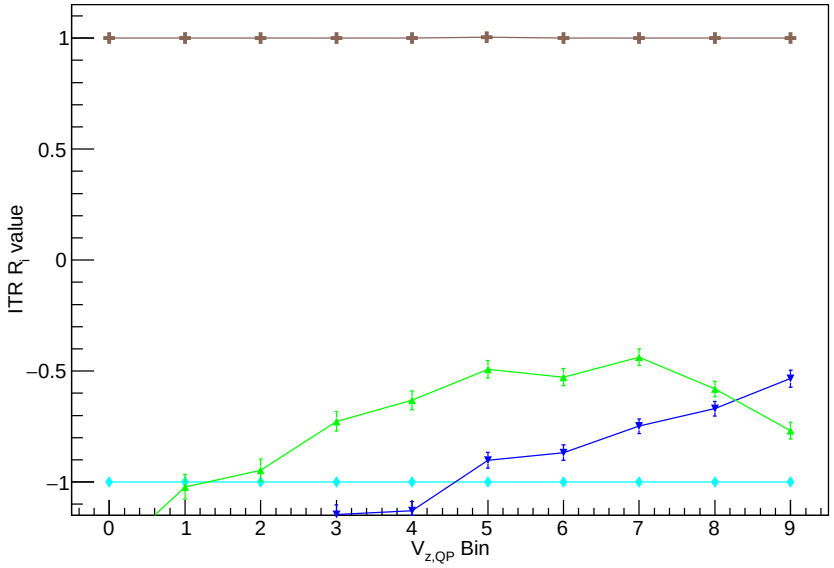

Figure D.36: Isospin Transport Ratio R_i for the A=3 isobar as a function of $V_{z,QP}$ bin in the "asy-stiff" CoMD for the A=64 set of reaction systems: $^{64}Ni + ^{64}Ni$ (brown crosses), $^{64}Ni + ^{64}Zn$ (blue triangles), $^{64}Zn + ^{64}Ni$ (green inverted triangles) and $^{64}Zn + ^{64}Zn$ (light blue diamonds).

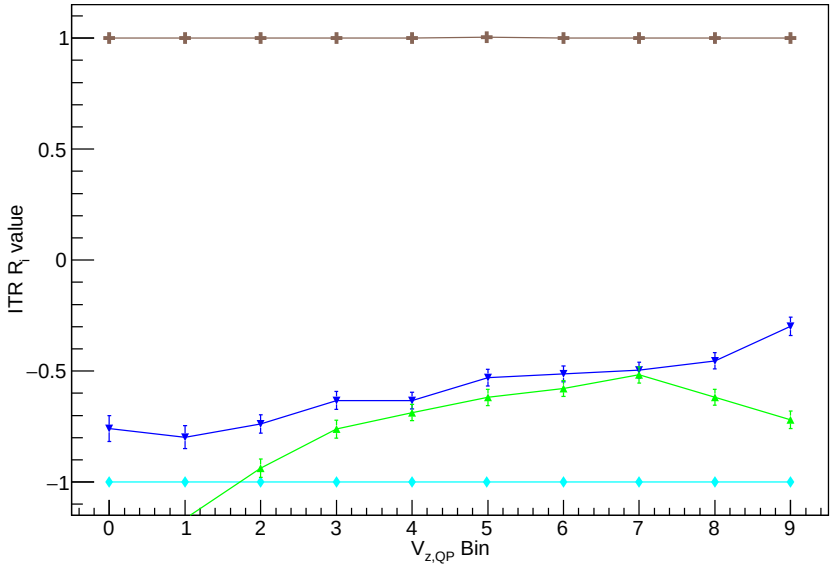

Figure D.37: Isospin Transport Ratio R_i for the A=3 isobar as a function of $V_{z,QP}$ bin in the "asy-super-stiff" CoMD for the A=64 set of reaction systems: $^{64}Ni + ^{64}Ni$ (brown crosses), $^{64}Ni + ^{64}Zn$ (blue triangles), $^{64}Zn + ^{64}Ni$ (green inverted triangles) and $^{64}Zn + ^{64}Zn$ (light blue diamonds).

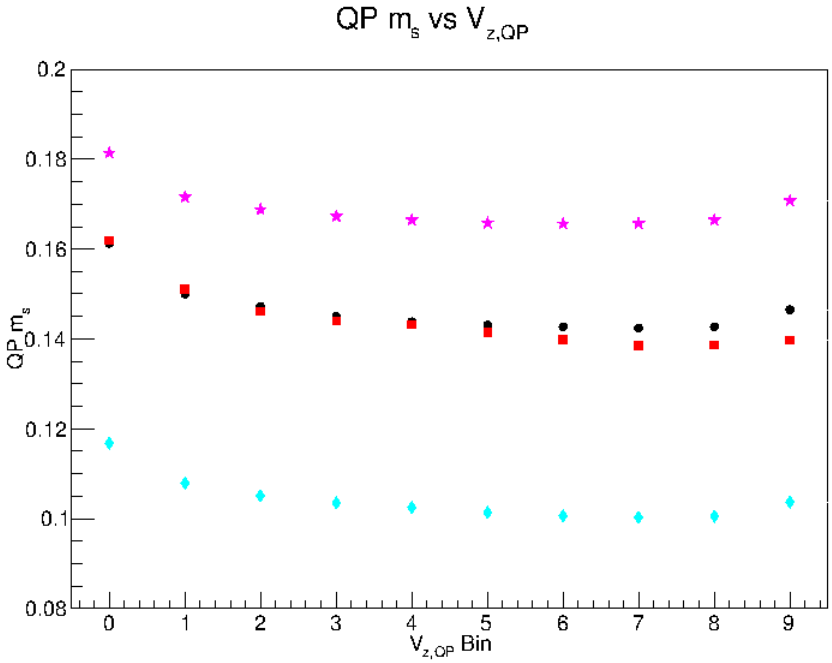

Figure D.38: Quasi-projectile m_s as a function of $V_{z,QP}$ bin in the experimental data for the Zn set of reaction systems: $^{70}Zn+^{70}Zn$ (pink stars), $^{70}Zn+^{64}Zn$ (black circles), $^{64}Zn+^{70}Zn$ (red squares) and $^{64}Zn+^{64}Zn$ (light blue diamonds).

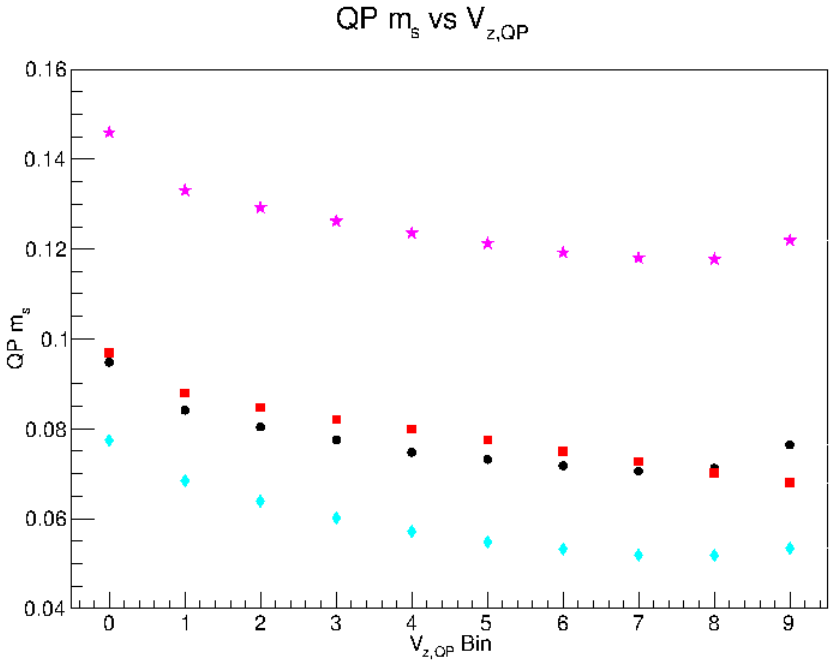

Figure D.39: Quasi-projectile m_s as a function of $V_{z,QP}$ bin in the "asy-soft" CoMD for the Zn set of reaction systems: $^{70}Zn + ^{70}Zn$ (pink stars), $^{70}Zn + ^{64}Zn$ (black circles), $^{64}Zn + ^{70}Zn$ (red squares) and $^{64}Zn + ^{64}Zn$ (light blue diamonds).

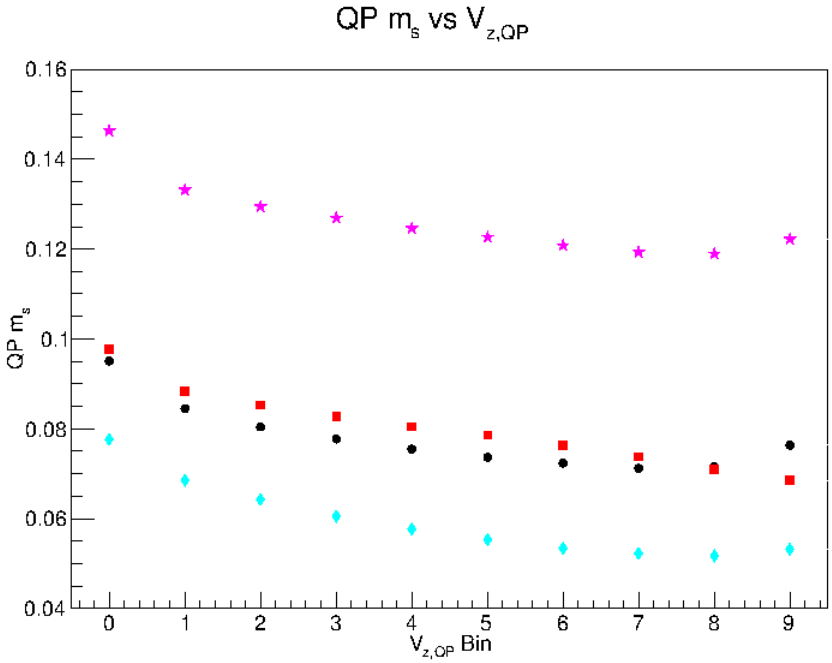

Figure D.40: Quasi-projectile m_s as a function of $V_{z,QP}$ bin in the "asy-stiff" CoMD for the Zn set of reaction systems: $^{70}Zn + ^{70}Zn$ (pink stars), $^{70}Zn + ^{64}Zn$ (black circles), $^{64}Zn + ^{70}Zn$ (red squares) and $^{64}Zn + ^{64}Zn$ (light blue diamonds).

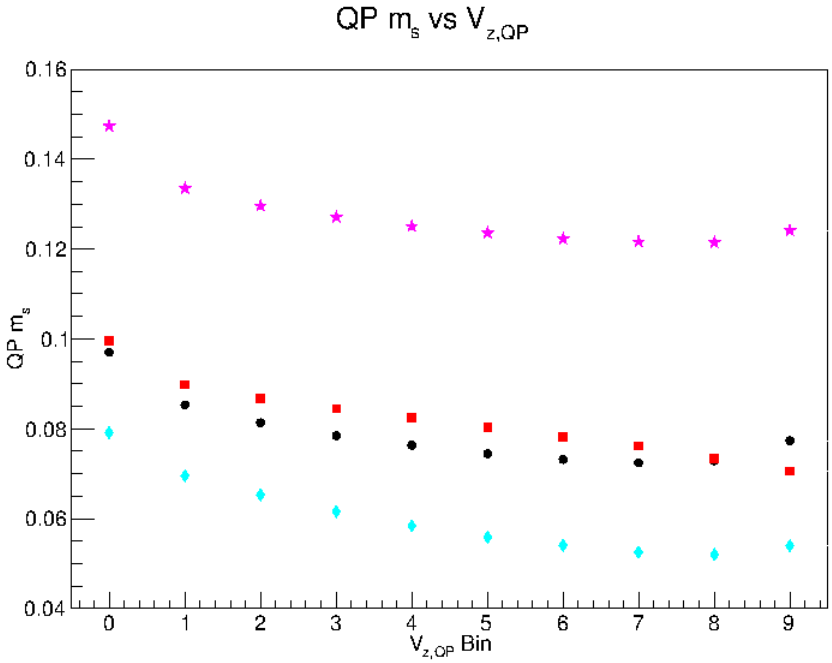

Figure D.41: Quasi-projectile m_s as a function of $V_{z,QP}$ bin in the "asy-super-stiff" CoMD for the Zn set of reaction systems: $^{70}Zn + ^{70}Zn$ (pink stars), $^{70}Zn + ^{64}Zn$ (black circles), $^{64}Zn + ^{70}Zn$ (red squares) and $^{64}Zn + ^{64}Zn$ (light blue diamonds).

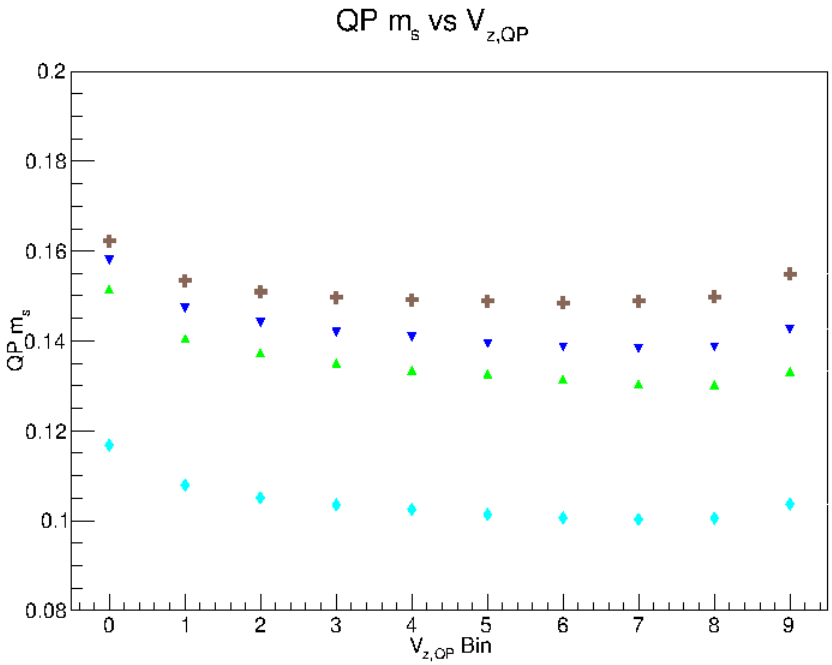

Figure D.42: Quasi-projectile m_s as a function of $V_{z,QP}$ bin in the experimental data for the A=64 set of reaction systems: $^{64}Ni+^{64}Ni$ (brown crosses), $^{64}Ni+^{64}Zn$ (blue triangles), $^{64}Zn+^{64}Ni$ (green inverted triangles) and $^{64}Zn+^{64}Zn$ (light blue diamonds).

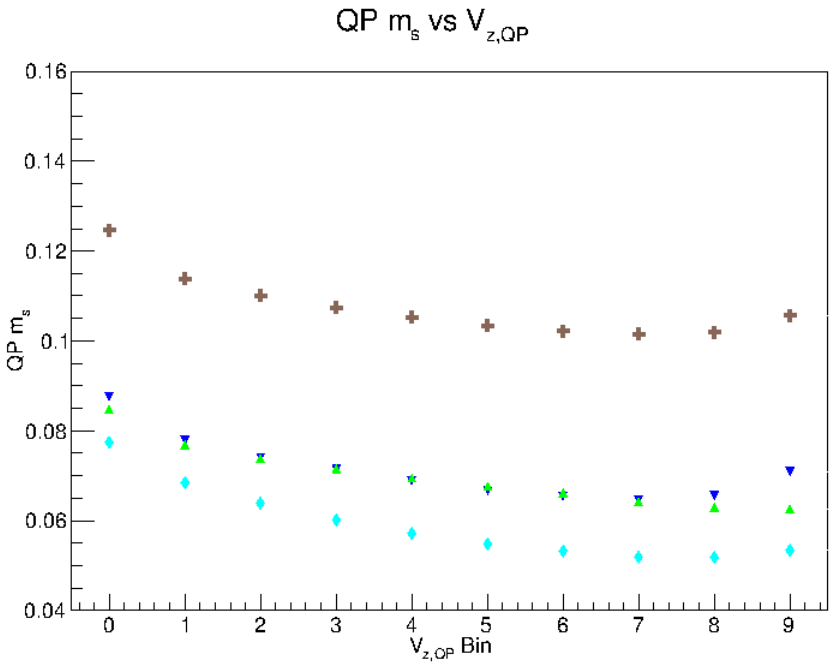

Figure D.43: Quasi-projectile m_s as a function of $V_{z,QP}$ bin in the "asy-soft" CoMD for the A=64 set of reaction systems: $^{64}Ni + ^{64}Ni$ (brown crosses), $^{64}Ni + ^{64}Zn$ (blue triangles), $^{64}Zn + ^{64}Ni$ (green inverted triangles) and $^{64}Zn + ^{64}Zn$ (light blue diamonds).

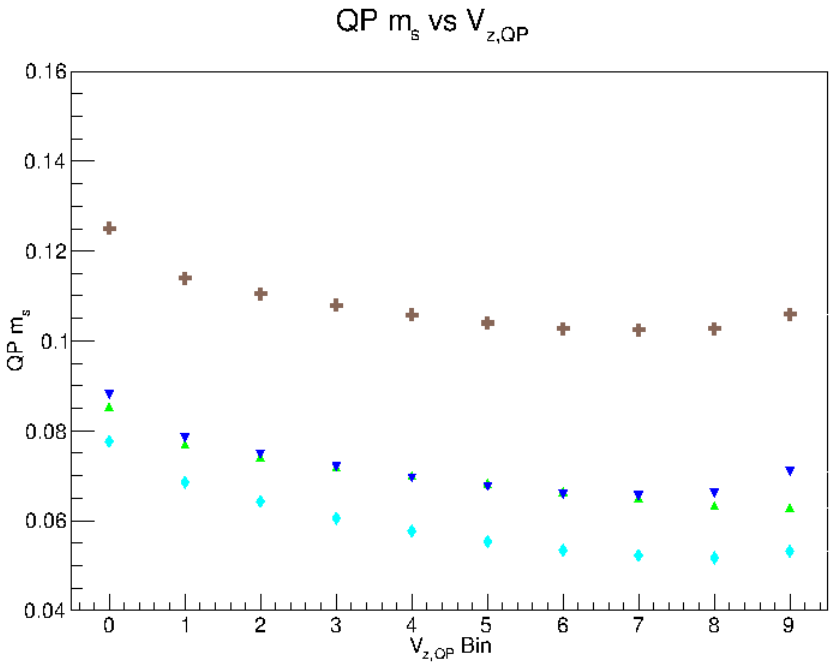

Figure D.44: Quasi-projectile m_s as a function of $V_{z,QP}$ bin in the "asy-stiff" CoMD for the A=64 set of reaction systems: $^{64}Ni +^{64} Ni$ (brown crosses), $^{64}Ni +^{64} Zn$ (blue triangles), $^{64}Zn +^{64} Ni$ (green inverted triangles) and $^{64}Zn +^{64} Zn$ (light blue diamonds).

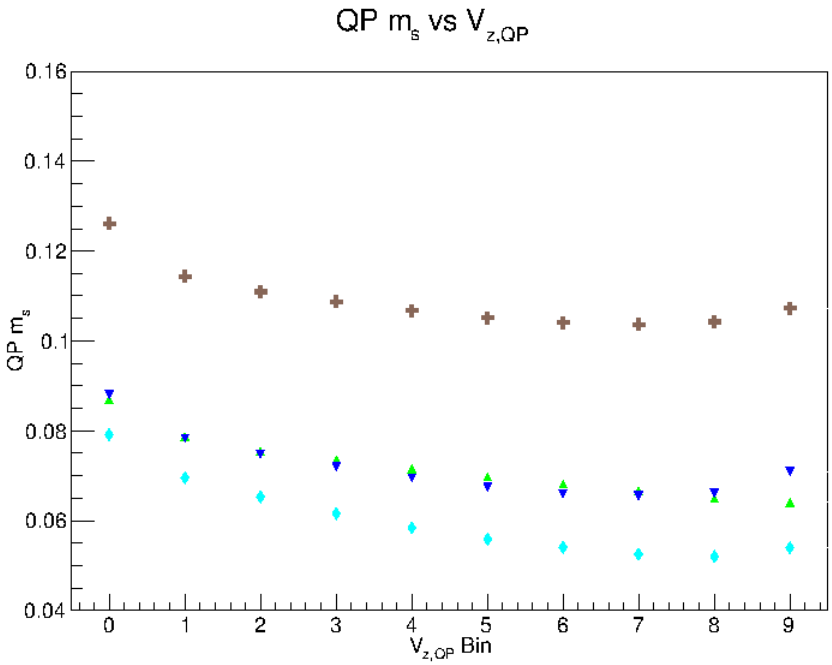

Figure D.45: Quasi-projectile m_s as a function of $V_{z,QP}$ bin in the "asy-super-stiff" CoMD for the A=64 set of reaction systems: ^{64}Ni+^{64}Ni (brown crosses), ^{64}Ni+^{64}Zn (blue triangles), ^{64}Zn +^{64} Ni (green inverted triangles) and ^{64}Zn +^{64} Zn (light blue diamonds).

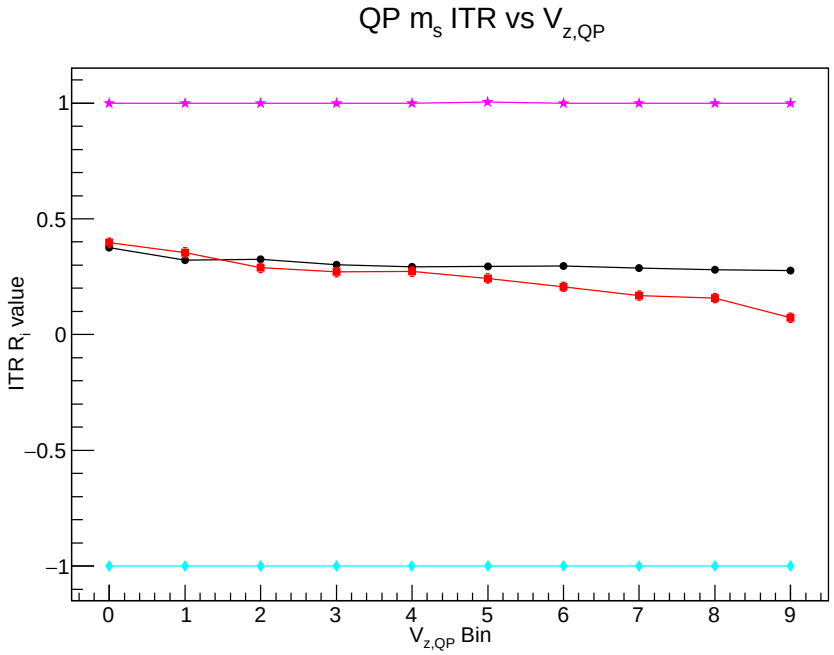

Figure D.46: Isospin Transport Ratio R_i for the QP m_s as a function of $V_{z,QP}$ bin in the experimental data for the Zn set of reaction systems: $^{70}Zn + ^{70}Zn$ (pink stars), $^{70}Zn + ^{64}Zn$ (black circles), $^{64}Zn + ^{70}Zn$ (red squares) and $^{64}Zn + ^{64}Zn$ (light blue diamonds).

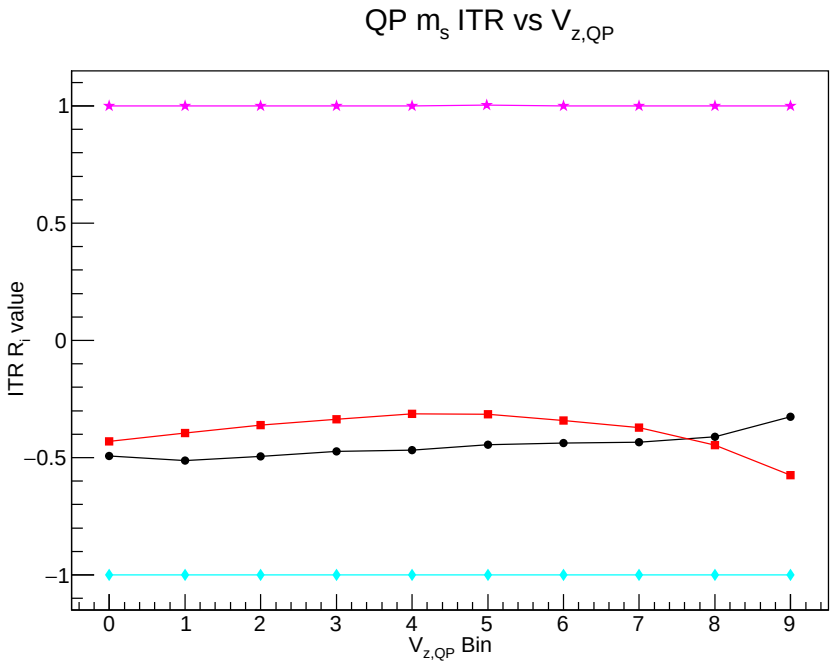

Figure D.47: Isospin Transport Ratio R_i for the QP m_s as a function of $V_{z,QP}$ bin in the "asy-soft" CoMD for the Zn set of reaction systems: $^{70}Zn + ^{70}Zn$ (pink stars), $^{70}Zn + ^{64}Zn$ (black circles), $^{64}Zn + ^{70}Zn$ (red squares) and $^{64}Zn + ^{64}Zn$ (light blue diamonds).

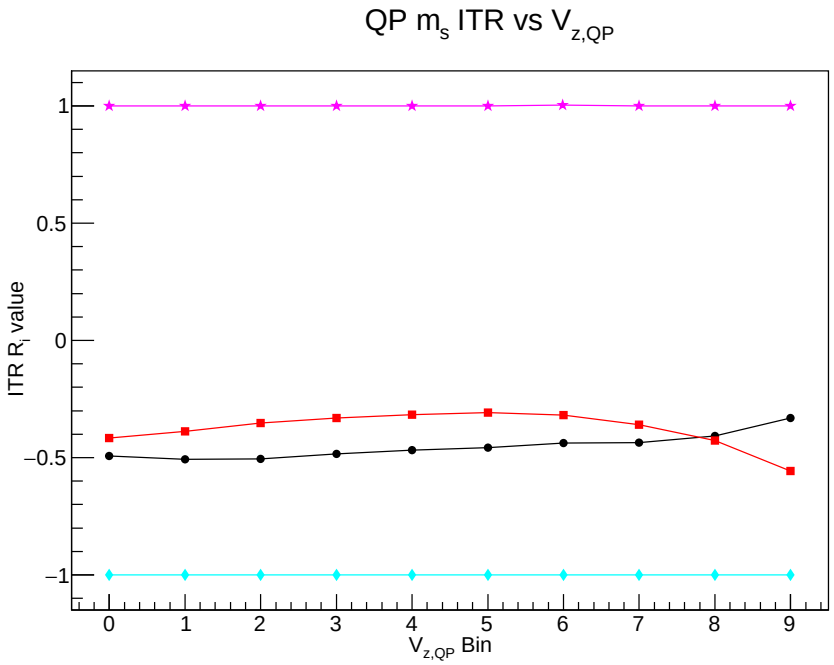

Figure D.48: Isospin Transport Ratio R_i for the QP m_s as a function of $V_{z,QP}$ bin in the "asy-stiff" CoMD for the Zn set of reaction systems: $^{70}Zn + ^{70}Zn$ (pink stars), $^{70}Zn + ^{64}Zn$ (black circles), $^{64}Zn + ^{70}Zn$ (red squares) and $^{64}Zn + ^{64}Zn$ (light blue diamonds).

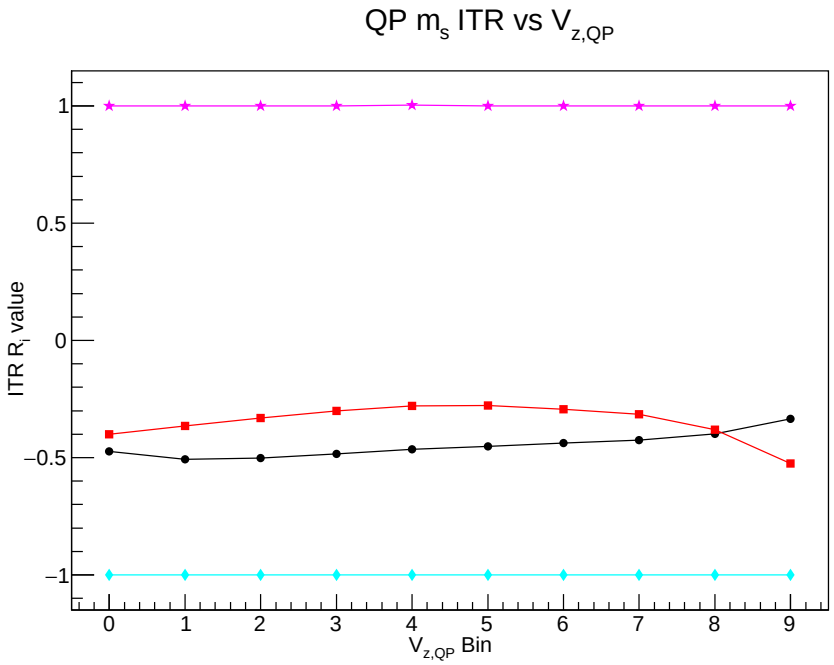

Figure D.49: Isospin Transport Ratio R_i for the QP m_s as a function of $V_{z,QP}$ bin in the "asy-super-stiff" CoMD for the Zn set of reaction systems: $^{70}Zn+^{70}Zn$ (pink stars), $^{70}Zn+^{64}Zn$ (black circles), $^{64}Zn+^{70}Zn$ (red squares) and $^{64}Zn+^{64}Zn$ (light blue diamonds).

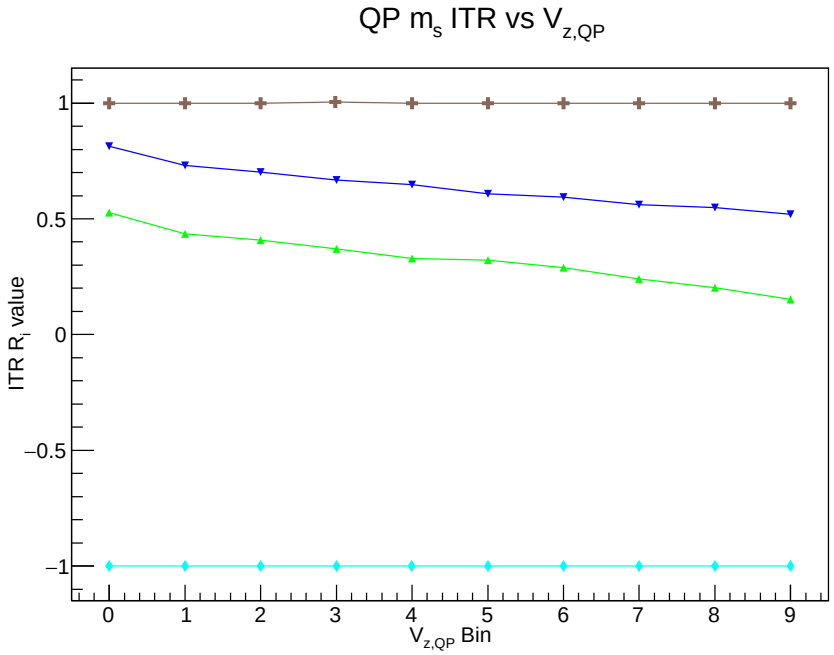

Figure D.50: Isospin Transport Ratio R_i for the QP m_s as a function of $V_{z,QP}$ bin in the experimental data for the A=64 set of reaction systems: $^{64}Ni + ^{64}Ni$ (brown crosses), $^{64}Ni + ^{64}Zn$ (blue triangles), $^{64}Zn + ^{64}Ni$ (green inverted triangles) and $^{64}Zn + ^{64}Zn$ (light blue diamonds).

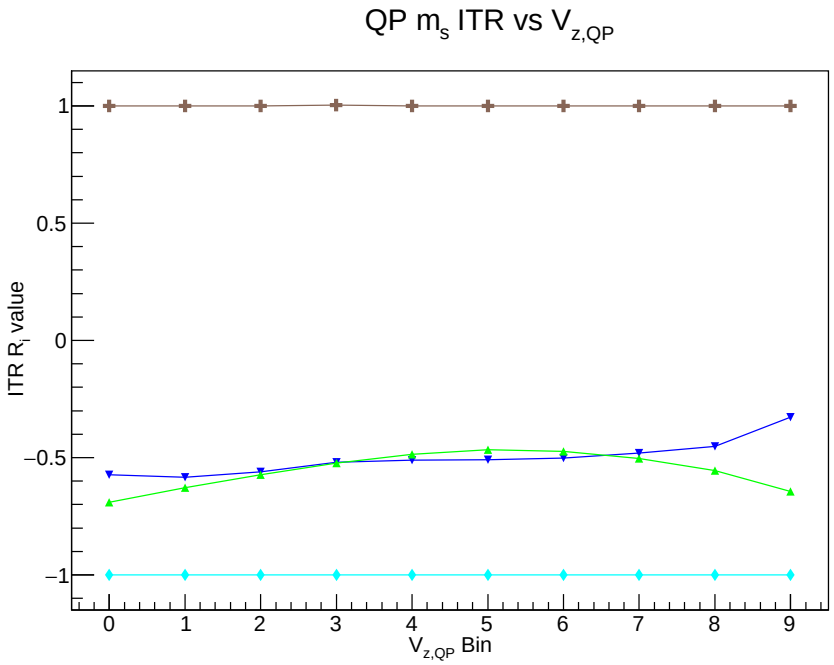

Figure D.51: Isospin Transport Ratio R_i for the QP m_s as a function of $V_{z,QP}$ bin in the "asy-soft" CoMD for the A=64 set of reaction systems: $^{64}Ni + ^{64}Ni$ (brown crosses), $^{64}Ni + ^{64}Zn$ (blue triangles), $^{64}Zn + ^{64}Ni$ (green inverted triangles) and $^{64}Zn + ^{64}Zn$ (light blue diamonds).

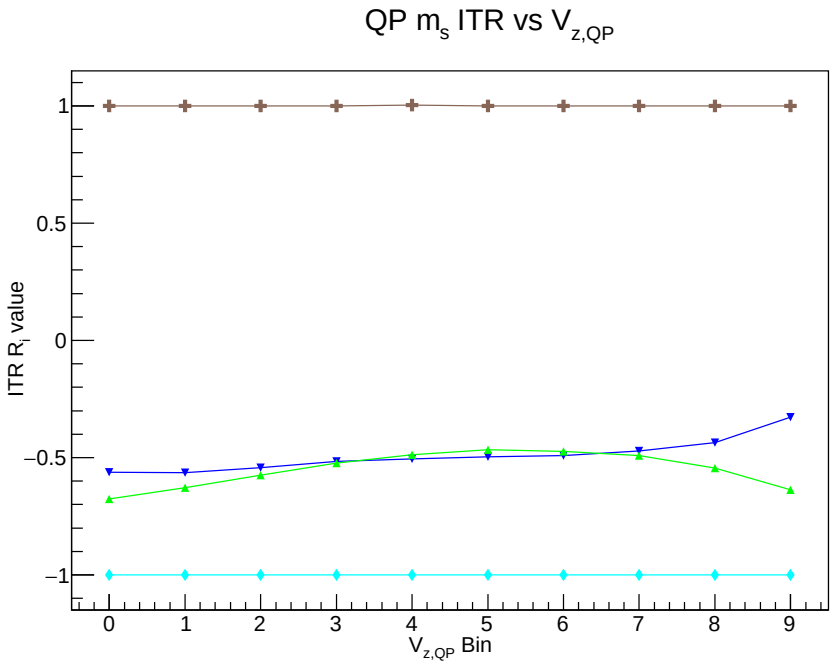

Figure D.52: Isospin Transport Ratio R_i for the QP m_s as a function of $V_{z,QP}$ bin in the "asy-stiff" CoMD for the A=64 set of reaction systems: $^{64}Ni + ^{64}Ni$ (brown crosses), $^{64}Ni + ^{64}Zn$ (blue triangles), $^{64}Zn + ^{64}Ni$ (green inverted triangles) and $^{64}Zn + ^{64}Zn$ (light blue diamonds).

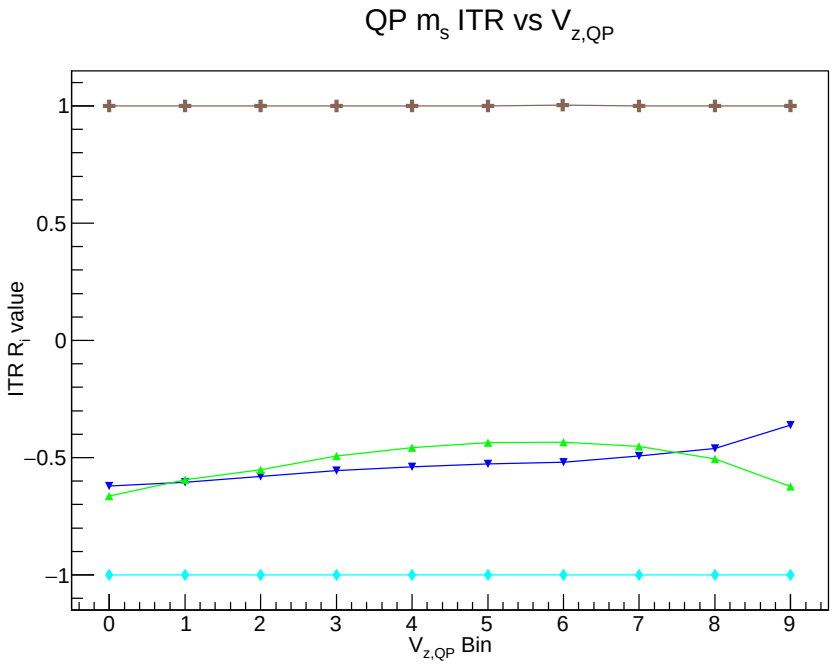

Figure D.53: Isospin Transport Ratio R_i for the QP m_s as a function of $V_{z,QP}$ bin in the "asy-super-stiff" CoMD for the A=64 set of reaction systems: $^{64}Ni + ^{64}Ni$ (brown crosses), $^{64}Ni + ^{64}Zn$ (blue triangles), $^{64}Zn + ^{64}Ni$ (green inverted triangles) and $^{64}Zn + ^{64}Zn$ (light blue diamonds).

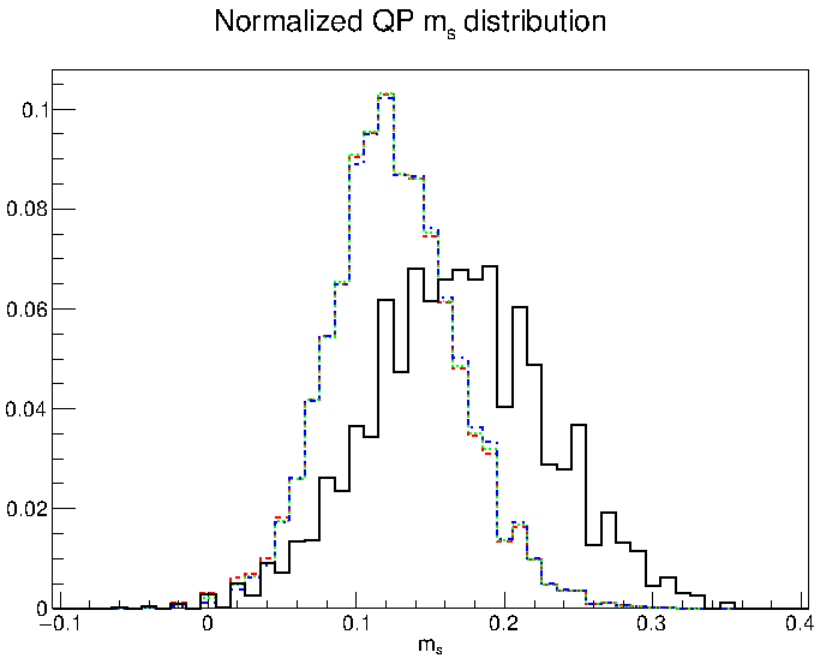

Figure D.54: The QP m_s distribution for the $^{70}Zn + ^{70}Zn$ reaction by the four different data types: experimental data (solid black line), "asy-soft" CoMD (dashed red line), "asy-stiff" COMD (dotted green line) and "asy-super-stiff" CoMD (dot-dashed blue line).

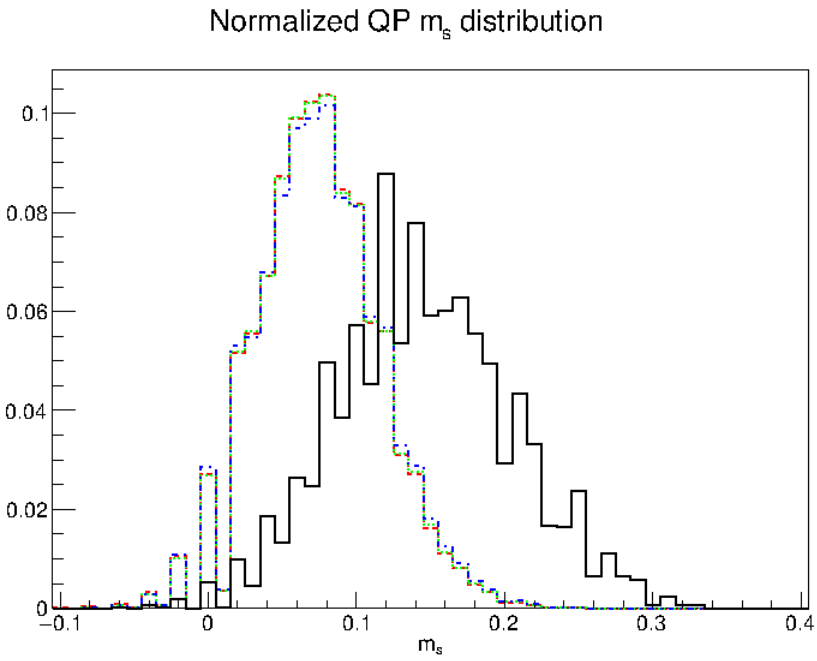

Figure D.55: The QP m_s distribution for the $^{70}Zn + ^{64}Zn$ reaction by the four different data types: experimental data (solid black line), "asy-soft" CoMD (dashed red line), "asy-stiff" COMD (dotted green line) and "asy-super-stiff" CoMD (dot-dashed blue line).

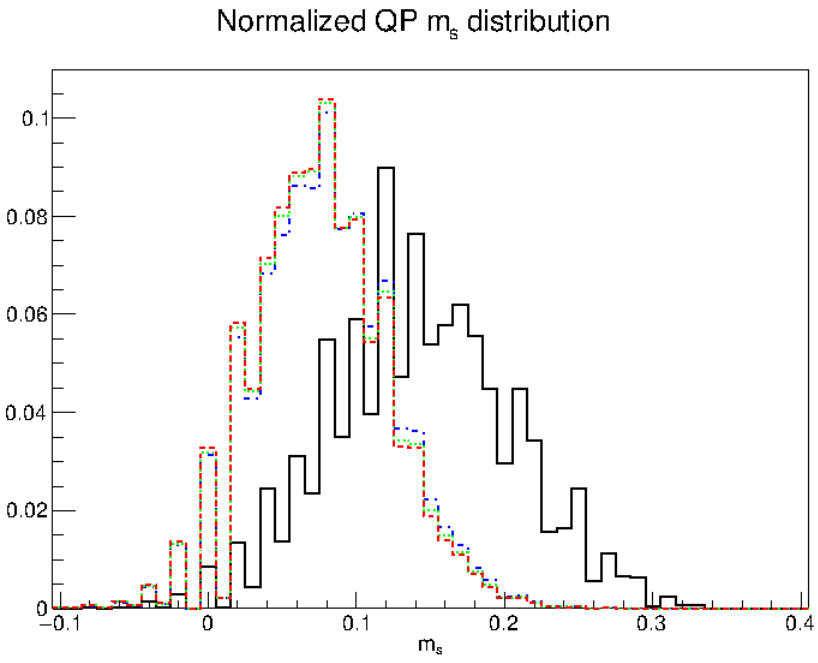

Figure D.56: The QP m_s distribution for the $^{64}Zn + ^{70}Zn$ reaction by the four different data types: experimental data (solid black line), "asy-soft" CoMD (dashed red line), "asy-stiff" COMD (dotted green line) and "asy-super-stiff" CoMD (dot-dashed blue line).

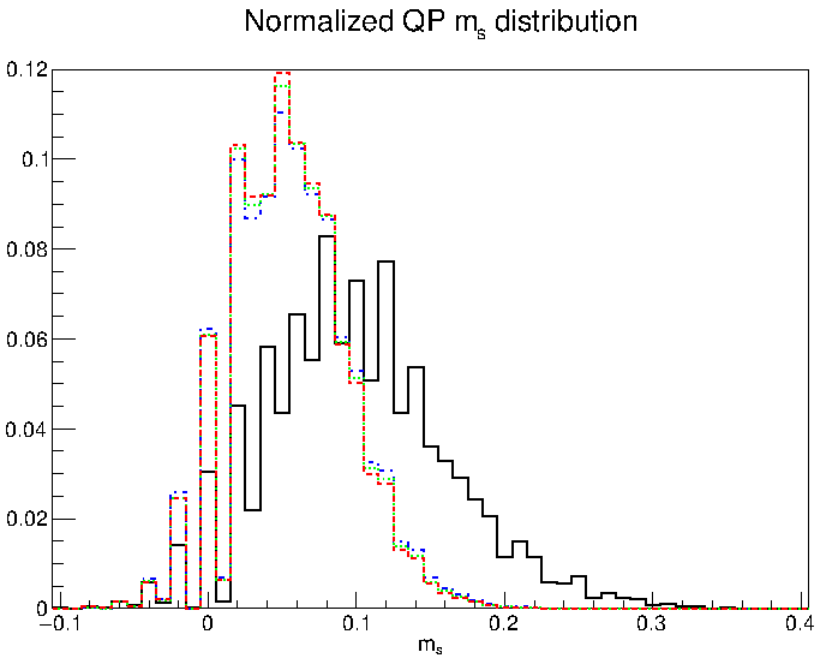

Figure D.57: The QP m_s distribution for the $^{64}Zn + ^{64}Zn$ reaction by the four different data types: experimental data (solid black line), "asy-soft" CoMD (dashed red line), "asy-stiff" COMD (dotted green line) and "asy-super-stiff" CoMD (dot-dashed blue line).

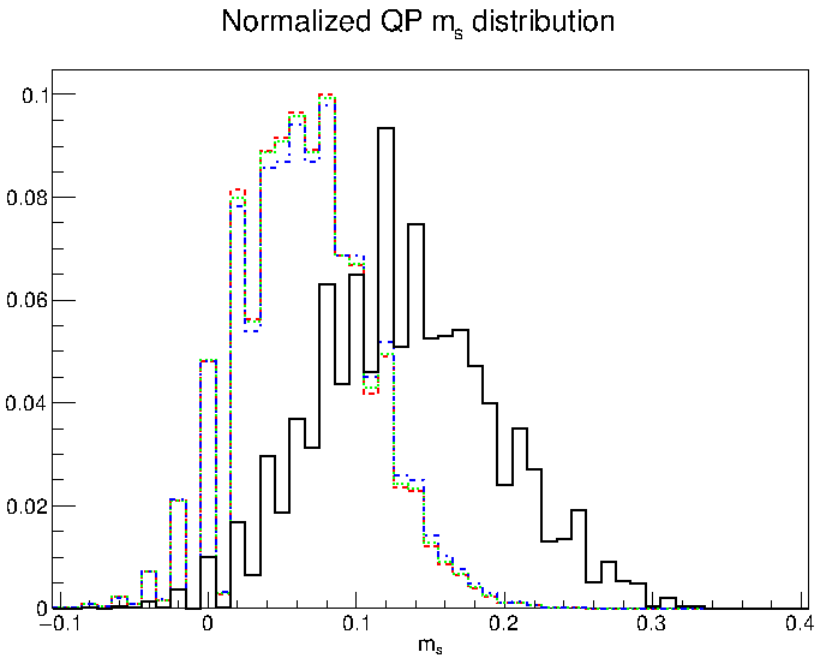

Figure D.58: The QP m_s distribution for the $^{64}Zn + ^{64}Ni$ reaction by the four different data types: experimental data (solid black line), "asy-soft" CoMD (dashed red line), "asy-stiff" COMD (dotted green line) and "asy-super-stiff" CoMD (dot-dashed blue line).

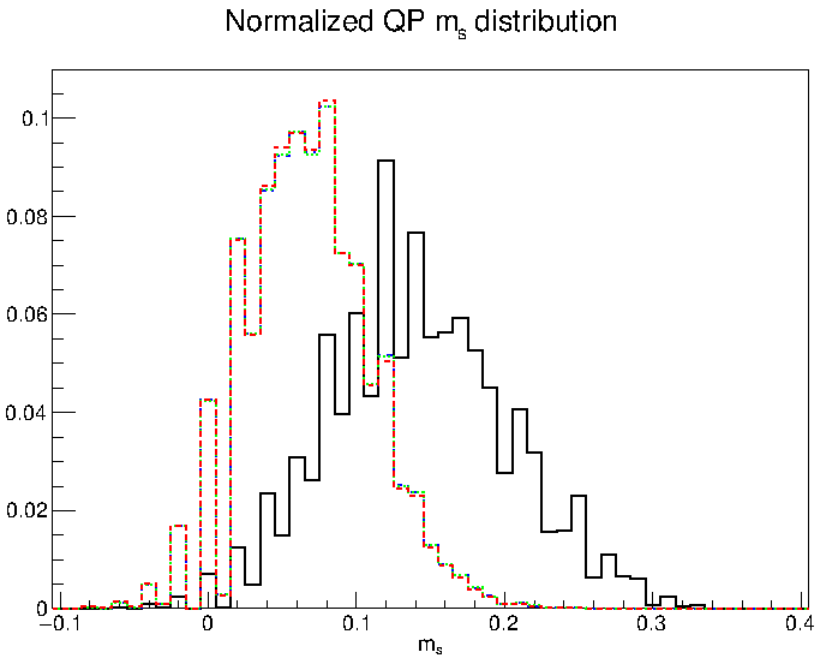

Figure D.59: The QP m_s distribution for the $^{64}Ni + ^{64}Zn$ reaction by the four different data types: experimental data (solid black line), "asy-soft" CoMD (dashed red line), "asy-stiff" COMD (dotted green line) and "asy-super-stiff" CoMD (dot-dashed blue line).

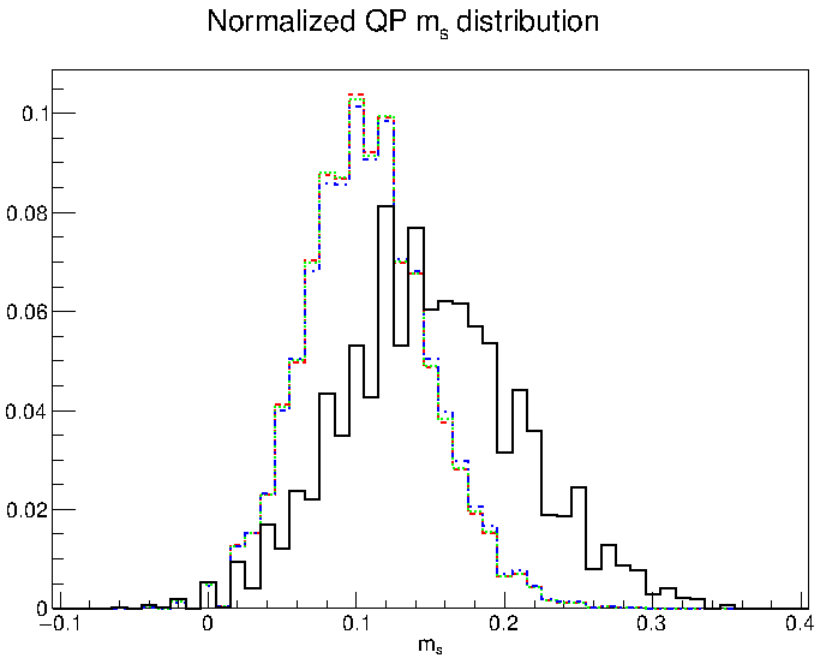

Figure D.60: The QP m_s distribution for the $^{64}Ni + ^{64}Ni$ reaction by the four different data types: experimental data (solid black line), "asy-soft" CoMD (dashed red line), "asy-stiff" COMD (dotted green line) and "asy-super-stiff" CoMD (dot-dashed blue line).